Heat transport in a single quantum dot device

Danial Majidi

THÈSE

Pour obtenir le grade de

DOCTEUR DE L'UNIVERSITE GRENOBLE ALPES

Spécialité : **NANOPHYSIQUE**

Arrêté ministériel : 25 mai 2016

Présentée par

Danial MAJIDI

Thèse dirigée par **Hervé COURTOIS, Université Grenoble Alpes**
codirigée par **Jukka PEKOLA, Aalto University, et**
Clemens WINKELMANN, Grenoble INP - UGA

préparée au sein du **Laboratoire Institut Néel, CNRS**
dans **l'École Doctorale Physique**

Transport de chaleur dans une boîte quantique

Heat transport in a single quantum dot device

Thèse soutenue publiquement le **15 décembre 2021**,
devant le jury composé de :

Madame Anne ANTHORE
Professeur, Université de Paris, Rapporteure

Monsieur Stefano RODDARO
Professeur Associe, Scuola Normale Superiore-Pisa, Rapporteur

Monsieur Silvano DE FRANCESCHI
Directeur de recherche, CEA Grenoble, Examinateur

Monsieur Heiner LINKE
Professeur, Faculty of Engineering, Lund University, Examinateur

Monsieur Franck Balestro
Professeur, Université Grenoble Alpes, Président

Acknowledgment

My first and foremost appreciation goes to my supervisor Hervé Courtois for giving me the opportunity to pursue my PhD in his group. Thanks for taking care of all the details, from guiding me for moving to France from Iran, and everything that you have done to make my work successful. I have always been really impressed by your passion and dedication to manage different responsibilities at the university and being a great scientist. Despite his busy schedule, he had always time for me. Hervé's persistence in understanding every phenomenon always motivated me to work harder and find answers to his questions. I never forget your phrase about my plots i.e., 'beauty is important', I will always keep this in mind, in particular whenever I want to plot data or prepare any presentation. Without his professional instruction ranging from sample fabrication to enthusiasm towards research, and reading my chapters during his vacations, this thesis could have not existed in the form it is now. I have learned so much from you as a scientist, a leader and from your personality. Hervé, Thank you for your role as a nurturing advisor.

Second, I wish to thank Clemens Winkelmann, my co-supervisor, whose door was always open to me whenever I ran into trouble and had a question about any ideas and wanted to discuss something, both big and small. His extensive knowledge on a broad range of scientific topics inspired me a lot. Starting from the first day, he set me on a track and taught me patiently almost everything for running experiments, handling a home-made dilution fridge and coming with me to cleanroom for different trainings. Thanks for rehearsing me before my presentations and giving your insightful pedagogical suggestions for making my presentations more intriguing and attractive. I do appreciate you for initiating many fruitful collaborations and involving me in there. I am grateful for trusting me and giving me freedom to conduct our collaborative projects.

I am also extremely grateful to my co-supervisor Jukka Pekola, for supporting and hosting me in his lab for two months during my visit in Helsinki. Those two months brought me lots of insight in device fabrication and thermometry techniques. Your positive attitude

at work, and sense of humor have influenced me a lot. It was really unfortunate that Covid-19 kicked in and I was not able to come back to continue conducting measurements with CBTs in Aalto.

When mentioning Helsinki and Aalto University, I wish to thank Joonas Peltonen, Marco Marin Suarez, Bayan Karimi, Rishabh Upadhyay, Diego Subero, Yu-Cheng Chang, Elsa Mannila, Olivier Maillet and Azat Gubaydullin. A special chapter of this story in Finland is dedicated to Joonas and Marco. They were always kind and supportive. We shared many long working days in the lab, and they instructed me very carefully, often solving my problems and answering my questions even before they actually arose.

I had a great opportunity to meet and collaborate with different scientists during doing my PhD. Especially, Ville Maisi from Lund University, who was like my unofficial co-supervisor. I would like to appreciate his limitless kindness and support. Special thanks to Martin Josefsson, Martin Leijnse, and Lars Samuelson, who were invaluable during our collaboration with Lund. Martin Josefsson has taught me a lot about the theory behind the experiments we conducted, and I am grateful that our collaboration was a success.

Along the same lines, I would also like to thank Nicola Lo Gullo, Elke Scheer, Alejandro Silhanek, Denis Basko, Benjamin Sacépé, Jean-Yves Veuillen, Pierre Mallet, Hermann Sellier, Laurence Magaud, Jeremie Viennot, and Brahim Lounis for all of the stimulating scientific and nonscientific discussions.

I thank Guido Piaszenski and Axel Rudzinski who hosted my secondment at RAITH GmbH headquarter in Germany. I really enjoyed my time at Dortmund. It was a very valuable experience to be in such dynamic environment at RAITH which provided a chance for me to learn so many things regarding electron beam lithography.

I thank Marie Skłodowska-Curie Actions and of course our amazing project manager, Hendrika Borsje-Hekking who has been very nice and supportive all along this path.

I wish to thank the jury, Anne Anthore, Stefano Roddaro, Silvano De Franceschi, Frank Balestro and Heiner Linke for their helpful advice, honest feedback, and insightful questions related to my research.

I would like to thank to my close friends, Alvaro, David W, Hugo, Chantal, Hadrien ,Ramla, David P, Wenmin, Simon (in Belgium), Marco (in Helsinki), Jacob, Charlote, Guillaume, Guislain, Monica who have been very supportive and reliable friends over this period. Without you this time would have looked very different to me. There is

no replacement for who you are to me, and I am grateful to you for your friendship and support!

I would also like to extend my gratitude to the fellows at the Institut Néel, Farshad, Bivas, Junliang, Jonathan W, Katee, Rini, Efe, Julliette, Alessandro, Corentin, Marco G, Alexi, Aymen, Riadth, Patrick, Arnaud, Cyril, Zahra, Sidd, Bernhard, Karthik, and at LMGP, Dorina, Alexandre, Chiara, Adrien, Carlose, Damir, Maxime, Morgan, Adria, and the others who all together have been a huge support during the challenging times of being a doctoral student. I wish also to thank the QuESTech friends, particularly, Willy, Danilo, Rebbeka, Naveen, Laura and Ananthu for the wonderful time we spent together and all their supports.

There are also many people behind administrative, technical, organizational matters and nanofab team that it would be hard to imagine all this work being done here without their assistance. Therefore, I would like to send my thanks to Florence Pois, Anne-Laure Jaussent, Angélique Simoes, Christophe Guttin, Thierry Crozes, Bruno Fernandez, Gwénaëlle Juile, Jean-Francois Motte and the others that have directly or indirectly contributed to make sure things were running smoothly at the Institut Néel.

Eventually, I want to extend my most profound appreciation to my beloved wife, my parents, my brother, my in-laws, Elmira, Marco, and my friends in Iran in particular Khashayar Shahravan, Mohammadreza Hassannejad Bibalan, Mohammad Dosaranian-Moghadam and Ali Shahhoseini. Despite the fact that some of you were not present here, talking to you on a regular basis has always been motivating and very important to me. In particular my beloved wife, Tabassom, who was a big part of my life here and supported me the most. She stood my coming home late, working on weekends, and listened to my stories and difficulties. Tabassom, without your continual support, this journey would not have been possible.

Abstract

Quantum dots are an attractive model system for basic studies and applications in thermoelectricity, owing to their tunable electronic transmission and electron-hole asymmetry. In the weak coupling regime, the discreteness of the quantum dot energy spectrum makes electronic transport processes strongly selective in energy. The net heat flow is zero in such a device since electrons tunnel back and forth exactly using the same energy level. Therefore, a weakly coupled quantum dot is in principle a good thermal insulator as heat conductance is zero regardless of the position of the quantum dot level with respect to the energy.

We investigate heat flow in two different quantum dot devices. First, in a metallic single quantum dot junction, fabricated using the electromigration technique, we experimentally measured heat conductance in the presence of strong co-tunneling effects using a sensitive superconductor-normal metal-superconductor (S-N-S) junctions as a local temperature probe of the leads. We demonstrate the gate control of the electronic heat flow, in agreement with the numerical calculations. Electron temperature maps taken in the immediate vicinity of the junction, as a function of the gate and bias voltages applied to the device, reveal clearly defined Coulomb diamond structures. In addition, we combine charge and heat conductances which demonstrate a violation of the Wiedemann-Franz law in the intermediate coupling regime.

Then, we move to InAs nanowire based-devices, as they have attracted considerable attention due to their remarkable tunability on the coupling of the quantum dot and their stability in time for thermoelectric applications. We report on a simultaneous measurements of heat and charge transport using a sensitive superconductor-insulator-normal metal (S-I-N) electron thermometer integrated inside the device. We demonstrated an adjustable and strongly energy-selective heat conduction significantly below the Wiedemann-Franz prediction. Moreover, the observed phenomena in both experiments agree well with the theoretical calculations.

Résumé

Les boîtes quantiques constituent un système attrayant pour les études fondamentales et les applications en thermoélectricité, en raison de leur transmission électronique ajustable et de leur asymétrie électron-trou naturelle. Dans le régime de couplage faible, la discrétisation du spectre d'énergie d'une boîte quantique rend les processus de transport électronique fortement sélectifs en énergie. Le flux net de chaleur est nul dans un tel dispositif puisque les électrons se déplacent par effet tunnel en utilisant exactement le même niveau d'énergie. Par conséquent, la conductance thermique est nulle quelle que soit la position du niveau de la boîte quantique par rapport à l'énergie. Une boîte quantique faiblement couplée est aussi un bon isolant thermique.

Nous étudions le flux de chaleur dans deux dispositifs à boîtes quantiques différents. Premièrement, dans une jonction métallique à boîte quantique unique, fabriquée à l'aide de la technique d'électromigration, nous avons mesuré expérimentalement la conductance thermique en présence de forts effets de co-tunneling en utilisant une jonction sensible supraconducteur-métal normal-supraconducteur (S-N-S) comme sonde de température locale. Nous démontrons le contrôle par la grille du flux de chaleur électronique, en accord avec les calculs numériques. Les cartes de température des électrons prises dans le voisinage immédiat de la jonction, en fonction de la grille et des tensions de polarisation appliquées au dispositif, révèlent des structures en losange de Coulomb clairement définies. En outre, nous combinons les conductances de charge et de chaleur à travers une jonction de boîtes quantiques réalisée par cette méthode, ce qui démontre une violation de la loi de Wiedemann-Franz dans le régime de couplage intermédiaire.

Ensuite, nous passons aux dispositifs à base de nanofils d'InAs, car ils ont attiré une attention considérable en raison de leur remarquable ajustabilité sur le couplage de la boîte quantique a ses contact et de leur stabilité dans le temps. Nous rapportons des mesures simultanées du transport de chaleur et de charge unique en utilisant un thermomètre électronique sensible de type supraconducteur-isolant-métal normal (S-I-N) intégré dans

le dispositif. Nous montrons une conduction thermique ajustable et fortement sélective en énergie, significativement inférieure à la prédiction de Wiedemann-Franz. En outre, les phénomènes observés dans les deux expériences concordent bien avec les calculs théoriques.

Contents

List of Figures

List of Tables

Outline

In this fast-paced world, people are often tangled up with their own lives. This leads people to follow a common notion, 'the faster, the better', 'the more compact, the better', 'the more durable, the better'. Rapid progress in high-speed and densely-packed electronic devices has imported outstanding advantages to our society. However, this technology trend has in reverse led to a substantial increase in heat dissipation, which degrades device performance and lifetime [1]. Therefore, heat flow plays a significant role because it is either a parasitic effect and is therefore undesired, as is the case in thermoelectrics, or because high heat flow is critically required for thermal management [2, 3, 4, 5, 6].

When the size of a material is reduced into a nano-scale, the material properties change significantly and the new variable length scale, i.e. electron wavelength, impacts their charge and heat transport properties. As depicted in Fig. 1, this size-dependent change in the density of states is commonly referred to as quantum confinement . As the system size approaches nanometer length scales, there are dramatic differences in the electronic density of states (DOS) of the system. The density of states is varying roughly speaking from the square root dependence $E^{1/2}$ in a bulk, through a step-like dependence E^0 in quantum wells and an inverse square root dependence $E^{-1/2}$ in quantum wires to discrete delta function in a quantum dot [7]. In the case of bulk structures, the carried charge and heat by the electrons in the system is in the order of k_BT, whereas this picture can be significantly modified in the presence of interactions and correlations in 1D and 0D devices [7]. For instance, the discrete nature of the energy states causes a unique energy selective transport property of quantum dots, which can not be observed with higher dimensionality systems.

The study of charge transport in the quantum dot device has already allowed the exploration of a large palette of physical effects at play, heat transport and thermoelectric properties have been investigated in a limited number of cases, e.g. in quantum dots formed in a two-dimensional electron gas (2DEG) [8, 9, 10] and in semiconducting nanowires

[3, 11, 5]. As opposed to charge transport processes, the understanding of electronic heat transport and generation across a nano-scale object is, experimentally, still in its infancy [12, 13, 14].

Quantum dots can generate a large electric current from a temperature gradient but with a minimal heat flow which is the cornerstone of thermoelectric applications [15, 16, 17, 18, 19]. Therefore, they became the "best thermoelectric" as theorised by Mahan and Sofo [20], because carriers can be tuned so that they carry the same amount of charge but more or less heat current depending on where the quantum dot level happens to be. This idea of having such an ideal high energy electron filtration was further explored by Humphrey *et al* [16, 21] and Dutta *et al* [22] in recent years.

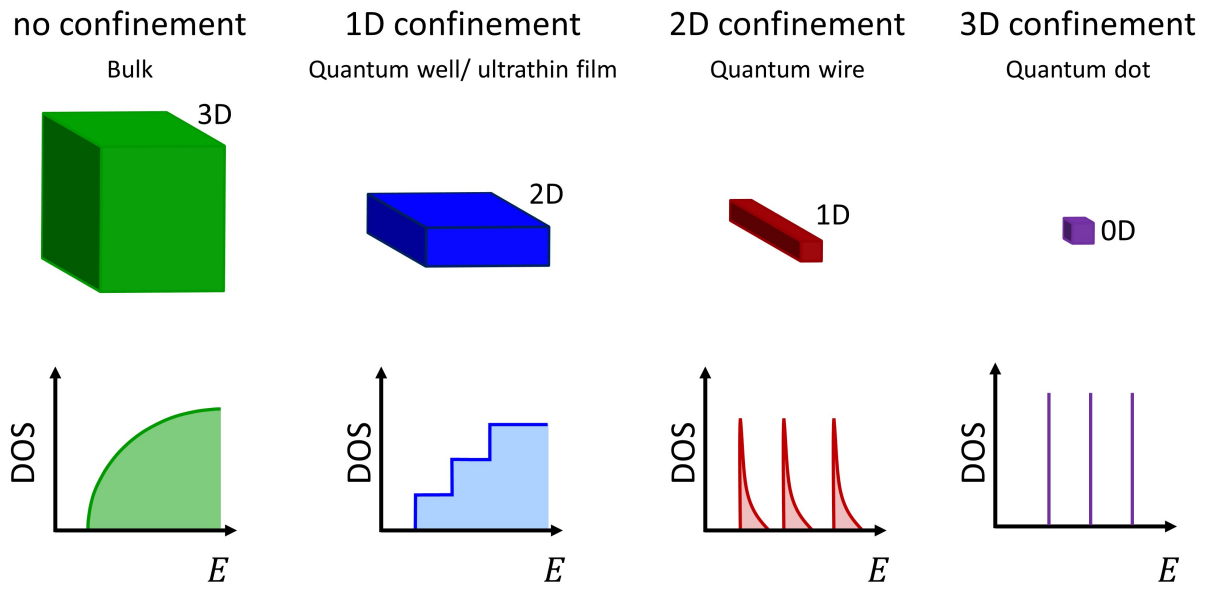

Fig. 1: Schematic illustration of the density of states (DOS) as a function of energy for a 3D, 2D, 1D and 0D electronic systems.

An important ingredient in all thermoelectric experiments is to have a local electronic thermometer, as measuring a temperature or gradient temperature is a significant problem in such studies. Local thermometry has been achieved only in a very limited number of quantum devices. The temperature dependence of the critical current of a superconducting weak link was used in scanning probe experiments to reveal for instance the scattering sites in high-mobility graphene [23, 24]. Yet, to date, these experiments are limited to temperatures above 1 K. At milliKelvin temperatures, local thermometry can be performed in quantum devices formed in a 2DEG by a variety of methods [25, 26] that have recently been pushed to quantitative accuracy [6, 27, 28]. Noise thermometry was applied to thermo-

electric measurements in InAs nanowires [29]. In metallic devices, electronic thermometry is usually based on the temperature dependence of charge transport in superconducting hybrids, either in the tunnelling regime for Normal metal-Insulator-Superconductor (NIS) junctions [30, 31] or at higher transparencies allowing for superconducting correlations [32, 33]. This has recently allowed the realization of a photonic heat valve with a superconducting qubit coupled to heat reservoirs (probed by NIS probes) through coplanar waveguide resonators [34].

Combining single electron transistor (SET) with the NIS thermometry technique, enables the measurement of the thermal conductance of a metallic SET [22]. Despite the continuous density of states in the metallic island, electron interactions readily lead to striking deviations from the Wiedemann-Franz law [35]. Going beyond this simple case, two questions arise: (i) how does such a SET behave thermally beyond equilibrium, that is, at finite voltage bias and/or at large temperature difference where both Joule heat and heat transport are to be taken into account, and (ii), if the central island is replaced by a quantum dot (QD), how would the discrete nature of its energy spectrum manifest in the thermal properties of the device? In the weak coupling regime, the discreteness of the QD energy spectrum makes electronic transport processes strongly selective in energy. At zero net particle current, whatever the gate voltage, the heat flow is zero since electrons tunnel back and forth exactly at the energy level defined by the QD. The heat conductance is thus zero at all gate voltages. Heat transfer is predicted only at non-zero particle current, when the QD energy level is positioned just above or below the Fermi level of the hot lead, so that high-energy electrons can escape through the dot, or low-energy electrons can be injected there [36, 26].

In conductors, a higher electrical conductance G is generally associated to a correspondingly higher heat conductance κ. The Wiedemann-Franz (WF) law indeed stipulates that at a given temperature T, the ratio defined as $L = \kappa/GT$ is constant and equal to the Lorenz number $L_0 = (\pi^2/3)(k_B/e)^2$. Deviations indicate departures from Fermi liquid physics [37] such as those found in superconductors [38], correlated electron systems [39], Majorana modes [40] or viscous electron flow [41]. In quantum nanodevices, Coulomb interaction and charge quantization in metallic nanoislands were also shown to lead to departures from the WF law [35, 22, 27].

In semiconductors, the WF law is notoriously well obeyed for the electronic contribution to heat conductance, including semiconducting nanostructures displaying transport in

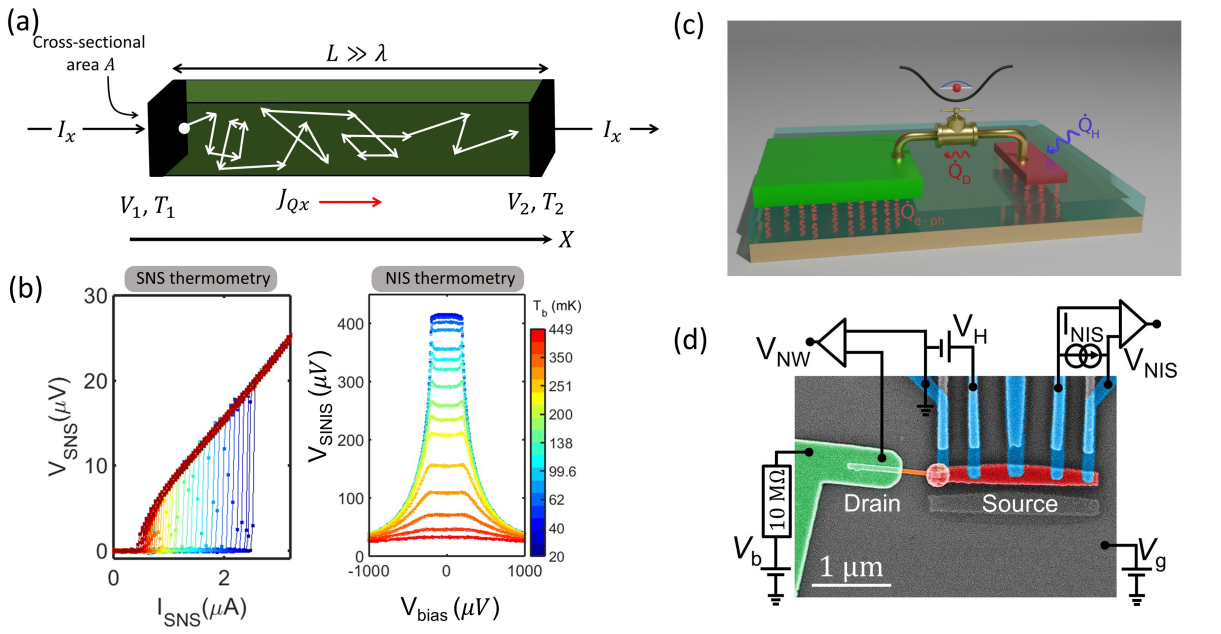

Fig. 2: Abstract graphic of different chapters discussed in this thesis. (a) theoretical background chapter 1. (b) Superconducting hybrid thermometery in chapter 3. (c) Heat valve effect in chapter 4. (d) Heat conductance of an InAs nanowire in chapter 5.

the quantum Hall state [6, 28]. This property imposes severe limitations for instance in thermoelectrics, for which it is desirable to maximize the charge flow while minimizing that of heat. The most common figure of merit for thermoelectric conversion, ZT, is indeed directly proportional to L^{-1}. Nevertheless, semiconducting nanostructures can display adjustable and strongly energy-selective transport processes, which could also lead to breaking the WF law, even in the absence of interaction effects. This can be provided for instance by the quantization of the energy levels in a single-quantum-dot junction, allowing for an adjustable narrow transmission window in energy. Although the theory has predicted a vanishing L/L_0 for weakly tunnel-coupled quantum dots at low temperatures [42, 43, 44, 18, 45, 46], it was experimentally shown that higher-order effects restore a significant electronic heat leakage [47]. The validity of the WF law in a single-quantum-dot device has however not yet been quantitatively investigated because of the difficulty in measuring the extremely small heat currents.

I have been involved in many projects since the beginning of my PhD at Néel institute and had the opportunity to establish the following fruitful collaborations.

- Direct probe of the Seebeck coefficient in a Kondo-correlated single-quantum-dot transistor.

B. Dutta, **D. Majidi**, A. García-Corral, P. Erdman, S. Florens, T. A. Costi, H. Courtois, C. B. Winkelmann. *Nano Lett., 19(1), (2018), pp. 506-511*

I carried out the literature study, took part in device fabrication, had significant role in the measurements and participated to the writing.

- A Single-Quantum-Dot Heat Valve.

B. Dutta, **D. Majidi**, N. W. Talarico, N. Lo Gullo, H. Courtois, C. B. Winkelmann. *Phy. Rev. Lett., 125(23), (2020), p.237701*

I fabricated the device together with B. Dutta, performed the characterization of the device and carried out a part of the measurement. I built sample holders used in cryostat. I also did numerical calculation to answer referee's questions. All the six co-author including me co-wrote the manuscript.

- Quantum confinement suppressing electronic heat flow below the Wiedemann-Franz law

D. Majidi, M. Josefsson, M. Kumar, M. Leijnse, L. Samuelson, H. Courtois, C. Winkelmann, V. F. Maisi. *Nano Lett. 22(2), (2022), pp. 630–635*

I was involved in the design of the sample, I had main responsibility of the data analysis, prepared all the figures, wrote the major part of supplementary information and contributed to the writing of the main paper.

- The effect of co-tunneling on heat transport of a single quantum dot.

D. Majidi, T. Arjmand, V.F. Maisi, C. B. Winkelmann, H. Courtois.

Under preparation

I fabricated the sample, performed all of the experiments, result analysis and wrote the majority of the manuscript.

- Probing quasiparticle excitation in a hybrid Single Electron Transistor (SET).

D. Majidi, M. Marín-Suárez, C. B. Winkelmann, H. Courtois, J. Peltonen, J. Pekola.

Under analysis - Ongoing

I worked basically on 3 projects in parallel: improving quasiparticle relaxation, measuring electron-phonon coupling constant of thin AlMn films and fabricating Coulomb

blockade thermometers (CBTs) for high temperature thermometry during my secondment in Aalto University. I fabricated different SETs, I measured some of them there. I have been analyzing data together with M. Marín-Suárez.

- Targeted modifications of monolithic multiterminal superconducting weak-links.

S. Collienne, **D. Majidi**, H. Courtois, C. B. Winkelmann, A. V. Silhanek.

In press, Nanoscale, (2022).

I fabricated the single and multiterminal superconducting weak-links, and SQUIDs on Silicon and Sapphire substrates. In addition, I participated in the measurements done in Grenoble.

- Calorimetry of a quantum phase slip

E. Gümüs, **D. Majidi**, D. Nikolić, P. Raif, B. Karimi, J. T. Peltonen, E. Scheer, J. P. Pekola, H. Courtois, W. Belzig, C. Winkelmann. *arXiv:2202.08726*

I designed the sample, I optimized the recipe for two generation of the samples and carried out a significant part of fabrication. I also participated in the data interpretation and writing the manuscript.

Unfortunately, Not all of these projects can be fitted to the scope of this thesis. A large part of the two main chapters are taken from my two publications that have been accomplished in collaboration with my colleagues. During the first year of my PhD, with my predecessor Bivas Dutta, we fabricated a QD device and measured the Seebeck coefficient in a tunnel-contacted and gate-tunable individual single quantum dot junction in the Kondo regime which can be found here [48]. In addition, in cooperation with Bivas, we measured some of the temperature maps that I will present in chapter 4. However the sample that we fabricated with Bivas was not stable enough and it passed away during the measurement. When Bivas left, I continued fabricating other samples and eventually, I was able to conduct thermal transport measurements in a QD device realized with the electromigration technique (the second part of chapter 4). After demonstrating that a single QD device can act as a heat-valve controlled by a gate voltage and showing preliminary results on thermal conductance of a single quantum dot, we moved on a different realization of quantum dot based on InAs/InP nanowires in close collaboration with Dr. Ville Maisi. We began to use heterostructured nanowires provided by NanoLund and integrating them with proximized SNS local thermometers at Néel Institute, and at

the same time Dr. Maisi was fabricating hybrid devices with NIS thermometers using bare InAs nanowires. The device fabrication and the experiment we present in chapter 5 were conducted by Dr. Maisi at Lund University and I took over of the data analysis.

During both works, collaborations with the theory groups in Finland (Dr. N. W. Talarico and Dr. N. Lo Gullo), and in Lund (Dr. M. Josefsson, Prof. M. Leijnse) were lead and benefit the overall thesis project.

A brief description of the content of my work here follows as, this thesis presents heat transport in 0D structures, i.e. metallic and semiconductor nanowire quantum dots as shown in Fig. 2. The physical concepts presented in chapter 1 will extensively be considered for the investigation of thermal transport through quantum dot devices in chapter 4 and 5. The nanofabrication techniques to have single quantum dot devices coupled to local electronic thermometers are discussed in chapter 2 and the optimization of thermometers operation together with their theory described in chapter 3. These three chapters will be important ingredients to report on the operation of a single metallic quantum-dot heat valve in chapter 4, where we measure heat flow thanks to strong co-tunneling effects. Eventually, we report on the violation of Wiedemann-Franz law in a metallic quantum dot in the second part of chapter 4. We demonstrate a tunable ratio of heat to charge conduction in an InAs nanowire in chapter 5.

Chapter 1

Thermoelectric transport coefficients

In this chapter, we discuss the physics of thermoelectricity using a quite simple mathematical argument to develop the basic equations for thermoelectric coefficients. First, our discussion assumes a 1D conductor and diffusive transport. Once we get the mathematical description of thermoelectricity coefficient, then, we extend everything to describe thermoelectricity in 0D, 2D or 3D and under ballistic or quasi-ballistic conditions.

Contents

1.1 Thermoelectricity

Thermoelectric devices are able to convert heat into electricity or electric power into cooling or more trivially heating power. Naively speaking, thermoelectricity is about heat and charge current flow due to temperature and bias differences. The underlying physical concept of thermoelectricity is quite easy to appreciate. The goal of this chapter is to translate these physical concepts to simple mathematical expressions for thermoelectric coefficients using Landauer approach that will be utilized to analyze real devices in chapter 4 and 5 of this thesis. Eventually, we discuss the relation of all the four thermoelectric coefficients together to understand the fundamental physical properties of nano-devices and give some experimental examples to show how one can measure all these quantities in real life.

1.1.1 The experiment

In general, when it comes to current flow, usually one starts from a macroscopic set of equations. The basic experiment that we are going to discuss is illustrated in Fig. 1.1. It assumes a slab of conductor (e.g. a resistor), many mean-free-paths long, i.e. in the regime of diffusive transport $L \gg \lambda$, (L is the length of our conductor and λ is the mean-free-path). Later on, we will talk about quantum dots but for the moment we start with bulk thermoelectrics. The experiment consists of doing the following: (i) An electrical current I_x is forced through the resistor, (ii) We impose a temperature gradient, (iii) A voltage, $V_2 - V_1$ or electric field $\mathcal{E}_x = (V_2 - V_1)/L = dV/dx$ is measured across the device. (iiii) We also measure the heat current through this resistor.

The electrons carry heat as they go from one end to the other end of the device. The atomic lattice also carries heat but its discussion is beyond the scope of our studies [49]. Electron flows in such a conductor are a well-known and well-documented fact [50, 51, 52]. The current flowing in our conductor shown in Fig. 1.1 is written in the limit of zero temperature bias as,

$$J_x = \sigma.\mathcal{E}_x \qquad (A/m^2) \tag{1.1}$$

which can also be written as

$$\mathcal{E}_x = \rho J_x \tag{1.2}$$

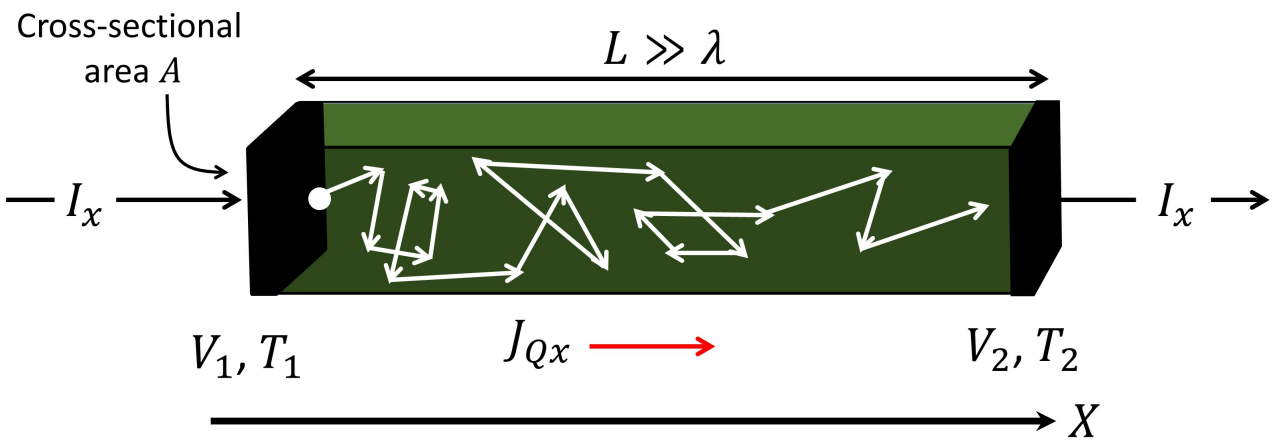

Fig. 1.1: An illustration of a nanoscale electronic device. The voltage, V_2, lowers the Fermi level of contact 2 by an amount, qV. T_1 and T_2 are the temperature of the left and right contacts, respectively.

The electric field ($\mathcal{E}_x$) is thus related to the current density (J_x) multiplied by resistivity (ρ). When it comes to thermoelectricity, one would add an extra term which would be related to temperature gradient and rewrite the Eq. (1.1) as:

$$\mathcal{E}_x = \rho J_x + S\frac{dT}{dx} \tag{1.3}$$

where S is the thermopower (i.e Seebeck coefficient) in V/K and $\frac{dT}{dx} = (T_2 - T_1)/L$ is the temperature gradient across the device. This effect was introduced for the first time in 1821 by Thomas Johann Seebeck. He observed that a temperature difference across a junction of two different metals produce a voltage, or an electric current if one closes the circuit [53].

In addition to the equation for the charge current, we need an equation for the heat current too. Electrons going from the left contact to the right contact, carry heat from one side to the other side. As this heat follows Fourier's law the temperature gradient, one would expect an equation in the form of,

$$J_{Qx} = -\kappa\frac{dT}{dx} \qquad\qquad (W/m^2) \tag{1.4}$$

The above Eq. (1.4) is completed in the presence of an electric field as,

$$J_{Qx} = \pi J_x - \kappa_e\frac{dT}{dx} \tag{1.5}$$

there

$$\pi = T \cdot S \tag{1.6}$$

is the Peltier coefficient which was introduced a few years after the Seebeck effect in 1834 by Jean Charles Athanase Peltier. He demonstrated that the Seebeck effect can also work in reverse. He showed that an electric current could be used to produce a temperature difference. These phenomena were later known as thermoelectric effect [54]. In addition, in Eq. (1.5), κ_e is the electronic thermal conductance for an open-circuit condition (zero current flow).

The Eq. (1.3) and (1.5) are known as coupled flows' equations . A temperature gradient produces an electrical current, and an electrical current produces a flow of heat. In other words, both the electric field and the heat current are related to the charge current that is forced and the temperature gradient that is imposed to the device. The Seebeck and Peltier coefficients are fundamentally related quantities through the Kelvin relation. This is a specific example of *Onsager relation*, which relates the coupling terms in the coupled flows' equations [52].

1.1.2 Mathematical expression for thermoelectric coefficients

Let us start by introducing a conceptual picture which is a small nano-device with a length L as illustrated in Fig. 1.2. We have two electrical contacts to the device which are very large regions compared to the device with lots of inelastic scattering that maintain the thermal equilibrium constantly. Each contact has a well-defined Fermi level. However, the Fermi functions might differ, i.e. each contact may have different temperatures or different bias voltages.

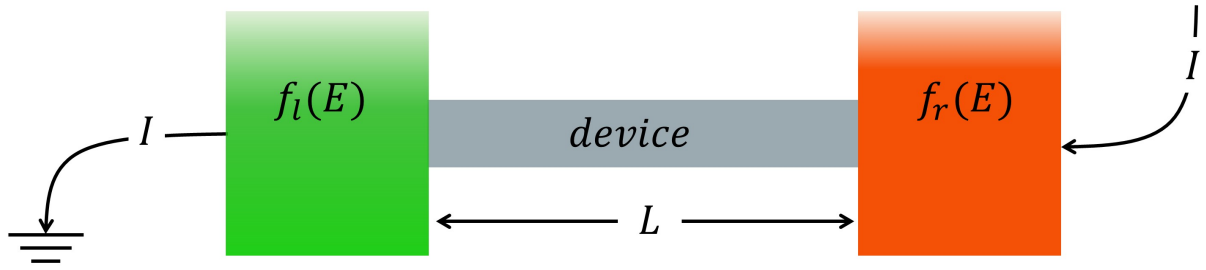

Fig. 1.2: A conceptual thermoelectric device in an imbalance situation. L is the length of the device channel that in our work is in the order of few hundreds nanometers. Electrons in each reservoir are non-interacting and obeying Fermi-Dirac statistics. $f_l(E)$ and $f_r(E)$ are Fermi distribution functions at left and right contacts, respectively.

1.1.2.1 Electrical and heat current

The current passing through the mentioned device in Fig. 1.2 can be calculated using the general Landauer transport theory [55, 50, 51, 56] as,

$$I = -I_x = \frac{2e}{h} \int_{-\infty}^{\infty} \mathcal{T}(E) \cdot M(E) \cdot \Delta f \; dE, \tag{1.7}$$

where

$$\Delta f = f_r - f_l, \quad f_n = \left(\exp\left(\frac{E - \mu_n}{k_B T_n} \right) + 1 \right)^{-1}, \tag{1.8}$$

where k_B is the Boltzmann constant. Here T_n and μ_n are the temperature and chemical potential of the left or right contacts, respectively. In addition, e and h are the charge of electron and Planck's constant, respectively. Eventually, $\mathcal{T}(E)$ is the transmission of the system and $M(E)$ is the number of channels for electrons to flow at energy E from the left to the right contact.

One can write an expression for the heat current in the same way according to the Landauer formalism [51, 56] by keeping in mind that electrons are particles that can carry both charge and heat. The only thing that we should do is to bring the e and replace it with $E - \mu_n$ in Eq. (1.7) inside the integral, because now the energy with which electrons are being transferred is considered. Consequently, the heat is,

$$\dot{Q}_l = \frac{2}{h} \int_{-\infty}^{\infty} (E - \mu_l) \mathcal{T}(E) \cdot M(E) \cdot \Delta f \; dE, \tag{1.9}$$

$$\dot{Q}_r = \frac{2}{h} \int_{-\infty}^{\infty} (E - \mu_r) \mathcal{T}(E) \cdot M(E) \cdot \Delta f \; dE, \tag{1.10}$$

where $\dot{Q}_l$ and $\dot{Q}_r$ correspond to the extracted heating from the left contact and deposit it to the right contact, respectively. Assuming no heat drained to phonons, one can write

$$\dot{Q}_l - \dot{Q}_r = I \Delta V \tag{1.11}$$

where ΔV is the voltage difference between left and right contacts, respectively.

Let's consider each quantity used in Eq. (1.7) and Eq. (1.10) before moving forward with thermoelectric coefficients.

Transmission ($\mathcal{T}(E)$): Transmission simply tells us if we inject electrons from one contact, these electrons experience a stochastic process while going from the left contact to the right contact of the device and eventually, only a fraction of them exit from the other

end of the device. In a ballistic regime where a conductor is short enough so that electrons can travel straightforward from one electrode to the other one like a bullet (without changing momentum), the transmission is $\mathcal{T}(E) = 1$. However, not all of conductors are short enough for electrons to behave the like bullets. In particular, when the sample length is much longer than the mean-free-path ($L \gg \lambda$), but still in the elastic regime, the transport process is called diffusive. The energy-dependent mean-free-path $\lambda(E)$ is the average distance at which an electron can travel before getting scattered and L is the length of channel. In the latter regime, which is particularly interesting for us, $\mathcal{T}(E)$ is a number between 0 and 1 and reads as [57]

$$\mathcal{T}(E) = \frac{\lambda(E)}{\lambda(E) + L}. \tag{1.12}$$

Eq. (1.7) can be applied for calculating the current in smaller devices (0D, i.e. a quantum dot), however, one should be careful and define the $\mathcal{T}(E)$ correctly. In single level devices, the connection of the contacts to the channel is described by a characteristic time τ, which explains how long it takes electrons to get in and out of the quantum dot's level and it is controlled by the contacts. If we assume a single level quantum dot or a single molecule in the channel, then a tunnel coupling can be expressed in the unit of energy according to $\Gamma = \hbar/\tau$. This quantity has a clear physical interpretation which indicates the broadening of the quantum dot level due to the finite lifetime of the electrons in the level [55, 56]. A conventional approximation for $\mathcal{T}(E)$ in Coulomb blockaded regime of a quantum dot is a Lorentz approximation which is an approximation for $\mathcal{T}(E)$ near a resonance [58], i.e. at charge degeneracy point given by,

$$\mathcal{T}(E) = \frac{4\hbar^2\gamma_l\gamma_r}{\Gamma^2} \frac{\left(\frac{\Gamma}{2}\right)^2}{(E - (\varepsilon - e\alpha V_g))^2 + \left(\frac{\Gamma}{2}\right)^2}, \tag{1.13}$$

where $\Gamma = \hbar(\gamma_l + \gamma_r)$.

Number of modes $M(E)$: The number of channels is proportional to the density of states $D(E)$, i.e. the more states a system has, the more channels it has. But electrons need to have a velocity in order to move in these states. So, $M(E)$ is defined as [55, 50, 51, 56],

$$M(E) = \frac{h}{4}\langle v_x \rangle D(E) \tag{1.14}$$

where $\langle v_x \rangle$ is the average velocity in the direction that the current is flowing (1D, only x direction), and D(E) is the density of states.

	1D	2D	3D
$\langle v_x \rangle$	$v(E)$	$\frac{2}{\pi}v(E)$	$\frac{1}{2}v(E)$
$D(E)$	$\frac{L}{\pi\hbar}\sqrt{\frac{2m^*}{E-E_c}}\Theta(E-E_c)$	$W\frac{m^*}{\pi\hbar^2}\Theta(E-E_c)$	$\Omega\frac{m^*\sqrt{2m^*(E-E_c)}}{\pi^2\hbar^3}\Theta(E-E_c)$
$M(E)$	$\Theta(E-E_c)$	$W\frac{\sqrt{2m^*(E-E_c)}}{\pi\hbar}\Theta(E-E_c)$	$\Omega\frac{m^*}{2\pi\hbar^2}(E-E_c)\Theta(E-E_c)$

Tab. 1.1: Expressions for velocity (v), density of states (D) and number of modes for 1D, 2D and 3D conductor with single parabolic band model defined as $E(k) = E_c + \hbar^2k^2/2m^*$ where k is the wave vector. E_c is the bottom of the conduction band, m^* is the electron effective mass, Θ is the unit step function, W and Ω are the width and the area of the 2D and 3D conductors, respectively.

We now assume a parabolic dispersion relation with energy bands of,

$$\frac{1}{2}m^*v^2(E) = E - E_c \rightarrow v(E) = \sqrt{2(E-E_c)/m^*} \tag{1.15}$$

where m^* is the effective mass and E_c is the bottom of the conduction band. We consider the average of velocity in the direction of the current flow. In a 1D conductor, there is only one direction, therefore, the average velocity is equal to just velocity as shown in Eq. (1.15). For a 1D conductor the density of state goes one over square root of energy, as the following,

$$D(E) = \frac{L}{\pi\hbar}\sqrt{\frac{2m^*}{E-E_c}}\Theta(E-E_c) \tag{1.16}$$

where Θ is the unit step function. By multiplying Eq. (1.15) with Eq. (1.16), one can get the number of modes as,

$$M(E) = \Theta(E-E_c). \tag{1.17}$$

As it can be seen from Eq. (1.17), $M(E)$ is independent of energy above the bottom of the conduction band E_c as energy terms in $v(E)$ and $D(E)$ cancel out together.

A 2D or 3D case is relatively a straightforward extension of the above discussion. The corresponding density of states and velocity [57, 51, 56] are summarized in table 1.1 and plotted in Fig. 1.3.

The difference between Fermi levels Δf: An important key concept to understand the current flow in Eq. (1.7) is the Fermi function. Essentially, whatever makes the right f_r and the left f_l Fermi function go out of equilibrium with respect to the other one can

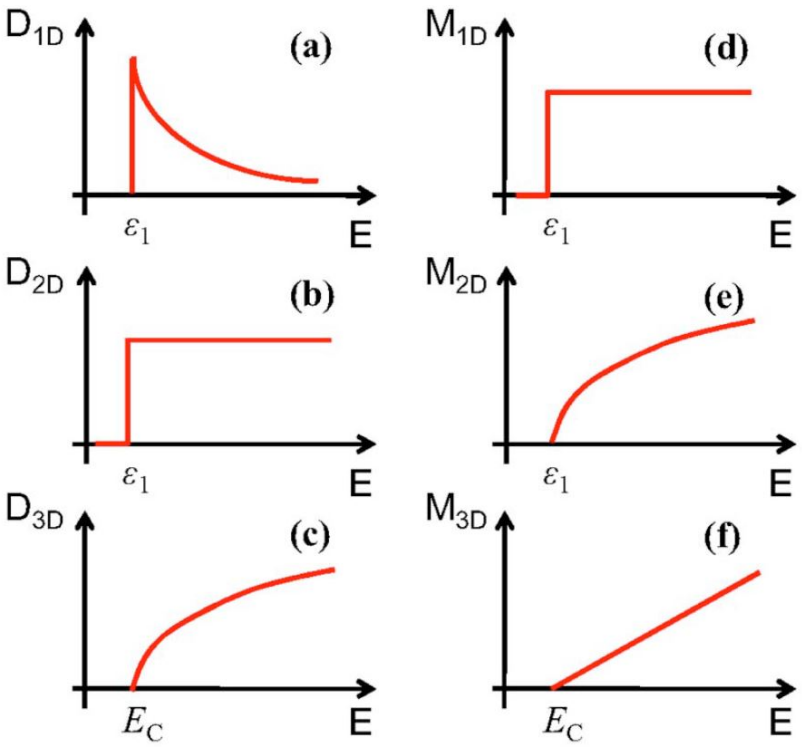

Fig. 1.3: Illustrations of (a-c) the density of states $D(E)$ and (d-f) number of modes $M(E)$ for 1D, 2D and 3D conductors with the assumption of single parabolic band. Adapted from [57]. The density of states for (a) 1D conductor goes as one over square root of energy, (b) for 2D, is independent of energy as long as we are above the bottom of conduction band. (c) for 3D, it evolves with a square root of energy.

lead to a non-zero Δf. In other words, applying a bias voltage across the device or any temperature difference in each contact, results in having different f_l from f_r.

First, let us consider the case in which we have a uniform temperature as depicted in Fig. 1.4.

Fig. 1.4 plots the Fermi function of the left contact $f_l(E)$ in Eq. (1.8) at a finite temperature in green solid line. Now, if we apply a small positive bias voltage, eV, on the right contact, it shifts the Fermi level of the right contact $f_r(E)$ to the right by $\mu = eV$ as shown in red dashed-line. One can see that there is a region of energy E over which the difference between two Fermi functions $f_l(E) - f_r(E)$ is positive, therefore, a current will flow. This region where we have current flow is called Fermi window. In the linear response regime, which refers to extremely low bias voltage where $f_l(E) \approx f_r(E) \approx f(E)$, the difference between two Fermi functions $f_l(E) - f_r(E)$ can be expanded in a Taylor series as the following,

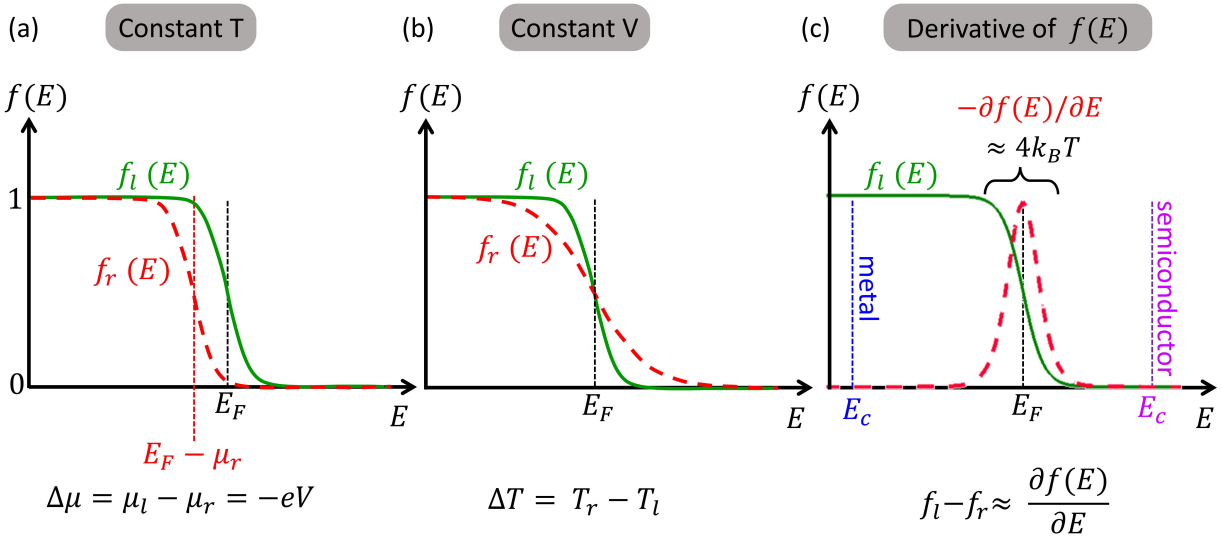

Fig. 1.4: Fermi functions of the left and right electrodes for: (a) temperatures of two contacts are identical $T_l = T_r$ but a small bias voltage $\mu_r = E_f - eV$ is applied on the right contact and (b) the two voltages are identical $\mu_l = \mu_r = 0$ but temperatures are different in the right and the left contact $T_r > T_l$. (c) Fermi function of the left electrode in green and the normalized (dimensionless) thermal broadening function $(-\frac{\partial f}{\partial E})$ in red dashed-line. In a metal, the bottom of conduction band, E_c, is way below the Fermi energy, E_F (see blue dashed-line). In contrary, E_c is way above the E_F in a non-degenerate semiconductor shown in magenta dashed-line

$$f_l(E, \mu_l) - f_r(E, \mu_r) = \left(-\frac{\partial f}{\partial E}\right) eV \tag{1.18}$$

Eq. (1.18) is mostly concerned in charge conductance problems in the linear response regime and it shows that the $f_l(E) - f_r(E)$ is proportional to the small voltage that we applied on the right contact of the device.

Another approach which could lead the current to flow is to have the same voltage in both contacts but different temperatures, i.e. a small temperature difference as shown in Fig. 1.4b. Assuming that the right contact has a slightly higher temperature, then the transition from zero to one is smeared out in energy (see the red dashed-line in Fig. 1.4) and one can have a difference between Fermi functions. It is worth mentioning that the $f_l - f_r > 0$ is positive below the Fermi energy and $f_l - f_r < 0$ is negative for energies above, therefore, this may lead to changing the sign of thermoelectric coefficients for n-type or p-type semiconductors [59, 4, 2]. When the temperature is small, we can use again the Taylor series expansion. This time, the expansion reads for the small temperature difference and the identical chemical potentials $\mu_l = \mu_r = \mu$ as,

$$f_l(E,T_l) - f_r(E,T_r) = \left(-\frac{\partial f}{\partial E}\right)\frac{E-\mu}{T}\Delta T \tag{1.19}$$

Moreover, the derivative of the Fermi function with respect to energy $\left(-\frac{\partial f}{\partial E}\right)$ is plotted in Fig. 1.4c. We can see that the only place in which the Fermi function (green solid line) has a non-zero derivative is few k_BT around the Fermi energy E_F. Therefore, the derivative of this function $\left(-\frac{\partial f}{\partial E}\right)$ is sharply peaked at Fermi energy E_F, as illustrated in Fig. 1.4c with red dashed-line. In a metal, everything happens few k_BT around E_F. On the contrary, in a non-degenerate semiconductor shown in magenta dashed-line, the flow of charge and heat currents exist thanks to the tail of Fermi function. In chapter 5 of this thesis, it is shown experimentally that by having a gate electrode to move the chemical potential plus a device with a sharp density of state i.e. a delta function density of states (a quantum dot), one can control the charge and heat currents separately as predicted by theory [20].

In general, both quantities can be different in the left and right contacts of the device at the same time ($\Delta T = T_r - T_l$ and $\Delta\mu = \mu_r - \mu_l$). As a consequence, one can write the $f_l - f_r$ as,

$$f_l(E,\mu_l,T_l) - f_r(E,\mu_r,T_r) = \left(-\frac{\partial f}{\partial E}\right)\cdot\left(e\Delta V + \frac{E-\mu_0}{T}\Delta T\right) \tag{1.20}$$

where μ_0 is the average value between the left and right chemical potential. Eq. (1.18)-(1.20) is valid in the linear response regime, i.e. assuming small voltage and temperature biases.

1.1.2.2 Charge conductance

Measuring electrical conductance (G) in a material provides information about how easily a material allows electric current to flow through it. For the device introduced in Fig. 1.2, by inserting the right parameters in Eq. (1.7) one obtains,

$$I = \frac{2e}{h}\int_{-\infty}^{\infty}\mathcal{T}(E)\cdot M(E)\cdot\left(-\frac{\partial f}{\partial E}\right)eV\ dE, \tag{1.21}$$

there Δf is replaced by Eq. (1.18) for a constant temperature in a linear response regime assumption. The conductance expression thus reads as,

$$I = GV \rightarrow G = \frac{2e^2}{h}\int_{-\infty}^{\infty}\mathcal{T}(E)\cdot M(E)\cdot\left(-\frac{\partial f}{\partial E}\right)\ dE, \tag{1.22}$$

where $M(E)$ can be written according to Tab. 1.1 for a 1D, 2D or 3D conductor. In addition, the transmission $\mathcal{T}(E)$ =1 for a ballistic conductor and is given by Eq. (1.12) for a diffusive limit.

1.1.2.3 Seebeck effect

Now we deal with a situation in which there is in addition a temperature difference between the left and right contacts. A thermoelectric voltage (V_{th}) can appear in response to this gradient temperature across the device (open-circuit) which is called thermopower or known as Seebeck effect [53]. In order to develop an expression for thermopower in a linear response, one can begin again with Eq. (1.7), and plug in Eq. (1.20) instead of $f_l - f_r$ as,

$$I = \frac{2e}{h}\int_{-\infty}^{\infty}\mathcal{T}(E)\cdot M(E)\cdot\left(-\frac{\partial f}{\partial E}\right)\cdot(e\Delta V + \frac{E-\mu_0}{T}\Delta T)\ dE, \tag{1.23}$$

Eq. (1.23) looks pretty much similar to Eq. (1.22) with an additional term which belongs to the temperature bias in the device. We can rewrite Eq. (1.23) as the following,

$$I = G\Delta V + GS\Delta T \tag{1.24}$$

where S is the Seebeck coefficient and reads as,

$$S = -\frac{1}{eT}\frac{\int_{-\infty}^{\infty}\mathcal{T}(E)\cdot M(E)\cdot\left(-\frac{\partial f}{\partial E}\right)(E-\mu_0)\ dE}{\int_{-\infty}^{\infty}\mathcal{T}(E)\cdot M(E)\cdot\left(-\frac{\partial f}{\partial E}\right)\ dE}, \tag{1.25}$$

Seebeck coffecient has been already measured in a variety of structures such as metallic atomic size contacts [60, 61], nanowires [2, 4, 5] and quantum dots [62, 63, 59, 64, 8, 65]. One gets zero Seebeck coefficient if $M(E)$ and $\mathcal{T}(E)$ are symmetric in E at μ_0.

Turek and Matveev have introduced S as a powerful experimental spectroscopic tool which contains important information about the energy-dependent transmission of the system by writing S as [62],

$$S = -\frac{\langle E\rangle}{k_B T} \tag{1.26}$$

This equation evidently implies that Seebeck coefficient is simply related to the average energy of charge carriers $\langle E\rangle$ at which the current flows with respect to the Fermi level in the contacts. The sign of S gives some direct information whether the channel of the device has an n-type or p-type characteristic. Correspondingly, one may use the terms

electron-like or hole-like thermopower if the average energy of charge carriers is far above the Fermi energy $\langle E \rangle > E_F$ or below the Fermi energy $\langle E \rangle < E_F$, respectively.

Another interpretation of S is provided by the famous Mott's law,

$$S = -\frac{\pi^2}{3} \cdot \frac{{k_B}^2 T}{e} \frac{\partial \ln G(E)}{\partial E}|_{E=E_f} \tag{1.27}$$

Eq. (1.27) plainly shows that the Seebeck coefficient is sensitive to the slope of the energy-dependent charge conductance $G(E)$ at the Fermi energy,. It is noteworthy that the foundation of Mott's law assumes the transmission function to have small changes with energy and in addition, it neglects the electron-electron interaction terms. One might expect that Mott's law would definitely fail to give insight in most low dimensional devices as these assumptions are not valid. However, many experiments have shown a strikingly good agreement [8, 10, 66]. Particularly, it was found to be valid more recently by H. Linke's group in the presence of a Kondo-correlated system [65].

Measuring the thermopower of a device requires in principle to address the open-circuit voltage of a high-impedance device. This is experimentally challenging, first because the voltmeter itself may shunt the divergent impedance of the device and, second, because the equilibration time to reach the true zero-current state (as required by the definition of the Seebeck coefficient S) at such high impedances can be extremely long. For this reason, several experiments have preferred focusing on the thermocurrent at zero applied bias rather than on the thermovoltage, and thus the Seebeck coefficient, although only the latter has a direct physical interpretation as a fundamental transport coefficient [5].

In the beginning of my thesis, together with my predecessor, we measured thermovoltage for a quantum dot device in the Kondo regime in our group [48] by measuring the current map in the presence of temperature bias as shown in Fig. 1.5. We defined $-V_{th}$ as the bias voltage at which the current goes through zero, thus realizing a perfect open-circuit condition [67]. As this result was already discussed in B. Dutta's thesis, therefore, all the the information can be found elsewhere [48]

1.1.2.4 Peltier effect

Here we explain that if we just run a current through a device which has a particular density of states, one can naturally cool one side and heat the other side as high energy electrons are going from one side to the other side. Let's start from heat current Eq. (1.9), which essentially tells us how much heat current is being produced by a charge current

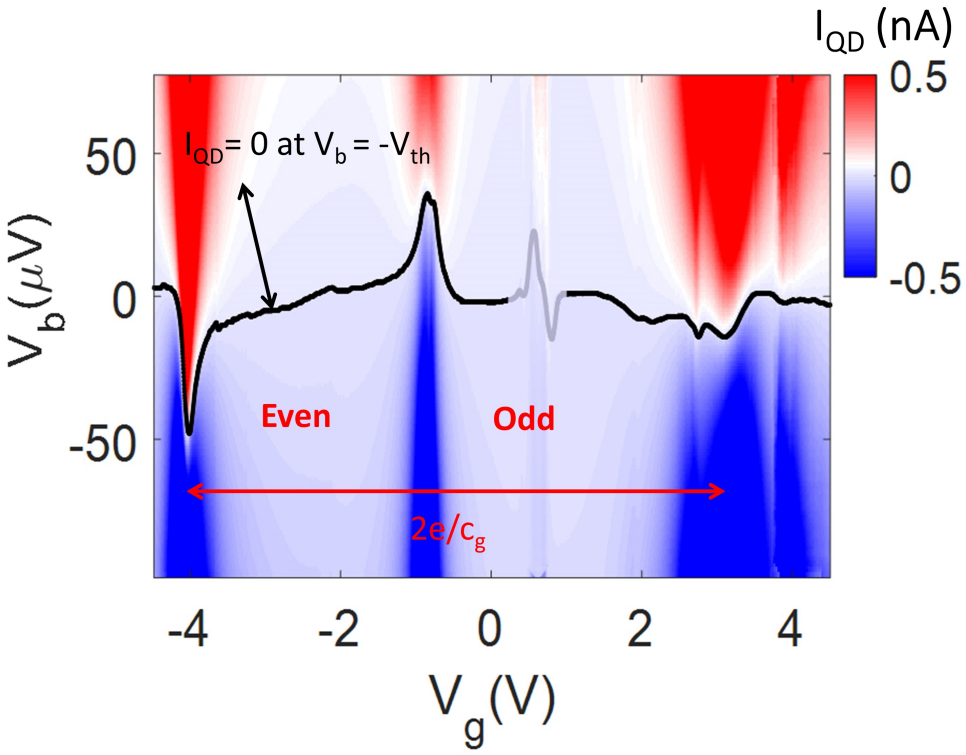

Fig. 1.5: The current map of a quantum dot device fabricated using electromigration technique taken in the presence of Kondo correlation for a small temperature gradient. Adapted from Dutta, Majidi et al. [48]. The black line follows the points of vanishing current; it is thus equal to $-V_{th}$. the thermovoltage changes sign at consecutive integer charge states, resulting in a $2e$-periodicity of the thermopower response, that directly follows from the presence of Kondo anomalies in odd charge diamonds. The thermoresponse at about $V_g = 0.7$ V associated to the second, weakly coupled quantum dot, is greyed out for better readability. Adapted from Dutta, Majidi et al. [48].

in the device. We should note that temperatures in both contacts are identical, $\Delta T = 0$. Using a linear response assumption, one can plug Eq. (1.19) into Eq. (1.9), leading to

$$\dot{Q} = \frac{2}{h}\int_{-\infty}^{\infty}(E-\mu_n)\mathcal{T}(E)\cdot M(E)\cdot\left(-\frac{\partial f}{\partial E}\right)e\Delta V\ dE, \tag{1.28}$$

and ΔV can be replaced by imposing $\Delta T = 0$ in Eq. (1.23) as $\Delta V = \frac{1}{G}I$. Therefore, the final expression reads,

$$\dot{Q} = \Pi I, \tag{1.29}$$

where Π is

$$\Pi = -\frac{1}{e}\frac{\int_{-\infty}^{\infty}\mathcal{T}(E)\cdot M(E)\cdot\left(-\frac{\partial f}{\partial E}\right)(E-\mu_0)\ dE}{\int_{-\infty}^{\infty}\mathcal{T}(E)\cdot M(E)\cdot\left(-\frac{\partial f}{\partial E}\right)\ dE}, \tag{1.30}$$

From comparing Eq. (1.25) and Eq. (1.30), it turns out that there is only a temperature coefficient (T) different between the two equations, hence, one can simply write $\Pi = TS$. This relation holds in the linear response regime. In addition, time reversal symmetry should not be broken in the system [37].

Peltier coolers were demonstrated in 1834 by Peltier [68] and plenty of progress has been made in large scale electronics as well as nano scale devices in normal metal-insulator-superconductor (NIS) [31], single electron transistors [69], quantum dots [26] and superconducting qubits [70, 71]. In particular, Pekola's group showed experimentally that an efficient Peltier refrigerator can be achieved by paring two NIS junctions together. They demonstrated the capability of SINIS tunnel junctions to cool the electrons in a normal metal island to a temperature of about 100 mK starting from 300 mK [72].

1.1.2.5 Heat conductance

The last thermoelectric coefficient that we discuss in this section is the electronic heat conductance. The electronic heat conductance is related to the heat current in an *open-circuit* condition as we showed in Eq. (1.5). In other words, if one would impose open-circuit in the problem so that the electrical current reaches zero, then the heat current would be entirely determined by the temperature difference between the left and the right contacts of the device. Theoretically, it is much easier to derive the *short-circuit* heat conductance and following that the open-circuit electronic heat conductance can be deduced by imposing $I = 0$ in the final equation. In a pretty similar way to the discussion of the other coefficients, we can plug Eq. (1.18) into Eq. (1.9) and evaluate the heat current for a short-circuited device,

$$\dot{Q} = \left[-\frac{2}{h} \int_{-\infty}^{\infty} \frac{(E-\mu)^2}{T} \mathcal{T}(E) \cdot M(E) \cdot \left(-\frac{\partial f}{\partial E} \right) dE \right] \Delta T, \quad (\Delta V = 0) \tag{1.31}$$

we can see from Eq. (1.31) that the heat current is proportional to the difference in temperature and the content of the bracket can be written in a short form as,

$$\dot{Q} = \kappa_0 \Delta T, \tag{1.32}$$

where κ_0 is the short-circuit heat conductance. Now, by making the sum of the two contributions related to ΔT and ΔV in Eq. (1.29) and (1.32), respectively, one can get a new expression for the heat current,

$$\dot{Q} = \Pi I + \kappa_0 \Delta T, \tag{1.33}$$

However, this equation does not have the electronic heat conductance κ_e. There is a relatively easy way to get that by applying the short circuit condition $\Delta V = 0$ to Eq. (1.23),

$$I = -GS\Delta T, \quad (\Delta V = 0) \tag{1.34}$$

using the above short-circuit current we obtain,

$$\dot{Q} = -\Pi SG\Delta T + \kappa_0 \Delta T \rightarrow \dot{Q} = (\kappa_0 - \Pi SG)\Delta T \tag{1.35}$$

where the electronic heat conductance is defined as:

$$\kappa_e = \kappa_0 - \Pi SG \tag{1.36}$$

κ_e is known as the electronic thermal conductance for zero charge flow condition.

We can summarize all these four thermoelectric quantities with a little bit of rearrangement in the form of a matrix as,

$$\begin{bmatrix} \Delta V \\ \\ \dot{Q} \end{bmatrix} = \begin{bmatrix} \frac{1}{G} & S \\ \\ \Pi & \kappa_e \end{bmatrix} \begin{bmatrix} I \\ \\ \Delta T \end{bmatrix} \tag{1.37}$$

All the thermoelectric coefficients can now be calculated as long as we know how the channels are distributed in energy, the transmission, and what the mean-free path for scattering is.

1.1.2.6 Wiedemann-Franz Law

The secondary diagonal elements of matrix (1.37), i.e. the electronic charge and heat conductances are intimately related in the limit of linear response regime through a law known as Wiedemann-Franz (WF). In order to make this relation more clear-cut, at least for our parabolic-band assumption, we can start from Eq. (1.36). Based on Eq. (1.31), and Eq. (1.34) , κ_0 and S can be written as:

$$\kappa_0 = T \cdot \left(\frac{k_B}{e}\right)^2 \left\langle \left(\frac{E - \mu_0}{k_B T}\right)^2 \right\rangle \cdot G \tag{1.38}$$

and

$$S = \left(\frac{k_B}{e}\right)^2 \left\langle \left(\frac{E - \mu_0}{k_B T}\right) \right\rangle \tag{1.39}$$

Eq. (1.38) simply tells us that the average value of the square of energy matters for κ_0, whereas only the average energy of charge transport is important for the Seebeck

coefficient. Now, by plugging this into the electronic heat conductance κ_e (Eq. (1.36)), we obtain,

$$\kappa_e = T \cdot G\left(\frac{k_B}{e}\right)^2 \left\{ \left\langle \left(\frac{E-\mu_0}{k_B T}\right)^2 \right\rangle - \left\langle \left(\frac{E-\mu_0}{k_B T}\right) \right\rangle^2 \right\} \tag{1.40}$$

The part inside the curly brackets is constant and can be hidden in Lorenz number $\mathcal{L}$, in the following from,

$$\kappa_e = TG\mathcal{L} \tag{1.41}$$

where $\mathcal{L}$ relies upon the degree of degeneracy and the shape of the band. It is assumed to be related to the density of states so that it is verified in most of cases to be equal to $\mathcal{L}_0 = \pi^2/3(k_B/e)^2$. Although, the ratio of the electronic heat conductance to the charge conductance can take other values [73]. Eq. (1.41) implies that the ratio of electronic heat conductance κ_e to charge conductance G and temperature T is constant and it is given by Lorenz ratio $\mathcal{L}$. It plainly has a physical interpretation that whenever an electron flows from the right contact to the left contact it carries a charge of e and a heat in the order of $k_B T$. Therefore, in most cases, it is expected that the higher the charge conductance, the higher the heat conductance as these two quantities are dependent.

The fact that the heat conductance is proportional to the temperature of the device contacts, implies a quadratic relation between electronic heat flow $\dot{Q}_e$ and the temperature difference in the system as shown by Eq. (1.42).

$$\kappa_e = \frac{\partial \dot{Q}_e}{\partial T} \Longrightarrow \dot{Q}_e = \int_{T_b}^{T_e} G\ L\ T\ dT = \frac{GL}{2}({T_e}^2 - {T_b}^2) \tag{1.42}$$

It is noteworthy that, as marked by Mahan and Bartkowial [74], we should regard the Wiedemann-Franz law to be a 'rule of thumb' and not a law of nature, because is not as fundamental as other relations, i.e. the Kelvin relation. The WF law is remarkably valid in many devices, however, it has turned out that it highly depends on material details, scattering, dimensionality, interactions and so on [75, 76, 38, 39, 41, 77, 22, 27, 6, 6, 43]. In chapters 4 and 5, we will experimentally demonstrate the breakdown of the WF law and a linear power law for heat flow $\dot{Q}_e$ with the temperature in metallic and semiconductor quantum dots.

1.1.3 Transport in a 0D device

Up to now we have not considered the effect of electron-electron interactions because it plays a minor role for 1D, 2D and 3D dimensional systems. This section considers charge

and heat transport using a pretty similar approach as we discussed earlier, but now we extend our discussion for very small puddles of electrons, i.e. 0D structures, which are known as quantum dots.

1.1.3.1 Charge transport

In quantum dot devices, Coulomb interaction can play a significant role in comparison with other energy scales. Another difference between other nanostructures and quantum dots is that quantum dots can be weakly coupled to their environment, because they are coupled to lattice vibrations and thermal radiations at low enough temperature. We generally consider the schematic drawing in Fig. 1.6 for intuitively describing the Coulomb blockade effect in such a system. Fig. 1.6a depicts a quantum dot which is electrically connected to electron reservoirs (the source and the drain) via tunnel barriers [78, 79]. In addition, it has a gate electrode, which is capacitively coupled to the system. One can move the discrete electrochemical potentials for the given number of electrons of the quantum dot $\mu(N)$ by changing the voltage of the gate electrode. These discrete level of the chemical potentials in the dot are equidistant in energy as shown in Fig. 1.6.

The linear conductance G (the measured current divided by the applied voltage), exhibits a Coulomb peak, i.e. a sharp resonance, if the chemical potential of the dot $\mu(N)$ is aligned with the chemical potential of the source and drain electrodes (see Fig. 1.6c). If one keeps changing the position of the level in the dot, the electrostatic blockade gives rise to regions of suppressed current, i.e. Coulomb blockade (see 1.6b) [58].

Fig. 1.7-left exemplifies the process shown in Fig. 1.6 by measuring a conductance through a nanowire-based quantum dot. A very small bias voltage (V_b) in the order of 0.1 μV is applied between the source and the drain electrodes of the device. Then the linear conductance of the device was measured at the bath temperature $T_b = 100$ mK as a function of back gate voltage (V_g). A such small bias voltage V_b, the linear conductance in Fig. 1.7-left can be obtained by $G = I/V_b$ as the current through the quantum dot has a linear relation with the applied bias voltage between the source-drain electrodes.

Coulomb blockade can also be seen in the measurement of current as a function of bias voltage $I(V_b)$. Fig. 1.7-right plots two $I(V_b)$ curves, one of them was measured at the back gate voltage of conductance peak, which is called on-resonance (at degeneracy point) current and is shown in solid green line. The other one, off-resonance, was measured in a valley between two conductance resonances (degeneracy points). One can see that the

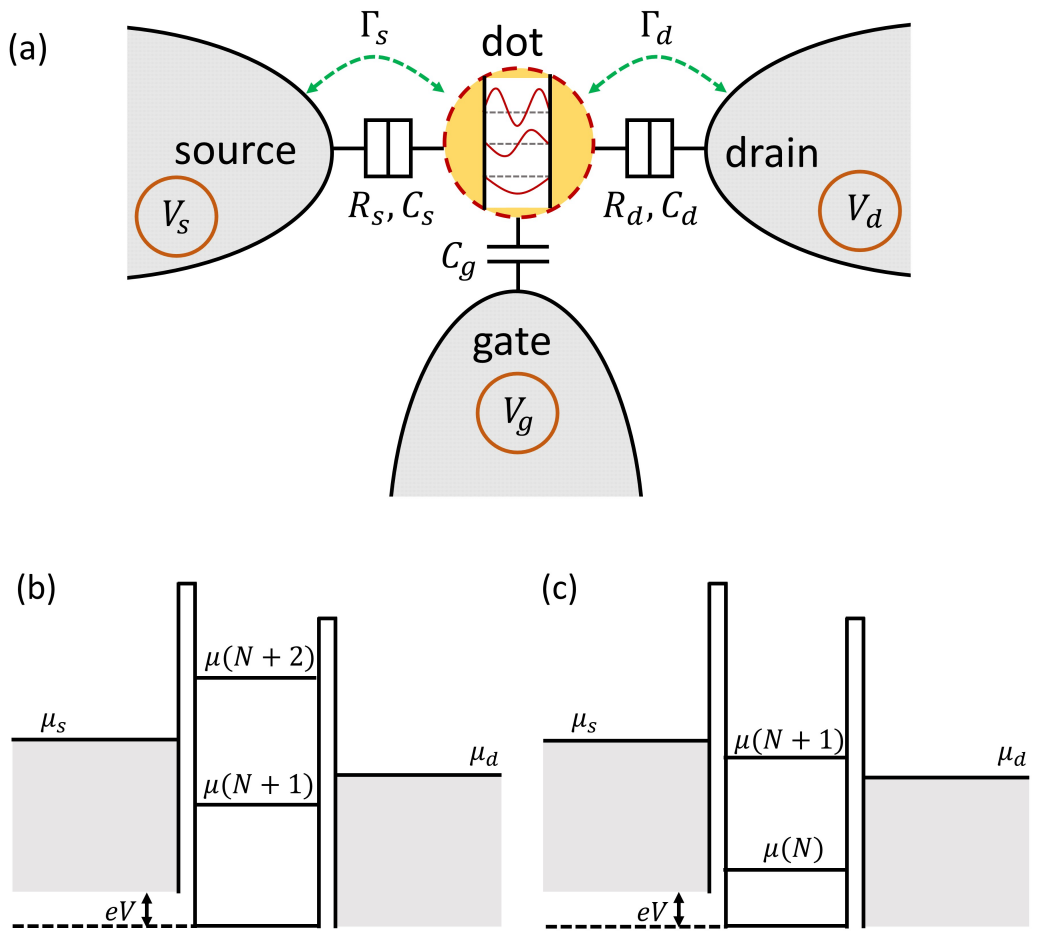

Fig. 1.6: (a) Schematic representation of energy diagram of a quantum dot with the drain, source and gate electrode. (b) The quantum dot is represented by discrete energy levels and positioned for the Coulomb blockade regime. eV is a small bias voltage. The chemical potential of the quantum dot $\mu(N)$ is shown here. The difference between two levels is given by $E_{add} = 2E_c + \delta E$. (c) Particular position of energy levels shows the situation in which the conductance is maximum as the energy level of the dot is situated in the energy range between μ_s and μ_d, therefore, it allows a current to flow between the source and drain electrodes.

traced current for the on-resonance case increases linearly with the bias voltage (V_b) in the region of $|V_b| < k_B T_b/10$ and then, shows current steps due to the contribution of additional energy levels. On the contrary, the measured current between Coulomb peaks rising only at very large bias voltages and is extremely small for values of $|V_b| < k_B T_b/10$. In principle, in the latter case, it is the charging energy that gives the threshold.

Another appealing feature that can be shown experimentally is the asymmetry in currents both in "on" and "off" resonance cases. According to Fig. 1.7-right, the measured current is higher for negative bias voltages compared to the positive ones, this characteristic can be related to the asymmetry between the coupling of the source Γ_s and drain Γ_d

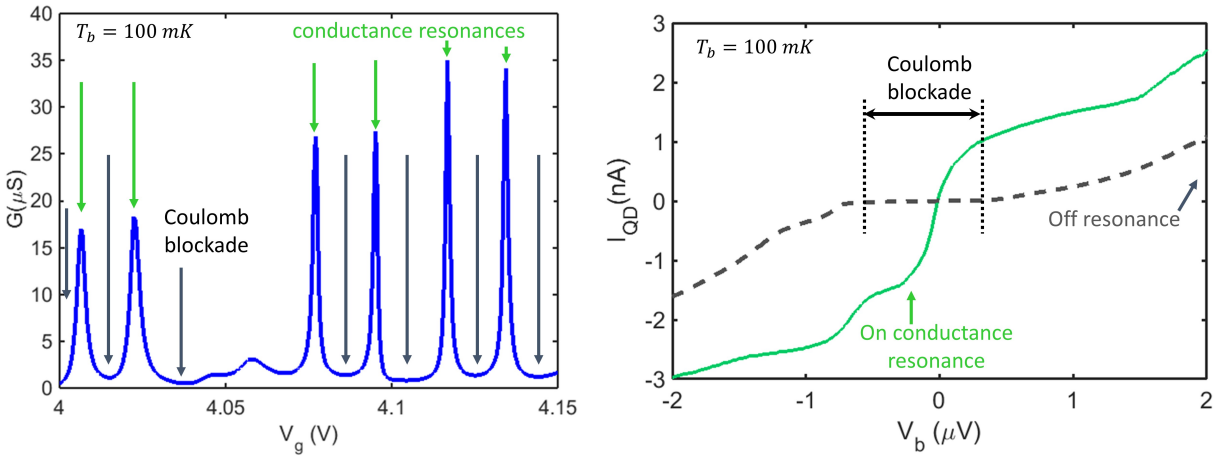

Fig. 1.7: Linear conductance and traced current of two different InAs quantum dots. Left-hand side: Quantum dot linear conductance as a function of the back gate voltage. Green and black arrows are pointing to Coulomb oscillations and Coulomb blockades, receptively. Right-hand side: Measured $I(V_b)$ trace through a quantum dot at a given gate voltage (V_g). The current on a conductance resonance (solid green line) and off resonance (dashed line).

electrodes to the dot. In the limit of very different tunnel barriers, the bottleneck for charge transport is the thicker barrier [80]. This effect is also more pronounced in the stability diagrams in Fig. 1.8.

1.1.3.2 Quantum dot characterization

Mapping a quantum dot device's conductance as a function of gate and bias voltages (stability diagram) can reveal a great amount of information about the parameters of the quantum dots. It is known that a stability diagram can be used as a spectroscopic tool to reveal possible excitations. It gives access to some important information such as charging energy, lever arm and the source-drain capacitive coupling in the system [81, 82]. The excited states appear as conductance lines running parallel to the Coulomb diamond edges as can be seen in Fig. 1.8. These excitations can be due to some phonon and vibrational modes [83], or the density of states of the leads as the contact electrodes are being nanostructured [84]. For instance, C. Winkelmann *et al.*, were able to probe the electron transport through a single molecule using a superconductor as contacting leads [85]. Not only did their data strikingly show the excitation modes of a C_{60} molecule in agreement with previous studies [83], but they also demonstrated the effect of interactions, correlations and superconductivity in C_{60} molecules over a broad range of tunnel coupling strength as shown in Fig. 1.9.

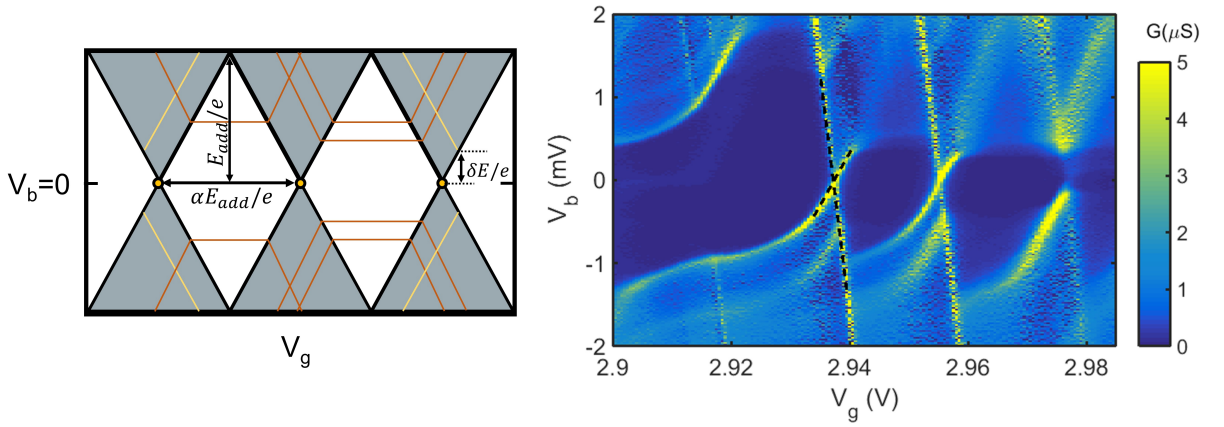

Fig. 1.8: Left: Schematic of a differential conductance map for a quantum dot device. Orange lines show that higher order tunneling process enter the bias window and tunneling electrons through the quantum dot via excited states are shown with yellow lines running parallel to the Coulomb diamond edges. The gray color shows the tunneling regime and the white represents the Coulomb blockaded regime. Right: Conductance map of an InAs nanowire quantum dot, studied in this thesis, showing clear Coulomb diamond structures.

In this thesis, our focus is on the low bias (linear) regime where we have assumed that only a single level contributes to the transport through the dot. This is not completely true in the high bias regime.

Source, drain and gate-capacitive couplings

By looking at the stability diagrams, one can immediately determine the asymmetry in the capacitive coupling of the source and drain electrodes, gate coupling, i.e. as lever arm, and charging energy as the following. The positive slope of the Coulomb diamonds in Fig. 1.8 is characterized by $\beta = \frac{C_g}{(C_d+C_g)}$ and the negative one is given by $\beta' = \frac{C_g}{C_s}$. The C_s, C_d, C_g are the capacitances between the dot and the source, the drain and the gate, respectively. The asymmetry in the capacitive coupling of the source and drain can be expressed by the ratio of the source and drain capacitance $\frac{C_d}{C_s}$. Eventually, the total capacitance of the dot to the outside world is the sum of all the capacitances as $C_\Sigma = C_s + C_d + C_g$.

Lever arm α

The lever arm can be directly obtained from the two slope of diamond and is defined by the ratio $\alpha = \frac{C_g}{C_\Sigma}$. This value basically tells us the effective change in the dot (island) potential per unit volt applied to the gate electrode. The value of α is always positive and in an experiment can be considered a constant in the vicinity of one charge state but it typically varies with large changes in the gate voltage. For metallic gates this value

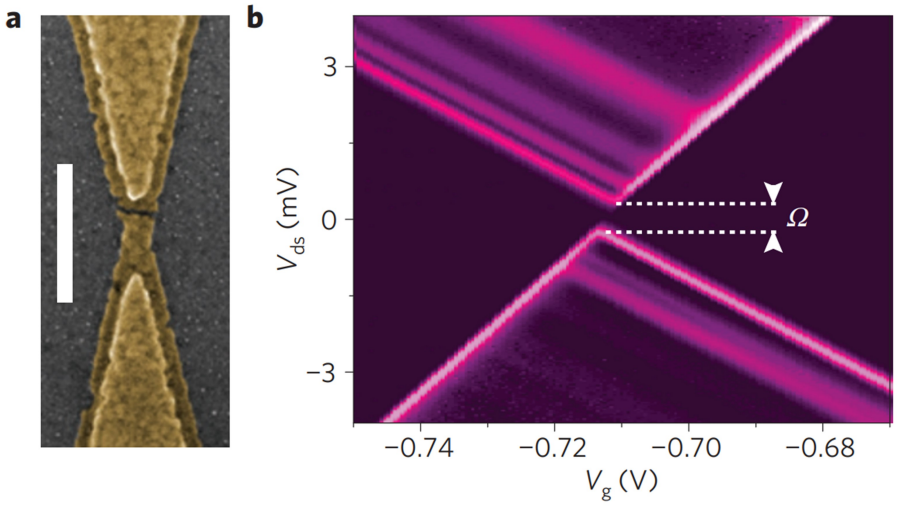

Fig. 1.9: Superconducting C_{60} transistor in a weak-coupling regime. Adapted from [85]. (a) SEM image of an aluminium nanogap obtained by electromigration. The scale bar is 300 nm. (b) The differential conductance map (dI/dV) of the device as a function of gate and bias voltages shows excited states of C_{60} transistor. Ω is a spectroscopic source–drain voltage gap, which is estimated to be of about 680 μV near the degeneracy point. This gap, reflecting the quasiparticle spectrum of the contacting electrodes, is a typical feature of a nanostructure weakly coupled to superconducting electrodes [85].

is small and the lever arm is well defined. However, in quantum dots where regions of a 2DEG are used as so-called in-plane gates, or with nanowire quantum dots, the lever arm might change slowly as a function of the voltage applied due to the change in the electron density of the semiconductor.

Charging energy E_c

The energy scale associated with discreteness of the electron charge is expressed by:

$$E_{add} = e\alpha\Delta V_{BG} = \delta E + 2E_c; \qquad E_c = \frac{e^2}{2C_\Sigma} \tag{1.43}$$

where C_Σ is the total capacitance of the device as explained earlier. This expression tells us how much energy is needed to charge the island with an additional electron assuming that there are already N electrons on the island (see Fig. 1.6b,c for more details). This difference between the total energies for $N+1$ and N electrons is often referred to as the addition energy E_{add}, where δE is the level spacing. Higher energy levels of the dot do not contribute to the transport if the temperature is small compared to the level spacing of the quantum dot, i.e. $k_B T < \delta E$.

Tunnel coupling Γ

By tuning the gate voltage, it is possible to position a level between the electrochemical

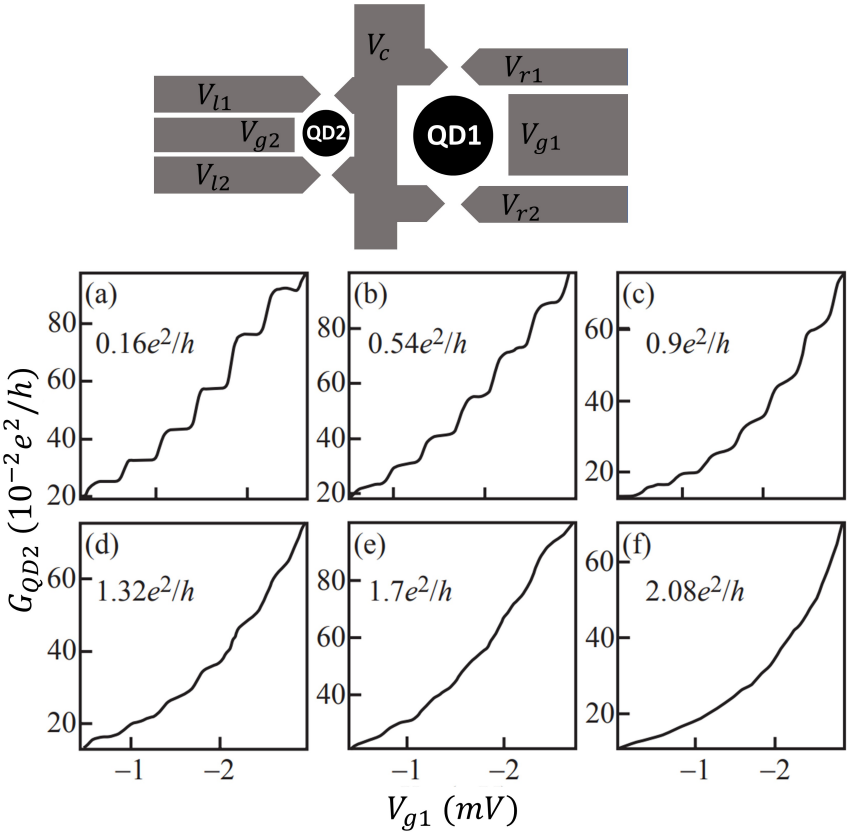

Fig. 1.10: Top: Schematic of the device. Bottom: Conductance quantization in a quantum dot as a function of the gate voltage for the different tunnel coupling strength Γ to the source and drain electrodes. Adapted from [86]. The tunnel coupling strength is increasing from (a) to (f). The bottom-right point contact $V_c - V_{r2}$ is completely pinched-off by applying a large negative voltage. Therefore, electrons enter or leave through a channel defined by the upper right point contact $V_c - V_{r1}$ for QD1. In these situations, no current flows through the QD1, but the charge can be capacitively induced on the QD1 by applying a voltage on V_{g1}.

potentials in the source and the drain, allowing electrons to tunnel on and off the dot one at a time. To observed quantized number of electrons in a quantum dot, the tunnel coupling should be smaller compared to the charging energy ($\hbar\Gamma < \frac{e^2}{2C}$), plus the fact that conductance should also be much less than conductance quantum ($G < \frac{2e^2}{h}$).

This fact is illustrated in the experiment in Fig. 1.10, adapted from [86]. Fig. 1.10-top shows a schematic diagram of the device containing a quantum dot, QD1, and a quantum dot charge detector, QD2. The detector is tuned to the steep slope of its conductance resonance using the side gate voltage V_{g2}. The number of electrons in QD1 to be measured is varied with the right side gate V_{g1}. Figs 1.10a-f plot the conductance of QD2 as a function of V_{g1} for different values of QD1 tunnel conductance between the $V_c - V_{r1}$ from $0.16e^2/h$ (weak coupling regime) to $2.08e^2/h$ (strong coupling regime) [86]. For the weakest cou-

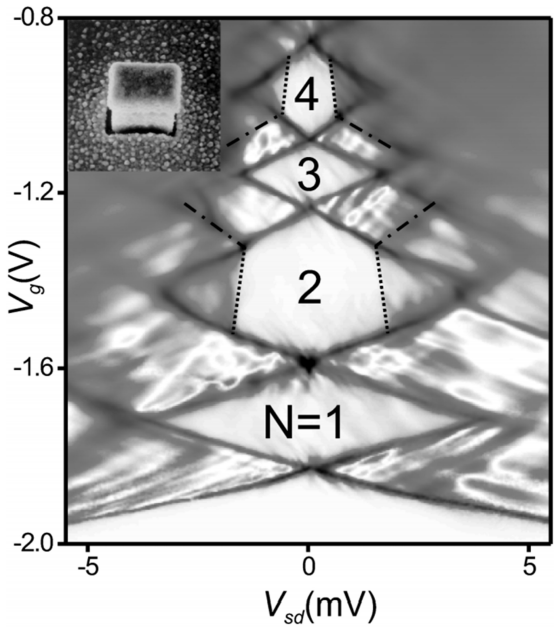

Fig. 1.11: Measured stability diagram of a quantum dot at the bath temperature of 15 mK . Dotted lines have been superimposed to highlight the onset of inelastic cotunneling. The dot-dashed lines indicate the onset of first-order tunneling via an excited state. Inset: scanning electron micrograph of the device. Adapted from [87].

pling of QD1 to its leads in Fig. 1.10a, the conductance shows a series of very sharp steps demonstrating the charge quantization in QD1. All the steps wash out gradually as the coupling increases. Eventually, they disappear completely once the coupling to the leads has reached a value of about the conductance quantum $2e^2/h$. This result intuitively illustrates that charge quantization for a quantum dot happens if the tunneling conductance G of the quantum dot to its surroundings far less than the quantum conductance $2e^2/h$ [86, 58, 51, 56].

Temperature is another important parameter to observe the level quantizations. The temperature should be relatively small compared to the main energy scale of the system, i.e. $k_BT \ll E_c$. To accomplish this condition in the real experiment, one needs to fabricate the island sufficiently small so that it results in having a small capacitance. In chapter 4 of this thesis, we will use the electromigration technique to connect a metallic nanoparticle of about 5-10 nm. We can easily get a charging energy at least of the order of 100 mV [85, 48, 83]. One can tune the size of island much easier by moving to InAs nanowire-based transistors [88]. The reader is referred to chapter 2, 4, and chapter 5 for further details about both techniques.

By comparison of temperature scale and tunnel coupling Γ of the dot, one is able to distinguish two regimes: The conductance smearing is dominated by (i) the temperature, i.e. $k_BT \gg \Gamma$ or (ii) by the tunnel coupling of the leads, i.e. $k_BT \ll \Gamma$, which is of particular interest of us.

Co-tunneling

When first-order single electron transport is banned by Coulomb blockade at low temperature, virtual tunneling processes dominate the transport away from charge degeneracy and lead to the tunneling of two or more electrons coherently. These second-order transport processes are called co-tunneling [87]. When the quantum dot is left in an excited state, the co-tunneling is classified as inelastic tunneling, otherwise, it is called elastic. The co-tunneling becomes significant when the tunnel conductance of the quantum dot is comparable to the conductance quantum, i.e. strong tunnel coupling. De Franceschi *et al.* measured both elastic and inelastic co-tunneling on a semiconductor quantum dot embedded in an InGaAs layer [87]. They evidently discriminated between these two contributions and showed that inelastic events can occur only if the applied bias exceeds the lowest excitation energy. The differential conductance of the quantum dot [87] of Fig. 1.11 shows that elastic co-tunneling is dominant in Coulomb blockade regime at low bias voltages and gives rise to non-vanishing conductance shown as light gray region (this non-zero current inside Coulomb diamond can also be seen in our experiments in Fig. 1.7 and Fig. 1.8). The inelastic process contributes to the transport when the applied bias voltage is larger than the level spacing, i.e. $|eV_b| > \delta E$. As a result, inelastic co-tunneling turns on along the vertical (dotted) lines in Fig. 1.11. At the edge of the Coulomb diamond, the condition for the onset of inelastic co-tunneling connects to that of the onset of first-order tunneling via an excited state (dot-dashed lines).

1.1.3.3 Heat transport

As we have already seen in the previous sections, charge transport in quantum dot devices has reached a great level of understanding since last 30 years. Recent developments on heat transport on metallic single-electron transistors have shown that by employing Coulomb charging energy, only high energy electrons act as the carriers favoring a higher heat flow than expected by the WF law [77, 22, 27, 6, 43]. This was shown theoretically by Kubala *et al.* in 2008 and has been experimentally verified by Dutta *et al.* in 2017 in a single electron transistor (SET) [22]. In the latter work, the thermal conductance of

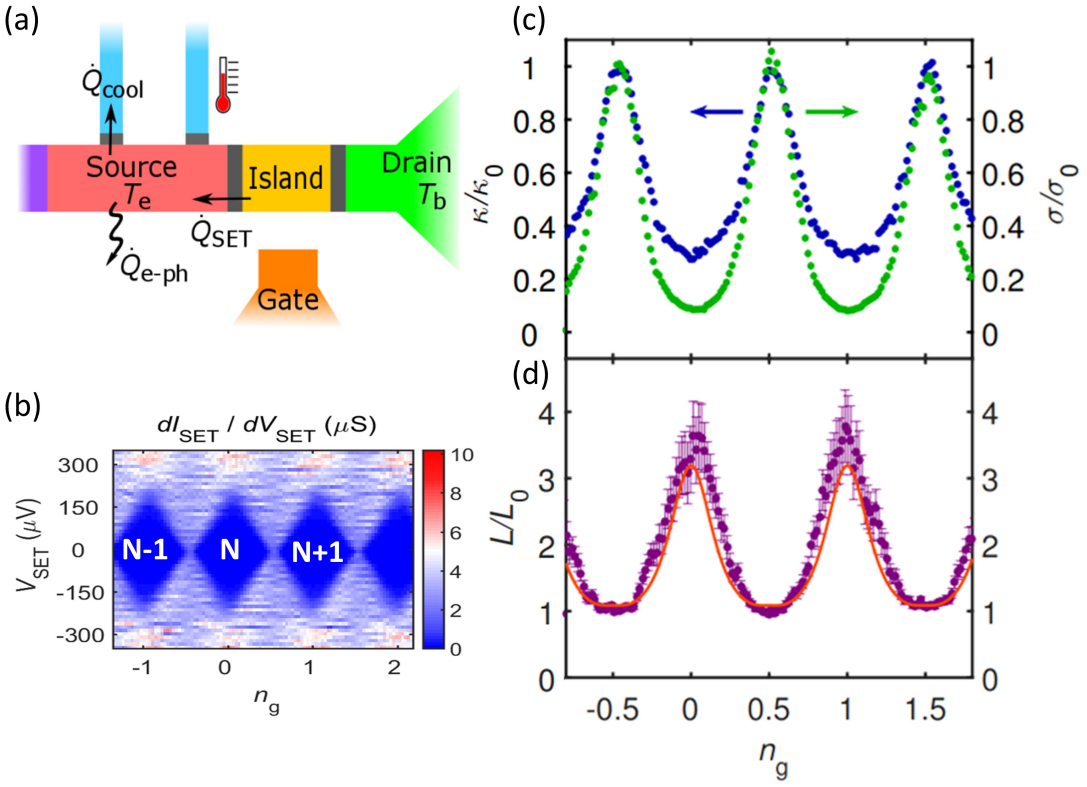

Fig. 1.12: (a) Schematic of the device, with the different elements shown in colors. (b) Measured differential conductance map as a function of drain-source and gate voltages. (c) Top: Normalized thermal (blue dots) and charge (green dots) conductances of the SET at a bath temperature of 152 mK. Bottom: Lorenz ratio (purple dots) together with theoritical calculation in solid red line. Adapted from [22].

a metallic SET was measured using on-chip NIS thermometres and heaters. Fig. 1.12a shows the circuit diagram of the device in which different elements of the circuit have different colors. They measured both charge and heat conductances at the same time as a function of the gate voltage. A strong deviation from the Wiedemann-Franz law is observed when the transport through the SET is directed to the Coulomb blockade regime, as the electrons face energy filtration due to Coulomb blockade [89]. Notably, in an SET the heat conductance is better than predicted by WF law, that is $L/L_0 > 1$.

This electron energy selection is even stronger in quantum dots and makes these quantum devices in principle almost a perfect energy filter. Mahan and Sofo [20] theorized that the "best thermoelectric" is a device with a Dirac delta function density of states in 1996. In such a device, electron transport happens only at a certain energy while the transport at all other energies is forbidden. Quantum dot junctions potentially possess this feature as they have a very well-defined electronic structure similar to that shown in Fig. 1.7. After Mahan and Sofo, this idea of having such an ideal high energy elec-

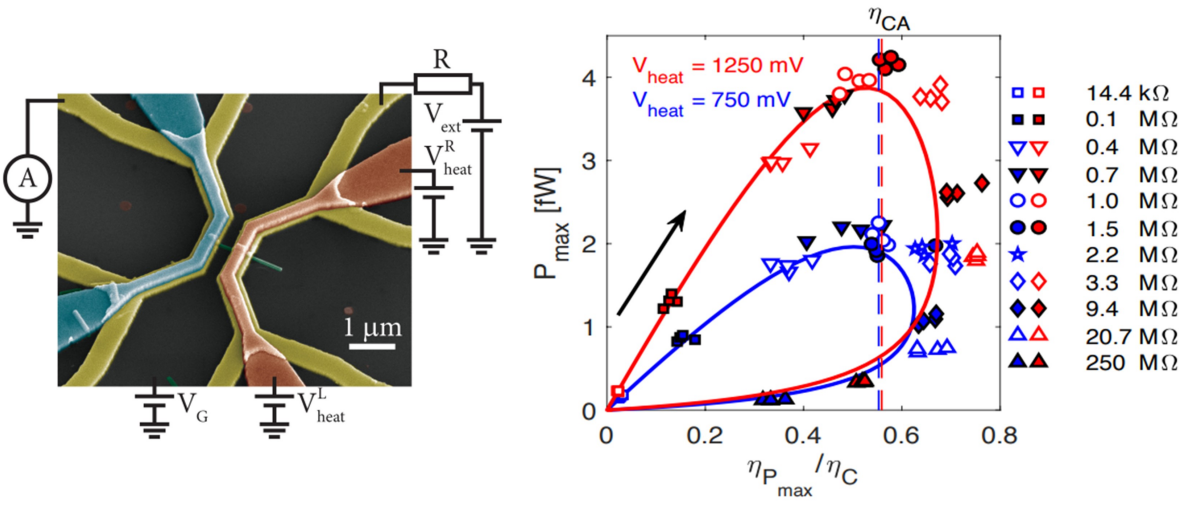

Fig. 1.13: Left: A false-colored SEM images together with charge and heat circuit diagram of a typical nanowire quantum dot. Adapted from [3]. The nanowire is shown in green and ohmic contacts to the nanowire in yellow. Top heating technique is used to make a temperature gradient between the source and the drain electrodes of the device. Right: device operation at maximum power (markers) compared with the theoretical prediction. Adapted from [3].

tron filtration was further explored by Humphrey *et al.* [16, 21]. In the same group (H. Linke's group), recently, Josefsson *et al.* tested experimentally a quantum dot heat engine with a performance near the thermodynamic efficiency limit with a remarkable agreement with theoretical prediction [3, 65, 90]. They utilized a quantum dot embedded in an InAs nanowire as a thermal insulator and were able to keep a temperature gradient across the device by a novel top heating technique. Eventually, by forcing the produced thermal current through a load resistor and by making a load matching technique, they were able to achieve thermoelectric conversion efficiency for different powers [3, 65] as shown in Fig. 1.13. Moreover, they found that second order tunneling processes can significantly reduce the electronic efficiency [3, 90]

Another measurement conducted by Roddaro's group shown in Fig. 1.14 has also presented thermoelectric conversion in InAs/InP nanowire quantum dots at higher temperatures (30 K) limit but still in the linear response regime [5]. First, in this experiment the charge conductance G and the thermopower S were measured and showed a quantitative agreement with a four-level theoretical model. Then, they calculated the electronic heat conductance κ using the fitting parameters obtained from the experimental $G(V_g)$ and $S(V_g)$. Eventually, using experimental G and S together with theoretical κ, they

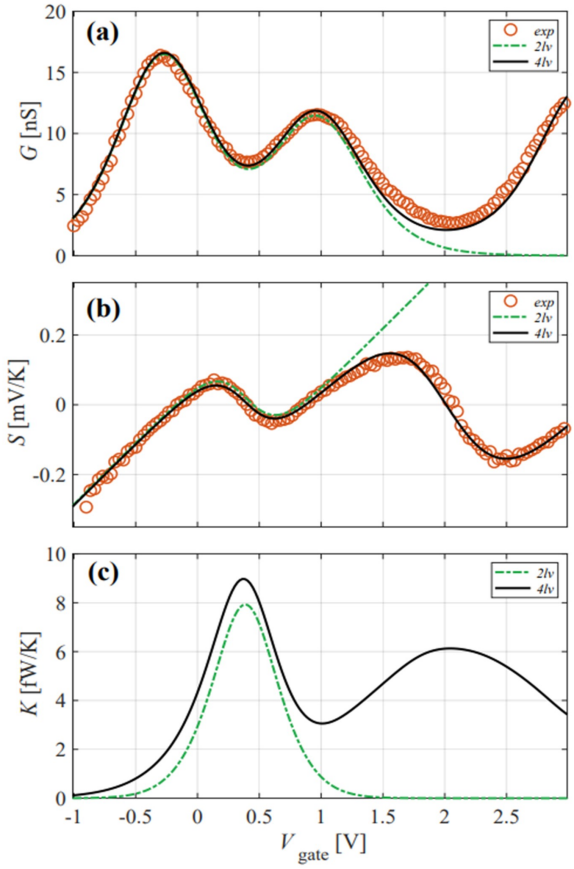

Fig. 1.14: Experimental charge conductance (a) and thermopower (b) are compared with two-level and four-level theoretical model to extract the quantum dot coupling. (c) Electronic thermal conductance κ obtained theoretically based on the extracted the quantum dot parameters using charge conductance and thermovoltage measurement. Adapted from [5].

showed an amazingly high electronic figure of merit $ZT \approx 35$ at 30 K, utilizing nanowire quantum dots.

The above experiments have demonstrated that thermoelectric experiments in quantum dots require a great control on thermal bias over a nanometer distance, as well as a reliable temperature measurement. In addition, the measurement of heat flow through a single level quantum dot has so far been limited and always needed some degree of modeling [90]. Furthermore, these experiments also very well highlighted the need for measuring electronic heat conductance as this quantity enters directly in the thermoelectric efficiencies. The electronic heat conductance of such devices has in general not been measured independently as these experiments have only focused on measuring short-circuit thermal current or open-circuit thermovoltage instead. However, in both of the above cases, they strikingly achieved an excellent quantitative agreement for electronic efficiency estimation by accurately measuring and understanding the experimental charge conductance and

thermocurrent/thermopower. Therefore, extracting all the parameters of quantum dots based on the charge transport and the thermal current leads only to an estimation of the electronic thermal conductance κ_e.

It is worth mentioning that the electronic heat conductance remarkably has been experimentally measured to the scale of a single atom and molecule contacts [75, 76], in superconductors [38], in correlated electron systems [39] and more recently in graphene-based devices [41]. Nevertheless, the electronic heat conductance and the validity of the WF law of metallic and semiconductor quantum dots have not been experimentally and quantitatively investigated, to date. This is the object of this work as it will be explained in more detail in chapter 4 and 5 of this thesis.

Chapter 2

Fabrication of quantum dot devices

This chapter discusses two different methods for fabricating quantum dot devices, which were used for conducting the main experiments in this thesis. We first explain briefly the fabrication of a metallic single quantum dot junction using electromigration technique for showing the effect of higher-order tunneling processes in heat transport (chapter 4). In the following section, we consider the fabrication of a typical quantum dot device based on semiconductor nanowires that will be discussed in chapter 5. We particularly discuss integrating different local electronic thermometers with the nanowire quantum dot devices in detail. The device design and the processes involved in sample preparation prior to nanowire metallization are also discussed thoroughly.

Contents

2.1 Fabrication of single-quantum-dot junctions

Our quantum dot junctions are realized using the electromigration technique, which has been successfully applied for studying a variety of single quantum dot systems, such as single molecules and metallic nanoparticles [91, 92, 93]. Using electron-beam lithography and a three-angle shadow evaporation, we fabricate devices as pictured in Fig. 2.1, on top of a local back gate. A detailed overview of the fabrication recipes and electromigration technique can be found in the thesis of former PhD students in our group [84, 94, 95]. However, a brief discussion regarding the fabrication the devices studied in chapter 4 is presented in the following.

2.1.1 Sample fabrication

We fabricate samples on a 2 inch Si <100> wafer with a 500 nm thermal oxide. The first step of the fabrication process is the gate layer (see Fig. 2.1a). We use a metallic plane covered with an oxide layer as the gate of the quantum dot device. The reason for choosing this local back-gate is that, using this gate configuration, we can easily achieve a very small distance (< 10 nm) between the gate and the gold nano-particles and thereby achieve a strong gate coupling. We use laser lithography to pattern the gate structures on top of a cleaned Si wafer coated with a double layer of photo resist LOR3A/S1805. After development of the exposed area, we evaporate 3 nm of titanium (Ti), 30 nm of gold (Au) and again 3 nm of Ti. Both Ti layers act as an adhesive for the following layers. After liftoff and cleaning, the wafer with metallic gate structures is coated with an approximately 8 nm layer of Al_2O_3 using the atomic layer deposition (ALD) technique.

We designed the main parts of the quantum dot device on top of this gate using electron-beam lithography (Fig. 2.1e,f). The source, constriction, drain and the four probes of the device are patterned on the processed wafer coated with a double layer of e-beam resists P(MMA-MAA) 9% and PMMA 4 %. After development of the exposed area, we load the sample in an e-beam evaporator with a rotatable sample stage to evaporate metals. First, we deposit 11 nm of platinum (Pt) at an angle of -42^o w.r.t. the source of the evaporator, this forms the *bow-tie* shaped constriction of the device, as shown in Fig. 2.1f. Then we rotate the sample stage and deposit 25 nm of Au at an angle of -22^o, which forms the source and drain of the device (orange and green color in Fig. 2.1e,f), on top of the Pt constriction. At the same angle, a 3 nm of Ti is then deposited to protect the Au

layer from intermixing with the following aluminum (Al) layer. After that we rotate the sample to $+20^o$ and deposit 80 nm thick Al contacts, which form the four Al probes on top of the Au source with a clean interface (cyan color in Fig. 2.1e,f), making four $S-N$ junctions. After liftoff with acetone, IPA and cleaning with O_2 plasma, the device is ready for the nano-particle (NP) deposition.

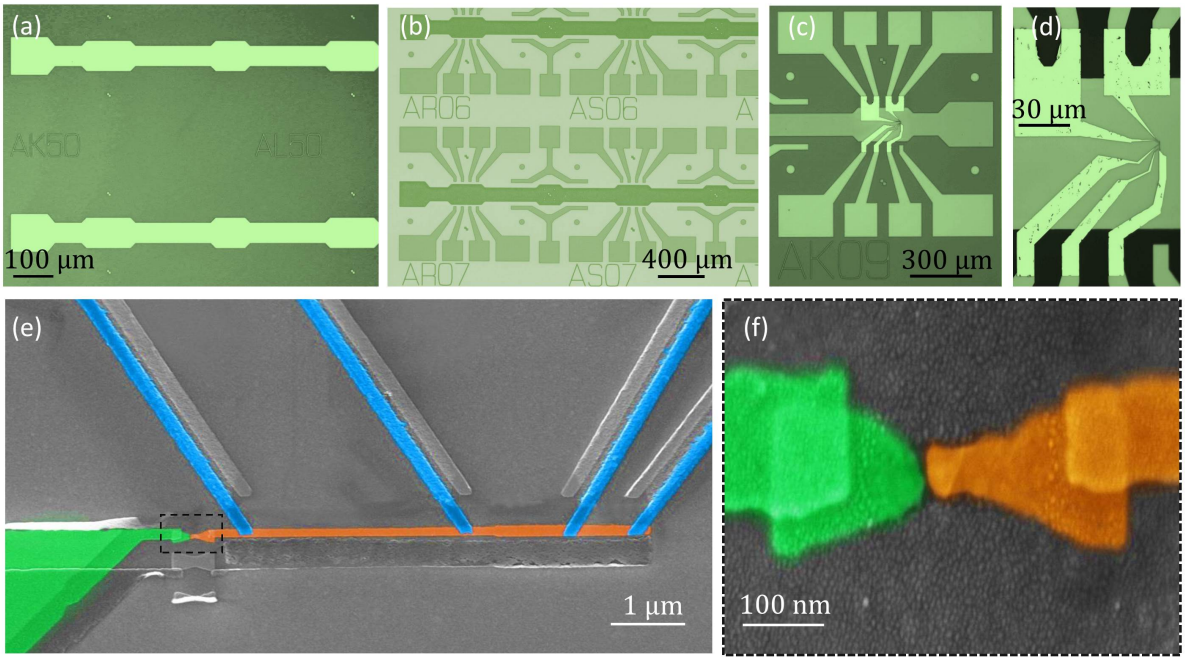

Fig. 2.1: Optical images of the Gate (a) and contact pads (b) made by laser lithography, (c-d) e-beam lithography made mask prepared for three- angle evaporation. (e-f) False-color scanning electron micrograph of the sample made by three angle shadow evaporation technique. The colors in the images below correspond to the drain (green), source (orange), thermometer and heater (blue). The *bow-tie* shaped *Pt* constriction is shown in green-orange, the Au/Ti-made *drain* and *source*, connected through the constriction, are shown in green and orange, respectively. The four Al probes, connected to the *source* via transparent contact are shown in cyan color. The nano-gap created using electromigration inside the cryostat at 4 K under cryogenic vacuum.

2.1.2 Nano-particle deposition

There has been a lot of research revealing the use of several methods for deposition of nano-particles and eventually trapping them into the electromigrated junction as: drop-casting [84, 95, 91, 85], self-assembling [96, 97, 98], di-electrophoresis trapping [99, 100, 101, 102] and sub-monolayer of Au evaporation [103, 48, 47]. Fig 2.1f and Fig. 2.2a-d show the SEM images of samples made using different methods for NP deposition.

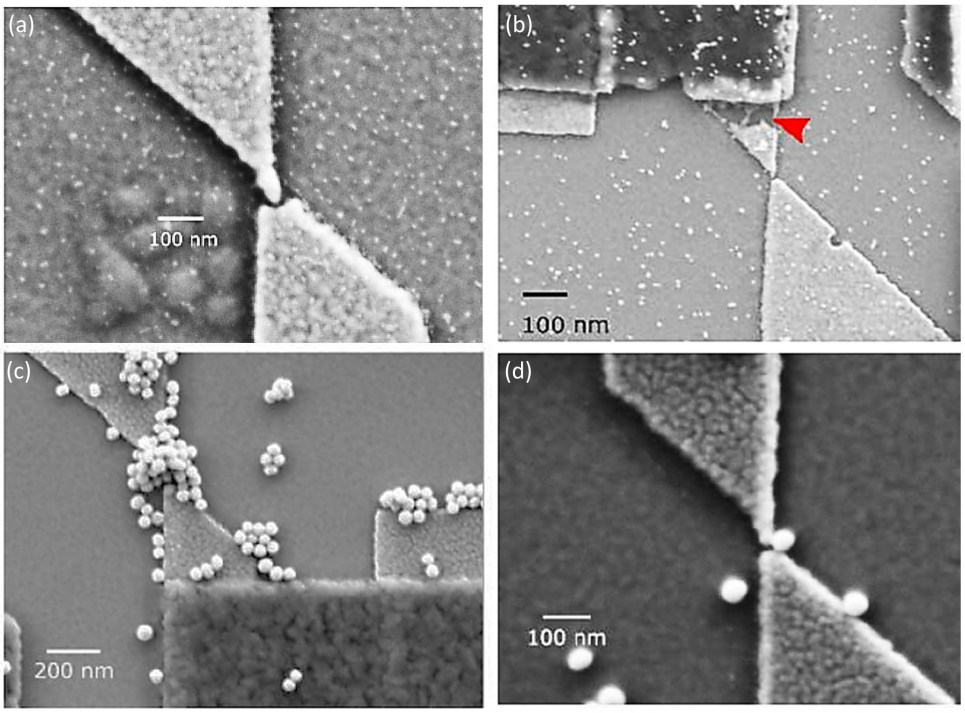

Fig. 2.2: SEM images of devices after NP deposition. (Adapted from [94]). a) drop-cast method, b) self-assembling, c) agglomeration in di-electrophoresis trapping, and d) 50 nm NP deposition using di-electrophoresis trapping

Table 2.1 compares the mentioned methods regarding four selected issues that one may consider in the process of connecting a particle to electromigrated junctions. Overall, It can be seen that the density of NP, which can increase the chance to get a working device, is high in sub-monolayer of Au deposition compared to other methods (see Fig 2.1). NPs using self-assembling method can be obtained by being dispersed in citric acid solution which can be corrosive for the aluminum leads [94] and destroy or remove them completely from our sample, the damage is shown in Fig. 2.1b by a red arrow. Therefore, we are not able to use this method as we utilize Al leads for electronic thermometery in our devices. The di-electrophoresis is suitable for NPs bigger than 50 nm below which the agglomeration of particles can be seen in Fig. 2.1c. Having a metallic particle bigger than 50 nm is pretty much similar to nano-islands in a single electron transistor (SET) which results in having very small charging energy in the order of hundreds of μV. Hence, forming a single level quantum dot is not possible (see Fig. 2.1d). That is why this method is also discarded from our fabrication process. At the beginning of my PhD, I used the drop-casting method, but the yield of getting a successful working device was very low due the low density of particles. Furthermore, given the statistic nature of electromigration and having some technical constraints, using a technique which gives us the highest yield

issues	drop-casting	self-assembling	di-electrophoresis	sub-monolayer of Au
Density of NP	low	low	very low	high
Easy to use	✓	✓	✓	✓
Contamination	–	✓	–	–
Size of NP	5-12 nm	5-12 nm	$>$ 50 nm	5-10 nm

Tab. 2.1: Comparison between different NP deposition method.

of quantum dot fabrication is demanded. Therefore, we eventually used the sub-monolayer of Au deposition (see Fig. 2.1f). Due to extreme thinness and to surface tension forces, the evaporated Au forms a self-assembled layer nano-particles on top of the sample [103]. The size of the gold nano-particles lies in the range of 5-10 nm, which serves as the quantum dot in our device. On the one hand, the size of the particles produced in this method is not under our precise control, on the other hand, the advantage of employing this technique is that the yield of a successful single-quantum dot device is rather high (about 70 %). Based on this NP deposition method, I have successfully fabricated several devices [48, 47] some of which will be discussed in chapter 4 of this thesis.

2.1.3 Electromigration

The bow-tie shaped Pt electromigration junction forms the central part of the device on which 5–10 nm diameter Au nanoparticles are deposited, forming a dense layer of quantum dots, see Fig. 2.1(f).

To complete the fabrication process and place a quantum dot in between the *source* and *drain* leads, we electromigrate the constriction, by passing a current through it in a controlled manner [104, 105, 106]. As a result, a nano-gap is created between the *source* and *drain* leads, bridged by one or sometimes several of the previously deposited gold nano-particles. In order to achieve a strong tunnel coupling between the leads and quantum dot, we perform the electromigration inside the cryostat at 4 K and under cryogenic vacuum. After cooling the device down to a temperature of 4 K, the nanometer-sized gap was created within the Pt constriction by means of electromigration [107, 48]. Here we have chosen Pt as the electromigrated material in order to ensure the source local density of

states at the QD contact to be free of superconducting correlations induced by the nearest Al contact [108]. Devices showing conductance oscillations were further cooled *in situ* down at the cryostat base temperature of about 70 mK to investigate in detail. In chapter 4 of this thesis, we will conduct two experiments to measure heat conductance of the devices realized by this technique.

2.2 Fabrication of InAs nanowire QD devices

I have also worked on the preparation of devices based on InAs/InP nanowires in close collaboration with Dr. Ville Maisi from the University of Lund. This approach can have several advantages as:
First, nanowire quantum dots are pretty much stable in terms of electrostatic switches at low temperature and in different cool-down process. In addition, the stability of the devices is maintained over time, so that one can keep a fabricated device for a long time before or after using them in the cryostat. Furthermore, the nanowire growth technique that we will briefly explain in the following sections, provides a possibility to control the tunnel barrier while growing nanowires [109, 110]. These features can open doors to study quantum dots in different regimes from sequential tunneling regime [3] to very strong tunneling regime in which Kondo effect manifests itself [65]. However, there are some difficulties to integrate and contact nanowires that will be explained in the following sections in detail.

2.2.1 Nanowire growth

A nanowire is an elongated rod-shaped structure that normally has a diameter of less than 200 nm and a length of a few μm [111]. The high aspect ratio of nanowires ideally allows the confinement of electrons in two of the three dimensions, implying that they are 1D objects [112]. However, it is preferable to consider nanowires as quasi-1D systems with respect to electron transport as they have a certain cross-sectional area. The choice of InAs as the base material for making nanowire devices is natural because of its physical properties: First of all, the bandgap is small, only 0.35 eV, consequently, problems with electrical contacting of wires should be minimal. Secondly, the low electron effective mass of InAs ($m^* = 0.023m_0$), which is three times lower than for GaAs, provides strong quantum confinement effects and a large energy level separation in the wires. The mobility is expected to be high due to the low effective mass.

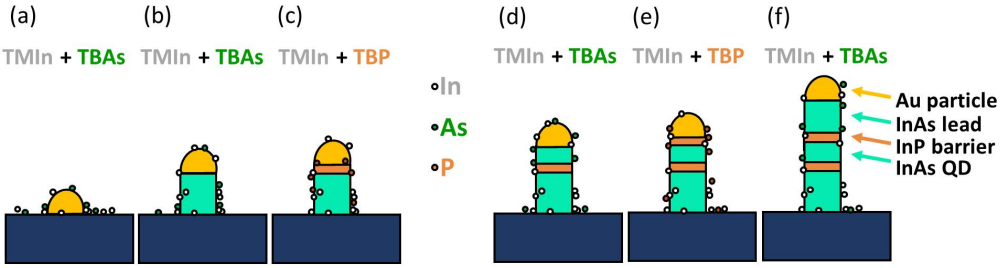

Fig. 2.3: llustration of InAs/InP nanowire growth process. (a) Nucleation: a gold seed particle is deposited on the growth substrate. TMIn and TBAs are supplied in the growth chamber providing In and As atoms that alloy with the gold seed particle. The growth of the InAs nanowire starts when the gold particle is supersaturated with In and As atoms. Then the InAs crystal precipitates at the interface between the seed particle and the growth substrate. (b) InAs growth: Continued supply of TMIn and TBAs in the growth chamber provides In and As atoms for continued growth of InAs. (c) When the length of the first InAs segment is sufficient, the group-V precursor is switched from TBAs to TBP and InP is grown instead. (d) Once an InP barrier of the appropriate length has been grown, the precursor is switched back to InAs growth: The TBP supply is cut and TBAs is supplied in the chamber again. The InAs growth follows the description in (b) and (c).

Another important feature for us, is that the Fermi level of InAs is known to pin in the conduction band at the surface, at least for the bulk material. Because of this, there is an accumulation of carriers at the surface. In principle any metal should thus provides a good Ohmic contact to InAs. However, a disadvantage with a strong pinning in the conduction band could be that it prevents realization of p-type InAs nanowires [113, 114].

One of the most interesting characteristics of nanowires is their capability to accommodate strain [115]. Materials with different lattice constants, such as InAs (6.058 Å at 300 K) and InP (5.869 Å at 300 K), can therefore be grown on top of each other without disturbing the crystallinity of the nanowire. Combining layers of material in a nanowire in this manner is referred to as axial heterostructure growth, and it can be used to create quantum dots in nanowires. This possibility of making heterostucture nanowires using a technique called chemical beam epitaxy (CBE) opens up incorporating the intermediate bandgap material (InP) within nanowires of the low bandgap material (InAs). This provides nearly atomically sharp interfaces that yield excellent experimental system for testing quantum effects.

The heterostructured InAs and InAs/InP nanowires, which are used in this thesis, have been grown by our colleagues at Lund University Dr. Ville Maisi and Prof. Lars

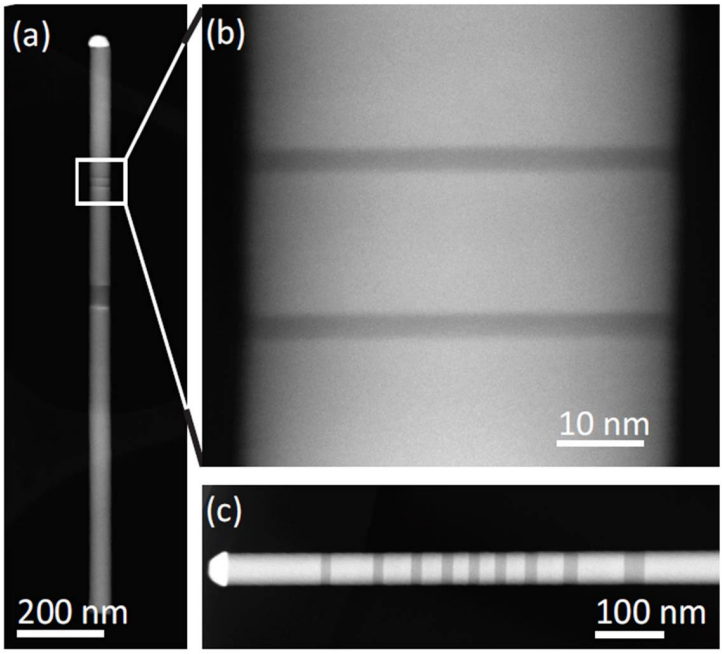

Fig. 2.4: (a-c) High-angle annular dark-field scanning transmission electron microscopy (HAADF-STEM) image of an InAs nanowire (bright contrast) with InP barriers (darker contrast) forming an InAs quantum dot. Adapted from [110]. (a) The gold seed particle is visible on top of the nanowire. (b) Short InP segments delimiting the quantum dot. (c) A HAADF-STEM image showing that it is possible to switch back and forth between InAs and InP many times once the right growth conditions have been established.

Samuelson. CBE has been used as an ultra-high vacuum approach where the precursors are fed to the growing wires as a beam rather than as a vapor. The growth species in CBE are metal-organics, where Trimethyl indium (TMIn) is used as a source of In atoms and the As and P sources are tertiarybutylarsine and tertiarybutylphosphine, respectively. In atoms can diffuse on the surface of the substrate and the nanowire side facets, reaching the gold particles whereas only the As atoms released from the TBAs molecules incident to the gold particle contribute to the growth.

Fig. 2.3 illustrates the growth process of InAs/InP nanowires and a quantum dot can be defined in a nanowire by changing the growth precursors for short periods of time, alternating between materials with a smaller and a larger bandgap [116]. It is important that the InAs segment be sufficiently long to accommodate an electrical contact, and these parts of the nanowire are referred to as leads, as shown in Figure 2.3f. A more detailed description of nanowire growth with CBE can be found in Ref. [109, 117, 118].

Figure 2.4(a) - (c) show transmission electron microscopy (TEM) images of an InAs quantum dot defined by InP barriers in an InAs nanowire. The gold seed particle is visible

on top of the nanowire. Figure 2.4b shows a zoomed image of the short InP segments focusing on the quantum dot. Fig. 2.4c, HAAD-FSTEM image shows the possibility to switch back and forth between InAs and InP many times to make series of quantum dots once the right growth conditions have been established.

2.2.2 Fabrication of a nanowire device

In order to use a nanowire for electrical and thermal measurement, several steps of fabrications are required, including: gold contact pads fabrication, coordinate grid deposition, nanowires dispersion and integrating it with local electronic thermometers. The first two steps are required to connect the smallest structure and reliably finding the position of a nanowire respectively. We have frequently used the well known laser lithography and electro-beam lithography techniques, the details of the technique can be found elsewhere [119, 120]. We give here a brief overview of the various stages of the sample fabrication process. It is worth nothing that the exact process parameters varied between sample fabrication runs. The figures given below represent typical values.

2.2.2.1 Gate and Contact pads

Our fabrication begins with the fabrication of the contact pads and the gate electrode. Gate electrodes can have different shapes in different mesoscopic experiment depending on the sample requirements or constraints in nanofabrication. For nanowire-based devices it is known to use either planar back-gate or lateral gate. In the first one, a 200-300nm SiO_2 capped highly degenerate silicon wafer is used. The oxide isolates the substrate from the fabricated structures on top, allowing it to be used as a global back gate. The latter is patterned by lithography techniques after transferring the nanowires.

First then the wafer is cleaned with (0) plasma oxygen reactive ion etching (RIE) for 1 min and (1) bake it at 200^oC for 4 min. After that (2) a first layer of photo-resist LOR3A is spun for 30 s at 4000 rpm and (3) baked at 200^oC for 2 min. (4) Immediately after, the second layer S1805 resist is spun on top for 30 s at 4000 rpm and (5) baked 115^oC for 1 min. One might use a single layer resist for such a simple lithography, but there is a high chance to have upstanding edges after lift-off which can cause discontinuity for connecting nanowire bonding pads in the following steps of the fabrication [84]. Therefore, to have a high quality and clean bonding pads without any defect and discontinuity, we use a bilayer laser lithography technique, which was developed at Institut Néel by former PhD students

#	Description	Equipment	Comments
0	cleaning	RIE oxygen plasma	1 min
1	preback	hotplate	200^oC, 4min
2	spin coat LOR3A	spincoater	30 s, 4000 rpm
3	bake LOR3A	hotplate	2 min, 180^oC
4	spin coat S1805	spincoater	30 s, 4000 rpm
5	bake S1805	hotplate	1 min, 115^oC
6	laser exposure	Laser Heidelberg	—
7	development	MF26A	1min sec
8	rinse & dry	DI water, N2	1 min
9	metal deposition	Plassys e-gun evaporator	3 nm Ti (0.08 Å/s), 35 nm Au (0.1 Å/s)
10	lift-off (1)	acetone	1 h
11	lift-off (2)	hot NMP	2 h 80^oC
12	rinse & dry	acetone, IPA, N2	——

Tab. 2.2: The detailed recipe to fabricate high quality local bonding pads by using a bilayer resist technique laser lithography

in our group [84, 95]. The fabrication is followed after exposure by (8-9) developing the wafer in MF26A for 1 min, after which the wafer is rinsed in DI water and dried with N2. we proceed with (9) the deposition of metals and eventually (10-12) lift-off and rinsing in Acetone and IPA. Fig 2.5 shows bright and dark-field optical images of bonding pads geometry after development and dicing the wafer into 5 × 10 mm chips.

2.2.2.2 Coordinate grid

After fabricating the bonding pads, a layer of e-beam resist is spun onto the wafer using the parameters indicated in Tab. 2.3. A pattern of (150 nm × 150 nm) small crosses is thereafter exposed on the wafer and the fabrication is followed by development, metal

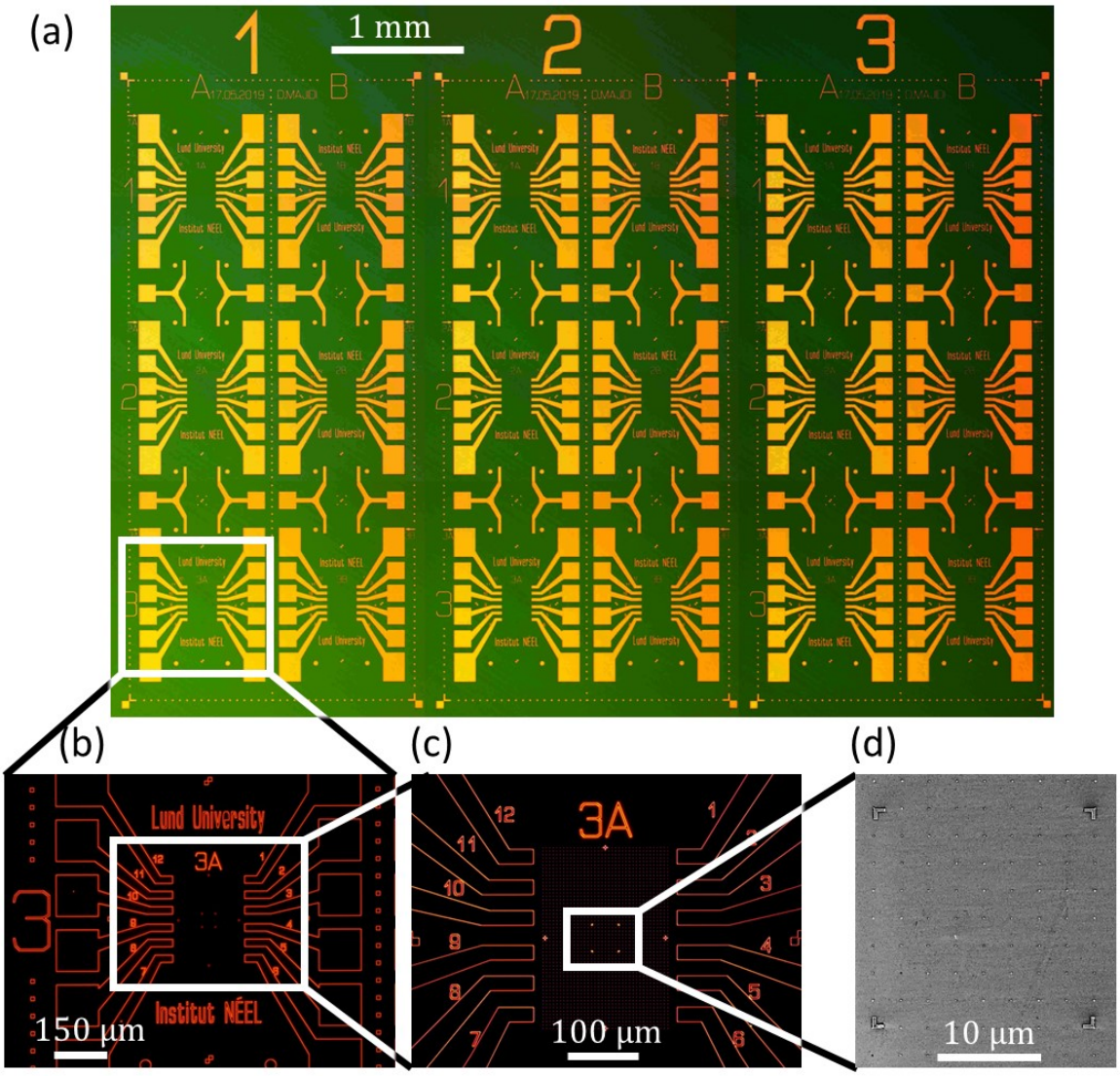

Fig. 2.5: (a) Bright-field optical image of a Si/SiO2 chip used to make contacts to nanowires, showing the pre-defined markers and bonding pads. The typical size of the chip is 10 × 10 mm, here it is diced in two 5 × 10 pieces. A blank chip with 6 device fields arranged in a 2 × 3 array is used for dispersing nanowires. (b) A dark-field optical image focused on one of the device-field, each device field features 12 contact pads to contact one or more nanowires. (c) Scanning electron microscope (SEM) images of the contact pads towards a write-field showing coordinate grid done by e-beam lithography. (d) SEM image of the center of coordinate grid.

evaporation and lift-off. Figure 2.5c-d shows a closer example of one of the write field. These small crosses make a coordinate grid that we use to map nanowire's positions once they are deposited onto the substrate. The markers are separated by 5 μm from each other and cover a 150 by 150 μm area that is surrounded by the tips of the contact pad extensions. The coordinate grid also contains four unique corner markers in $\pm$20 μm

#	Description	Equipment	Comments
0	cleaning	RIE oxygen plasma	1 min
1	spincoat PMMA 4%	spincoater	30 s, 4500 rpm
3	bake PMMA 4%	hotplate	5 min, 200^oC
4	ebeam exposure	NanoBeam nB5 [1]	—
5	development	MIBK:IPA	1min sec
6	rinse & dry	DI water, N2	1 min
7	metal deposition	Plassys e-gun evaporator	3 nm Ti (0.08 Å/s), 30 nm Au (0.1 Å/s)
8	lift-off (2)	hot NMP	2 h 80^oC
9	rinse & dry	acetone, IPA, N2	—

Tab. 2.3: The detailed recipe to fabricate 200 nm markers to map nanowires.

coordinate points from the center (0,0) that allow easier mapping of the nanowire positions (see Fig. 2.5d).

2.2.2.3 Contacting a nanowire and fabricating thermometers

In our device fabrication process, wires are mechanically transferred onto our pre-patterned 5×10 mm chip. Individual nanowires are then located with a scanning electron microscope and electrodes are patterned to selected wires again using electron beam lithography. Fig. 2.6 shows SEM image of dispersed nanowires within the write-filed and coordinate grid. A significant corner mark is shown in Fig. 2.6, which is located in the position of x =20 μm and y =-20 μm from the center. Typically we need two SEM images, one including only four small cross markers (inset Fig. 2.6) and the other one including a corner marker. The first one is used to correct the angle of the images using the four points and the latter one is used to calculate precisely the distance of the wire from the center.

After extracting the nanowire coordinates, we need two rounds of electron beam lithography and subsequent passivation/etching the intrinsic oxide of nanowire, metal deposi-

[1] NanoBeam Limited manufactures advanced Electron Beam Lithography systems.

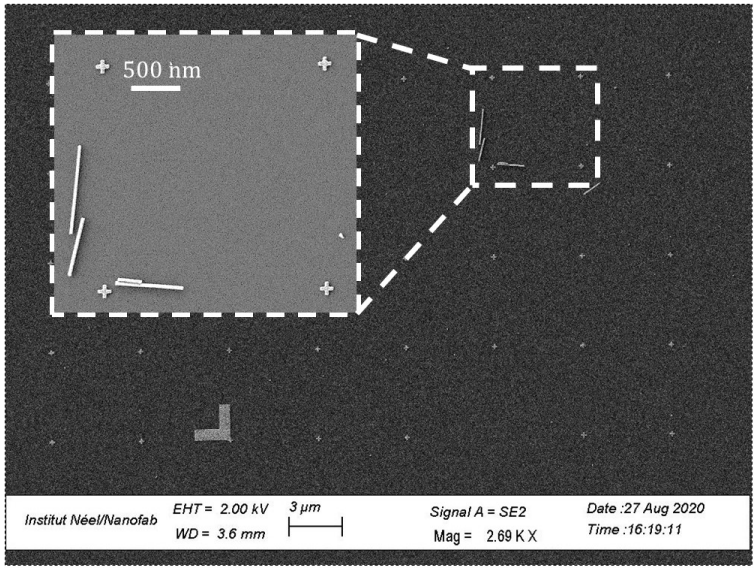

Fig. 2.6: Scanning electron microscope (SEM) image of a nanowire deposited on a substrate within the write field. A significant corner mark, is used to determine the exact position of the nanowire within the write field. Inset: a close-up SEM image of the same nanowire.

tions in order to arrive to a final device. All the processes are illustrated briefly in Fig. 2.7.

The main challenge for those who work with NWs is to remove the intrinsic oxide layer using hydrofluoric acid (HF), $(NH_4)_2S_x$ or ion milling prior to the evaporation of any metal, then run to the evaporator and introduce the NW device into the evaporation chamber, pump the chamber quickly to prevent the re-oxidation of the NWs. Regardless of what approach it is used, one needs to find an optimized and proper etching time. The initial plan was to make all the contact pads at the same evaporation to the NWs in one step, i.e. contacting NWs as well as thermometer and heater junctions coupled to the wire without breaking the vacuum using the shadow evaporation technique. This turned out to be very tough mainly due to self-blocking of the shadow mask due to the first deposited thick film to cover the nanowire, and need to increase other thickness at other angles.

Therefore, we defined the fabrication into two steps as schematized in Fig. 2.7 , i.e. first contacting only the nanowire using Ar milling or hydrofluoric acid (HF) passivation after the first lithography (Fig. 2.7c) and then making the second lithography for connecting the source electrode together with the SNS or NIS thermometer and heater to the NW using a shadow evaporation (see Fig. 2.7g). In the first lithography round, a bulky drain (shown in green in Fig. 2.8, 2.9 and 2.7a-e) and a part of the source (visible as a rectangle

in Fig. 2.8b or a circle in 2.9 on the right hand side of the nanowire) is patterned. After development, the nanowire oxide is etched with an in-situ Ar milling and followed by the metal evaporation as a stack of Ti (30 nm)/ Au (80 nm) for the device in 2.8. For making the same ohmic contact of the device in Fig. 2.9, a HF passivation is used instead of Ar milling and is followed by a fast rinsing in deionized water and immediately loaded to an evaporator chamber for making the stack of Ni (30 nm)/ Au (60 nm) on the nanowire. The Ti or Ni layers help with adhesion to the SiO_2 substrate and prevent having Schottky contact to the nanowire. The process of this step is identical to the one of the marker exposure (which is described in detail in table 2.3), except that now we have an oxide etch step prior to the evaporation.

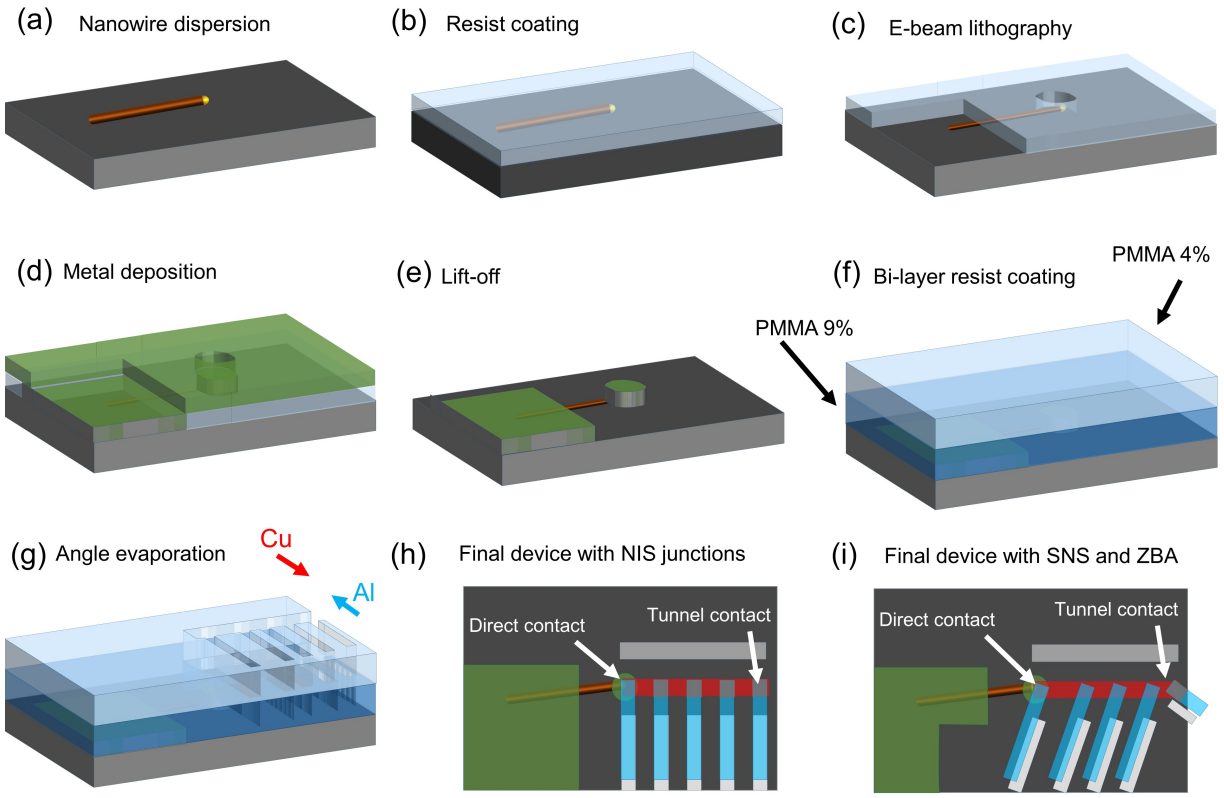

Fig. 2.7: Illustration of different steps for making electrical contacts to a single nanowire together with NIS or SNS thermometers and heaters.

Following a standard lift-off, P(MMA-MAA) copolymer is spincoated to form a relatively thick sacrificial resist with an increased sensitivity to electrons. Next, PMMA 4% is spincoated to form a much thinner resist and normal sensitivity to electrons (see Fig. 2.7f-g). The difference in electron sensitivity between the two resists leads to a large undercut which enables us to deposit different metals at different angles without breaking the vacuum. This technique is explained in detail in [84] and was also used in the proceeding

section with electromigration samples. This EBL step defines the SNS and NIS junction for devices in Fig. 2.8 and 2.9, respectively.

After e-beam lithography, the mask is cleaned by oxygen plasma, then again is loaded into an evaporator equipped with a tiltable sample holder. This allows fabricating both the normal-metal (red) and the superconducting probes (blue) using the same mask in a single vacuum cycle.

In Grenoble, we fabricated devices with transparent (SNS) and semi-transparent (ZBA) junctions as thermometers (see Fig. 2.7i and 2.8), whereas in Lund, the fabricated device (will be studied in chapter 5) is based on NIS thermometers (see Fig. 2.7h and Fig. 2.9). The exact details of each fabrication are given in the following:

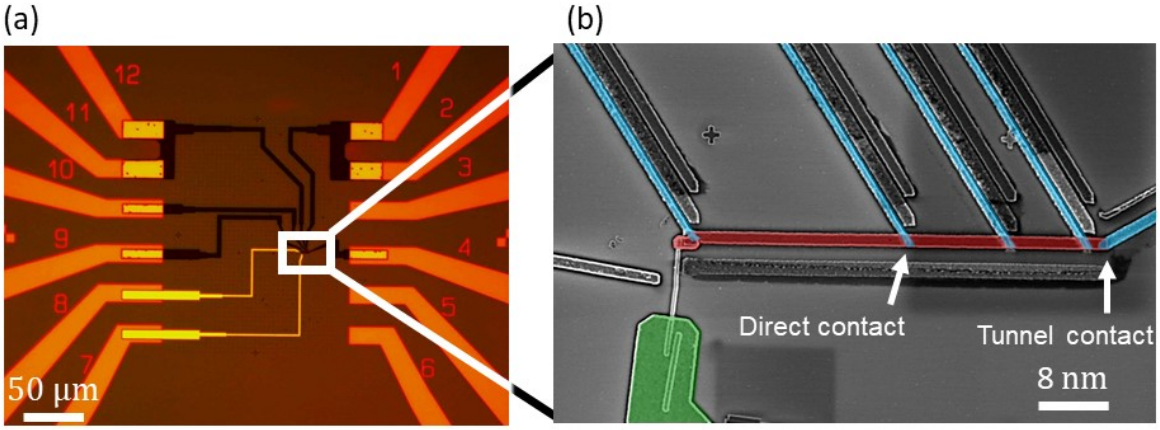

Fig. 2.8: Sample images of a finished device. (a) Optical microscope image of the contact pads and their extensions towards a device area with a finished device. Yellow shining pads (7,8) were done in first step ebeam lithography and black wires coming in from almost the top where connect the bonding pads 1-4 and 9-12 to the nanowire were done during the second step lithography. (b) Scanning electron microscope (SEM) image of the same contacted device. The device leads going out to the contact pad extensions and make contact to them. From the right to the left, ZBA thermometer, SNS thermometers (closely spaced pair $\approx$ 800 nm), SNS heater (widely-spaced pair ≈ 3 μm), side-gate and the the drain can be seen respectively.

Forming SNS and ZBA thermometers

1. First, we deposit 25 nm of Aluminum (Al) at an angle of -25^o with respect to the rotation angle. This creates the right most Al lead in Fig. 2.8b and it is followed by *in-situ* static oxidation for very short time (1 mbar for 5 sec) immediately after the deposition is completed. Short oxidation provides us a semi-transparent contact (We usually target

resistances around 5-10 kΩ for a good zero-bias peak) which will be used as a zero-bias anomaly (ZBA) thermometer [121].

2. Then the sample holder is rotated to the opposite angle and we deposit 40 nm of copper (Cu) as our source island. The island goes over the nanowire at one end, and from the other end we have a connection to ZBA thermometer. We designed our source island so that it is thermally decoupled from its environment as it is only connected to the bonding pads through Al leads i.e. only Al leads touch the island not any normal metal.

3. Then we rotate again the sample holder to the same direction of the first deposition but slightly higher angle and bring a 100 nm thick Al down in clean contact (resistances around 5-10 Ω) to the source island forming SN junctions. In this step we create the four Al leads shown in Fig 2.8b in the center.

With the mentioned three-angle evaporation through the PMMA mask and the same lithography, we are able to have both transparent (SNS) and semitransparent (NIS) in the same device.

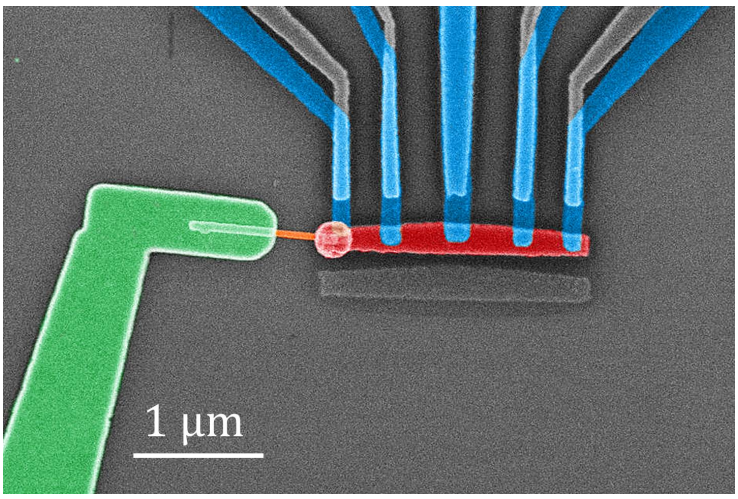

Fig. 2.9: Scanning electron micrograph of a single InAs nanowire device realized with two steps fabrication and shadow-evaporated Al-proximity junctions.

Forming NIS thermometers and heaters

1. First, a 35 nm thick film of Al is deposited at $+16^o$ with respect to the evaporation source to form 5 superconducting electrodes, they are indicated Fig. 2.9 in blue color. In order to form the AlOx tunnel barriers for NIS probe tunnel junctions, the deposited Al layer is subjected to *in-situ* static oxidation immediately after the deposition is completed.

This was accomplished by venting the chamber at air followed by an immediate pumping of the system.

2. To complete the fabrication, a 60 nm Cu is evaporated with the sample now tilted -16^o in the opposite direction compared to the Al deposition as the final film to be deposited. This upwards-shifted copy of the mask pattern forms the source island colored in red in Fig. 2.9. The purpose of this Cu layer is to form the main part of the source electrode, connecting to the small source lead which was deposited in the first step

It is worth mentioning that the oxidation time here is much longer than the previous fabrication, the reason is because we are making an opaque junction for NIS thermometery i.e one reads a resistance of a order $\approx$ 200 kΩ where as in the semi-transparent one targets $\approx$ 5-10 kΩ. As a result of the two-angle evaporation through the same mask, two projections of the complete mask pattern will be formed on the substrate. The irrelevant, partially overlapping shadow copies of the various structures, evident in Fig. 2.9 are shown uncolored.

The evaporated metal is then lifted off for both case by putting the sample in NMP for 30 min at 80^o C or Acetone and followed by rinsing in Acetone, cleaning properly in IPA and drying by N2. SEM images of samples after liftoff are shown in Figs 2.8b and 2.9. The irrelevant, partially overlapping shadow copies of the various structures is also evident for both structures.

Chapter 3

Local thermometers coupled to nano-devices

In the design of any low-temperature thermal experiment, local electron thermometery technique and thermal insulation are central topics. In this chapter, first, we discuss two mesoscopic thermometers based on superconducting hybrid junctions that can be used at cryogenic temperatures. Then, the possibility of using such junctions as a heater to provide a temperature gradient is explained. Eventually, an experiment in order to show the bolometric operation and our thermometers' ability to detect a minute change in electronic temperature is conducted.

Contents

3.1 Bolometer Vs Calorimeter

Measuring a temperature or temperature gradient is a significant problem in every thermoelectric experiment. Therefore, having a reliable local thermometer plays an important role in such studies. A thermometer usually includes (i) a temperature sensor which allows any small temperature changes in the system to be detected. (ii) a reliable strategy to convert this change into numerical values. When it comes to the temperature sensing at nanoscale, this is a real challenge [122, 22, 123, 121]. To this end, we present the working principle of two bolometers in the following sections which will be used in chapter 4 and 5 for measuring thermal conductance of quantum devices.

A bolometer measures an incident power via the heating of a material which is attached to absorber at T_b through a thermal conductance G_{th} [124]. The temperature change can be detected with a thermometer, usually made of a temperature-dependent electrical resistance or the resistance of the absorptive metal can itself be used as a thermometer [124, 125]. As depicted in Fig. 3.1a, the absorber carriers a heat capacity of C_e, such as a thin layer of metal, which converts the absorbing incoming packets of energy to heat. We consider that a constant heating power $\dot{Q}_H$ and/or an instant energy packet in the form of $\Delta E\delta(t-t_0)$ is applied to the absorber. Both forms of power increase the temperature of the absorber from T_b to T_e.

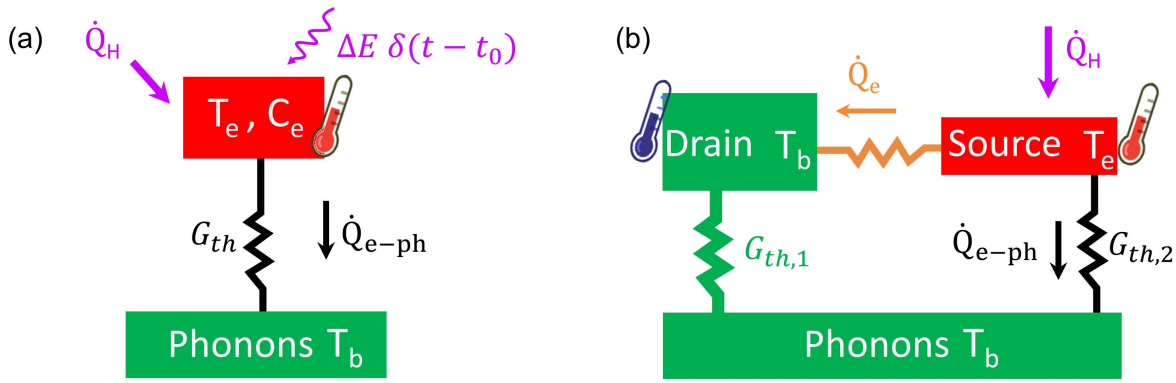

Fig. 3.1: An equivalent thermal model of (a) a device with a finite-size reservoir thermalized at T_b and elevated electronic temperature T_e. C_e is the heat capacity coupled to phonon reservoir at T_b. $\dot{Q}_H$ is a constant heating power and $\Delta E\delta(t-t_0)$ is an instantaneous heat applied to the absorber. (b) A device with two finite-size reservoirs with a tunable heat current $\dot{Q}_H$ showing how the injected heat from the heater is equilibrated via electron-phonon coupling.

However, in the experiments that we present in the next chapters, we have two electronic baths. The geometry illustrated in Fig. 3.1b consist of a bulky electrode that is assumed to be thermalized at cryostat temperature and it is fixed to T_b. While on the other side of the device, we are able to change the temperature of the second absorber. This allows us to apply a gradient temperature across our devices and determine the heat flow from the hot to the cold electrode.

In Fig. 3.1, T_e is the electronic temperature of the system that can be different from the phonon temperature, because at low enough temperatures, the electrons in a metal are weakly coupled to the phonons. Therefore, the incoming power drives the electronic system out of equilibrium in comparison with phonons' temperature. Consequently, it creates hot electrons [126]. Usually the phonons in a metallic system are well-coupled to substrate phonons and as a result, they play the role of a thermal reservoir that is thermalized at the lowest temperature T_b.

In the case of constant heating power $\dot{Q}_H$ as depicted in Fig. 3.2, the temperature of the absorber in the linear regime approaches the limiting value of:

$$T_e - T_b = \frac{\dot{Q}_H}{G_{th}}, \tag{3.1}$$

which depends on the thermal conductance G_{th} between the absorber and the phonon reservoir. We should emphasize here that the temperature of the system does not change with time and the system is in a steady-state regime.

On the contrary, when an instantaneous heat like $\Delta E\delta(t-t_0)$ is applied to the absorber, it induces a temperature peak at t_0 which results in increasing the temperature of the absorbing element sharply. This rise in temperature highly depends on the heat capacity of the absorber as illustrated in Fig. 3.2 and its relaxation reads as:

$$C_e \cdot \frac{d\Delta T}{dt} = -G_{th}\Delta T \tag{3.2}$$

When the radiation is switched off, the temperature relaxes back with a thermal time constant of $\tau = C_e/G_{th}$ to T_b. This time-resolved response is important, because the temperature changes with time and the device works in a dynamic regime.

Since the goal of this thesis is to use a bolometer for measuring the temperature of the devices, more details about calorimeters can be found elsewhere [127, 128, 129, 130]. However, I have designed, optimized and fabricated some devices for another PhD student

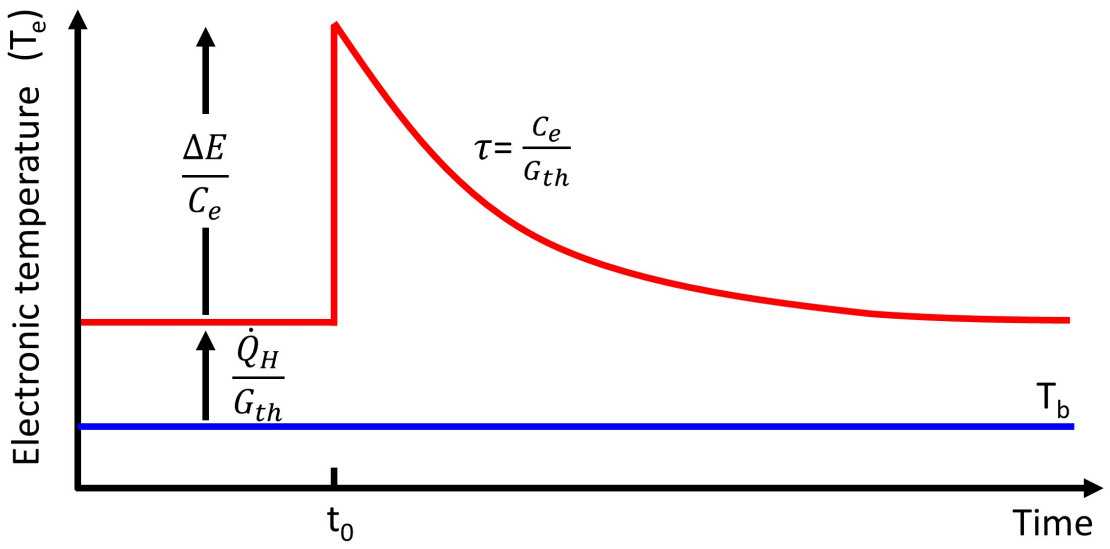

Fig. 3.2: The temperature measurement of the absorber in Fig. 3.1a shows the working regime of a calorimeter and bolometer in response to external heating powers.

in our group (Efe Gümüs), for calorimetery purposes where it will be found in Annex B.3 in detail.

Local thermometry has been achieved so far only in specific types of quantum devices. The temperature dependence of the critical current of a superconducting weak link was used in scanning probe experiments to reveal for instance the scattering sites in high-mobility graphene [23, 24]. Yet, to date, these experiments are limited to temperatures above 1 K. At milliKelvin temperatures, local thermometry can be performed in quantum devices formed in a 2DEG with a variety of methods [25, 26] that have recently been pushed to quantitative accuracy [6, 27, 28]. Noise thermometry was applied to thermoelectric measurements in InAs nanowires [29, 131]. In metallic devices, electronic thermometry is usually based on the temperature dependence of charge transport in superconducting hybrids, either in the tunneling regime for Normal metal-Insulator-Superconductor (NIS) junctions [30, 31] or at higher transparencies allowing for superconducting correlations [32, 33, 132].

In chapter 4 of this thesis, we develop a highly sensitive proximity SNS thermometer whose switching current is used to probe the temperature of the source island of our metallic quantum dot. We opt for transparent contacts in that experiment mainly because one needs a negligible access resistance to perform electromigration. As we move to nanowire devices in chapter 5, we choose our thermometer in the tunneling regime, i.e. NIS, essentially because these thermometers do not modify the density of states (DOS)

of the normal metal and a simple measurement gives access to electronic temperature. In both techniques, there are some drawbacks and advantages that will be discussed in the following.

3.2 Proximity Josephson junction thermometry

As the first on-chip bolometer, we explain a proximity Josephson junction which is composed of Superconductor-Normal metal-Superconductor (SNS) junction. For applications that demand very low-impedance thermometers at nanoscale, e.g. integrating a local thermometer with electromigration junctions, SNS thermometry technique may be a desirable candidate compared to tunnel contact thermometers. A dissipation-less current I_s flows once two supercondutor electrodes are (weakly) coupled, i.e. supercondutors interrupted by a thin barrier layer. This barrier can either be an insulating tunnel junction as predicted by Josephson in 1962 [133], a constriction [134], a normal metal [135, 136, 137, 138] or other exotic nanostructures as nanoparticles (a QD) [84], graphene [139], a semiconductor nanowire [140], a carbon nanotube [141] and so on. In the limit of weak coupling, the amplitude of I_s is simply related to the difference between the phases ϕ of superconductors order parameters [142, 143] as:

$$I_s = I_c sin\phi \tag{3.3}$$

Eq. (3.3) is the 1st Josephson equation, where I_c is the maximum current (critical current) of the junction, a value above which a non-zero voltage (higher that noise floor) can be read across a Josephson junction. In addition, the 2nd Josephson equation describes the time-evolution of phase difference across the junction:

$$\frac{\partial\phi(t)}{\partial t} = \frac{2eV}{\hbar} \tag{3.4}$$

It it worth emphasizing that the SNS configuration that we are interested in has a more complicated behavior and it is not fully sinusoidal [142] compared to Eq. (3.3). Moreover, the junction dynamics can be described by the resistively and capacitively shunted junction (RCSJ) model [144].

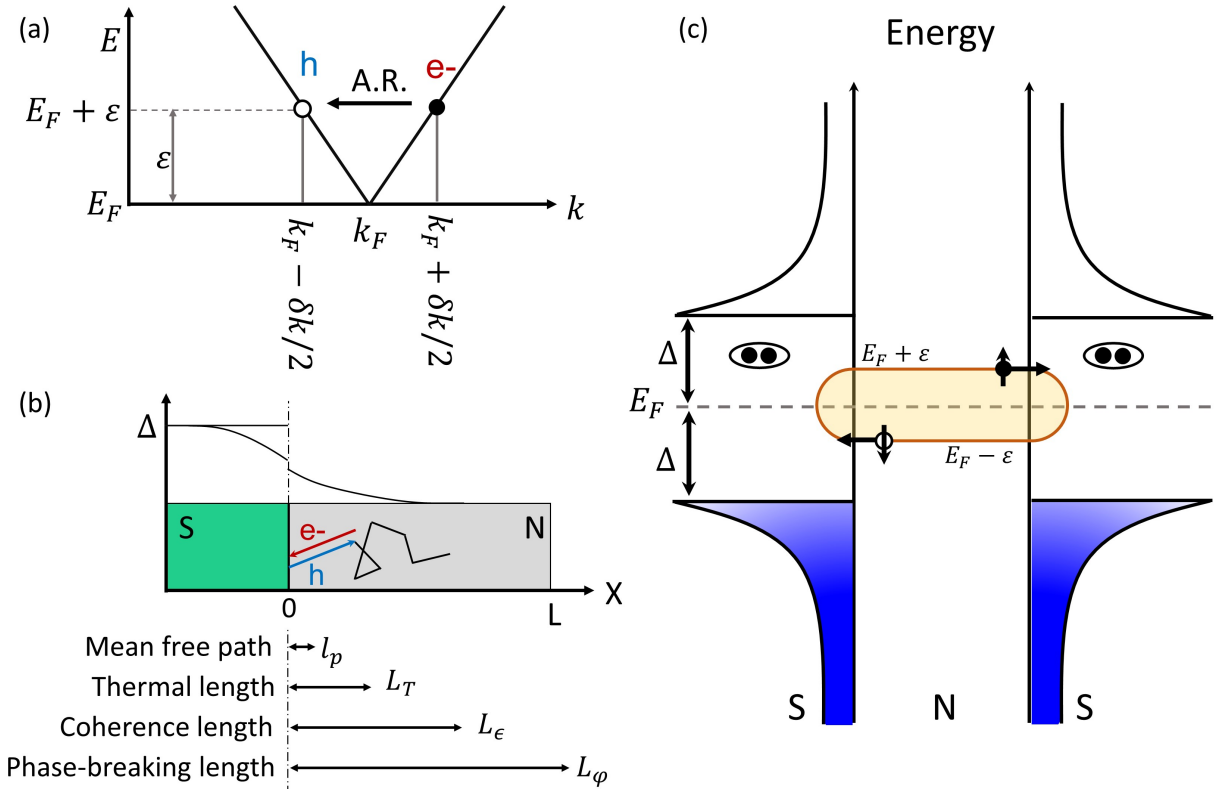

Fig. 3.3: (a) The schematic of the Andreev reflection process. (b) The relevant length scales with their schematic respective amplitude in a metallic thin film. (c) The density of states vs energy schematic of a S-N-S junction showing multiple Andreev reflection across the junction.

3.2.0.1 The Andreev Reflection

Naturally, one may wonder how the transition of the supercurrent by Cooper pairs in S and dissipative current by single electrons in N, may happen at the interface between a normal metal (N) and a superconductor (S). For small voltages (V) and below T_c, which is the superconducting transition temperature of S, all the relevant energy scales such as thermal energy k_BT and the electrostatic energy eV are much smaller than the energy gap Δ of S. A single electron with an energy of $\epsilon > 0$ compared to the Fermi level of the normal metal can not enter the supercondutor, because there is not any available state at $\epsilon < \Delta$. As a consequence, the electrons arriving from N will be Andreev-reflected (AR) at the interface of N-S [145, 146, 147] as depicted in Fig. 3.3. Let us consider that an incident electron with the energy of $E = E_F + \epsilon$ slightly above Fermi energy E_F, impinges on the N-S interface with the electron wave-vector larger than Fermi wave-vector as $k_e = k_F + \delta k/2$ and spin $S = \sigma$, is reflected as a hole which has a different wave-vector $k_h = k_F - \delta k/2$ and spin $S = -\sigma$ (see Fig. 3.3a,b). i.e., a Cooper pair with the charge of $2e$ is created in the superconductor and a vacancy in an electron state below the Fermi level in the metal.

Now if another superconductor electrode is placed in clean contact to this normal metal, an SNS junction is formed. The reflected hole with the energy of $E = E_F - \epsilon$ travels through the normal metal hits again the interface of the new NS junction. Therefore, it is reflected as a phase-coherent electron but with an opposite wave-vector into the normal metal as pictured in Fig. 3.3c. This process results in transporting a Cooper pair from one S through N to the other S via a so-called phase-coherent (multiple) Andreev reflection [148, 145]. This results in a supercurrent in the SNS junction.

The critical current of SNS junctions is determined by the length and energy scales as the following. It is worth mentioning that different possible regimes might be achieved by choosing different length scales. (i) electron pairs arriving at the normal metal may loose their coherence at an average scale determined by the thermal coherence length L_T, which is roughly speaking $L_T \approx 100$ nm and $L_T \approx 300$ nm at 1K and 100 mK, respectively [137, 142]. (ii) The actual coherence length L_ϵ of Andreev pair varies from about the thermal coherence length L_T at high energy $\epsilon \approx k_B T$ and it is limited by the phase-breaking length L_φ at low energy (Fermi level $\epsilon \approx 0$). The value of L_φ is associated with both elastic and inelastic scattering on impurities and phonons [137, 142]. (iii) The critical current of the junctions scales exponentially with the length of the normal metal island $I_c \propto \exp(-L/L_T)$ as indicated in Fig. 3.3b, where L is the length of the normal metal. Four $S-N$ junctions are embedded in the experiment of chapter 4. In two of them, the normal metal length L is larger than the thermal length L_T and smaller than phase-breaking length L_φ, $L_T \ll L \ll L_\varphi$. Consequently, a diffusive and phase-coherent transport is expected. (iiii) The typical energy scale of a diffusive SNS junction is Thouless energy $E_{Th} = \hbar D/L^2$ [137, 138, 145], where $D = v_f l_e/3$ is the diffusion constant of the normal metal and v_f is the Fermi velocity in the normal metal.

3.2.0.2 Temperature dependence of critical current

The interplay of the superconducting energy gap Δ and the Thouless energy E_{Th} on SNS junctions might result in two different regimes. The first one is short-junction limit, where the superconducting energy gap Δ is much smaller than Thouless energy E_{Th} ($E_{Th} \gg \Delta$). The second one, which is of a particular interest for us, is the long-junction limit, where the superconducting energy gap Δ is much bigger than Thouless energy E_{Th}, ($E_{Th} \ll \Delta$). Therefore, only electrons within an energy window centered the Fermi level and of width the Thouless energy participate in transporting a supercurrent by phase-coherent

Andreev reflections at the $N-S$ interface. The zero-temperature critical current of such a junction varies linearly with Thouless energy E_{Th}, hence, the production of the normal state resistance R_N and critical current I_c reads as [137]:

$$eR_N I_c(T=0) = 10.82 E_{Th} \tag{3.5}$$

where R_N is the normal state resistance. In our experiment, the junction length L is much larger than $\sqrt{\hbar D/\Delta}$, that corresponds to $\Delta \gg E_{Th}$. which sets our condition to be in the long junction limit [137, 135].

In the high temperature limit, i.e. $k_B T \gg E_{Th}$ or equivalently $L \gg L_T$ with $L_T = \sqrt{\hbar D/2\pi k_B T}$, the critical current can be written by neglecting the mutual influence of the two superconducting electrodes as the sum of different contributions associated with each Matsubara frequency $w_n = (2n+1)\pi k_B T$ from the Usadel equations [137, 149]:

$$eR_N I_c(T) = 64\pi k_B T \sum_{n=0}^{+\infty} \frac{L}{L_{w_n}} \frac{\Delta^2 \exp(-L/L_{w_n})}{[w_n + \Omega_n + \sqrt{2(\Omega_n^2 + w_n \Omega_n)}]^2} \tag{3.6}$$

where $\Omega_n = \sqrt{\Delta^2 + w_n^2}$ and $L_{w_n} = \sqrt{\hbar D/2w_n}$. For $k_B T > 5E_{Th}$, the contribution associated with high Matsubara frequencies becomes trivial and only the first term $w_0 = \pi k_B T$ with $L_{w_0} = L_T$ remains influential. Therefore, the expression for the critical current of SNS junctions in Eq. (3.6) can be estimated in the limit of $\Delta/E_{Th} \to \infty$, i.e. long junction limit, as:

$$eR_N I_c(T) = \frac{32}{3+2\sqrt{2}} E_{Th} \left(\frac{L}{L_T}\right)^3 e^{-L/L_T} \tag{3.7}$$

In low temperature limit (T is low but not zero), i.e. $k_B T \leq E_{Th} \equiv L \leq L_T$, the assessment of the critical current I_c includes the solution of the complete Usadel equation for all energies, i.e. for the whole range of Matsubara frequencies. However, in $\Delta/E_{Th} \to \infty$ limit, a good analytical estimation is given by:

$$eR_N I_c(T) = aE_{Th}\left[1 - b\exp\left(-\frac{a}{3.2}\frac{E_{Th}}{k_B T}\right)\right] \tag{3.8}$$

here $a = 10.82$ and $b = 1.30$. It should be noted that Eq. (3.8) converges to Eq. (3.5) for $T \to 0$.

The temperature dependence of $eR_N I_c$ product is calculated using Eq. (3.5) -(3.8) and shown in Fig. 3.4. As one can see in Fig. 3.4, the critical current of an SNS junction is a monotonous function of the temperature. Consequently, the temperature dependent

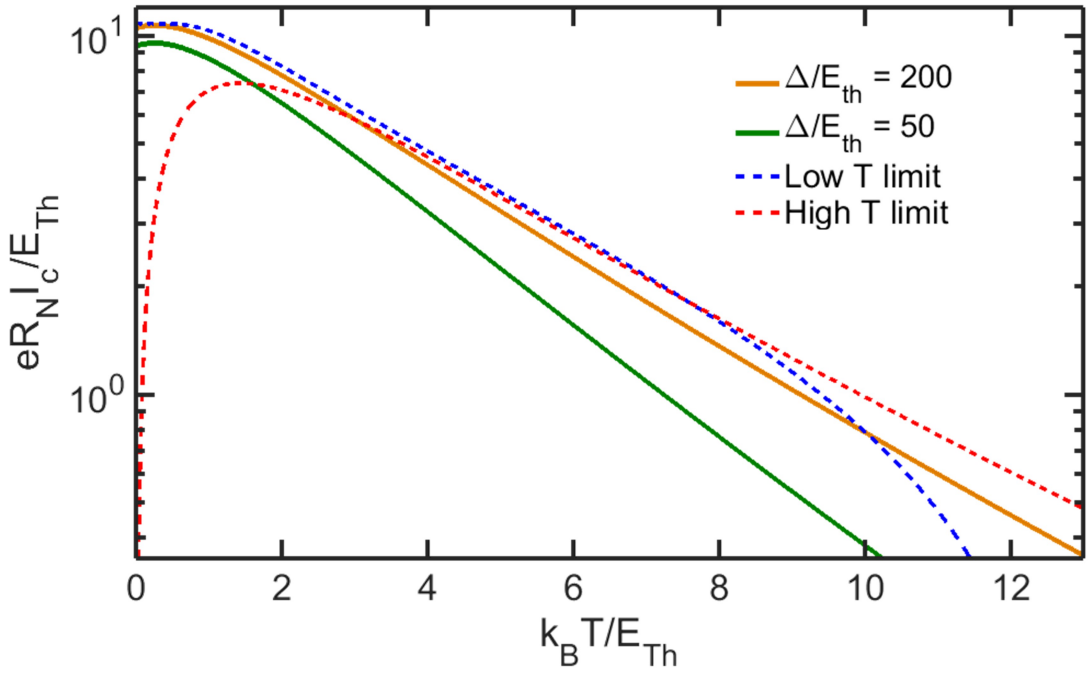

Fig. 3.4: The calculated normalized $eR_N I_c/E_{Th}$ product as a function of temperature. Solid lines are calculated with Eq. (3.6) for $\Delta/E_{th} = 200, 50$ ratio. The red and the blue dashed lines show the calculation in high and low temperature limits, respectively.

feature of the SNS junction can be used as a secondary thermometer in order to measure the local electronic temperature of the normal metal. We should emphasize here that if we increase the distance L to about 5 μm between two superconducting electrodes, then one might not be able to measure any critical current. Therefore, very long junctions ($L > 5$ μm) can be served as a local heater. A detailed discussion will be given in thermal bias section.

3.2.0.3 DC measurement of critical current

One of the typical measurements that is performed at low temperature in order to check the critical current of SNS jucntions is shown together with its DC measurement circuit in Fig. 3.5. For small current-bias I_{SNS} values, the junction shows a zero-resistance and one reads zero voltage (within noise) across the junction. As I_{SNS} is increased above a certain value, the junction switches to a resistive state with almost linear IV characteristics. The switching current is identified as the critical current I_c. In the backward sweep at which the junction switches back from its resistive state to the superconducting state, a retrapping current I_r is defined. The retrapping current is often lower than the junction's

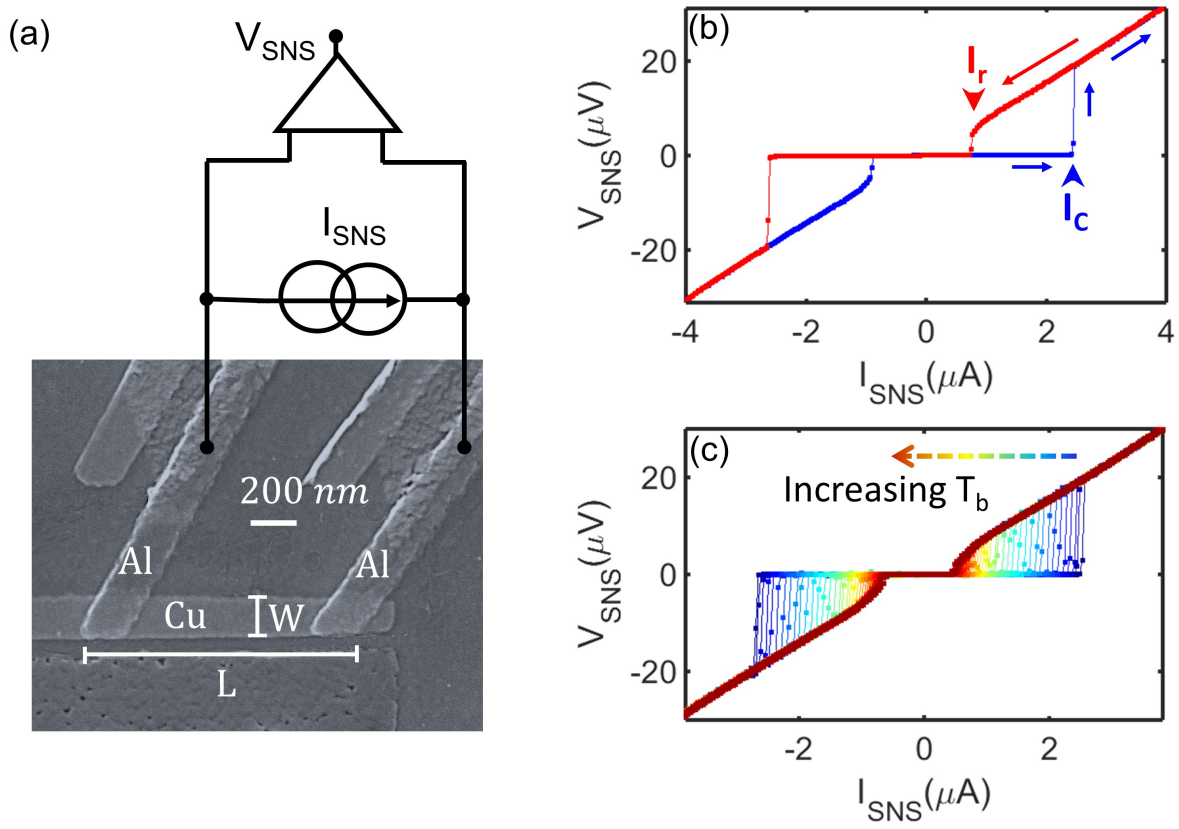

Fig. 3.5: (a) Scanning electron micrograph of the device used in chapter 4 with the DC measurement circuit. two transparent superconducting Al contacts are used for SNS thermometry. (b) IV curve of a typical SNS junction shows hysteresis at $T_b = 70$ mK. (c) The temperature dependence of the critical current of the SNS thermometer was measured from $T_b = 70$ mK (dark blue) to $T_b = 350$ mK (dark red) by the DC setup.

critical current. In the case where $I_r < I_c$, the junction shows a significant hysteresis as illustrated in Fig. 3.5b. DC IV characteristics of a SNS thermometer junction at different bath temperatures are shown in Fig. 3.5c.

In 2008, Courtois et al. investigated the origin of hysteresis in such an SNS junction [138]. They utilized two NIS tunnel probes in series forming SINIS structure. The SINIS probes acted as a thermometer for metallic island. So, they were able to measure the temperature of the normal metal while measuring the IV through SNS junction as shown in Fig. 3.6. In this experiment, according the SINIS thermometer probe, the electronic temperature is at the bath temperature $T_e \sim T_b$ when the junction is in non-dissipative supercurrent state. While the junction is switched in the resistive state with linear IV characteristics, an overheating is observed due to Joule dissipation. This Joule dissipation results in an abrupt jump in electronic temperature of the normal metal from $T_e = 50$

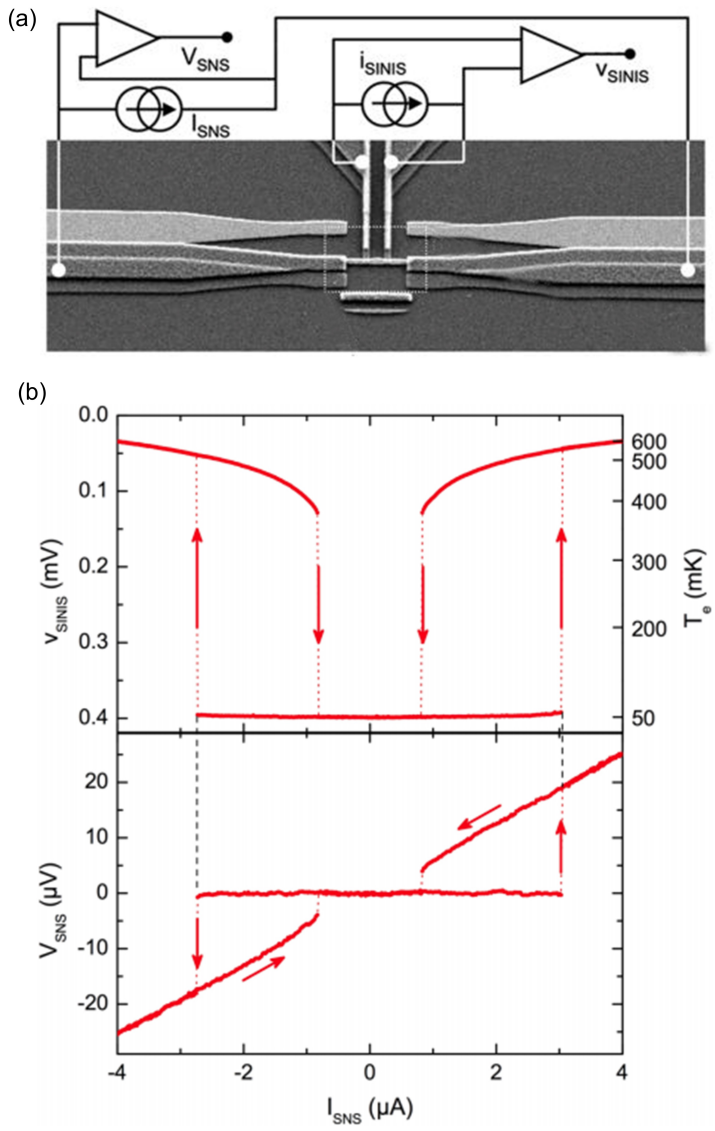

Fig. 3.6: Adapted from [138]. (a) The SEM image of the device showing an S-N-S junction of 1.5 μm length with a sketch of the measurement circuit. Two tunnel probes in series form SINIS structure in the middle are connected to the normal metal embedded between two superconducting banks (on the left and right sides of the image). (b) The current-voltage characteristics of the S-N-S junction device (bottom panel) shown on the same current scale with the S-I-N-I-S thermometer voltage response (top panel) was measured simultaneously at a 50 mK cryostat temperature. In the top panel, the right vertical axis gives the corresponding electron temperature .

mK to $T_e \approx 500$ mK as demonstrated in Fig. 3.6b. Strikingly, when the current is swept back below the critical current I_c, the temperature remains at the same elevated temperature until reaching accurately the retrapping current I_r, then, it drops immediately to $T_e = 50$ mK (see Fig. 3.6b for more details). This demonstration assuredly shows that the hysteresis in IV characteristics of our experiment in Fig. 3.5b has a thermal origin

and results from the increase in the normal-metal electron temperature once the junction switches to the resistive state [138].

3.2.0.4 Statistical measurement of the critical current

As it is difficult to keep the junction environment unchanged during critical current measurement, any thermal fluctuation can act as an additional bias. This results in making the junction switch at I_{sw} before the actual critical current of the device sets in [150]. Ideally, the critical current I_c of an SNS junction can be measured by simply measuring the switching current of the junction in a single sweep of the biasing current as explained in the previous section for other applications rather than thermometery. However, for thermometery purposes, the measurement of such a single event can be of limited use, as the switching of the junction is a stochastic process [135] and one needs to impose a statistical measurement to determine the critical current I_c accurately.

To this end, the statistics of the switching current is probed using an oscilloscope by biasing the junction through a bias resistor with an AC signal [151, 152, 33]. The $R_{bias} = 100$ kΩ is much larger than the junction's resistance, therefore, it meets the condition for a current bias. Moreover, the AC signal in our experiment has a triangular shape with a frequency of 300 Hz, and an amplitude of $V_p = 250$ mV. Fig. 3.7a shows the output signal, which is measured by a Femto voltage amplifier, and the applied signal (input current bias) in pink and yellow, respectively.

According to Fig. 3.7a, the measured output voltage is almost zero within the noise level (1) and an abrupt jump (2) can be seen as soon as the input current exceeds the critical current of the junction. (3) A trigger voltage is set above the noise level (zero-based line) indicated by a white arrow to $V_{trigger} = 44$ mV. Consequently, the oscilloscope can probe the value of the input signal at which the junction's current I_{sw} is switched for each period of the triangle signal form the superconducting to the resistive state. Fig. 3.7b illustrates a distribution of the switching current which is the outcome of measuring approximately more than 3000 switching events that are recorded in 10 seconds by the oscilloscope. It is intriguing to see a long tail for the distribution of the switching current with this measurement technique. It is worth mentioning that an asymmetry in the histogram is expected at low temperature anyway. The large tail could be the signature of an environmental noise going to the junction [150]. Therefore, one would see a more pronounced behavior at higher bath temperatures [47].

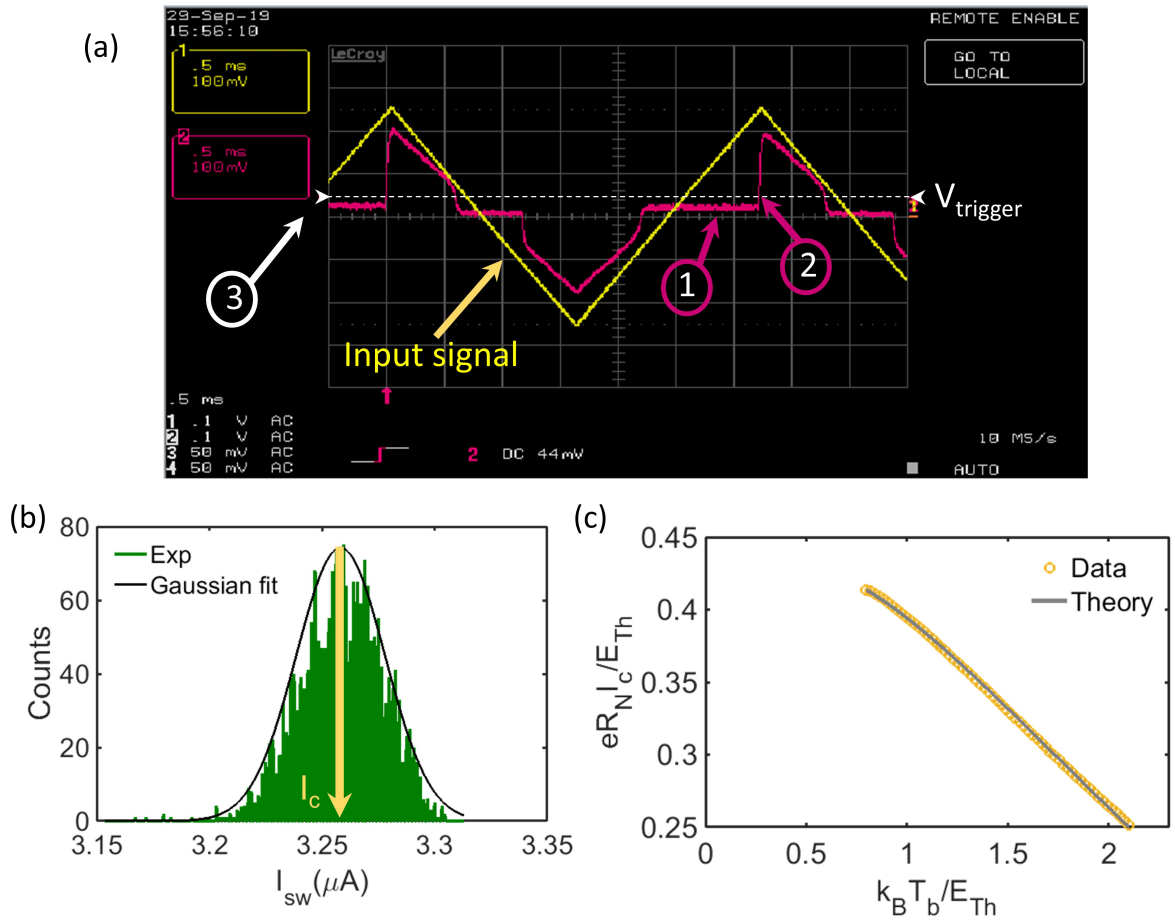

Fig. 3.7: Statistical measurement of critical current. (a) The oscilloscope screen displays the applied triangle signal in channel one (yellow) and the measured voltage across the SNS junction in channel 2 (pink). A trigger of 44 mV (above noise level) sets for channel two for detecting the switching current. (b) Histogram of the stochastic switching event recorded by the oscilloscope at $T_b = 80$ mK, with a fitted Gaussian envelope in black. The critical current is shown by a light yellow arrow pointing downward. (c) The critical current I_c as a function of the bath temperature (calibration) for device B in chapter 4. The axis being normalized with normal state resistance and the Thouless energy. The orange solid line is a fit with the theory explained in section 3.1.0.2 Eq. (3.6).

We defined the actual critical current I_c as the most probable I_{sw}, which is the maximum of the distribution, shown by a yellowish arrow in Fig. 3.7b. The extracted critical current from the distribution at different bath temperatures is plotted in yellow in Fig. 3.7c together with its theory prediction in gray according to Eq. (3.6). The low Thouless energy $E_{Th} \sim 8$ μeV was deduced from the theoretical fit (gray line) in Fig. 3.7c. We used this calibration curve of the thermometer that is employed in device B in chapter 4. This low Thouless energy prevents from having a saturation of I_c at low temperatures and therefore, the thermometer remains sensitive where the thermal transport through

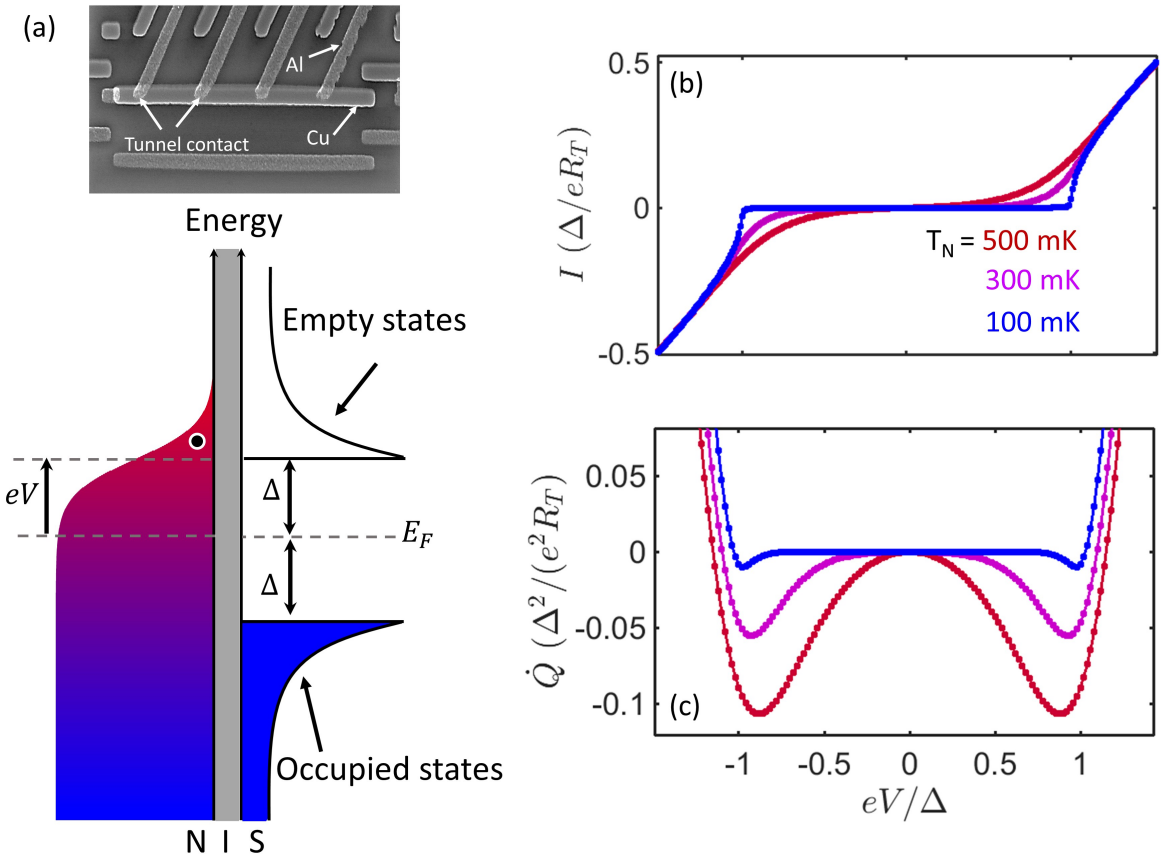

Fig. 3.8: (a) Top: A SEM image of a typical NIS junction fabricated by shadow evaporation. Bottom: Density of states of normal metal (N) - insulator (I) - superconductor (S) vs energy on the vertical axis. A bias voltage increases the chemical potentials of normal metal by eV which allows quasiparticles with energy $E > 2\Delta$ tunnel across the barrier.

the quantum dot gains importance in comparison with other heat relaxation processes in chapter 4.

3.3 Hybrid tunnel junction thermometry

Another thermometer that we utilize in chapter 5 of this thesis as a bolometer is based on normal metal–insulator–superconductor (NIS) junction. In this section, first, we briefly introduce the principle of electric transport through an NIS junction [153, 154]. We find expressions for the electric and heat currents. Then, we discuss a detailed estimation of the NIS probe parameters from independent electrical measurements by comparing with the established theory. In addition, a typical calibration curve of an NIS junction will be presented.

3.3.1 *NIS* Thermometer and cooler characterization

A tunnel junction is composed of an insulating barrier between two metallic electrodes. As it has already been explained in chapter 2, we fabricate a tunnel junction between Aluminum (Al) and Copper (Cu) by oxidizing the Al layer just after its evaporation and therefore, an Aluminum tunnel junction (AlOx) is formed. An SEM image of such Al-AlOx-Cu together with the energy diagram of an NIS tunnel junction at a finite bias eV is shown in Fig. 3.8a. The distribution function of the normal-metal N at a finite temperature that is governed by the Fermi distribution is drawn with respect to energy (vertical axis) on the left-hand side. The insulating layer shown in gray is in the middle and eventually, the density of states (DOS) of the superconductor is plotted in the right-hand side. At equilibrium, when there is no voltage or temperature bias, the Fermi level in the normal metal island is aligned with the Fermi level of the superconductor electrode and tunneling is forbidden at low temperature by the strong superconducting gap Δ. By applying a small voltage bias across the junction, one can raise (lower) the chemical potential of the normal metal (superconductor) and tunneling of quasiparticles across the barrier is possible. The I-V characteristics through a single NIS junction reads as [30],

$$I = \frac{1}{2eR_T} \int_{-\infty}^{+\infty} n_s(E,\Delta) \times [f_S(E-eV) - f_N(E+eV)]\, dE \tag{3.9}$$

where $n_S(E)$ is the normalized BCS density of states [143], and $f_S(E)$ and $f_N(E)$ are the quasi-particle occupation factors for the superconductor and normal metal. We assume that the quasi-particles in the normal and superconducting electrodes are in quasi-equilibrium, i.e. they follow a Fermi-Dirac distribution at some temperatures T_N and T_S, respectively.

At a finite temperature T and bias voltage eV, two main parameters describe the electric transport through the junction: (i) the tunneling resistance R_T, (II) the gap parameter Δ of the superconducting lead. In spite of the fact that the model is apparently simple, it can produce quantitatively correct predictions in many experimentally relevant cases [22, 123, 155].

Using Eq. (3.9), the IV curves of an NIS junction for different temperatures of the normal metal are plotted in Fig. 3.8b. The first eye-catching point is that, the sub-gap current varies strongly with the temperature of the normal island. This is because at higher temperatures, there are more electrons above Fermi level which can pass through

the barrier. In this regime where the $\Delta \gg k_B T$ and $0 \ll eV < \Delta$, one can re-write the Eq. (3.9) with a good estimation [156] as:

$$I(V) = \frac{\Delta}{eR_T}\sqrt{\frac{\pi k_B T}{2\Delta}} \exp \frac{eV - \Delta}{k_B T}. \tag{3.10}$$

For the bias voltages much greater than the superconducting gap $eV \gg \Delta$, the currents at different temperatures merge together to a single branch and show a resistive state.

We used Eq. (3.9) to fit the experimental IV of NIS junctions. The low-temperature experimental characteristics of the NIS junction of our device is shown in Fig. 5.5, both on linear and logarithmic scales, together with the theoretical $I - V$ characteristic using Eq. (3.9) at $T_b = 100$ mK. Approximately at voltage $\pm\Delta/e$, which will be refer to as the gap voltage, one finds an onset of current which becomes sharper as the temperature is decreased.

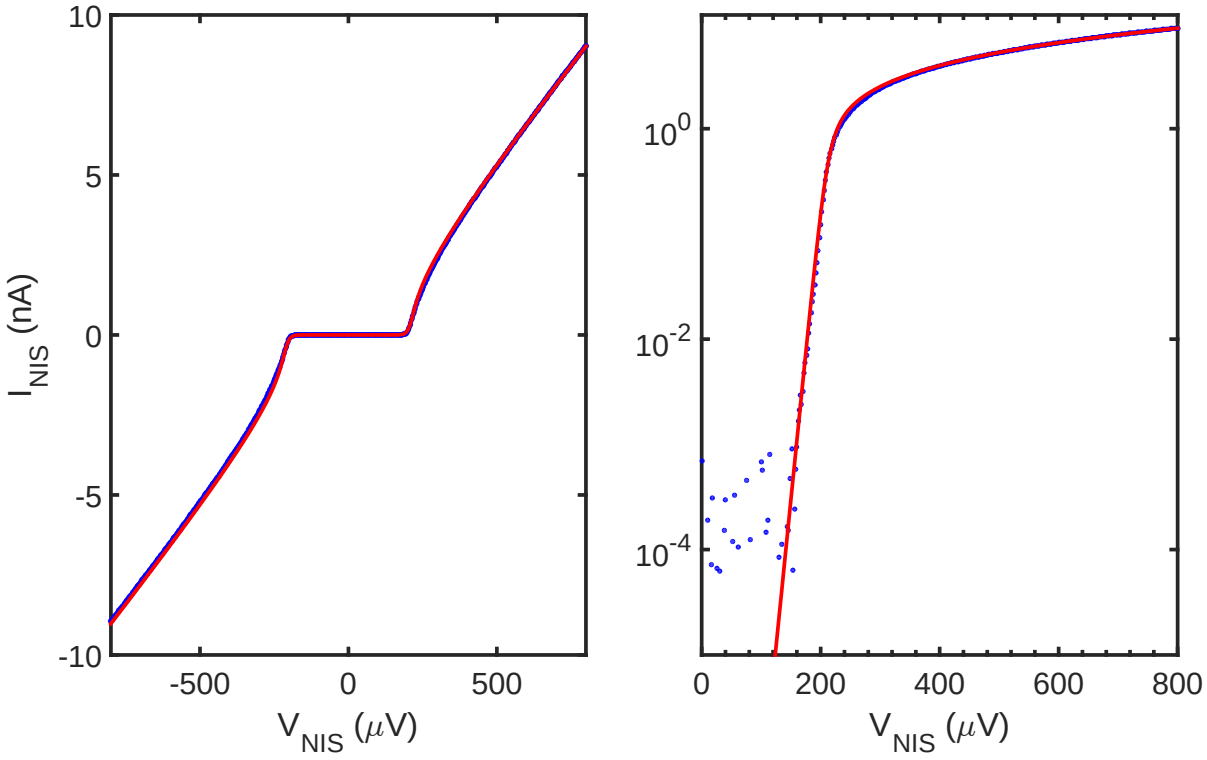

Fig. 3.9: Current–voltage curve of one NIS junction using linear (left) and logarithmic (right) scale. Fit to Eq. (3.9) is shown as red lines: $\Delta = 209$ μeV, $R_T = 85.6$ kΩ and T_b= 100 mK.

3.3.1.1 Heat transfer in an NIS junction

For many applications, it is important to consider the heat carried by the quasi-particles as well. A single quasi-particle of energy E deposited to (extracted from) an electrode

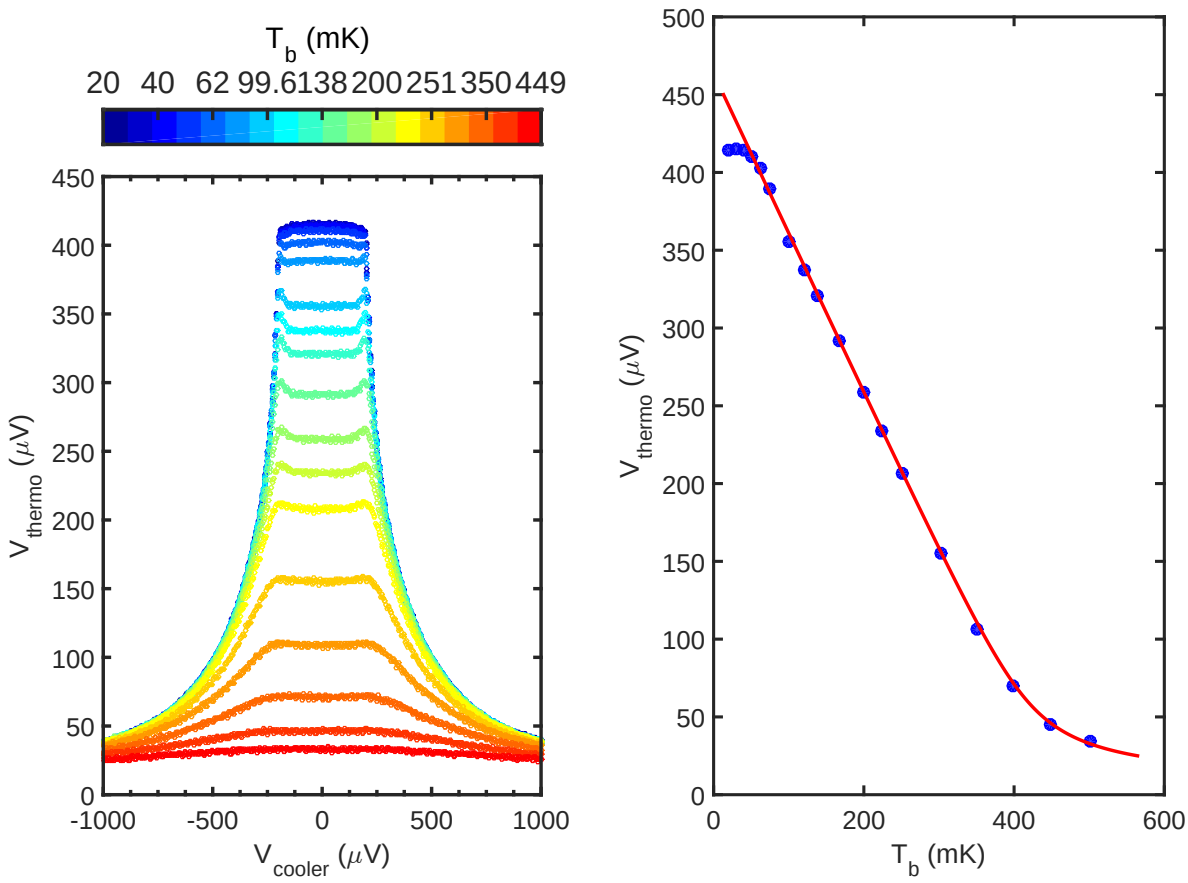

Fig. 3.10: (Left) Tunnelling current of a SINIS (pair of NIS) junction with respect to the applied heater/cooler voltage at different bath temperatures T_b. (Right) Measured voltage across a floating current (5 pA) biased SINIS junction as a function of the bath temperature at T_b and $V_g = 0$ V gives the calibration of the thermometer.

adds (removes) an amount $E - E_F$ of heat. Consequently similar to Eq. (3.9), we obtain the following integral forms for the average heat power incident on electrode N:

$$\dot{Q}(E) = \frac{1}{e^2 R_T} \int_{-\infty}^{+\infty} (E - eV)\; n_s(E, \Delta) \times [f_N(E - eV) - f_S(E)]\; dE \tag{3.11}$$

Fig. 3.8c shows a calculated power through NIS junction using Eq. (3.11). A peculiar property of the NIS junctions is that for bias voltages slightly less than the gap voltage Δ/e, one finds a region where $\dot{Q}(V)$ is negative, i.e. the normal electrode is cooled. Considering the preceding discussion on the heat carried by tunneling quasiparticles, it is evident that cooling can be brought upon by extracting quasiparticles from above the Fermi level or depositing them below it, which has been extensively studied in [31, 72, 30]. Equations (3.9)-(3.11) allow the electric and heat currents through an NIS junction to be evaluated for different bias voltages V and electrode temperatures T_S and T_N.

3.3.1.2 Calibration of NIS thermometers

After extracting basic parameters (R_T, Δ) of our NIS junctions using the mentioned theory to fit the experiment, we calibrate the NIS thermometer with respect to our known cryostat temperature. Calibration is done at equilibrium, so that the cryostat temperature (equal to the phonon temperature) can be attributed to the electronic temperature of the normal metal. A pair of NIS junctions is biased with a constant current of few pA (here 5 pA) and the voltage drop across the junction is measured as a function of the bath temperature [30]. The measured voltage of the SINIS (a pair of NIS) junction for the full V_{NIS} range is shown in Fig. 5.6 left. This measured voltage across the SINIS junction as a function of bath temperature gives us the calibration of the thermometer. Therefore, one can access to electronics temperature of the normal metal (source island) with the aid of the calibration curve shown in Fig. 5.6 on the right hand side.

3.4 Thermal bias

In addition to having a working mesoscopic device and sensitive thermometers, another important ingredient for conducting the heat conductance experiments is the ability to heat up the device, i.e. establish a temperature gradient ΔT while maintaining the low temperature to be able to probe the quantum dot physics. The thermal bias in nano-structures is traditionally applied through Joule dissipation. Unlike electronic cooling (refrigeration), a heating is simply obtained by passing an electric current through a resistor or in general by a resistive element on one side of a device while the other side is kept at the lowest possible temperature. Different means of providing a temperature gradient across a nano-object in particular in quantum dots have been developed and showed that heaters as well as thermometers have to be local at these small length scales [157, 158, 47, 159].

There are several approaches known perceptibly that have been so far utilized in thermoelectric experiments, mostly thermopower measurement [65, 110, 157, 158, 160, 66, 131, 161, 5, 162, 163, 164, 165, 166, 167, 168], or recently shown for noise thermometery [161, 131, 160], and only few of them allowed evaluating the heat conductance of quantum devices at sub-Kelvin temperatures [89, 27, 47].

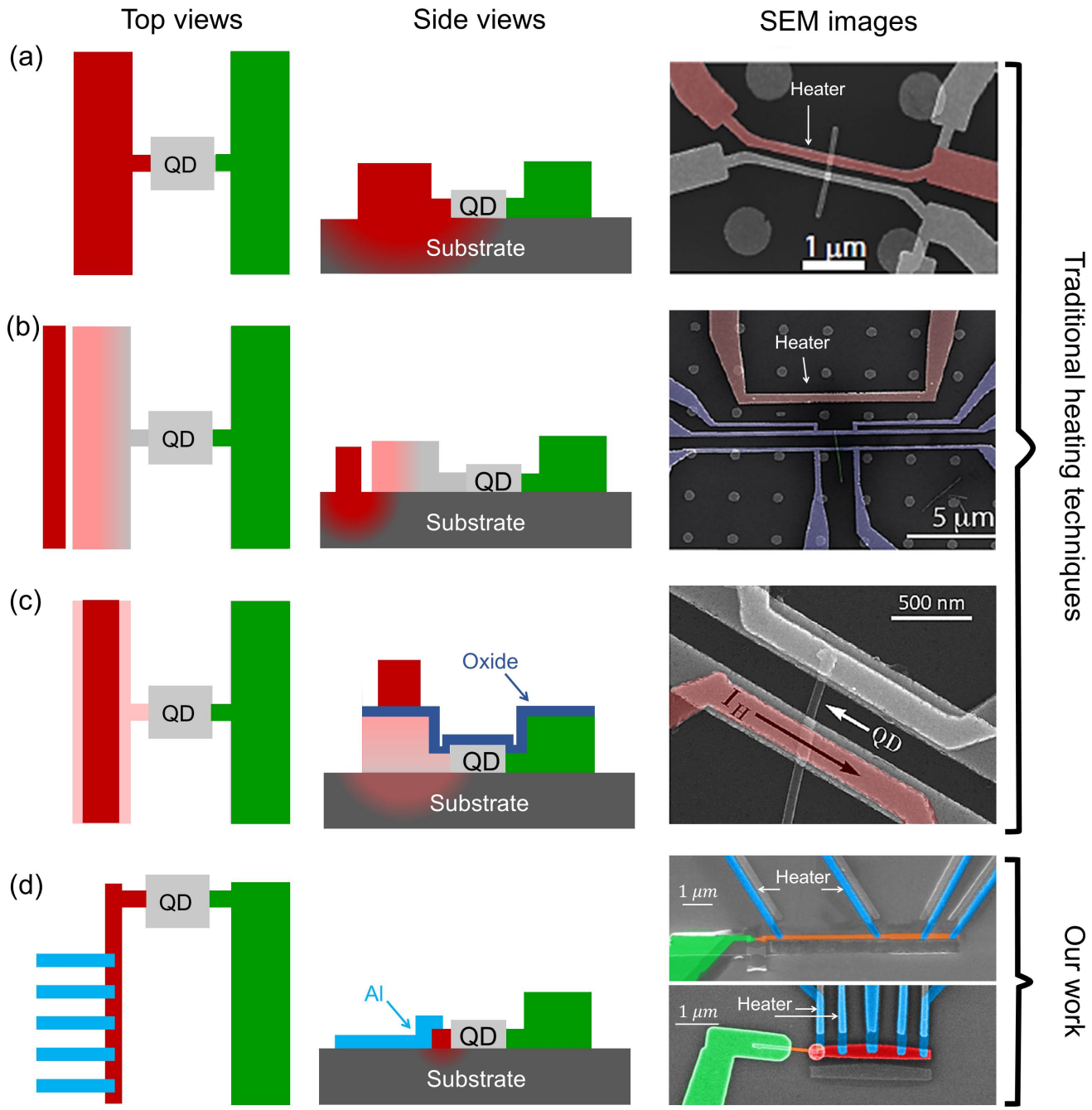

Fig. 3.11: The cartoon illustrates different QD thermal biasing approaches. (a) Contact heating (b) Side heating (c) Top heating. SEM images of a-c extracted from [162, 163, 3] (d) Superconducting hybrids' heater. The gray rectangle in the center represents a quantum dot between two contact leads. The contact lead that is indicated in red is warmer than the one indicated by green.

This section aims for comparing the techniques that are used in the later chapters of this thesis and giving some example of commonly used techniques for having a thermal bias in a quantum device.

3.4.0.1 Contact heating

One of the most widely-known heating techniques is contact heating which is schematized in Fig. 3.11a. In this method, one of the device's leads, e.g. the source electrode of a quantum dot, is heated as shown in red in Fig. 3.11a by applying a current directly through the source electrode. Therefore, this current can induce heating power in one side of the device. This approach was historically used to measure the thermopower of a quantum dot [66, 65, 110].

Providing local heating in the device is the first advantage of this technique, and the second one is that, as the heater and the contact to the device share the same electrode, no additional fabrication step is needed. However, there are two significant disadvantages, (i) Measuring a thermovoltage or thermocurrent is somewhat difficult [162, 163, 65, 110]. Significantly, there is a potential variation along the length of the heater electrode induced by the heater current. This potential should be carefully fine-tuned, otherwise it makes an unwanted overall biasing in the device which is difficult to compensate for from an experimental point of view. (ii) A big portion of applied heating power goes to the substrate which results in heating up the substrate together with heating the contact of the device. Therefore, it activates other heat leak channels and it is extremely tough to disentangle electronic heat flow from the rest of heat escape mechanisms.

Roddaro *et al,* have significantly improved the efficiency of this kind of heaters and they have been able to measure the thermopower of an InAs nanowire [160, 131, 161]. Nevertheless, it is still not the best technique for evaluating electronic heat conductance for our devices at sub-Kelvin temperatures.

3.4.0.2 Side heater

Another approach to obtain a temperature difference in the system is to introduce a dedicated side heater into the device so that a strip is placed in the vicinity of the source or drain electrode in the same fabrication step [163] as shown in Fig. 3.11b. The immediate advantage of this kind of arrangement is that the heating power can be tuned independently of the measurement setup as the heater strip is separated from the actual contact (the source or drain) of the device. Therefore, the thermovoltage can be measured using a simpler measurement circuit which has much less experimental uncertainties [166, 167, 168, 65, 110]. A considerable disadvantage of this method is that, the heat delivery from the strip to the actual contact should be done by thermal conduction via the substrate

as the heater is electrically disconnected from the device circuit. Hence, a fraction of the heating power is going to the actual contact of the device and the remaining heating power increases the surrounding temperature significantly i.e. the cryostat temperature. Therefore, this method brings lots of unwanted dissipation and is rather incompetent for measuring an electronic heat conductance of a device at low enough temperature.

3.4.0.3 Top heater

An alternative strategy is to utilize a top-heating technique developed by H. Linke's group at Lund University as depicted in Fig. 3.11c. They conducted extensive thermoelectric transport experiments that showed thermodynamic efficiency limits and thermovoltage measurement from weak-coupling to Kondo regime using a quantum dot above 1 K [3, 65, 162, 65, 110]. The top-heating technique somehow combines two previously mentioned methods. This time a heater strip is placed using a second fabrication run on top of the contact lead. Then, it is separated electrically by a thin layer of oxide following the first fabrication step. Similar to the side-heating technique, the advantage of this new design is that, there is a separate circuit for the top heater and therefore, one needs a simpler measurement setup. In addition, as the heater is much closer to the central part of the device i.e. the quantum dot compared to the side heating technique, it is easier to tune the heating power and minimize the substrate heating.

The biggest disadvantage of such method is that the heating of the contact is still via the oxide layer. Therefore, the heat can leak to the other side of the device as one needs to increase the heating power for having a desirable temperature difference. Moreover, two fabrication steps are needed to pattern this design.

3.4.0.4 Superconducting hybrids' heater

Figure. 3.11d highlights an approach that endeavors to combine the advantages of the previously described methods while minimizing by far the disadvantages of the other techniques. Making a temperature difference using superconducting hybrids approach provides an adequate heating power while the other part (the drain side) of the device remains at cryostat temperature. In this approach, the heater electrode is placed in direct contact (SNS) or tunnel contact (NIS) to the contact lead of the device (source electrode). Superconducting electrodes using shadow evaporation technique as explained in chapter 2 are utilized to form SNS or NIS junctions. For instance, in the case of clean contact heater,

a small heating power of $\dot{Q_H} = 100$ aW yields a gradient temperature of about $\Delta T = 3$ mK, which is significantly a more efficient way to create a temperature gradient compared to the preceding techniques at low temperature. Not only can an efficient heating be obtained but also on-chip cooling can be achieved using NIS junction (tunnel contact).

The main advantage of this approach is that supercondutors are thermal insulators, therefore, the source electrode of the device remains thermally decoupled from its environment below 300 mK. In addition, there is a negligible heat transfer between the source electrode and the substrate ($Si + SiO_2$) phonons as the volume of the source electrode (normal metal island) is chosen to be very small and narrow. Moreover, in terms of easy integration, the fabrication can be done in the same step with the same lithography mask as fabricating the device (for more details see chapter 2).

The noticeable disadvantage of this technique is that, the electronic heat conductance of nano devices can not be evaluated above ≈ 350 mK because the superconducting leads start to leak. Nevertheless, at this high temperature ($T_b > 350$ mK) heat conductance in the normal metal island is dominant by phonons and it is not the interest of this thesis.

The devices presented in chapter 4 and 5 utilize on-chip heaters. This allows us to heat up the electrons of source electrode locally with a constant heating power and measure the steady state response without having any significant heating effect on the other parts of the device, i.e. the drain electrode is thermalized at the cryostate temperature (T_b).

3.5 Performance of an SNS junction as a bolometer

In order to measure the heat flow through a QD junction, one needs to be able to access a very small change in electronic temperature. Moreover, one needs an operating temperature down to 100 mK or below, where the quantum dot heat flow dominates the other paths of heat relaxation such as electron-phonon coupling. These two necessities lead us to consider SNS proximity junction in chapter 4 and NIS hybrids in chapter 5 as heaters and thermometers that can fulfill both of these requirements. We have optimized the sensitivity of the SNS thermometer with several fabrication repetitions of the junctions parameters such as the length and thickness of the normal metal. In this way, we reduced the Thouless energy (E_{th}) of the SNS junction, which basically determines the lowest saturation temperature of the thermometer [137].

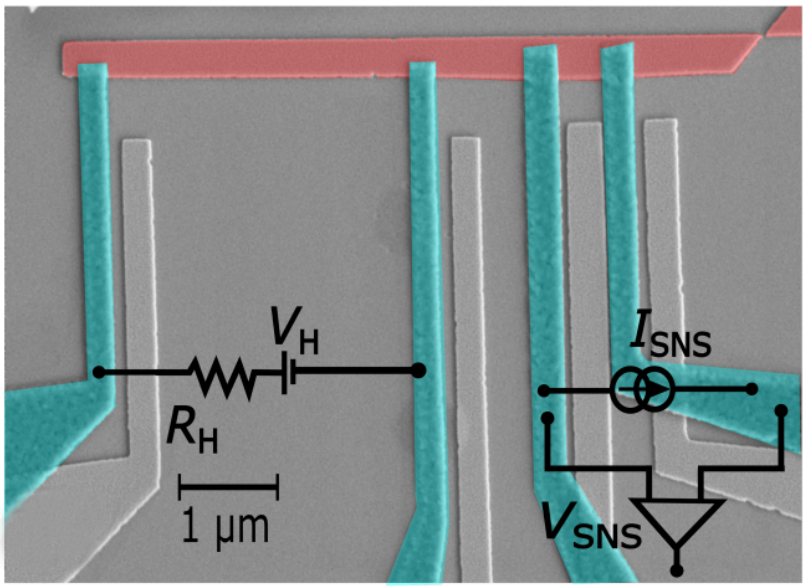

Fig. 3.12: (a) Colored scanning electron micrograph of one of our sample. The source side is separated from the drain by electromigration and there is no quantum dot placed on the junction. Therefore it can be considered as a small metallic island with a heater junction (two Al leads on the left) and a thermometer junction (two Al leads on the right).

Here we exemplify an experiment using SNS junctions, where we determine the sensitivity of our optimized SNS thermometer and test its operation as a bolometric detector. The SEM image of the device under test is shown in Fig. 3.12(a), where the normal metal Au is shown in red and the superconducting Al leads in light blue. The basic structure of the device is similar to that of the QD device described in chapter 4, with the only difference that there is no quantum dot placed in between the source and the drain after the electromigration. Therefore, the device can be essentially considered as a ~ 5 μm long and ~ 100 nm wide rectangular normal metallic island. Like the samples in chapter 4, we have here a very long SNS junction as the superconducting hybrids' heater to inject Joule heat into it and a short SNS junction to measure the electronic temperature.

We heat up the island by applying a constant but variable DC power through the heater junction, using a 1.3 V isolated DC power supply. The SNS thermometer is calibrated against the known bath temperature, by measuring the histograms of its stochastic switching current, as described in the previous sections. In this experiment, the bath temperature is at $T_b = 90$ mK and the heater junction is current-biased through a 200 MΩ biasing resistor which leads to a heating power of $\dot{Q}_H = 100$ aW. We continuously monitor the electronic temperature of the island by measuring a histogram of 500 switch-

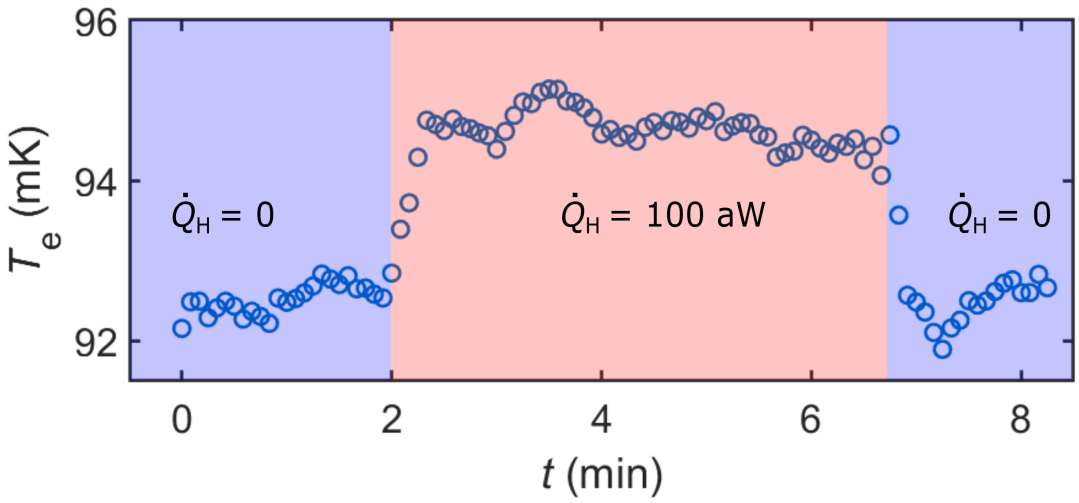

Fig. 3.13: A real-time measurement of the electronic temperature of the source island. Each point is a Gaussian maximum of the histogram of 500 measurements of stochastic switching current, taken in 1 sec. One can easily notice a change of the electron temperature by a few mK compared to the background temperature of 93 mK, whenever we turn on (off) the heater, set to an input heating power of 100 aW.

ing currents in about 1 second. The real time temperature trace of the island is shown in Fig. 3.13. One can easily identify the change of the electronic temperature by a few mK with respect to the background temperature of about 92 mK whenever the heater is turned on (off). Therefore the thermometer clearly detects an input heat as low as 100 aW, thus performing as a bolometric detector of a minute heating power. The noise equivalent power is about 100 aW/$\sqrt{\text{Hz}}$.

This observation of the island's electronic temperature can be determined by a heat-balance equation, as shown by a heat-balance model in the Fig. 3.2(a). The famous relation for describing energy flow rate from electrons to phonons in normal metal islands was developed by Wellstood et al [126]. They simplify the problem by considering a metal film with the thickness of t larger than the dominant thermal phonon wavelength $\lambda_{ph} = hv/k_BT$, where h is the Plank constant and v is the sound velocity of the dominant phonons. Under this assumption, the phonon distribution becomes three-dimensional (3D) in the metal. In addition, they only take into account longitudinal phonons which results in:

$$\dot{Q}_{e-ph} = \Sigma\Omega({T_e}^n - {T_b}^n) \tag{3.12}$$

where the constant $n = 5$, Ω is the metal volume and the e-ph coupling constant Σ is evaluated for a clean 3D metal as:

$$\Sigma = \frac{8\zeta(n)k^5{E_F}^2D(E_F)}{3\pi\hbar^4\rho v_F{v_l}^4} \tag{3.13}$$

where $\zeta(n)$ is the Riemann zeta function, k_B is Boltzmann constant and ϵ_F is the Fermi enrgy, $D(E_F)$ is the electronic density of state (DOS) per unit volume, ρ is the mass density and v_l is the longitudinal speed of sound. It is worth emphasizing once again that Eq. (3.13) was evaluated for a *clean* 3D metal, where as several studies have reported a deviation for the exponent from $n = 5$ to $n = 4 - 7$ [169, 170, 171, 172, 173, 174] in dirty-limit ($l/\lambda_{ph} \ll 1$), mainly due to the presence of different kinds of disorder in the system. Here l is electron mean free path and λ_{ph} is phonon wavelength.

Here we use $n = 5$ according to the reported $e - ph$ law for Au and Cu in the literature [33, 30] and the heat-balance is written as:

$$\dot{Q}_{\mathrm{H}} - \Sigma\mathcal{V}(T_{\mathrm{e}}^5 - T_{\mathrm{b}}^5) = 0, \tag{3.14}$$

where T_{e} and T_{b} are the electron and the bath (phonon) temperatures, respectively. Any parasitic heat source (sink) such as heat losses through the superconducting leads due to imperfect thermal insulation [175] or parasitic heating by the electromagnetic environment are taken into account within the injected heating power $\dot{Q}_{\mathrm{H}}$.

The electronic temperature of the island can be extracted by solving the above heat-balance equation (3.14). If we use an injected heating power $\dot{Q}_{\mathrm{H}} = 100$ aW, the material constant for Au $\Sigma = 2.4 \times 10^9$ $\mathrm{Wm^{-3}K^{-5}}$ [30], the volume of the island $\mathcal{V} = 2 \times 10^{-20}$ $\mathrm{m^3}$ and the bath temperature $T_{\mathrm{b}} = 90$ mK, we get an increase in the electronic temperature $\Delta T_{\mathrm{e}} \sim 3$ mK, which is consistent with the measured value. This justifies the analysis of the heat relaxation mechanism in the island as discussed above.

3.6 Conclusion

In the first part this chapter, we presented proximity Josephson junction (SNS junction) as a thermometer. In addition, a technique to measure electron temperature of a normal metal island [33, 47] was explained experimentally. In the second part, we introduced the hybrid tunnel junction (NIS) thermometery technique plus its theoretical background. Moreover, we compared the conventional heating technique for creating a temperature difference ΔT at sub-micrometer-sized devices with the superconducting hybrids' heater. Finally, we showed a bolometric detection of a minute power (100 aW) with our optimized SNS thermometery technique.

Chapter 4

The effect of co-tunneling on heat transport of a single quantum dot

In this chapter, we report on the operation of a single-quantum-dot heat valve, using a sensitive electron thermometer integrated inside the device. At charge degeneracy, the observed electronic cooling is the result of energy quantization in the dot, combined with strong tunnel coupling to the leads. When charge current flows through the device, Joule dissipation results in a temperature increase following the usual Coulomb diamonds' picture.

Contents

4.1 Heat transport in a metallic quantum dot junction

By using the electromigration technique and a custom-fabricated device, we form a single quantum dot (QD) junction and we report in this chapter on two investigated devices with an identical geometry but fabricated in two different runs. We demonstrate in device A the gate control of the electronic heat flow in a thermally-biased single-quantum-dot junction. A temperature map is measured and the effect of higher order tunneling in a single quantum level is shown and reveals clearly defined Coulomb diamond patterns. We also show that our result is in good agreement with NEGF theory. For device B, we perform a simultaneous measurement of charge and heat conductance and we deduce the heat conductance from the measured temperature map. In addition, a quantitative measurement evaluating the ratio of these two conductances is obtained.

4.1.1 Device preparation

The fabrication of the device is based on e-beam lithography, three-angle Au thin film evaporation and lift-off (see chapter 2 for further details). The electromigration junction is connected on the one side to a bulky *drain* electrode made of Cu, in fairly good contact to the thermal bath at a temperature T_b, and on the other side to a narrow *source* electrode, again made of Cu. Four Al leads provide contacts to the source through a transparent interface. At temperatures well below the superconducting critical temperature of Al, these leads are thermally insulating. The source is therefore fairly thermally decoupled from its environment. The closely spaced pair of Al leads to the source forms an SNS junction with a temperature-dependent critical current that will be used as an electronic thermometer. Conversely, the widely-spaced pair of Al leads forms instead a junction with a vanishing critical current, which allows it to be used as an ohmic heater. In contrast to prior work [22], we have chosen here transparent rather than tunnel contacts to the source, mainly because electromigration requires low access resistances, which is inherently incompatible with tunnel contacts which we will employ in the next chapter.

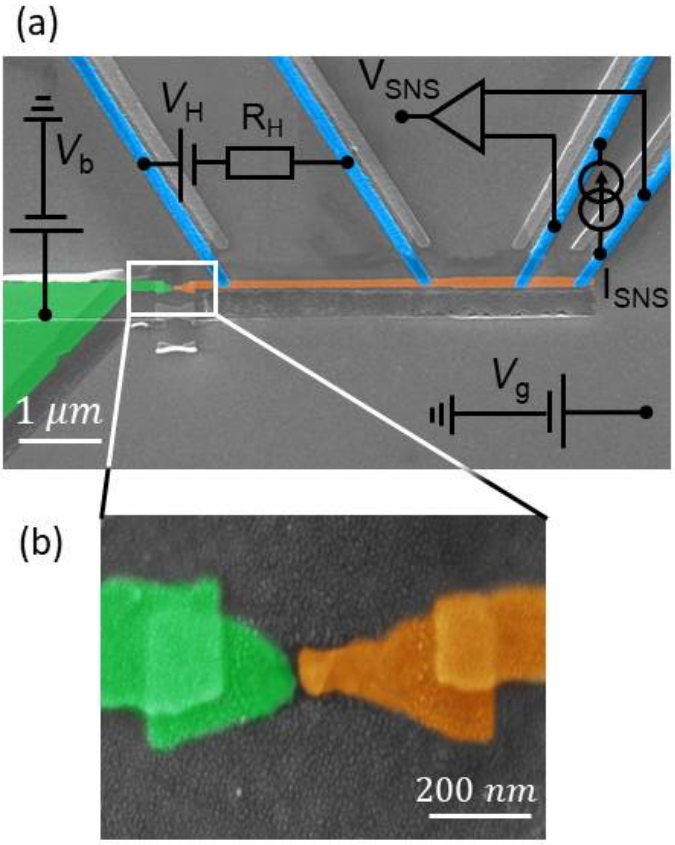

Fig. 4.1: a) False-colored SEM image of a typical device. The source is colored in red, the drain in green and the superconducting leads in blue. The circuit diagram shows the heat transport set-up. The longer (2.5 μm) SNS junction is used as a heater driven by a constant d.c. battery and the shorter (700 nm) SNS junction is used as a thermometer. (b) Zoomed-in view of the nano-gap between the *source* and *drain* created by electromigration and the nano-particles made by Au evaporation.

4.1.2 Charge transport

Figure 4.2 shows a differential conductance map of the QD junction as a function of bias (V_b) and gate voltages (V_g) for device A and B. It is important to emphasize that the conductances were measured with no additional heating in the source island. From the observed Coulomb diamonds, one can immediately access the charging energy E_C of the device which is about $\approx$ 4 and 6 meV for sample A and B, respectively. These values are estimated based on extrapolating the bias at the top of a diamond, which is actually twice the charging energy (more details in chapter 1). We did not measure these devices above bias voltages of about $\pm$ 3 mV, due to the rather large tunnel couplings, this voltage leads to currents of about 100 nA, beyond which there is a risk of burning the device. Therefore, a full spectroscopic characterization revealing several successive levels was not observed

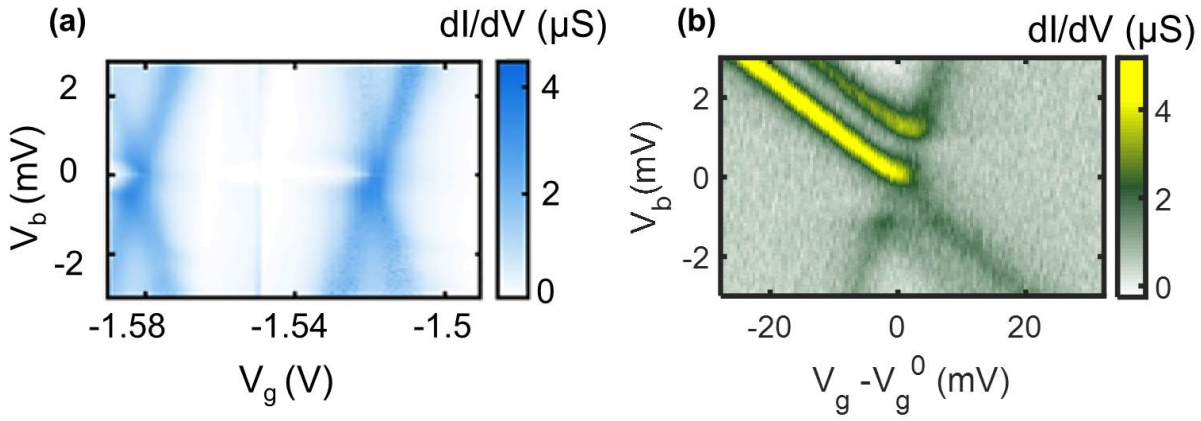

Fig. 4.2: a Differential conductance map of the device measured at 70 mK of device A in (a) and device B in (b) against the drain-source bias voltage V_b and the gate voltage V_g with no additional heating applied.

within this bias voltage range in device A, although we still can clearly see an excited state for device B in Fig. 4.2b.

The detailed shape of the Coulomb diamond pattern can also be used to determine the different capacitive couplings of the QD to its environment and a detailed discussion is given in the theory chapter of this thesis. In particular, the sum of the inverse of the diamond (positive and negative) slopes is equal to the ratio of the total capacitance to its leads over the capacitance to the gate α^{-1} [80]. The so-called coupling parameter or gate coupling α translates the effect of the gate voltage in terms of shift in chemical potential of the QD. Here $\alpha \approx 0.157$ for sample A and 0.11 for sample B were deduced (see Tab. 4.1).

One can notice that one edge of Coulomb diamond in both experiments is brighter than the others. It essentially tells us that the tunnel coupling of the quantum dot is strongly asymmetric. Hence, the coupling can directly be obtained from the full width at half maximum (FWHM) of the conductance peak of the brighter Coulomb edge. It is noted that, by this method we can extract the effective tunneling rate as it is assumed that the weak couple lead is the bottle-neck of the transport and the total coupling is determined by the stronger one.

We found a tunnel coupling $\hbar\Gamma$ value in the range 0.09 - 1.4 meV, depending on the considered degeneracy point or quantum dots, for a single energy level involved in low-bias electron transport. In a weakly coupled QD device, high-conductance lines running parallel to the Coulomb diamond edges are expected, in correspondence to single electron levels. presumably this washed out due to the large tunnel coupling $\hbar\Gamma \gg k_B T$. Nevertheless,

Device	α	Γ (mV)	E_C (meV)
A	0.157	0.2-1.4	4
B	0.11	0.09-0.3	6

Tab. 4.1: Extracted gate coupling, tunnel couplings and the charging energy from conductance maps for device A and B.

the coupling is not strong enough to induce Kondo effect. Here these features are absent for device A whereas in device B, one can easily resolve level excitation at least in one of diamond edges. The conductance map for device B displays a large coupling asymmetry that is also evidenced by the conductance asymmetry displayed by the on-state line in Coulomb diamond edge in Fig. 4.2b. All the values are listed in Tab. 4.1.

The formation of a nano-gap by electromigration depends sensitively on the structural details (precise width and thickness) of the constriction, therefore, the size of the gap (between the leads and dot) and its structural details vary from one electromigration to another one. As a result, the strength of tunnel coupling also varies. In both cases, Pt was used as the electromigration material, as it suppresses the superconducting proximity effect extremely efficiently, much more than Au. The charging energy of the dot depends on the actual size of the Au nano-island and the total effective capacitance with its environment, that is determined by both the precise nature of the evaporated Au droplets and the detailed structure of the nano-gap created by electromigration. Therefore, it is expected to have a different charging energy for two similar samples. Such metallic quantum dots were investigated in the 90s. In Ref. [176], an energy level separation of 0.7 meV and a charging energy of 6 meV were deduced from the measured energy spectra in 10 nm Al nanoparticles. The nanoparticles used in our work can be seen from SEM images to be about 5 nm in size and we expect an energy level separation of the order of a few meV. In the previous work [95] from our group, the weak coupling to leads enabled us to observe sharp resonances in the differential conductance map corresponding to an energy level separation of about 5 meV.

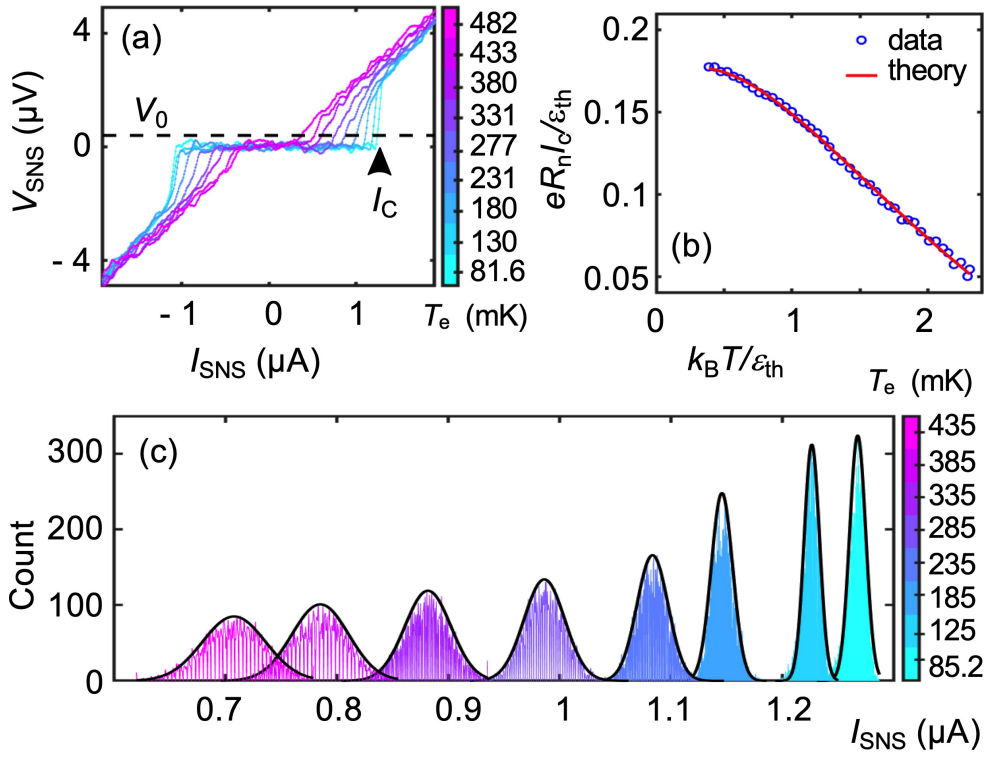

Fig. 4.3: (a) d.c. IV characteristics of the SNS thermometer junction at different bath temperature T_b, the current bias value at which the voltage exceeds a threshold $V_0 \simeq 1\,\mu$V defining the switching current. (b) The critical current I_c as a function of the bath temperature, the axes being normalized. It is defined as the most probable switching current extracted from the histograms. The calibration curve (red solid line) is a fit with the theory [137]. (c) Histogram of the stochastic switching current of the SNS junction at different bath temperatures, with a fitted gaussian envelope for each. (Adapted from Dutta, Majidi et al. [47])

4.1.3 SNS characterization

We employed superconductor-normal metal- superconductor hybrid (SNS) junction as a local electronic thermometer. The principle of such a junction has already been discussed in the thermometery chapter in more detail. In the following, thermometer characteristics of device A will be presented and for device B, the same information can be found in chapter 3.

The critical current I_c of an SNS junction is highly sensitive to the electronic temperature T_e in normal metal (N). The relevant energy scale is the Thouless energy $E_{Th} = \hbar D/L^2$, where D is the diffusion constant in N and L is the junction length [137]. For $T_e > E_{th}/k_B$, I_c decreases rapidly with increasing temperature, allowing it to be used as a secondary electron thermometer [32, 33]. In a single IV characteristic, the switching current is defined as the value of the current at which the voltage is larger than a threshold

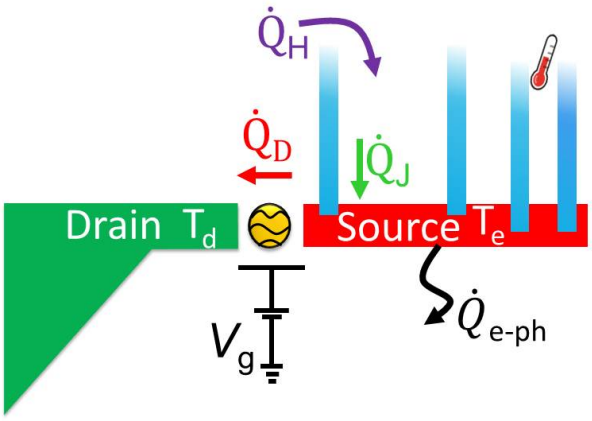

Fig. 4.4: (c) Schematic of the device, with the different heat flows to/from the source.

voltage chosen slightly above the measurement noise level. Figure 4.3(a) shows a series of such characteristics at different bath temperatures. Switching current histograms, together with a gaussian fit of their envelope, are shown in Fig. 4.3(c) for a series of bath temperature values. The histogram width increases with the temperature, consistently with a thermal energy fluctuating by $2k_BT$. In Fig. 4.3(b), the variation of the critical current with the bath temperature fits nicely the theoretical expectation [137], the latter being used as the thermometer calibration. The low Thouless energy $E_{th} \sim 5$ μeV was chosen in order to avoid a saturation of I_c. The thermometer thus remains sensitive at low temperature, where thermal transport through the QD gains importance compared to other heat relaxation processes.

4.1.4 Thermal balance and electron-phonon coupling

To investigate the power flow in the present device, our strategy is to study the thermal balance while modulating the conductance of the device. The normal metal island in our device was Joule-heated ($\dot{Q}_H$) by a floating homemade current source through the long pair of SNS junction, as depicted in Fig. 4.1. The electron temperature of the island was measured by the shorter SNS junction on the rightmost side of the island. The measurement circuit is completely depicted in Fig. 4.1. However, the applicability of the measurement scheme is based on the following facts:

(i) Heat leaks through the SN junctions are much smaller than the heat flow from electrons to phonons in the normal metal. Clean SN junctions provide an excellent electrical, but poor thermal conductivity at low enough temperature, i.e. it is known that superconductors make a perfect thermal insulator. In addition, the resistance of an SN

junction was found to be much lower than that of the normal metal island used in the measurements.

(ii) The density of states around the Fermi level in the normal electrode is suppressed by the proximity effect of the superconductor electrodes resulting in a decreased electron–phonon coupling. The relative energy scale here is the Thouless energy E_{Th}, i.e. $E_{Th}/k_B \approx 60$ mK below which the phonon thermal conductance is decreased and other relaxation mechanisms such as photonic ones become a dominant relaxation channel.

(iii) The electron-electron (e-e) scattering length is much smaller than the length of a normal metal wire. Hence, we have a fast electron–electron internal relaxation and electrons in the wire have a well-defined Fermi distribution [177, 178]. Therefore, the electron–phonon relaxation time is much slower compared to the electron–electron one and this lets us assume that the electronic system is always at internal thermal equilibrium [130].

(iv) Energy transfer thanks to photon emission [179] is a possible channel, but it is also insignificant on the one hand due to the "large" volume of the normal metal island and on the other hand because the photon wavelength varies with 1/T, where T is the working temperature. Therefore, one needs a much lower temperature to observe heat conductivity contribution through photons [180].

Based on the arguments (i)-(iv), it is nice and informative to check the thermometer and heater before starting the thermal transport through the quantum dot. A first experiment can be reading the electronic temperature and varying $\dot{Q}_H$ while the quantum dot is not at resonance, and analyze its value with a simple thermal model. This measurement brings us some important information about all the relevant escape heat mechanisms i.e. electron-phonon $(e-ph)$ constant in the source island of the device. To this end, we assume that there is no heat flow through the QD i.e., $\dot{Q}_{QD} = 0$ deep inside the Coulomb blockaded region and at $V_b = 0$. Therefore, the injected heat $\dot{Q}_H$ from the heater makes a balance via $e-ph$ coupling $\dot{Q}_{e-ph} = \Sigma V({T_e}^5 - {T_b}^5)$, which is considered as the main heat escape mechanism from the source island of the device. Consequently, the equilibrium thermal equation deep inside the diamond and zero bias voltage is given by,

$$\dot{Q}_H - \dot{Q}_{e-ph} = 0. \tag{4.1}$$

We can obtain the $e-ph$ constant (Σ) by solving the Eq. (4.1) using the measured steady state temperature in each device. For device B, the temperature was measured by

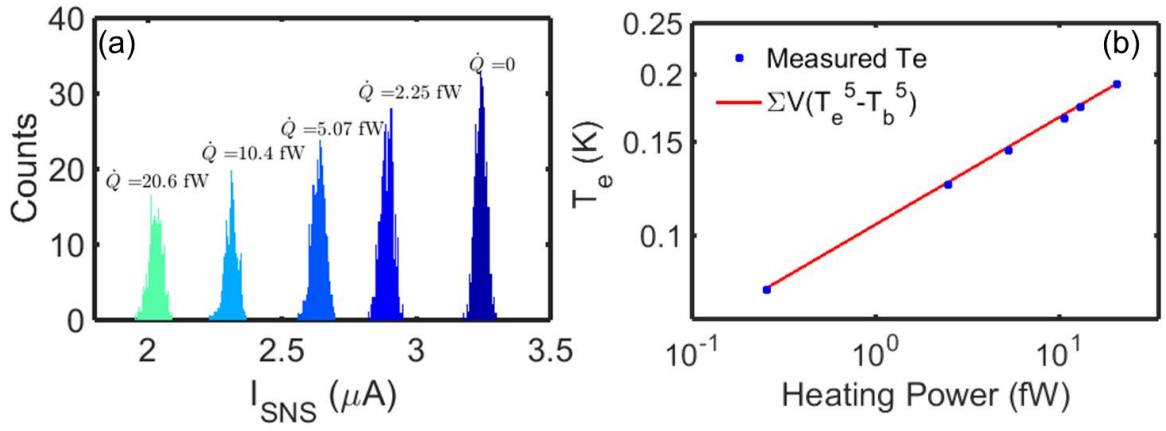

Fig. 4.5: Left: Histogram of critical current of SNS junction for different constant heating powers applied to the source island. Right: measured source electron temperature T_e in off QD resonance state for device B at $T_b = 80$ mK as a function of heating power $\dot{Q}_H$ applied to the source. The red curve is a fit to T^5 power law.

the statistical measurement of critical current as it was explained chapter 3 and eventually, the calibration curve for device B was used to convert the I_c of the SNS junction to temperature for different heating powers as it is shown in Fig. 4.5. This measurement first gives us data and allows us to fit the $T_e(\dot{Q}_H)$ with a T^5 law over a wide range of input powers and hence get access to more accurate parameters. We get $(\Sigma\mathcal{V})$ and we can estimate $\mathcal{V}$ from the geometry of the device i.e. $\Sigma = 2.6 \times 10^9\ Wm^{-3}K^{-5}$ and $\mathcal{V} = 2.8 \times 10^{-20}\ m^3$. Whereas for Device A, we only have one single power data point which heats up the island from $T_b = 80\ mK$ to $T_e = 164\ mK$. We deduced the $e-ph$ coupling parameter $\Sigma = 2.4 \times 10^9\ Wm^{-3}K^{-5}$, close to the expected value for Au [30] for the estimated volume of the source island $\mathcal{V} = 2.8 \times 10^{-20}\ m^3$. However, we should mention that the Σ value for device B is not far from the one in device A and it is consistent with the literature [30].

4.2 A single-quantum-dot heat valve

In this experiment we investigate device A and show that a quantum dot can act as a heat valve. The source is heated by applying a constant heating power $\dot{Q}_H = 6$ fW to the heater junction. The drain is biased at a potential V_b, the source side being grounded via one of the SNS thermometer contacts. Figure 4.6(a) shows a map of the source electronic temperature as a function of V_b and V_g. Its resemblance to the charge conductance map of Fig. 5.8(d) is striking. The source temperature T_e increases rapidly with increasing charge

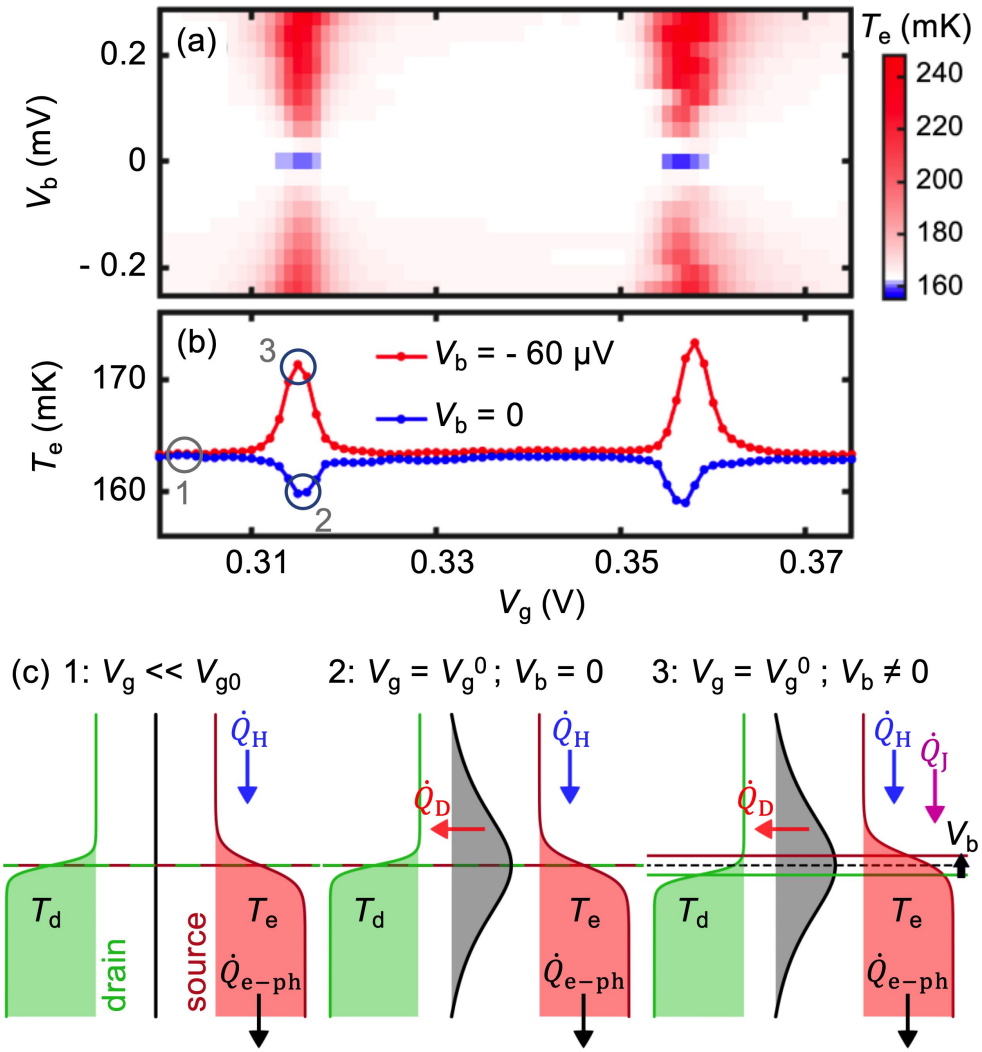

Fig. 4.6: (a) Experimental map of the source electronic temperature in the $V_b - V_g$ plane. (Adapted from Dutta, Majidi et al. [47]) (b) Individual gate traces of the source temperature at two different bias values. (c) Schematic energy diagram of the heat flows in/out the source in various conditions as indicated by labels in (b): (1) away from charge degeneracy and at zero bias (left), (2) at a charge degeneracy point $V_g = V_g^0$ but still at zero bias (middle) or (3) at non-zero bias (right). The gray profile depicts the quantum level spectral density. The ratio between the level broadening $\hbar\Gamma$, the bias V_b and the thermal energy $k_B T$ is in correspondence with panel (b) conditions. The arrows indicate the applied heating power $\dot{Q}_H$, the Joule power $\dot{Q}_J$, the electron-phonon coupling power $\dot{Q}_{e-ph}$ and the power flow through the QD $\dot{Q}_D$.

current due to the related Joule power. Right at the charge degeneracy point, the source temperature is lower than in the rest of the map. The higher resolution temperature map of Fig. 4.7(a) shows a clear cooling region of ellipsoidal shape, with slightly canted axes.

Figure 4.6(c) shows energy diagrams for three different cases indicated by circles in the temperature $T_e(V_g)$ profiles at two different bias value of Fig. 4.6(b). At zero bias and far away from charge degeneracy (case 1), there is neither Joule power nor heat flow through

the QD. The source is overheated up to $T_e = 163.5$ mK due to the balance between the applied power $\dot{Q}_H$ and the main thermal leakage channel, namely the electron-phonon coupling $\dot{Q}_{\mathrm{e-ph}}$. Still at zero bias, but near a charge degeneracy point (case 2), there is a heat flow $\dot{Q}_{\mathrm{D}}$ through the QD, but still no DC electrical current. This shows up (blue curve in Fig. 4.6(b)) as a temperature T_e drop by several mK at the charge degeneracy point. The gate-controlled QD junction thus acts as a heat valve. At higher bias (case 3), this cooling contribution is overcome by the Joule heat $\dot{Q}_{\mathrm{J}}$. A temperature maximum is thus observed at values of the gate potential close to the charge degeneracy point (red curve in Fig. 4.6(b)).

4.2.1 Comparison with NEGF simulations

The mere observation of cooling at the charge degeneracy point is in clear contradiction with the theoretical prediction in the weak coupling, sequential tunneling regime. It is noteworthy to say that the word 'cooling' is referred to heat conductance not refrigeration. Indeed the present experiment deals with a strong tunnel coupling between the QD and the leads, with a ratio $\hbar\Gamma/k_{\mathrm{B}}T_{\mathrm{e}} \approx 20$, rendering the weak coupling picture inapplicable.

We now go beyond the sequential tunneling approximation. In the vicinity of a charge degeneracy point, we can model our device as a non-interacting single energy level. As soon as we move away from the charge degeneracy point, the model would not be applicable anymore. We are interested in exploring the properties of the leads at stationarity and in particular their electronic temperature; in the NEGFs framework this is possible via the so-called inbedding technique [181, 182]. It is worth to mentioning that it is not based on a full heat balance model accounting for the heat flow via phonons and the superconducting leads. We instead assume that the electron-phonon coupling strength itself does not change appreciably within the temperature range of the map, which is equivalent to assuming that the main particle and energy redistribution processes in the lead are dominated by electron-electron interactions. By including in the theory the measured temperature (163.5 mK) of the source when decoupled from the QD, we effectively take into account its thermal coupling to the bath.

The theoretical temperature map around a charge degeneracy point is shown in Fig. 4.7(b) and reveals a nice agreement with the experimental data in Fig. 4.7(a). Here, the temperature of the drain T_{d} is set to 85 mK and the coupling of the QD to the drain is asymmetric with a coupling ratio $\Gamma_{\mathrm{L}}/\Gamma_{\mathrm{R}} = 3/17$ between left and right leads and $\Gamma = 0.25\mu V$. These

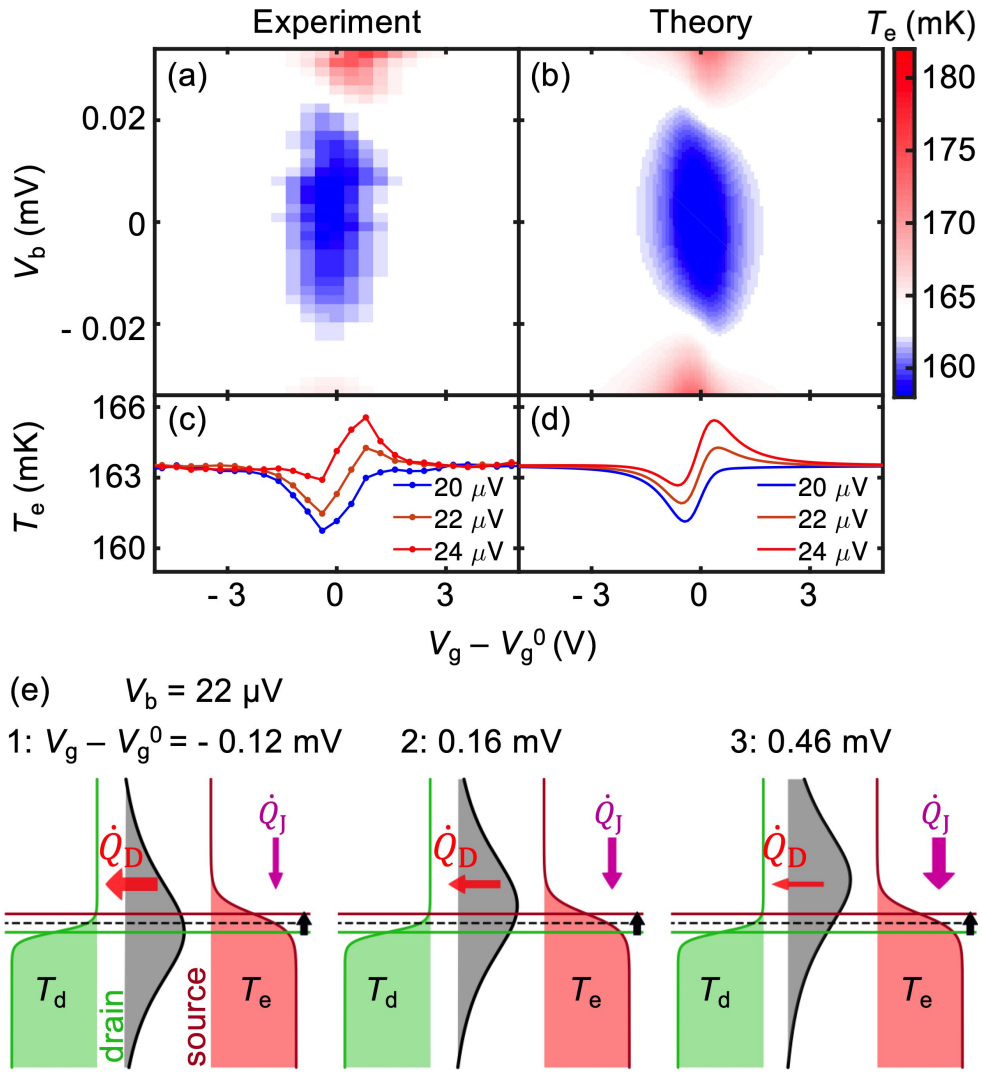

Fig. 4.7: (a) A highly-resolved map of the source electronic temperature at the same experimental condition as in Fig. 4.6 and around a charge degeneracy point defined by $V_g = V_g^0$. (Adapted from Dutta, Majidi et al. [47]) (b) Calculated temperature map obtained with the inbedding technique with $\Gamma = 0.25\mu V$, $\Gamma_L/\Gamma_R = 3/17$ and $T_d = 85$ mK. (c) Experimental and (d) theoretical variation of the temperature in the region where crossing from cooling to heating is observed; each curve refers to a given applied bias V_b: (blue) $20\mu V$, (orange) $22\mu V$, (red) 24 μv. (e) Schematics describing the crossover between the heat flow $\dot{Q}_D$ and the Joule heat $\dot{Q}_J$ as a function of the gate at a fixed bias, resulting in temperature decrease at $V_g - V_g^0 =$ - 0.12 mV (case 1, left) or increase at 0.46 mV (3, right). At 0.16 mV (2, middle), the two flows are equilibrated. The electron-phonon heat $\dot{Q}_{e-ph}$ as well as the injected heat $\dot{Q}_H$ are omitted for clarity. The widths of the arrows indicate their relative strengths.

best fit values allow us to reproduce semi-quantitatively the temperature profiles of the crossing region, see Fig. 4.7(c,d). The width in gate potential of the cooling region is independent of the bath temperature and increases with the coupling Γ. Conversely its extension in bias depends weakly on Γ and increases with the temperature difference across the junction.

The present case actually has some similarities with the regime of a metallic Single Electron Transistor where cooling at the charge degeneracy point was also found [77, 22]. Nevertheless, an asymmetry in gate voltage is clearly observed in the experimental and theoretical temperature map. For a bias voltage V_b around 22 μV, the source temperature can be tuned either below or above the reference temperature of 163.5 mK by acting on the gate voltage, see Fig. 4.7(c). This behavior is not to be expected in the case of a metallic island where electron-hole symmetry in the density of states makes transport properties symmetric across the charge degeneracy point. Therefore it is an unambiguous signature of the QD discrete energy spectrum. At a given bias, the value of the gate potential determines the position of the broadened energy level in the QD (see the grey profile in Fig. 4.7(e)) and thus the mean energy of the tunneling electrons. This in turn affects the heat balance in the source and modifies the boundary of the cooling region in the temperature map. The extension in bias of this crossover zone, where one can switch from cooling to heating by adjusting with the gate, depends on both the coupling Γ and the temperature difference across the QD.

For the set of parameters considered above, the calculated particle and heat currents for the source are shown in Fig. 4.8a,b. It is interesting to notice the resemblance between the heat current map and the temperature map shown In Fig. 4.7. It confirms that in the regime we explored the temperature changes in the source lead correspond indeed to a heat current to/from the source (panel (a) in Fig. 4.8). At large bias the source heats up; the system behaves as a heater, namely the energy of the bias is transformed into internal energy. At low bias we observe instead heat flow from the hot to the cold lead; the system behaves as a valve, meaning that it enables the natural flow of heat from the hot to the cold lead. It is also interesting to observe that there is a whole region in which heat and particle currents have opposite signs.

It is worth mentioning that this effect is not due to the onset of a thermovoltage which would make particles flow against the applied bias voltage without necessarily causing an inversion of heat current. The thermovoltage, although present, is very small compared to the extension in bias voltage. This is shown in Fig. 4.8 panel (c) where we plot the thermovoltage $V_{th}(V_g)$, together with the corresponding thermopower, defined as the bias voltage at which the particle current vanishes.

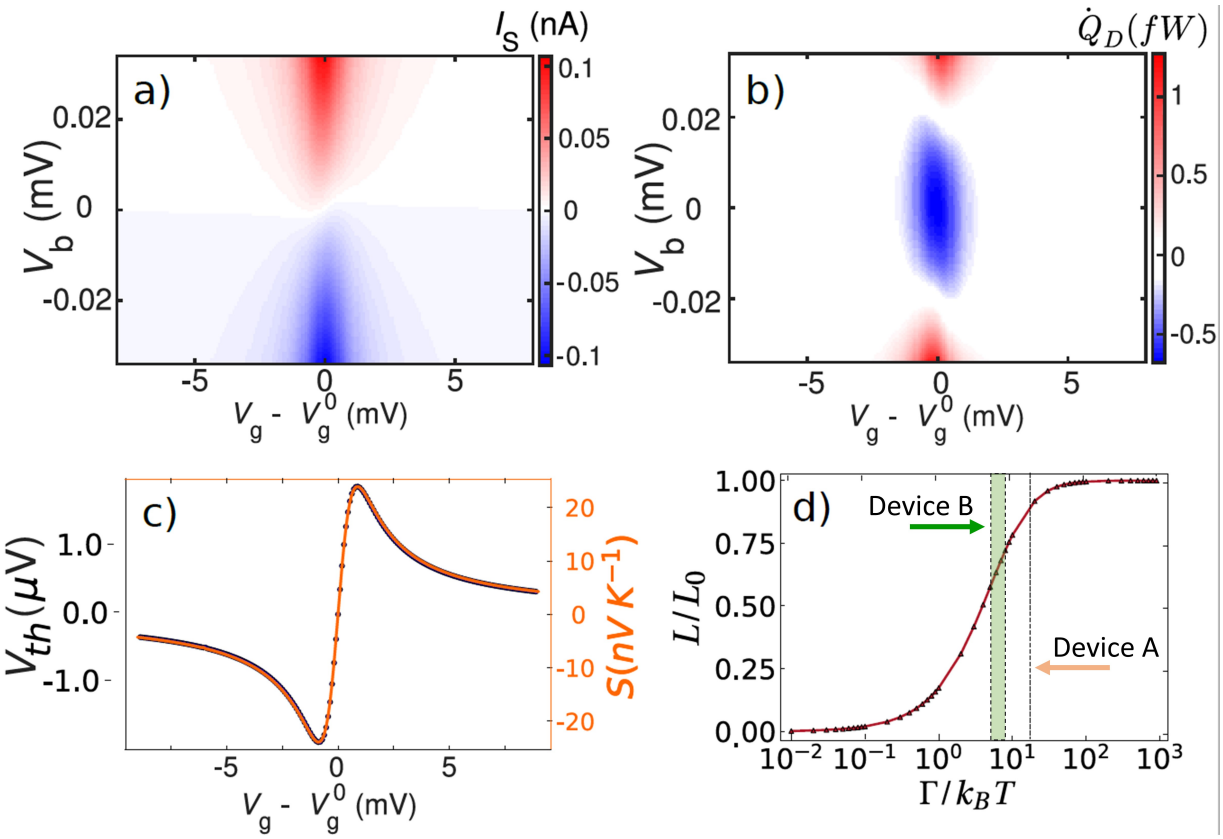

Fig. 4.8: Maps of the a) particle and b) heat current for the source lead. (Adapted from Dutta, Majidi et al. [47]) c) Thermovoltage V_{th} and corresponding thermopower $S = V_{th}/(\Delta T)$ as a function of the gate voltage V_g. The parameters for device A: coupling is $\Gamma = 0.25$ meV, and temperature of the drain at closed bias is $T_d = 85$ mK. (d) Lorentz ratio L/L_0 as a function of Γ/k_BT for a single level quantum dot. The right dashed lines shows the ratio for the device A $\Gamma/k_BT \approx 20$ and the left shaded area shows the possible range of coupling for device B. In both cases the dot is at the degeneracy point $V_g = V_g^0$.

4.2.2 Co-tunneling effect on thermal transport

The observed significant thermal conductance constitute a signature of the strong coupling of the QD to the leads. We computed the Lorentz ratio $L = \kappa/(T\sigma)$ where $\kappa = \partial\dot{Q}_s/\partial\Delta T|_{I_s=0}$ and $\sigma = \partial I_s/\partial V_b|_{\Delta T=0}$ are the thermal and electrical conductivities respectively. In panel (d) of Fig. 4.8 we plot the Lorentz number L/L_0 with $L_0 = (\pi^2/3)(k_B/e)^2$ at the degeneracy point $V_g = 0$. The dashed line corresponds to the ratio $\Gamma/k_BT \approx 20$ considered in the sample A. It is clear that the deviation from the WF law is small because of the strong coupling to the leads.

Figure 4.9 shows the map of the calculated electronic temperature for couplings (panels (a) and (c)) $\Gamma/k_BT \approx 5$ and (panels (b) and (d)) $\Gamma/k_BT \approx 50$ and for the same drain temperature at closed gate voltage $T_d = 85$ mK similarly to Fig. 4.6. A change in the

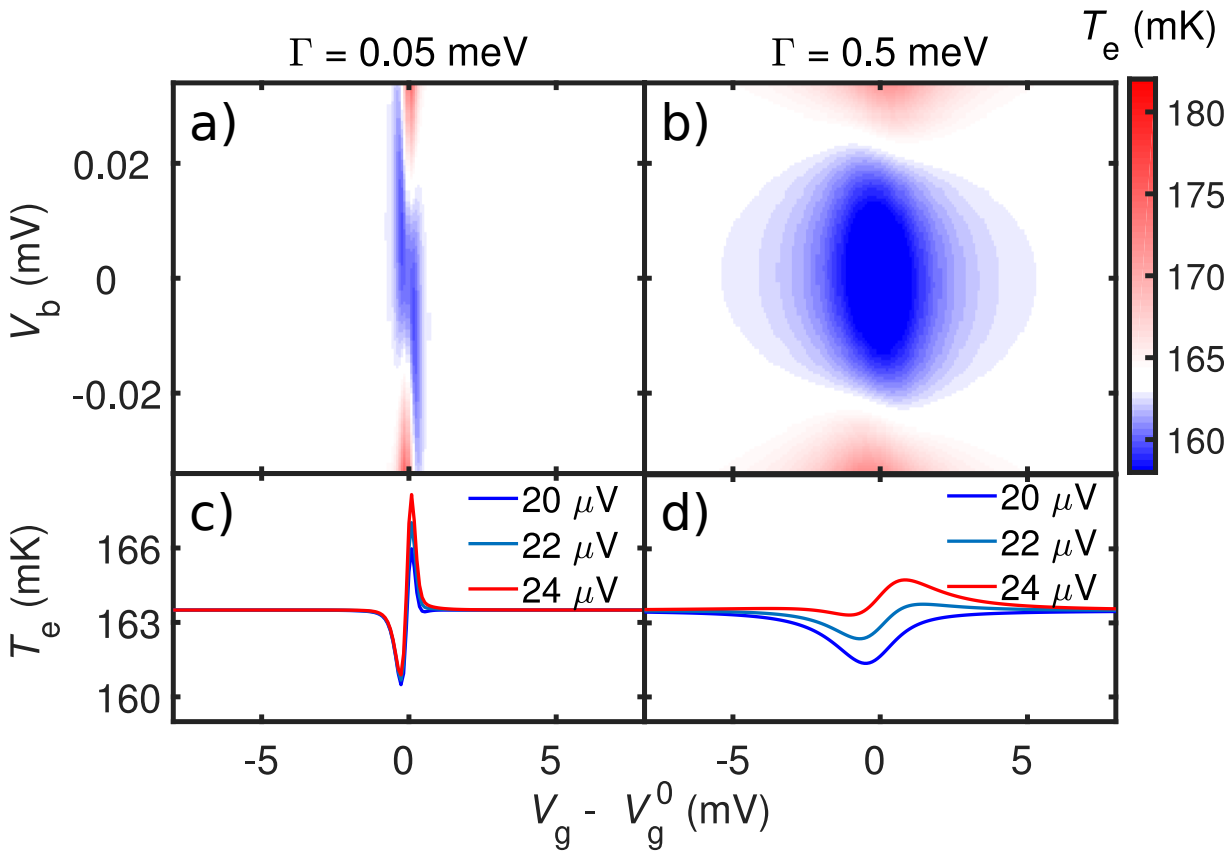

Fig. 4.9: Zoomed temperature map: Calculated temperature map of the source lead obtained with the inbedding technique with (a) $\Gamma = 0.05$ meV and (b) $\Gamma = 0.5$ meV. (Adapted from Dutta, Majidi et al. [47]) (c) and (d) variation of the temperature in the region where crossing from cooling to heating is observed; each curve refers to a given applied bias V_b: (blue) 20μV, (cyan) 22μV, (red) 24μV.

coupling changes the extension of the cooling region in the gate voltage but it does not affect dramatically the extension of the cooling region in the bias voltage nor the position of the transition from cooling to heating.

To give a more quantitative analysis we computed the extension of the cooling region in the bias voltage A_b at $V_b = 0$ and its width A_g in gate voltage for different couplings and temperatures of the drain at closed gate. The results are plotted in Fig. 4.10 in panels (a) and (b) where it can be appreciated that the coupling constant does not change significantly the extension in bias which instead strongly depends upon the difference in the equilibrium temperatures between the drain and source. Indeed as the temperature of the drain increases towards the temperature of the source the extension in V_b shrinks. Nevertheless the extension in the gate voltage is only determined by the coupling and does not present any significant dependence upon the closed gate temperature of the drain.

The transition region, namely the region where at fixed bias it is possible to obtain both heating and cooling by changing the gate potential, has a strong dependence on both

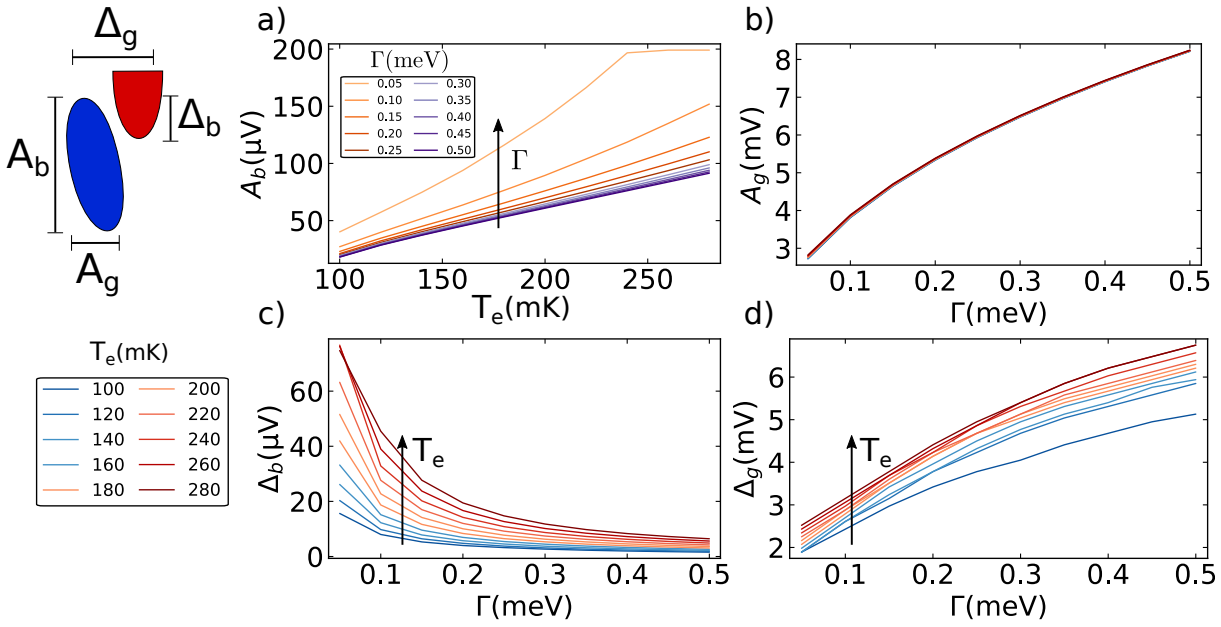

Fig. 4.10: Cooling region characterization: (a) and (b) show the width in gate potential and the extension in bias voltage of the cooling region as a function of the coupling Γ for different values of the temperature of the source lead at closed gate. (Adapted from Dutta, Majidi et al. [47]) (c) and (d) show the width in gate potential and the extension in bias voltage of the region in which cooling and heating can be observed at fixed bias by tuning the gate voltage as a function of the coupling Γ for different values of the temperature of the source at closed gate.

the coupling and the temperature difference at closed gate. This is shown in Fig. 4.10 panels (c) and (d) where we plot the width Δ_g and extension Δ_b of the transition region; they have been determined by finding the curve $V_b(V_g)$ such that T_e =163.5 mK and then taking $\Delta_b = \max(V_b(V_g)) - \min(V_b(V_g))$ whereas Δ_g is the difference between the voltage gates at which V_b is larger than its values at closed gate plus $0.1\Delta_b$ on both sides. It can be observed that this region becomes smaller as the coupling is increased whereas its width increases with the coupling. The width also decreases steadily as the temperature of the drain increases whereas the behavior of its width with temperature is less trivial. It decreases at large couplings whereas it increases as the temperature increases at small couplings.

4.3 Heat conductance of an electromigrated single QD junction

Probing simultaneously the charge and heat conductances in a quantum dot under temperature gradients has been a great experimental challenge. The main central thermoelectric quantity which has not been quantitatively measured so far in a QD is the electronic thermal conductance [5, 3]. This relates respectively to the heat current and the voltage resulting from a thermal imbalance in reservoirs tunnel-coupled through a nano-object under the condition of zero net electrical current. This quantity has been investigated at the nanoscale in metallic tunnel contacts [22, 27] and and in single molecules probed by an STM tip [17, 61]. Gate-tunable thermoelectric experiments, allowing to assess and control the electronic structure of individual quantum dots, have been conducted so far using semiconducting structures [5, 3] essentially without experimentally evaluating the electronic heat conductance. Conversely, only very few studies in a molecular or nanoparticle transistor geometry have been performed [12, 183].

In this part, we will study a complete thermal balance measurement together with a charge transport through a single metallic quantum dot junction (in device B). We measure temperature maps for different constant heating powers. In addition, we experimentally measure the heat conductance of an electromigrated single QD junction and show a violation of a Wiedemann-Franz law in such a transistor at the charge degeneracy point.

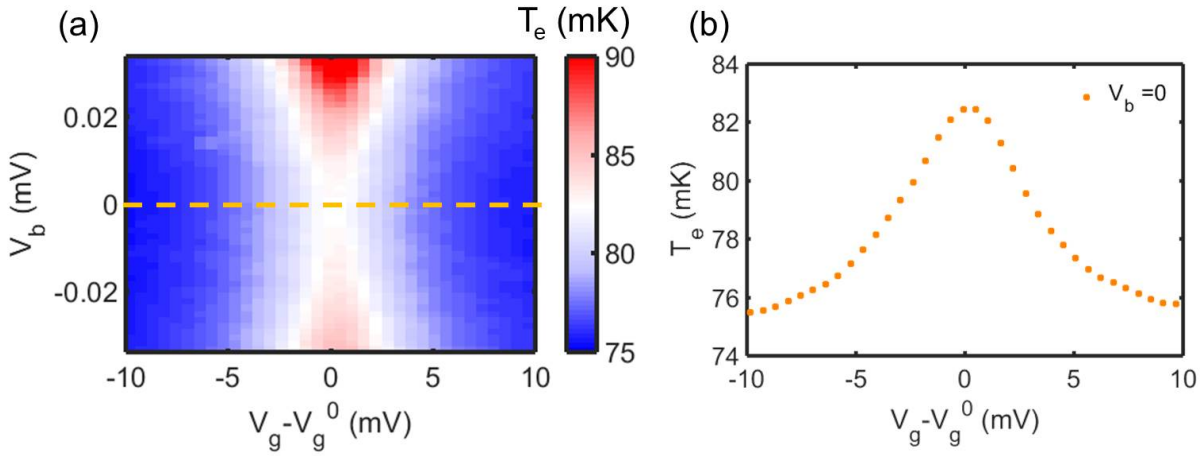

Fig. 4.11: (a) Experimental map of the source electronic temperature in the $V_b - V_g$ plane at $V_g{}^0$= - 0.76 V without applying heating power to the source island. (b) Individual gate trace of the source temperature at zero bias voltage.

4.3.1 Temperature map at an equilibrium

Let us remind that the charge transport properties of device B are determined by measuring the junction conductance G as a function of the bias voltage V_b and a gate voltage V_g, applied from a local back gate is shown at the beginning of this chapter in Fig. 4.2b. In addition, the tunnel coupling $\Gamma \approx 0.09$ mV of the device is determined from the width of the Coulomb diamond edge. As opposed to most experiments based on semiconducting systems, neither the quantum dot nor the tunnel barriers are electrostatically defined here. Thus, Γ is essentially independent of the gate voltage.

Figure 4.11 shows the measured temperature map in the absence of any applied heating power. As we explained in the thermal balance section, at zero-bias voltage and off-resonance, the electron temperature measured is equal to the phonon temperature, which we ascribe to the lowest measured cryostat temperature $T_b = 75$ mK in this experiment. Unexpectedly, we observe that $T_e(V_g)$ shows an increase whenever the gate voltage is on the charge degeneracy point in the absence of thermal gradient or a DC electrical current. This corresponds to an increase in the bath temperature of about 8 mK compared to its equilibrium temperature visible in the right hand-side of Fig. 4.11.

We thus propose that this increase in temperature is due to the effect of the bias noise from the electromagnetic environment. This appears as an effective oscillating bias, leading to an AC current noise when the level of the device is aligned with the source and the drain chemical potentials. This can result in a rise in the temperature by Joule dissipation in the source island. In our previous experiments we also observed that a very small bias noise in the order of few μV can induce a Joule dissipation of few Femto Watt which is roughly consistent with the temperature rise which was observed in our experiment with sample B.

4.3.1.1 Correcting for spurious heating at charge degeneracy point

In order to quantify this bias noise of amplitude ${V_b}^{noise}(t) = {V_0}^{noise}\sin(\omega t)$, a full heat balance equation is formulated assuming all the possible in-coming and out-going heat flows for an arbitrary gate voltage along the zero bias-line as the following:

$$\dot{Q}_H + \dot{Q}_{noise} - \dot{Q}_{e-ph} - \dot{Q}_{Dot} = 0 \tag{4.2}$$

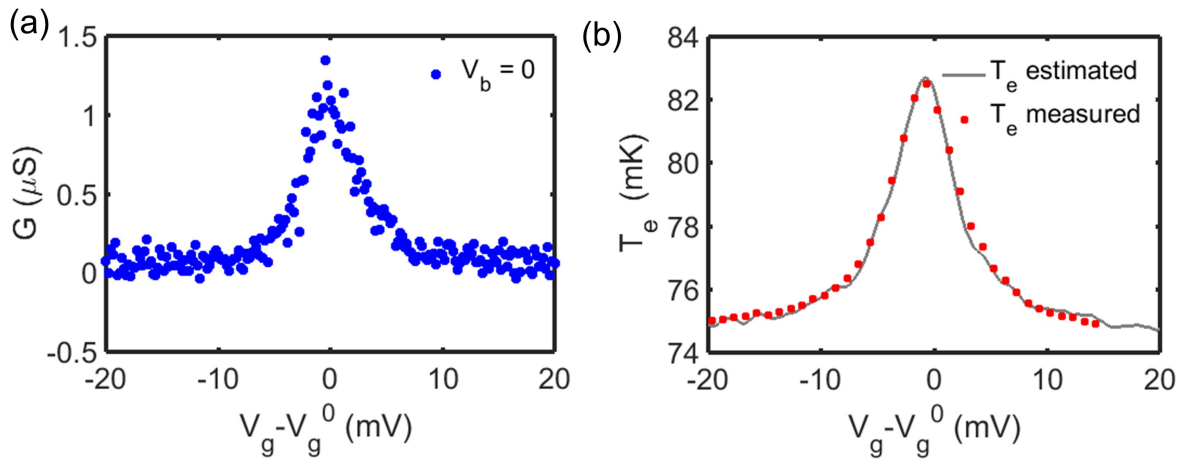

Fig. 4.12: (a) Conductance of device B at $V_b = 0$. (b) Estimated electronic temperature of the source island using Eq. 4.2 in blue and measured value of T_e in red.

Where $\dot{Q}_H$ is the heating power applied to the source island which is set to zero here and $\dot{Q}_{noise} = ({V_b}^{noise^2}/2) \times G(V_g)_{V_b=0}$ is the conductance-dependent heating. For $\dot{Q}_{Dot}$, we assume that WF law holds qualitatively and the heat flow through the QD is given by $\dot{Q}_{Dot} = 0.5 \times L_0 \times G \times ({T_e}^2 - {T_b}^2)$. Here L_0 is the Lorenz number and G is the linear conductance of the device shown for the full range of gate voltages in Fig. 4.12a. The result of solving Eq. 4.2 for T_e is plotted in solid-gray in Fig. 4.12b. A $V_0^{noise} \approx 10\ \mu$V is used as a fitting parameter to calculate the $\dot{Q}_{noise}$. In other words, at the charge degeneracy point, this $V_0^{noise} \approx 10\ \mu$V makes the temperature rise by approximately ≈ 8 mK, which corresponds to a heating power of $\dot{Q}_{noise} = 0.3$ fW. The measured temperature rise is superimposed with the estimated one in Fig. 4.12b. The good agreement suggests the validity of our interpretation. The $V_0^{noise} = 10\ \mu$V noise level is also in line with previous measurements conducted in our group [95]. In the heat valve section, the coupling of the device was stronger so that even in the charge degeneracy point the heat conductance was taking over of the heating produced by the noise. Unfortunately, we should accept that we have this ${V_b}^{noise} = 10\ \mu V$ noise. Finally, it turned out to have a is very significant contribution to heat balance.

4.3.1.2 Noise heating correction at finite bias

We applied the above analysis to the entire temperature map in Fig. 4.11a using a protocol presented in Fig. 4.13. Let us emphasize that the noise level is bias independent, however the heating produced is not bias-independent, and the instantaneous power can be written as,

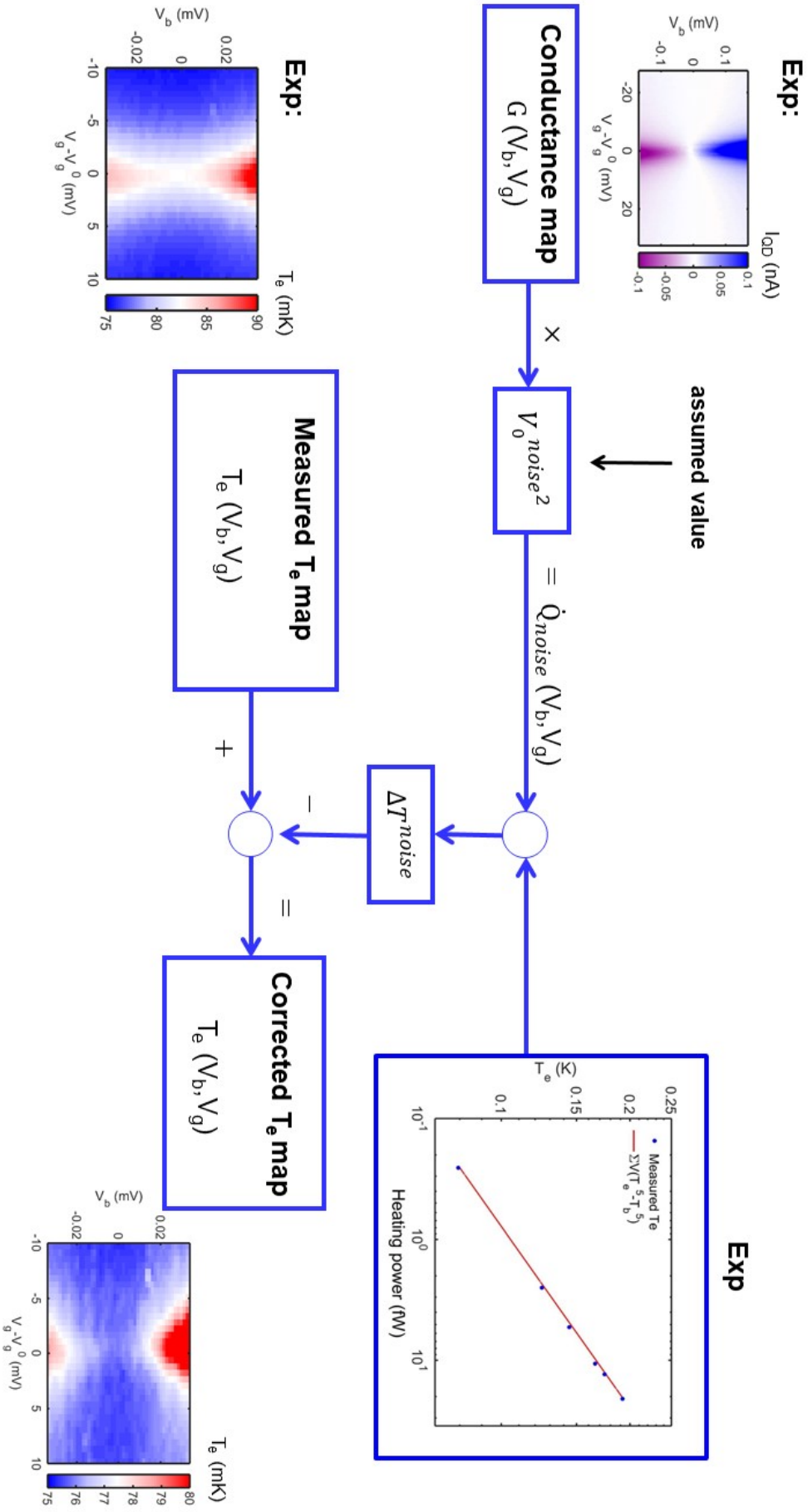

Fig. 4.13: Noise correction protocol

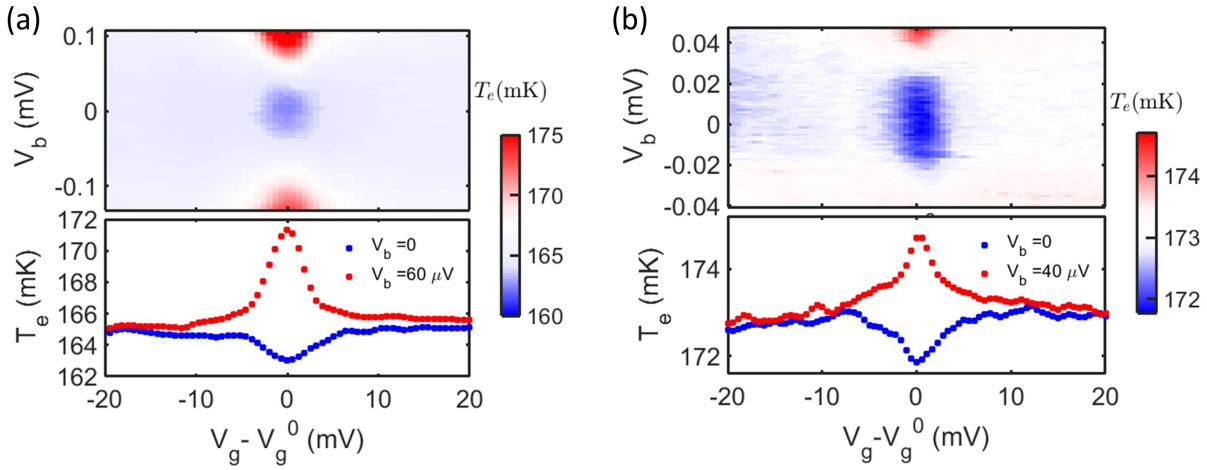

Fig. 4.14: (a), (b) Top, highly resolved temperature maps for two heating powers, $\dot{Q}_H = 5$ fW or $\dot{Q}_H = 6.5$ fW of device B after after correction for spurious heating, respectively. (a),(b Bottom: individual gate traces at two different bias voltage.

$$\dot{Q}_J{}^{total} = (V_b + V_0{}^{noise}\sin(\omega t))^2 \cdot G(V_b, V_g) \tag{4.3}$$

and can be extended as

$$\dot{Q}_J{}^{total} = V_b^2 + V_0{}^{noise^2}\sin^2(\omega t) + 2 \cdot V_b \cdot V_0{}^{noise}\sin(\omega t)) \cdot G(V_b, V_g) \tag{4.4}$$

where in average the total Joule heating can be written as:

$$\dot{Q}_J{}^{total} = (V_b^2 + \frac{V_0{}^{noise^2}}{2}) \cdot G(V_b, V_g) \tag{4.5}$$

the first term of the total Joule heating is the DC bias and the second term $\frac{V_0{}^{noise^2}}{2}$ is related to bias noise. As the bias noise level is bias independent, therefore, we can use pretty much similar procedure as before in the following:

Briefly speaking, $\dot{Q}_{noise}(V_b, V_g)$ is obtained by multiplying the $G(V_b, V_g)$ by $V_0{}^{noise^2}$, and according to Fig. 4.1b, $\dot{Q}_{noise}$ can be converted to a corresponding noise in temperature ($\Delta T_e{}^{noise}$) or vice versa. Eventually, after subtracting $\Delta T_e{}^{noise}$ from the raw temperature map shown in Fig. 4.11, one is thus left with a corrected temperature map which is presented in the bottom-right of Fig. 4.13. At zero bias, it can be seen from Fig. 4.13 bottom-right that there is no temperature rise anymore due to the noise as the gate voltage is swept through the charge degeneracy point.

4.3.2 Heat conduction and violation of Wiedemann-Franz law

Having established the origin of noise and the protocol to correct it in the next step, the source island is heated by a constant heating power $\dot{Q}_H = 5$ fW or $\dot{Q}_H = 6.5$ fW and the corresponding electronic temperature is measured. In the top panels of Fig. 4.14, the corrected electronic temperature of the source island in the $V_b - V_g$ plane is plotted and in the bottom panel two individual gate traces of the electronic temperature at a fixed bias are shown. Cooling is observed at low bias at the charge degeneracy point for device B. This experiment is confirming the results obtained in sample A. Here we are able to measure charge conductance of the same device which enables us to deduce heat conductance and therefore provides a first test of the WF law in a quantum junction. While these measurements suffer from some uncertainties due to the above discussion, this will be overcome in the next chapter.

We now focus on the analysis of heat conductance to systematically study the validity of the WF law in device B. For this purpose, this time we solve the thermal balance Eq. (4.2) for $\dot{Q}_{QD}$ using the relation between the applied Joule power $\dot{Q}_H$ to the source and its electronic temperature T_e, at a given gate voltage V_g. We assume that in the off-resonance state ($V_g = 0$ V), no electronic heat can flow through the quantum dot as we explained in section 1.1.4 and Fig. 4.5. Therefore, we take $\dot{Q}_H(V_g = 0) = \dot{Q}_{e-ph}$ as a reference, which comprises all heat leakage out of the source, other than the one originating from the quantum dot electronic contribution itself. After subtracting the e-ph contribution and the $G(V_b, V_g)$ dependent noise power from the main heat flow (see Eq. (4.2)), one is left with the quantity of interest, the electronic heat flow through the single level quantum dot, i.e. $\dot{Q}_{QD}(V_b, V_g)$, where I is set to zero as the WF law can be evaluated for open circuit condition.

In most situations, the heat exchange between two reservoirs at temperatures T_1 and T_2 is described by $\dot{Q} = \Sigma\,(T_1^n - T_2^n)$, introducing a system-dependent coupling constant Σ (often the interaction volume is explicitly factorized out of Σ) and exponent n. For electronic heat exchange along a conductor with conductance G, the WF law stipulates that $n = 2$ and $\Sigma = L_0 G/2$. In the limit of a small $\Delta T = T_1 - T_2$, this can equivalently be linearized to define the heat conductance $\kappa_e = \dot{Q}/\Delta T = L_0 G T_{\mathrm{avg}}$, with $T_{\mathrm{avg}} = (T_1 + T_2)/2$. Our main concern of here is to recurrently investigate the validity of this relation in quantitative detail in a quantum dot junction. Fig. 4.15 plots the linear charge conductance G together with the electronic heat conductance κ_{e} and corresponding T_{avg} of device B

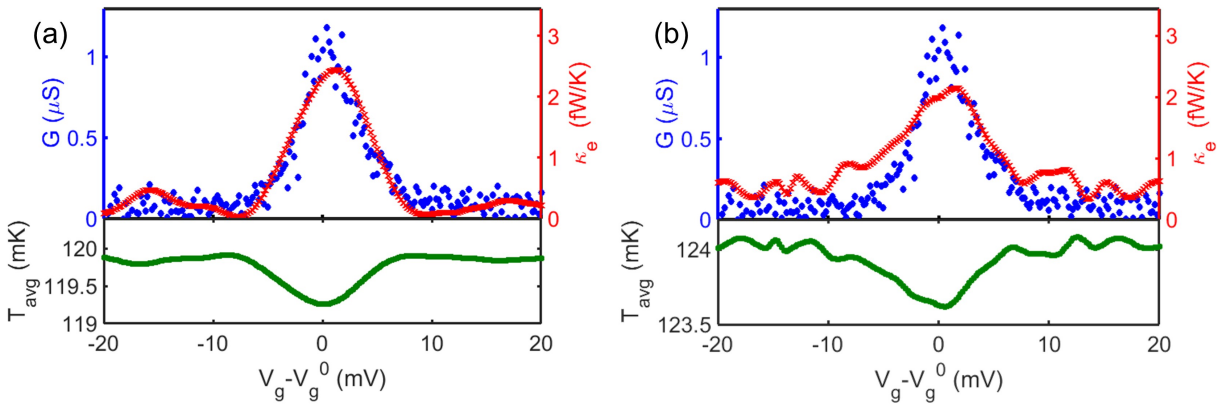

Fig. 4.15: (a),(b) top: charge (blue dots) thermal (red crosses) conductance of a single quantum dot at a bath temperature of $T_b = 75$ mK as a function of V_g for $\dot{Q}_H = 5$ fW and $\dot{Q}_H = 6.5$ fW, are shown respectively. (a), (b) bottom: present the corresponding average temperature (T_{avg}) across the device.

for two heating powers $\dot{Q}_H = 5fW$ and $\dot{Q}_H = 6.5fW$ in the left and right hand side, respectively.

Figure 4.16 shows the resulting L/L_0 as a function of gate voltage V_g. Due to uncertainty in the conductance and temperature measurement deep inside the Coulomb blockaded region, the following protocol for determining L/L_0, including error bars, is defined: First, the standard deviation STD of the heat conductance κ shown in Fig. 4.15 is calculated at small gate voltages ($V_g < -10$ mV). Then, the value of L/L_0 is calculated when all heat conductance data are shifted by $\pm STD$. These set the error bars on L/L_0. According to this which, far from degeneracy, the uncertainty is huge. Therefore, we are not able to be conclusive about the value of L/L_0 deep inside the blockaded regime, whereas, at the charge degeneracy point $L/L_0 < 1$ is robust wrt the standard deviation offset of κ. Based on the extracted tunnel coupling of device B, we would expect a value for L/L_0 between $0.5 - 0.7$ which is in line with the experimental observation in Fig. 4.16. Further theoretical modeling is required to get the precise tunnel coupling and determine the exact value of L/L_0 for device B.

As was already presented in Fig. 4.8d, L/L_0 changes with tunnel coupling of the device. According to the theory prediction, this value goes to zero in a very weak coupling regime. It is not surprising, because this basically tells us that if no current is flowing for a temperature difference, there will be no heat carried as particles tunnel back and forth using the same energy level. In contrast, the WF law is being recovered in the presence of a very large tunnel coupling (strong coupling regime), i.e, the tunnel coupling of the device is roughly bigger than the other relevant energy scales in the system $\Gamma \approx 100 k_B T$.

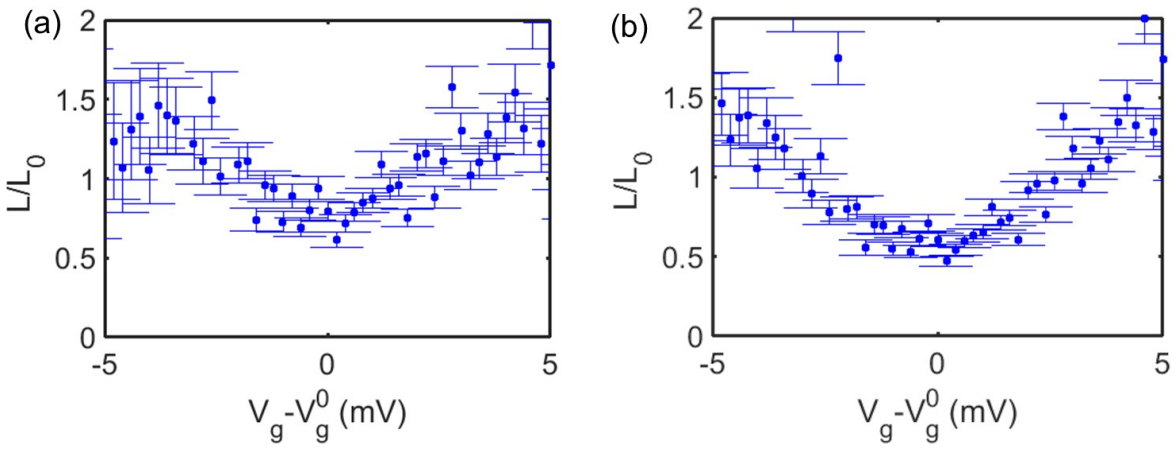

Fig. 4.16: Lorenz ration defined as L/L_0 as a function of V_g is plotted for (a) $\dot{Q}_H = 5$ fW and (b) $\dot{Q}_H = 6.5$ fW

The physical origin of this violation comes from energy selectivity of the device. As a consequence of this, a single-level device can cut the contribution of high energy electron which stems from the tail of Fermi function and therefore, it conducts less heat compared to charge.

4.3.3 Conclusions

We showed in this chapter that electronic heat transport through a QD junction can be modulated by a gate potential, making it act as a gate-tunable heat valve. The Coulomb diamond patterns in the temperature maps reveal the intimate relation between charge and heat transport on one hand and dissipation on the other hand. This behavior can have important consequences in the thermo-electric efficiency application of such a single quantum-dot junction [23].

We have also presented the violation of the celebrated Wiedemann-Franz law at the charge degeneracy point of the quantum dot. Unfortunately, the presence of a residual bias voltage noise obliged us to subtract a V_b, V_g dependent spurious Joule power from our measurement. Further experiments in the next chapter will allow us to make a full quantitative comparison between heat and charge transport properties, in a wide range of tunnel couplings in a nanowire-based quantum dot.

Chapter 5

Heat transport in an InAs nanowire

In this chapter, we demonstrate a highly tuneable ratio of heat to charge conduction in a gated semiconductor nanowire. At low carrier density and temperature, the formation of quantum dot states provides highly energy selective conduction channels in which, the device conducts significantly less heat compared to charge with respect to the value expected from the Wiedemann-Franz (WF) law. The WF law value can be recovered by tuning the transmission properties of the device.

Contents

5.1 Heat flow through a single quantum level

Quantum dots formed in an InAs nanowire grown by chemical beam epitaxy [184] allowed experimentally testing the Curzon-Ahlborn limit of thermoelectric conversion efficiency at maximum power [3] and thermoelectric conversion at high temperature[5]. Although entering directly in the thermoelectric efficiencies, the electronic heat conductance of such devices is in general not measured independently for two significant reasons:
(i) At temperatures above a few degrees Kelvin, the thermal transport properties of InAs nanowires are known to be strongly dominated by phonons [185]. Therefore, the *electronic* heat conductance of InAs can be experimentally probed only at milliKelvin temperatures.
(ii) Measuring heat conductance is not as easy as measuring charge conductance with a simple device such as an ammeter.
We have devised an experiment utilizing superconductor hybrids as a local electronic thermometer in contact with a single InAs nanowire. This provides simultaneous measurement of heat and charge conductances in such semiconducting devices for the first time.

5.1.1 Device specifications

The device was fabricated with two rounds of electron beam lithography (EBL) as we have already discussed in chapter 2 in detail. The leftmost Al electrode in Fig. 5.1 overlaps with the circular part of the source electrode made in the first lithography round. It therefore connects with a transparent contact to the source island without the oxidation, whereas the others connect via the oxide tunnel barrier through the Cu part of the source and hence display a large tunnel resistance. The leftmost lead allows for probing the charge transport of the nanowire. We do not observe any sign of a superconducting proximity effect on the nanowire caused by this electrode. This is most likely due to the fact that, in the absence of special care in cleaning the Au-Al interface *in vacuo*, residual contaminants such as a monolayer of water on the gold surface strongly reduce the interface transparency and thereby inhibit Andreev reflection. Further, the aluminum contact is much thinner (35 nm) than the nickel/gold island (90 nm) connecting the nanowire, which will further inhibit inducing superconducting correlations.

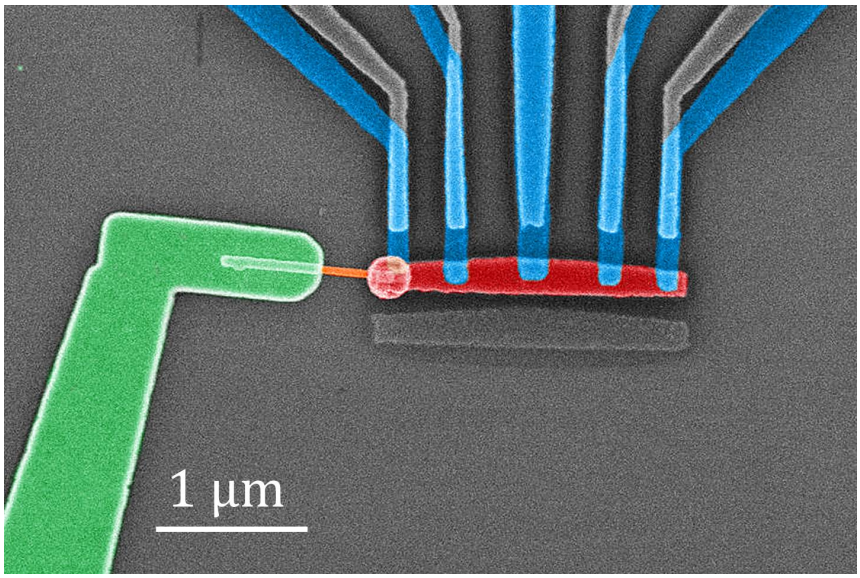

Fig. 5.1: Scanning electron micrograph of a single InAs nanowire device realized with two steps fabrication and shadow-evaporated Al-proximity junctions. In the first lithography round, a bulky drain (in green) and part of the source (visible as a circle on the right hand side of the nanowire) are patterned. In the second round , both the normal-metal island (red) and the superconducting leads (blue) using the same mask in a single vacuum cycle were made.

5.1.2 Charge transport

We start our measurement with the characterization of the nanowire device by checking the gate response of the wire at a very small bias. The direct ohmic contact allows for measuring directly the nanowire electrical conductance $G(V_g)$, as shown in Fig. 5.2 over a full range of gate voltage. The conductance measurement is in agreement with previous reports on similar structures [186]. The nanowire conduction is pinched off below $V_g \sim 2.9$ V. Fig. 5.2 is a composite of several sequential measurement, showing the depletion $V_g < 2.9$ V, followed by Coulomb oscillations at intermediate V_g and conductance oscillations at higher gate voltages.

Near pinch off, the conductance displays sharp resonances, which indicates that the nanowire conduction bottleneck at vanishing charge carrier densities will be provided by a quantum dot forming, owing to unavoidable charge disorder. Notably, even when reaching $\sim 2e^2/h$ at higher gate voltages, the charge conductance still displays strong, yet perfectly reproducible fluctuations, which point to disordered multi-channel transport in the nanowire.

Close to depletion the Coulomb peaks are somewhat irregularly spaced, which is commonly observed in few-electron QDs [187] and also in similar nanowires [188, 189].

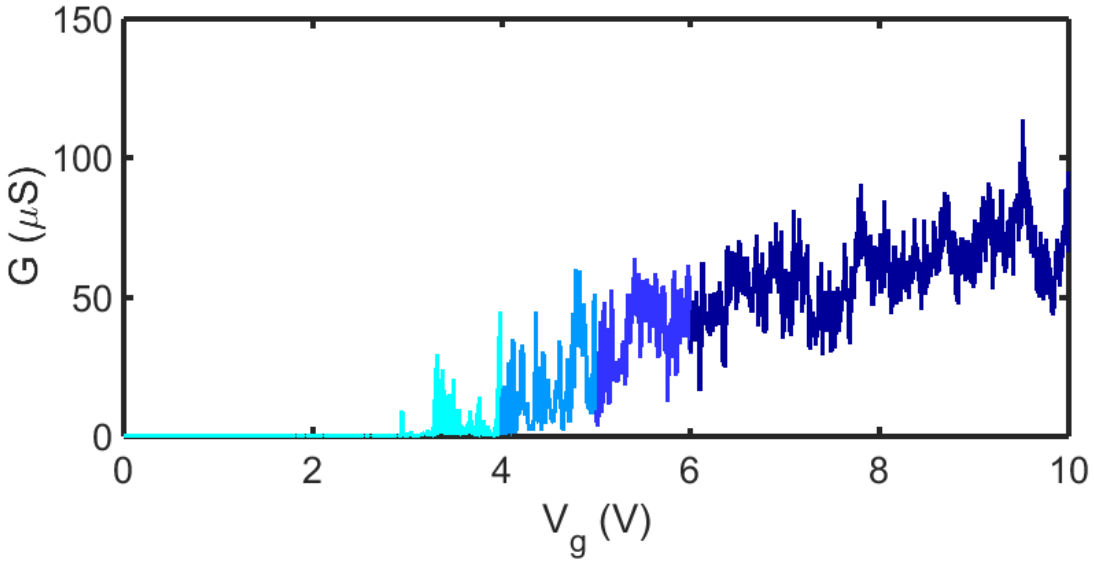

Fig. 5.2: Composite of sequential conductance measurement as a function of back gate voltage (V_g), distinguished by different colors from depletion of the wire ($V_g < 2.9$ V) to clear Coulomb oscillations ($V_g > 4$ V) and high conductance.

$V_g = 2.933$ V	$V_g = 4.095$ V	$V_g = 4.117$ V
$\alpha_l = 0.095$	$\alpha_l = 0.06$	$\alpha_l = 0.06$
$\alpha_m = 0.105$	$\alpha_m = 0.08$	$\alpha_m = 0.08$
$\alpha_u = 0.115$	$\alpha_u = 0.1$	$\alpha_u = 0.1$

Tab. 5.1: Extracted lower (α_l) and upper (α_u) bounds of gate couplings for the Coulomb peaks, and their mean value (α_m) at the resonances considered in the main article.

5.1.2.1 Quantum dot and Coulomb blockade analysis

We focus now on lower gate voltage regime $V_g < 4.7$ V, where we are able to see some nicely spaced Coulomb peaks in particular at around $V_g = 2.9V$ and $V_g = 4V$. The conductance map of Fig. 5.3 displays the measured current map on the left-hand side and the differential conductance maps, obtained by numerical differentiation, as a function of both the bias and gate voltages V_{NW} and V_g. Coulomb diamonds can be seen clearly and the charging energy of $E_c \sim 1.5 - 2$ meV is estimated from extrapolating the bias level to the top of a diamond.

A conductance map provides all information needed to determine the parameters of the quantum dot as already explained in chapter 1, the positive slope of the Coulomb

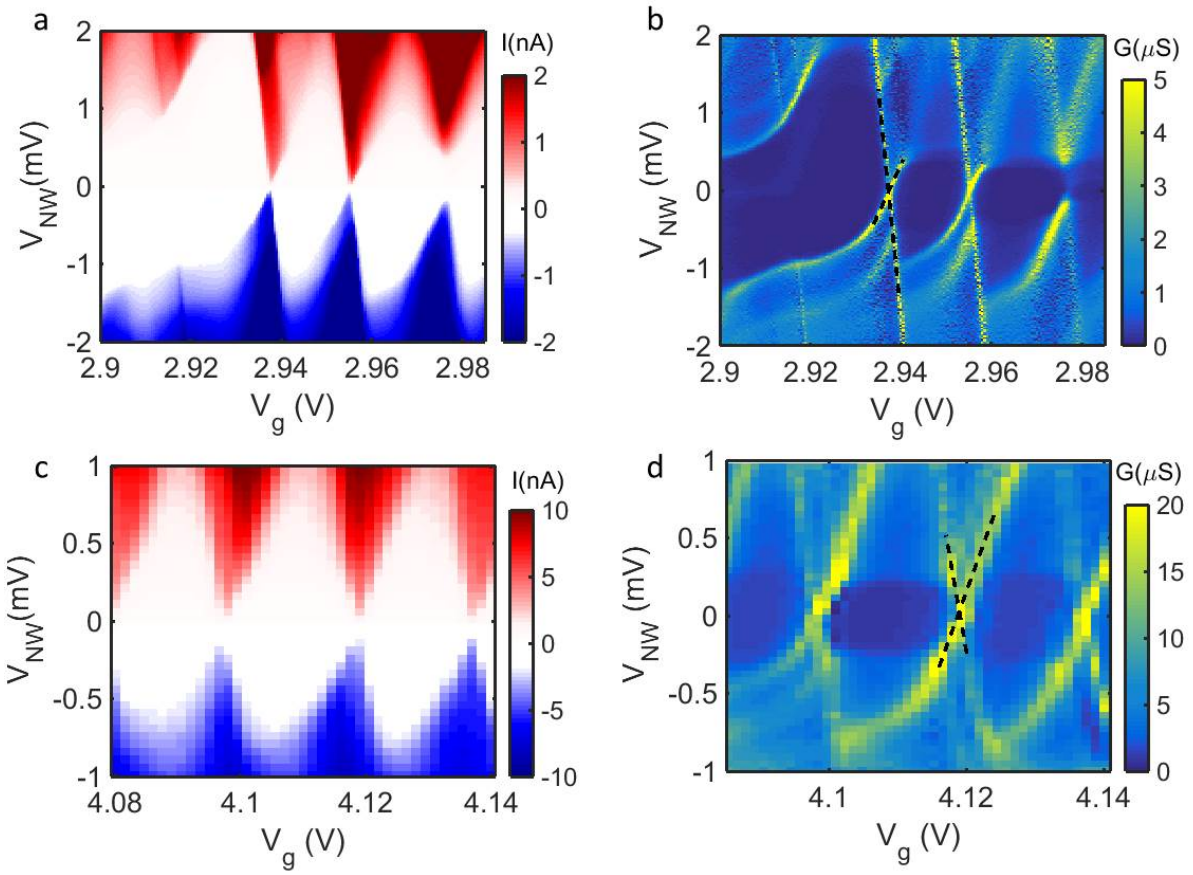

Fig. 5.3: Color map of current and conductance measurement for $V_g = 2.9V$ and $V_g = 4V$ showing clear Coulomb diamond structure. Additional slanted lines indicated by yellow colors in conductance map (b) and (d) outside the Coulomb diamonds display quantum dot levels excitations.

diamonds in Fig. 5.3 is given by $\beta = \frac{C_g}{C_d+C_g}$ and the negative one is given by $\beta' = \frac{C_g}{C_s}$. Here C_s, C_d, C_g are the capacitances between the dot and source, drain and gate respectively. The total capacitance of the dot to the outside world is the sum of all capacitances as $C_\Sigma = C_s + C_d + C_g$. An important parameter in the latter calculations is the lever arm defined by the ratio $\alpha = \frac{C_g}{C_\Sigma}$ as it translates changes in gate voltage to changes in the chemical potential of quantum dot, $\Delta\varepsilon = -e\alpha\Delta V_g$. From the conductance maps close to $V_g \sim 4.1$ V and $V_g \sim 3$ V we extract a local lever arm α_m from the slopes of conductance lines. We observe that the level arm value varies slightly with the gate voltage, see Tab. 5.1. In order to account for uncertainties in the determination of gate coupling, we performed the full theoretical analysis at $\alpha_m \pm 0.01$ for $V_g \sim 3$ V and $\alpha_m \pm 0.02$ for $V_g \sim 4.1$ V.

Next we extract a pair of tunnel couplings (γ_1, γ_2) for each Coulomb peak by fitting the calculated zero-bias conductance as a function of the gate voltage to the measured counterpart. The parameter values for the two tunnel couplings are obtained unambigu-

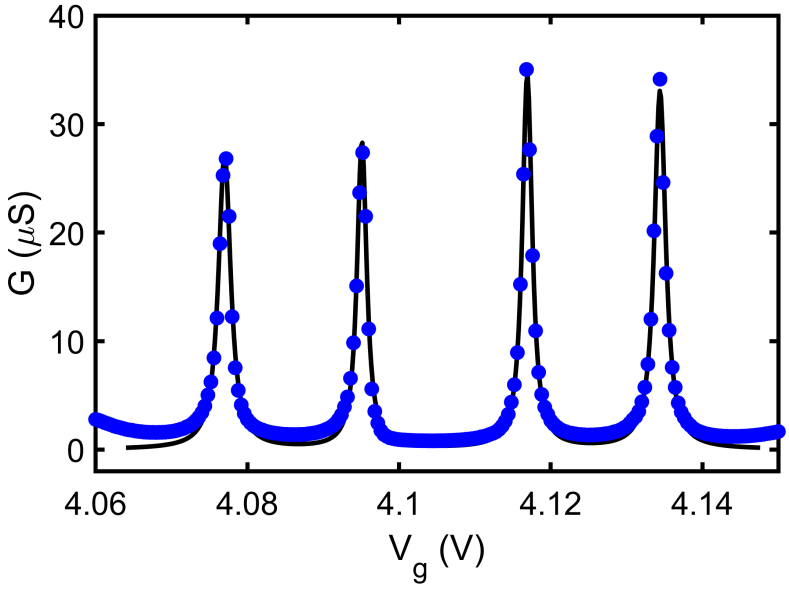

Fig. 5.4: Measured (blue markers) and calculated (solid line) charge conductance of the device around the charge degeneracy points close to 4.1 V. The full transmission function used for the theory prediction is obtained by adding and having one $\mathcal{T}(E)$ for each peak, determined by fitting the calculated G to the measured data in the vicinity of a single peak.

ously from the height $\propto \frac{\gamma_1\gamma_2}{\gamma_1+\gamma_2}$ and the width $\gamma_1+\gamma_2$ of the transmission function, which corresponds roughly to the height and width of the Coulomb peak. Since we have already determined the appropriate α, this fitting process involves no additional fitting parameters. When performing these fits, we restrict the G data to only cover a single Coulomb peak and use $T_b = T_s = T_d = 100$ mK, which was the temperature of the device during the measurement of G. The resulting best fits obtained using α_m are shown in Fig. 5.12 for $V_g \sim 3$ V and in Fig. 5.4 for the resonances at $V_g \sim 4.1$ V corresponding to the data presented in Fig. 5.13. The extracted values are shown in Tab. 5.2.

It is worth mentioning that around 4.1 V (Fig. 5.4), the total transmission function $\mathcal{T}(E)$ of the device is taken to be the sum of the four individual Lorentzian transmission functions for each Coulomb peak, centered around the V_g values listed in Tab. 5.2.

5.1.3 NIS thermometer and heater

The low-temperature experimental characteristic of the heater NIS junction of our device at $T_b = 100$ mK is shown in Fig. 5.5, both on linear and logarithmic scale, together with the theoretical $I-V$ characteristic using Eq. 3.9 (chapter3). We see that the theory line

V_g (V)	α	γ_1 (μeV)	γ_2 (μeV)
2.938	$\alpha_m = 0.105$	55.5	2.1
4.077	$\alpha_m = 0.08$	137.5	15.5
4.095	$\alpha_m = 0.08$	105.9	12.4
4.117	$\alpha_m = 0.08$	104.8	15.9
4.13	$\alpha_m = 0.08$	122.9	17.5

Tab. 5.2: Extracted tunnel couplings for the Coulomb peaks in two regimes $V_g \sim 2.9$ V, and $V_g \sim 4.1$ V.

catches all features except at the lowest currents where the noise of the current preamplifier contributes to the scatter and saturation of the data points see chapter 3 for more detail.

The heating of the source island was made by applying a voltage V_H to the heater as shown in Fig. 5.8a. The ensuing power $\dot{Q}_H$ can be calculated Eq. (3.11) (chapter 3).

Thermometry is performed by using two NIS junctions in series (SINIS). Such superconductor-insulator-normal metal (NIS) junctions are well-known to provide excellent electron heaters and thermometers in low temperature experiments [30] as discussed in chapter 3 in detail. We bias the pair of NIS junctions with a constant current of $I_{\rm NIS} = 5$ pA and measure the voltage drop $V_{\rm NIS}$ across the junctions to determine the electron temperature of the source island [30]. The thermometer is calibrated by varying the bath temperature T_b of the cryostat. The calibration is done at equilibrium without heating the source island, so that the electronic temperature of the source follows the cryostat temperature (equal to the substrate phonon temperature) and results in the response presented in Fig. 5.6.

The voltage bias $V_{\rm NIS}$ changes as a result of thermal excitations on the normal metal lowering the voltage from the low temperature threshold value corresponding to approximately the superconductor gap $\Delta/e \approx 200$ μV per junction. At low $T_b < 50$ mK, we indeed see a saturation at $V_{\rm NIS} \approx 400$ μV (see Fig. 5.6). All our measurements are performed at $T_e \geq 100$ mK (the vertical dashed line in Fig. 5.6), making sure that the thermometer operates well above the low temperature saturation.

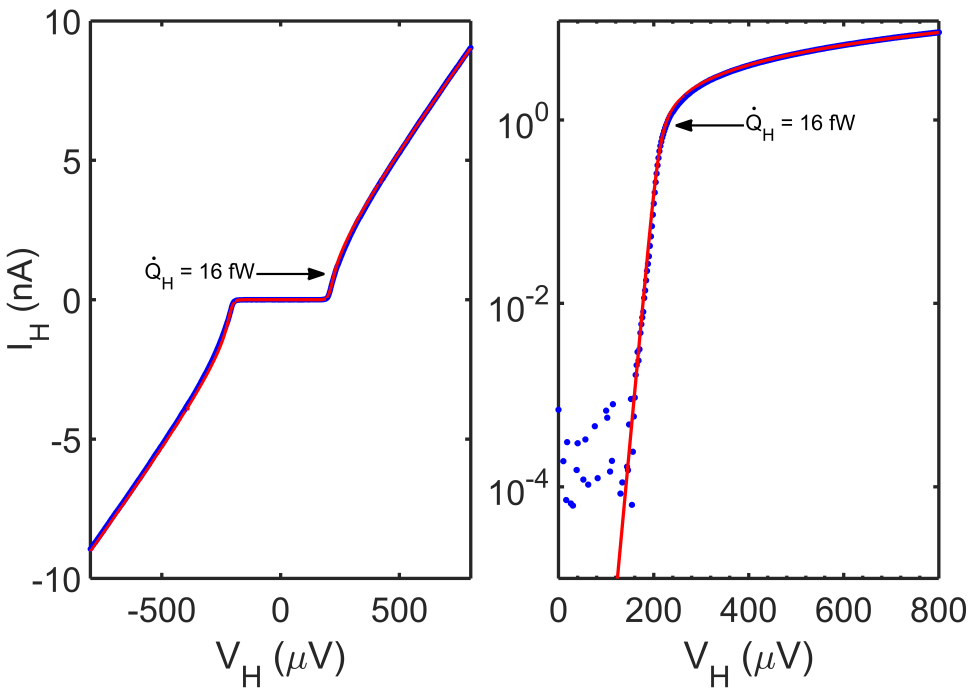

Fig. 5.5: Current–voltage curve of the heater NIS junction using linear (left) and logarithmic (right) scale. Fit is shown as red lines: $\Delta = 209$ μev , $R_T = 85.6$ kΩ and T_b= 100 mK.

5.1.4 Gate modulated heat flow at a constant heating power

As we have all the ingredients for our thermal transport measurement, it is worth checking the device response for a fixed heating power in heating and cooling regime of SINIS junction. This measurement allows us to observe the effect of gating on the nanowire by measuring only the temperature without the charge current being measured in a way similar as in [89].

Fig. 5.7 demonstrates the temperature variations of the heater/cooler NIS junction. As we explained earlier, while a pair of NIS junctions in contact with the source is utilized for measuring the temperature, the other part of junctions plays the role of the cooler/heater, as depicted by the circuit diagram in Fig. 5.8a,b. By applying a proper range of $V_{H/C}$ (low $V_{H/C}$), cooling is achieved below the phonon temperature T_b shown as a horizontal dashed line. We get the maximum cooling at $V_{H/C}$ =195 μeV, with a temperature drop in the order of $\approx$ 10 mK close to the Al superconducting gap. A larger temperature drop is obtained in the Coulomb blockaded regime (the difference between dots and circles in Fig. 5.7 in cooling regime) as can be seen in Fig. 5.7 bottom-right. Thanks to the physical properties of the SINIS heater, not only can such a junction be used as a cooler, but also it can be employed as a heater, as which we utilize it mainly in this work. By applying

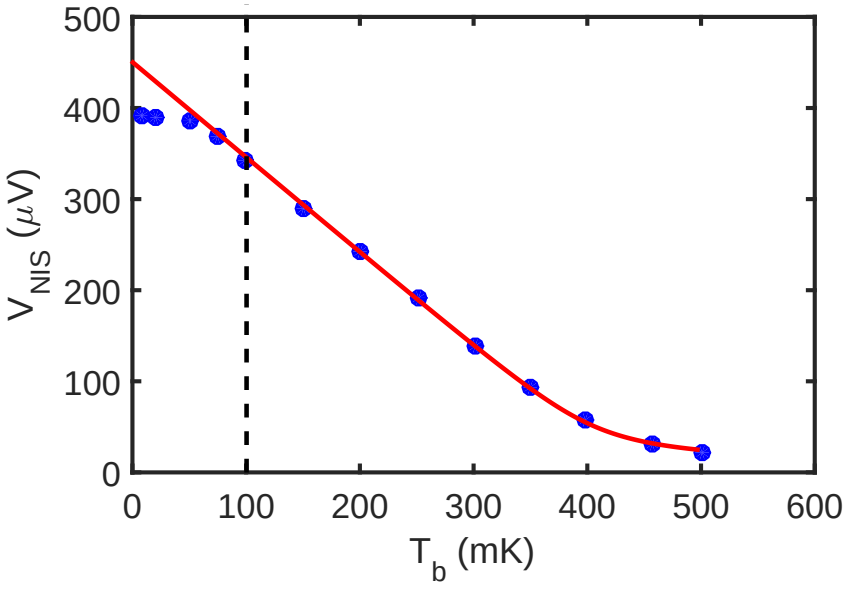

Fig. 5.6: Measured voltage across the thermometer junctions with a floating current of $I_{\mathrm{NIS}} = 5$ pA as a function of the bath temperature T_b. The dashed line presents the bath temperature $T_b = 100$ mK used in the heat flow measurements. The red line shows the expected response of Eq. (3.9) with $\Delta = 209$ μeV and $R_{T1} = R_{T2} \sim 96.2$ $k\Omega$ obtained from a similar fit as in Fig. 5.5.

higher voltage to the SINIS junction, for instance, $V_{H/C}$ =300 μeV ($V_{H/C} > \Delta$) we are overheating the electrons so that $T_e > T_b$. Fig.5.7 top-right shows the electron temperature increase in the Coulomb blockaded regime.

5.1.5 Simultaneous measurement of charge and heat flow

So far, we have demonstrated and measured charge and heat flow through the NW separately. A drawback of a separate measurement is that there is always some uncertainty about hitting the same degeneracy point, for instance due to electrostatic drift in the gate voltage. Therefore, it is absolutely fruitful to measure the two quantities simultaneously, i.e. one can be sure that the heat and charge flows are probed for the same charge degeneracy point. For performing this combined measurement of charge and heat flows, the nanowire conductance dI/dV_{NW} is measured through the leftmost Al lead (direct contact) using a voltage division scheme as pictured in Fig. 5.8a, involving a 10 MΩ bias resistor. At the same time, the other four aluminum leads to the source are in contact via tunnel barriers (heater and thermometer).

Because at mK temperatures both the electron-phonon coupling in metals and the heat conductance of superconductors are very low, the source island electrons are thermally well

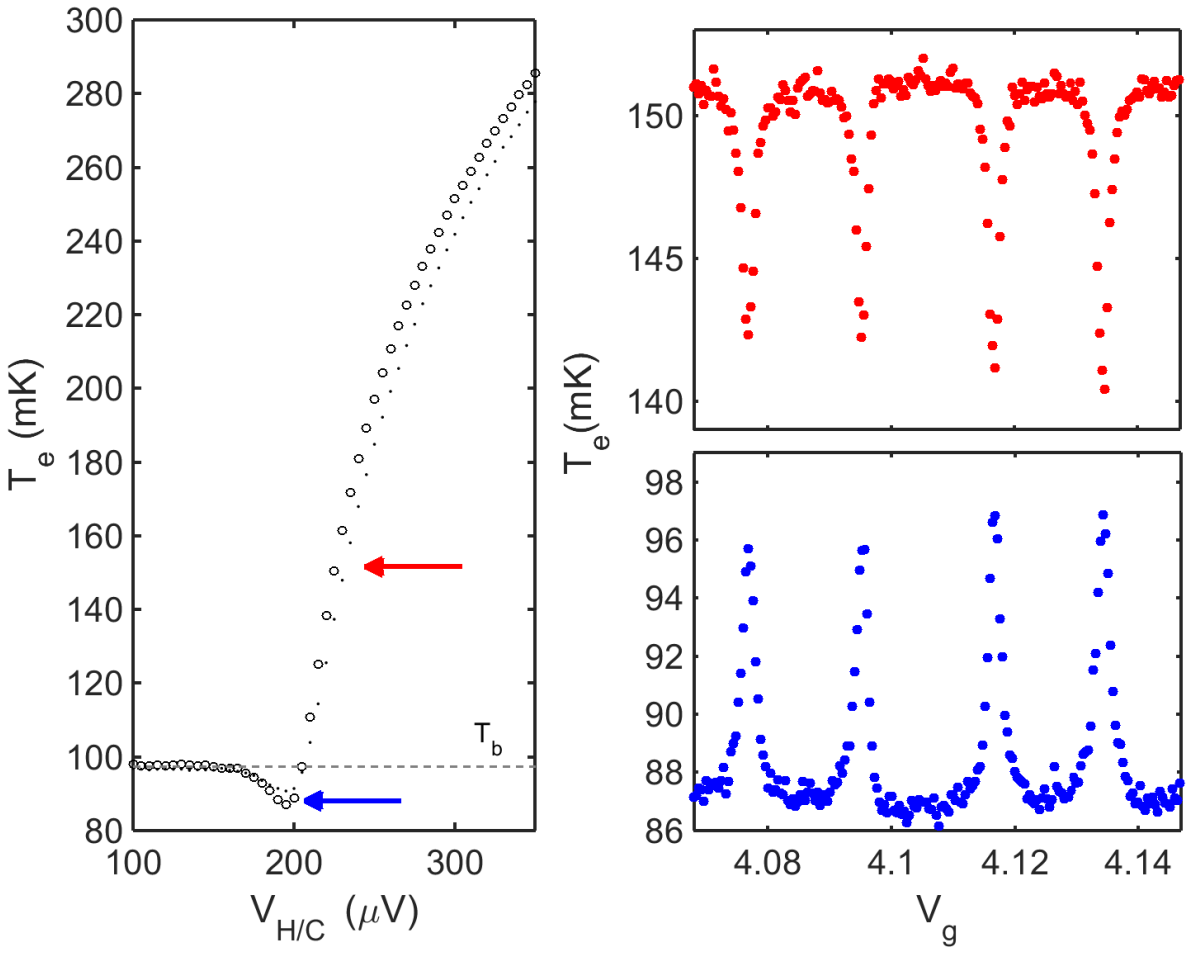

Fig. 5.7: Left: Electron temperature measurement at T_b=100 mK with the gate voltage tuned at the resonance (dots) and off the resonance (circles) as a function of heater (cooler) V_H (V_C). Right: temperature oscillations as a function of the gate voltage, with an opposite sign for over-heating (top-right) and the electron cooling regime (bottom-right).

insulated, such that the heat flow through the nanowire significantly contributes to the source island's heat balance. This is seen in Fig. 5.8d, in which a constant heating power $\dot{Q}_H = 16$ fW is provided to the source island via a voltage V_H applied on one tunnel lead. As the gate potential is swept, the variations of the source island electron temperature T_e are strikingly anticorrelated to variations of G. The heat balance of our device is schematized in Fig. 5.8b. Because the source island is overheated with respect to its environment, the gradual opening of electronic conduction channels in the InAs nanowire leads to increased heat flow out of the source island, and thus a lowering of T_e.

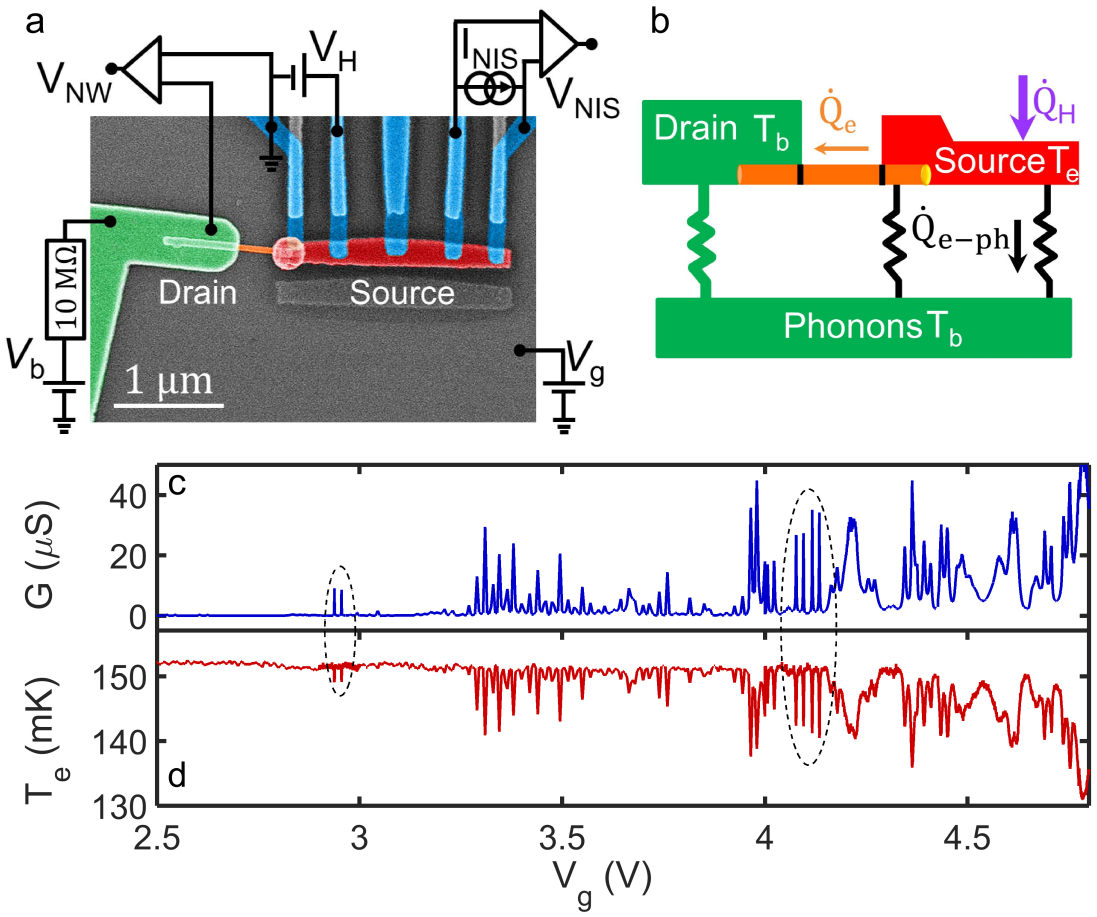

Fig. 5.8: Heat transport experiment through an InAs nanowire device. (Adapted from Majidi et al. [159]) (a) False-colored scanning electron micrograph of the device. The drain electrode, the source island and the nanowire are colored in green, red and orange, respectively. Five superconducting aluminum leads (light blue) are connected to the source island for heating the source side and measuring its electronic temperature. Thermometry is performed by measuring the voltage V_{NIS} at a fixed floating current bias I_{NIS}. (b) Heat balance diagram, which includes the applied power to the source island, $\dot{Q}_H$; the heat escaping due to electron-phonon coupling, $\dot{Q}_{\mathrm{e-ph}}$; and the electronic heat flow along the nanowire, $\dot{Q}_e$. (c) Electrical conductance at thermal equilibrium and (d) temperature response T_e of the source island with heating power of $\dot{Q}_H = 16$ fW as a function of the back gate voltage V_g. The dashed ellipses highlight resonances that will be studied in more detail. All measurement are taken at a bath temperature $T_b = 100$ mK.

5.1.5.1 Determining e-ph coupling of Cu island

An important issue in the determination of electronic heat flow is the proper identification of the parasitic heat escape via other channels, such as electron-phonon coupling [30]. Unless the latter can be neglected [6], the comparison to a reference, at which the electronic heat conductance is either assumed to be known [22], or negligible, is required.

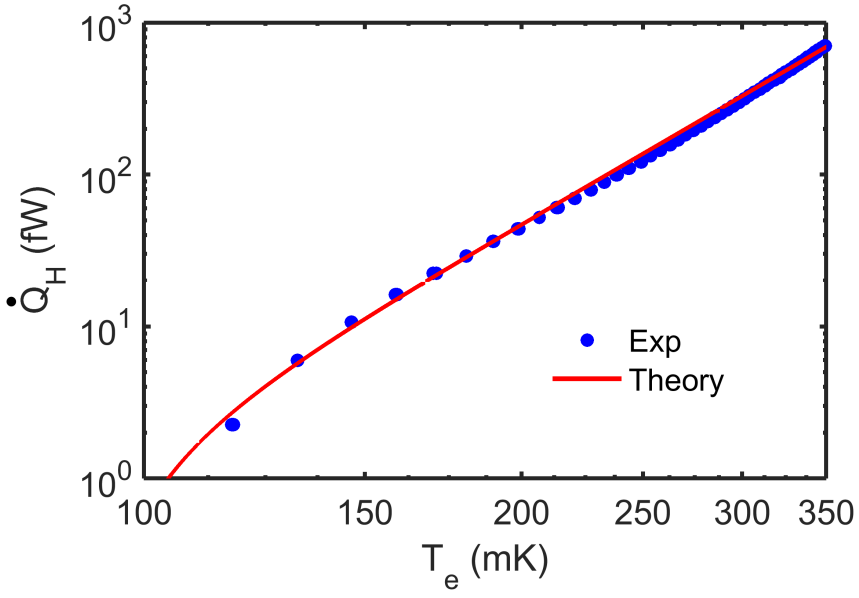

Fig. 5.9: Heating power $\dot{Q}_H$ applied to the source island as a function of the measured source electron temperature T_e at $V_g = 0$ V and $T_b = 100$ mK. The red curve is a fit, see text.

A widely utilized technique to measure $e - ph$ coupling at low temperature is heating up the normal metal island directly and measuring the temperature change. In order to understand the heat escape mechanism due to the presence of phonon in our device, we formulated $\dot{Q}_{e-ph} = \dot{Q}_H$ in the insulating regime of the device. The relation $\dot{Q}_H(T_e, V_g = 0)$ between the applied heating power and the source island electronic temperature at $V_g = 0$ (deep in the insulating regime) is measured and shown in Fig. 5.9. The good quantitative agreement with an electron-phonon type thermal law following Eq. 3.13 and [30] shows that electron-phonon coupling must be the dominant thermal leakage channel out of the source island, in the absence of electronic heat conduction through the nanowire. The red curve is a fit with $\dot{Q}_H = \Sigma\Omega({T_e}^5 - {T_b}^5)$. By using the geometrically estimated total volume $\Omega = 4.26 \pm 0.2 \times 10^{-20}$ m^3 of the source island, we obtain the fitted value $\Sigma = 2.5 \pm 0.1 \times 10^9$ Wm^{-3}K^{-5} of the average electron-phonon coupling coefficient in the metallic source island, in good agreement with the expected coupling coefficients of Cu and Au [30]. We stress that the gate-dependent part of the heat balance is considered and defined as $\dot{Q}(T_e, V_g) = \dot{Q}_H(T_e, V_g) - \dot{Q}_H(T_e, 0)$.

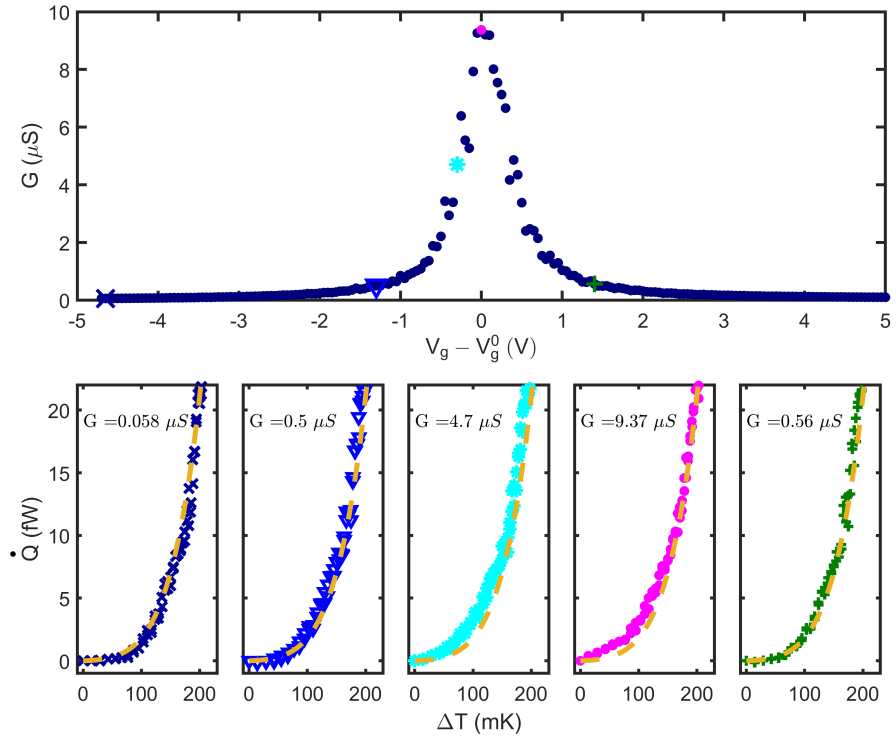

Fig. 5.10: Top : Charge conductance G peak around the resonance at ${V_g}^0 = 2.938$ V. Bottom : heat flow $\dot{Q}$ as a function of the temperature difference at several values of the gate potential indicated by color symbols in the bottom panel. The dashed line is the best $\propto (T_e^6 - T_b^6)$ fit obtained from the data in the leftmost sub-panel, and displayed identically in all sub-panels for reference.

5.1.5.2 Electron-phonon coupling in the InAs NW

During the analysis of $\dot{Q}(T_e, V_g)$, a slight gate dependence of $\dot{Q}(T_e, V_g)$ was surprisingly observed even before the conducting state of NW sets on. This is readily visible as a slightly negative slope of the $T_e(V_g)$ baseline in Fig. 5.8d. Thus, we conclude on a minute yet measurable and smoothly gate-dependent contribution to the source electron-phonon coupling, which calls for defining in addition a local reference. However, it is worth checking few items in detail.

In the source reservoir, which is shown in Fig. 5.8b, there is one piece of semiconductor that is in direct contact to the source island and that is at the elevated temperature (T_e), on the other side we have the other part of the semiconductor, which is at base temperature (T_b) and eventually we have the orange part in the middle at an intermediate temperature. Therefore, this red part of the semiconductor heats up together with the metallic source electrode and from this we get the e-ph background. If the semiconductor NW were

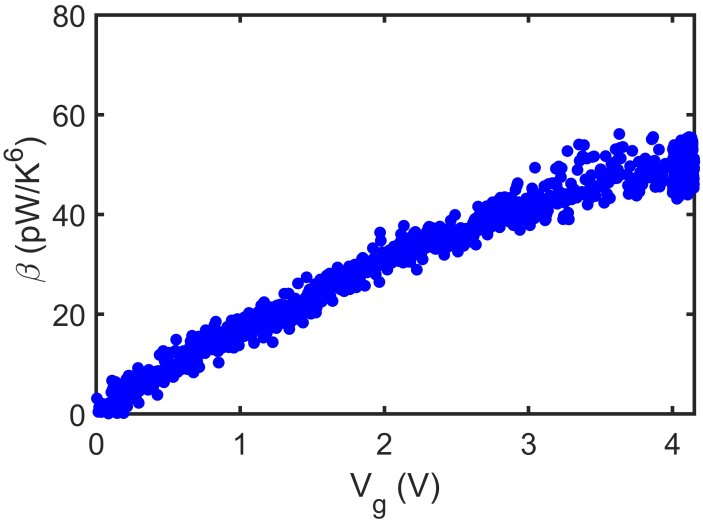

Fig. 5.11: Gate dependence of the electron-phonon coupling: β is extracted by fitting $\dot{Q}(T_e, V_g)$ at each V_g (excluding conduction resonances) with a $\beta(T_e^6 - T_b^6)$ power law.

completely a quantum dot, we would not have this background. We conducted different tests to determine if this picture is correct or not as listed below:

- Constant background over a narrow range: We observed that low electrical conductance data points, deep inside Coulomb blockade, yield the exactly same $\dot{Q}(T_e)$ curve within the measurement noise over a narrow range of V_g. Hence, the e-ph contribution (i.e. background) is more or less constant or varies slowly with the gate.

- Heat flow independent of G: The e-ph background should be independent of electrical conduction (G). To verify this point, the G dependence of the $\dot{Q}(T_e)$ curve is checked in the vicinity of our charge degeneracy point, i.e. the heat flow at the lowest electrical conductance point is compared with its value when the conductance is one order of magnitude higher. It turned out that $\dot{Q}(T_e)$ remains the same. This test would give us another indication that we have a rather slowly varying e-ph background. At a given resonance peak, the electronic heat conductance is experimentally determined by subtracting a local reference of heat $\dot{Q}$ measured close to the resonance at a point where the electronic contribution is negligible. Fig. 5.10 shows that the heat flow is constant within noise at low electrical conductance G far enough away from the main peak although G changes by one order of magnitude. Only close to the resonance peak, we observe an extra contribution identified as the electronic part. On both sides of the peak, $\dot{Q}$ has the same background level when G is small enough.

In order to understand this background contribution, we have analyzed the $\dot{Q}(T_e, V_g)$ curves in the entire non-conducting regime of the nanowire. For this purpose, we have first focused on the regime between $V_g = 0 \ldots 4.5$ V, excluding conduction resonances, that is, data sets at values of V_g at which $G > 0.5$ μS. In the second part of analysis we try to understand the underlying mechanism of e-ph coupling in high transparency regime. The background part of the heat flow increases steeply at $\Delta T \gtrsim T_b$ and is related to electron-phonon coupling in the nanowire. A $(T_e^6 - T_b^6)$ law provided by far the best agreement. Because on the microscopic level the e-ph coupling can be quite different in InAs and the metallic island, it is not surprising that we observe a different exponent for the e-ph coupling of both systems [30].

The prefactor β is plotted in Fig. 5.11. As expected, β increases smoothly with V_g, supporting the hypothesis of a dependence on the carrier concentration in a segment of the nanowire not belonging to the quantum dot. This could be for example the portion of the nanowire underneath the source island, of volume $V = 7.7 \times 10^{-22}$ m^3. Making this assumption, the e-ph heat conductance per unit volume in the metallic source is on the same order of magnitude as that of the nanowire. Note that our method is probably underestimating β by a constant shift, since we assumed its value to be 0 at $V_g = 0$ V.

Moving to yet larger gate voltages and thus electronic transmissions, the charge conductance no longer vanishes in between conduction resonances, limiting the identification and subtraction of a clear-cut local reference $\dot{Q}_e(T_e)$. This prevents a quantitative separation of the electronic heat flow from other heat escape mechanisms that could depend on V_g without being directly connected to G. Indeed, in InAs nanowires, a surprisingly strong e-ph coupling was found above 1 Kelvin [185], possibly due to piezoelectricity [190] and/or a lateral-confinement-enhanced peaked density of states [191].

In the following, we will experimentally show the breakdown of the WF law and a linear power law for heat flow $\dot{Q}_e$ with the temperature.

5.1.5.3 Violation of heat flow below Wiedemann -Franz limit

To obtain the quantity of interest at low transparency regime ($V_g < 4.5V$), i.e. the *electronic* heat flow through the nanowire at resonance, we need to differentiate the e-ph heat flow from the total heat flow on and off resonance (Fig. 5.12c) as: $\dot{Q}_e(T_e, V_g^0) = \dot{Q}(T_e, V_g^0) - \dot{Q}(T_e, V_g^0 + \Delta V_g)$. We stress that this additional background subtraction does not rely on any modeling of the heat balance, such as electron-phonon coupling. As

seen in Fig. 5.12d and already visible in the inset of Fig. 5.12c, $\dot{Q}_e$ at V_g^0 displays a strikingly linear dependence on ΔT. We see that the heat conductance $\kappa_e = \partial \dot{Q}_e / \partial T$, that is the initial slope in Fig. 5.12d, differs quantitatively from the WF prediction by a factor $L/L_0 \approx 0.65 \pm 0.1$. Further, beyond linear response, the temperature dependence qualitatively deviates from the parabolic law expected from WF according to 1.42 (dashed line).

For a theoretical description beyond the WF law, we use a Landauer-Büttiker non-interacting model, with an energy-dependent transmission $\mathcal{T}(E)$. We write the associated charge and heat currents, respectively as

$$I = \frac{2e}{h} \int_{-\infty}^{\infty} \mathcal{T}(E)\ \Delta f\ dE \tag{5.1}$$

and

$$\dot{Q}_e = \frac{2}{h} \int_{-\infty}^{\infty} (E - \mu_s)\ \mathcal{T}(E)\ \Delta f\ dE, \tag{5.2}$$

with Δf the difference in the source and drain energy distributions, and μ_s the source island chemical potential [55, 56]. The linear charge and heat conductances are then obtained as $G = \partial I / \partial V_{\mathrm{NW}}$ and $\kappa_e = \partial \dot{Q}_e / \partial(\Delta T)$, respectively, with $\Delta T = T_e - T_b$. We model each resonance as a discrete energy level coupled to the source and drain reservoirs. We then deduce the transmission function $\mathcal{T}(E)$ by fitting the calculated gate-dependent charge conductance $G(V_g)$ to the data. The accurate determination of $\mathcal{T}(E)$ requires accurately estimating independently the tunnel couplings and the gate lever arm, as both affect similarly the resonance widths. This is described in detail in chapter 1. On a technical note, we stress that the above theoretical expression of κ_e assumes open-circuit conditions, that is, no net particle current. For all heat conductance experiments the nanowire was biased in series with a 10 MΩ resistor at room temperature. Because we only consider data at gate voltages at which G is significantly larger than $(10\ \mathrm{M\Omega})^{-1} = 0.1\,\mu\mathrm{S}$, applying $V_b = 0$ is then equivalent to imposing open circuit conditions.

With the above analysis, the Landauer-Büttiker theoretical $\dot{Q}_{\mathrm{e}}(T_e, V_g)$ follows directly. As seen in Fig. 5.12d (solid black line), the agreement with the experimental data is very good, with no adjustable parameters, reproducing the observed approximately linear dependence on ΔT. The grey shaded region accounts for the uncertainties in the determination of $\mathcal{T}(E)$. The violation of the WF law observed here is therefore accurately described by a non-interacting scattering transport picture.

Intuitively, the deviation from WF at resonance can be understood as stemming from the energy selectivity of the device transmission, so that tunneling electrons carry an en-

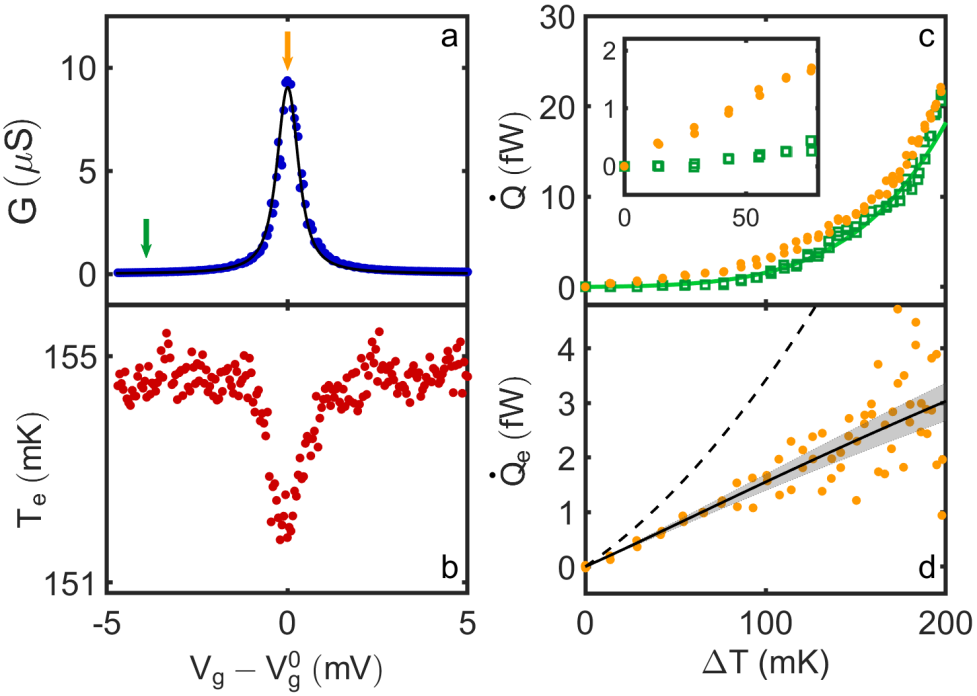

Fig. 5.12: Heat transport near an isolated conductance resonance. (Adapted from Majidi et al. [159]) (a) Linear charge conductance around $V_g^0 = 2.938$ V. The black line is a fit using scattering theory. (b) Source temperature T_e as a function of V_g, with a constant applied power $\dot{Q}_H = 16$ fW. (c) Full heat balance curve $\dot{Q}(T_e, V_g)$ on (green squares) and off (orange bullets) the transport resonance, as indicated by the arrows in (a). The green line presents a fit using $\dot{Q} = \beta(T_e^6 - T_b^6)$ with $\beta = 35 \pm 5$ pW/K^6. The inset highlights the electronic contribution, dominating at small temperature difference at the resonance. (d) Difference of the two data sets in c, displaying the purely electronic heat transport contribution $\dot{Q}_e$. The dashed and the full lines are the predictions from the WF law and scattering transport theory, respectively. The grey shaded area indicates the uncertainty of the scattering theory calculation, due to the determination of the gate coupling lever arm.

ergy bound by $\sim \gamma_s + \gamma_d$, thus suppressing heat exchange at zero net charge current. Together with a large Seebeck coefficient [2, 192], this reduction of heat conductance without suppressing particle conductance makes the quantum dot junction potentially the "best thermoelectric" as theorised by Mahan and Sofo [20]. With increasing tunnel couplings, the transmission function $\mathcal{T}(E)$ is broadened and the energy selectivity is gradually lost.

5.1.5.4 Recovering WFL for intermediate coupling regime

We show a gradual recovery of the WF law by studying the heat flow close to the conductance resonances observed at a larger gate voltage V_g. While at $V_g \approx 2.9$ V, a ratio $(\gamma_s + \gamma_d)/k_B T_b \approx 7$ placed the device in the intermediate coupling regime, still display-

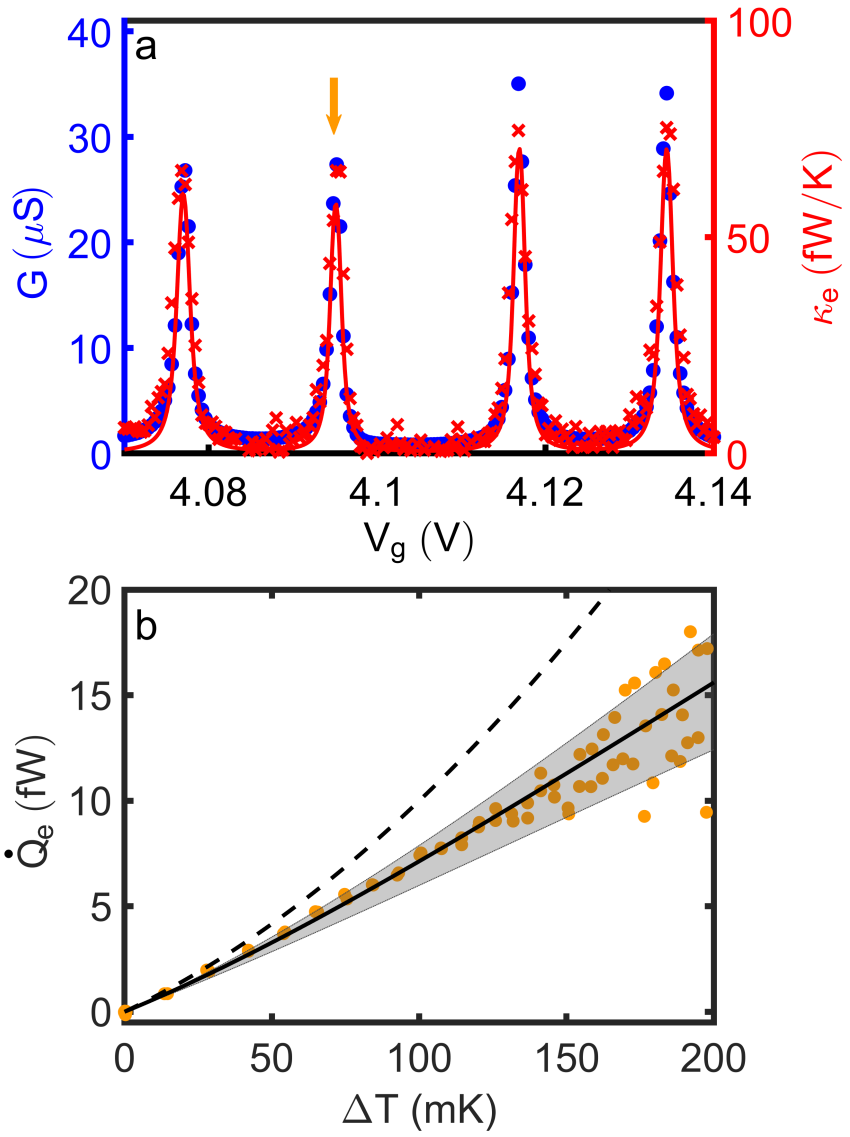

Fig. 5.13: Heat versus charge transport at higher transmissions. (Adapted from Majidi et al. [159]) (a) Heat (red crosses, right vertical scale) and charge (blue bullets, left vertical scale) conductance resonances at higher transmissions. The ratio of both vertical scales is set to $T_b L_0$, such that superimposed curves are indicative of the WF law being valid. The red line is the calculated κ_e from scattering transport theory. The L/L_0 for the four peaks are 0.99, 0.97, 0.87 and 0.90 (± 0.05) from left to right. (b) $\dot{Q}_e(T_e)$ curve taken at the conduction resonance at $V_g = 4.095$ V (arrow in (a)). The dashed and the full lines are the predictions from the WF law and scattering transport theory, respectively. The grey shaded area indicates the uncertainty of the scattering theory calculation, due to the determination of the gate coupling lever arm.

ing sizable energy selectivity (Fig. 5.12), at $V_g \approx 4.1$ V the tunnel couplings are about a factor 2.5 larger (Fig. 5.13a). We therefore expect a gradual transition to a WF-like heat conductance. This is seen in Fig. 5.13a, where we superimpose the experimentally determined G and κ_e on a vertical scale connecting both quantities via the WF law, that

is, $\kappa_e = GT_bL_0$. At the charge degeneracy points (conduction resonances) we observe that the dimensionless reduced heat conductance L/L_0 is now very close to, or barely below 1. Moving away from the conductance peak, G and κ_e also superimpose nearly exactly, within noise, as also expected from a scattering transport calculation with a now broader $\mathcal{T}(E)$ (line). Observing a sizable deviation from WF requires going beyond linear response (Fig. 5.13b) [193], where the experimental data and the scattering transport calculation remain nevertheless now much closer to the WF law. The main conclusion we draw here is that for increasing tunnel couplings, the scattering theory still describes the experimental data very accurately and over a large temperature difference range. In the linear response regime (small ΔT), the WF law and scattering theory yield convergent predictions.

5.1.6 Departure of WFL with the properties of transmission function: theory vs experiment

In addition to modelling the device at the operating conditions of the experiment, the theory also allows us to investigate how the Wiedemann-Franz law violations scale with system parameters. Focusing on the resonant condition, i.e. gating the device to the middle of a conductance peak, we calculate how L/L_0 scales with the width $(\gamma_1 + \gamma_2)$ and amplitude $(\frac{\gamma_1\gamma_2}{\gamma_1+\gamma_2})$ of $\mathcal{T}(E)$. The result is shown in Fig. 5.14, where the theory predictions for the five resonances analyzed in this work are also highlighted. From the figure it is evident that there are two paths for decreasing the L/L_0 ratio: lowering $\gamma_1+\gamma_2$ or increasing k_BT. It is known that tunnel coupling asymmetry plays a significant role in the transport properties [84], Fig. 5.14 shows an intriguing result similarly for the transport of heat too. It can be seen that the bottle neck for the transport of heat is the larger γ, whereas smaller γ is a limiting factor for the transport of charge. This predicts that if we somehow manage to optimally make two coupling as close as possible, so that we still have a large signal for the transport of charge, we therefore will be able to observe a larger breaking of WFL in a symmetric quantum dots device. However, lowering the tunnel couplings or even making them similar are non-trivial in our preset device as the quantum dot forms spontaneously at low carrier concentrations and there is little experimental control over the coupling strength.

In addition, an effect of overall lower values of γ_1 and γ_2 is a reduced heat flow, which can be hard to detect experimentally since the signal is more easily swallowed by the noise-floor. The other approach, to increase k_BT, also has its limitations as the NIS thermometer

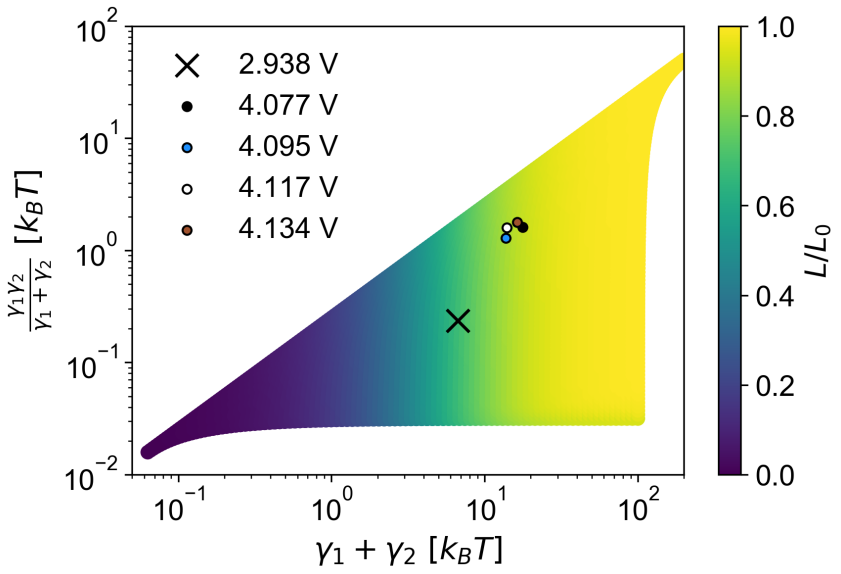

Fig. 5.14: Calculated L/L_0 on resonance as a function of the width $(\gamma_1 + \gamma_2)$ and amplitude $(\frac{\gamma_1\gamma_2}{\gamma_1+\gamma_2})$ of $\mathcal{T}(\mathrm{E})$. Markers show the theoretical predictions for the resonances studied in this chapter, as indicated by the legend.

requires the Al leads to be well below the critical temperature of the superconductor and the e-ph coupling of the source island to be small [30]. One can thus conclude that the present device is very well suited for studying violations of the Wiedemann-Franz law due to quantum confinement given the constraints of the state-of-art technologies used in the study.

5.1.7 Conclusions

In summary, our study reveals large conjunct evolution in the thermal and charge conductances of an InAs nanowire near pinch off. Around conductance resonances in the quantum dot regime of the nanowire, the heat conductance is significantly lower than expected from the WF law, with $\kappa_e/(GTL_0)$ reaching 0.65 in the intermediate coupling regime, in good agreement with a scattering transport calculation. As anticipated by theory [20], this establishes experimentally the huge potential of semiconductor nanowires and more generally quantum dot transistors, as promising high-figure-of-merit thermoelectrics.

Summary and perspectives

Quantum dots are an attractive model system for basic studies and applications in thermoelectricity, owing to their tunable electronic transmission and electron-hole asymmetry [194]. Further, as electronic devices' dimensions shrink towards the nano-scale, quantum effects associated to electron interactions [89, 6, 3] and correlation [48, 65] gain increasing importance. In this thesis, we reported on measurements of charge and heat transport in metallic and semiconductor quantum dot devices.

We first dealt with the nanofabrication of metallic quantum dots by employing the in-situ electromigration and depositing a thin layer of metal (Au). This method increased the success rate of fabrication of such devices compared to the already discussed methods. As we explained in detail, because of having more stability and enhanced ability to tune the tunnel coupling of quantum dot devices, we moved to utilize nanowires in order to perform thermal transport measurement in quantum-dot devices. Therefore, in the second part of fabrication chapter, we established the fabrication process of a single quantum dot based on InAs nanowires coupled to NIS junctions.

Then, we presented that electronic heat transport through a QD junction can be modulated by a gate potential, making it act as a gate-tunable heat valve. This behavior can have important consequences in the practical thermo-electric efficiency of such a single quantum-dot junction [195]. The Coulomb diamond patterns in the temperature maps reveal the intimate relation between charge conductance on one hand and heat transport and dissipation on the other hand. Further experiments have allowed us a quantitative comparison of thermal effects to the charge transport properties in an electromigrated quantum dot junction.

Eventually, we investigated an InAs nanowire device. Our study revealed large conjunct evolution in the thermal and charge conductances of an InAs nanowire near pinch-off. Around conductance resonances in the quantum dot regime of the nanowire, the heat conductance was significantly lower than that of expected from the WF law, with $\kappa_e/(GTL_0)$

reaching 0.65 in the intermediate coupling regime, in good agreement with a scattering transport calculation. As anticipated by theory [20], this experimentally established the huge potential of semiconductor nanowires and more generally quantum dot transistors, as promising high-figure-of-merit thermoelectrics.

Two fascinating open questions reside after reading this thesis, (i), the first one is in the role played by electron interactions [89] that may lead to deviations from the here-employed scattering transport picture away from resonances in quantum dot devices. (ii) the InAs based quantum dot devices can be used as a refrigerator. The initial measurements of quantum dot refrigerator were shown few years ago in 2DEG and three quantum dots. However, there are still some rooms left to utilize a single quantum dot device by choosing a proper coupling strength to give more insight into the underlying physics behind.

Appendices

A Landauer-Büttiker formalism for a quantum dot

We ascribed at the beginning of chapter 1 that the current flows due to an alignment between electrochemical potential in the source, the quantum dot and the drain contact. In the following, we consider the electron transport quantitatively using Landauer's scattering theory, also known as Landauer-Büttiker approach. This approach is capable of expressing and qualitatively describing charge and heat transport of non-interacting electrons through a quantum dot in a simple and elegant way. However, if one wants to investigate the effect of electron interaction on the system, then Landauer-Büttiker is not applicable anymore. In this situation, one needs to utilize Master-equation which determines the possibilities of a quantum dot being in various configurations [37, 158]. If the coupling of the quantum dot to the reservoirs is weak, i.e. the tunnel coupling is by far the smallest energy scale in the system, everything can be modeled by rate equation approach where Fermi golden rule approximation can be applied and the interaction of electrons in the dot can be introduced smoothly [81, 80]. A more accurate way to model quantum dots is to extend the Master equation approach to include the effect of higher order tunneling processes [196, 197, 198]. However, in the extreme case of very strong coupling regime, a more sophisticated and time consuming treatment is to use combined density functional theory (DFT) and non-rquilibrium greens function (NEGF), which treats interaction effects through a local density approximation (LDA) [37], or utilize numerical renormalization group (NRG) in the presence of Kondo effect [199]. We recommend a number of comprehensive references on the topic, for example Refs. [196, 58, 51], to which the reader is referred for further details.

Let us consider a quantum dot regime where the charging energy is the largest energy scale as $E_C \gg \hbar\Gamma > k_B T$, our approach is to assume that the quantum dot can be somewhat qualitatively modeled by a non-interacting case close to the charge-degeneracy

points (Coulomb peaks), as long as V_b remains small. In this case, the currents through a *single* quantum dot energy level can be calculated exactly using Landauer-Büttiker transport theory.

The Hamiltonian for a single level QD with spin-degeneracy is

$$H = H_R + H_{QD} + H_T, \tag{3}$$

$$H_R = \sum_{r=1,2} \sum_{k,\sigma,r} \epsilon_{k,\sigma,r} c^\dagger_{k,\sigma,r} c_{k,\sigma,r}, \tag{4}$$

$$H_{QD} = \sum_{\sigma} \varepsilon_\sigma d^\dagger_\sigma d_\sigma, \tag{5}$$

$$H_T = \sum_{r,\sigma} t_{r,\sigma} d^\dagger_\sigma c_{r,\sigma} + \text{H.c}, \tag{6}$$

where $d^\dagger$ (d) creates (annihilates) an electron on the QD, and $c^\dagger$ (c) are the reservoir counterparts. We define the tunneling rate between the QD and a reservoir as $\Gamma_{r,\sigma} = \frac{2\pi|t_{r,\sigma}|^2\nu_r}{\hbar}$, where from hereon we assume that tunneling is spin independent, that the density of states in a reservoir ν_r is constant over the relevant energy range, and that the QD spin states are degenerate, $\varepsilon_\uparrow = \varepsilon_\downarrow$.

Within the Landauer-Büttiker theory the charge and heat currents through the quantum dot are then calculated using similar expressions as Eq. (1.7) and Eq. (**??**), that we introduced in previous sections for calculating thermoelectric coefficients of 1D, 2D and 3D devices. The only difference is that the transmission of the system should be defined differently. The simplest phenomenological model of nonlinear situations is to take the transmission function for the linear response problem and allow its parameters to depend on the bias and temperature of the reservoirs and gates. For instance, one can assume that the three parameters Γ_l, Γ_r and $\mu(N)$ in Fig. 1.6 depend on the bias and temperatures of reservoirs and gates. In principle, a system could have almost any dependence of these parameters on the bias and temperatures of the reservoirs and gates. Thus, a uniform shift of the bias on all reservoirs and gates by eV should simply shift the transmission.

By plugging Eq. (1.13) as the transmission of the quantum dot, one can evaluate all the thermoelectric coefficients as we developed in the previous section in linear response regime. It is noteworthy that for going beyond the linear response regime, first, the charge and hear current should be calculated using Eqs. (**??**)-(1.7), then the relevant physical

quantities for this study are electrical and thermal conductances which can be obtained by sticking to the general definition for charge and heat conductances as, $G = \frac{dI}{dV}$ and $\kappa = \frac{dQ}{d(\Delta T)}\Big|_{I=0}$.

B Works that not explained in the present thesis

As mentioned in the outline of this thesis, I had a great opportunity to be involved in many projects since the beginning of my PhD at Institut Néel and could establish fruitful collaborations. Unfortunately, Not all of these projects could be fitted to the scope of this thesis. Therefore, I append some outcomes of my joint projects in the following.

B.1 Direct probe of the Seebeck coefficient

NANO LETTERS
Cite This: Nano Lett. 2019, 19, 506−511
Letter
pubs.acs.org/NanoLett

Direct Probe of the Seebeck Coefficient in a Kondo-Correlated Single-Quantum-Dot Transistor

Bivas Dutta,[†] Danial Majidi,[†] Alvaro García Corral,[†] Paolo A. Erdman,[‡] Serge Florens,[†] Theo A. Costi,[§] Hervé Courtois,[†] and Clemens B. Winkelmann*,[†]

[†]Université Grenoble Alpes, CNRS, Grenoble INP*, Institut Néel, 38000 Grenoble, France
[‡]NEST, Scuola Normale Superiore and Istituto Nanoscienze-CNR, 56127 Pisa, Italy
[§]Peter Grünberg Institut, Forschungszentrum Jülich, 52425 Jülich, Germany

Supporting Information

ABSTRACT: We report on the first measurement of the Seebeck coefficient in a tunnel-contacted and gate-tunable individual single-quantum dot junction in the Kondo regime, fabricated using the electromigration technique. This fundamental thermoelectric parameter is obtained by directly monitoring the magnitude of the voltage induced in response to a temperature difference across the junction, while keeping a zero net tunneling current through the device. In contrast to bulk materials and single molecules probed in a scanning tunneling microscopy (STM) configuration, investigating the thermopower in nanoscale electronic transistors benefits from the electric tunability to showcase prominent quantum effects. Here, striking sign changes of the Seebeck coefficient are induced by varying the temperature, depending on the spin configuration in the quantum dot. The comparison with numerical renormalization group (NRG) calculations demonstrates that the tunneling density of states is generically asymmetric around the Fermi level in the leads, both in the cotunneling and Kondo regimes.

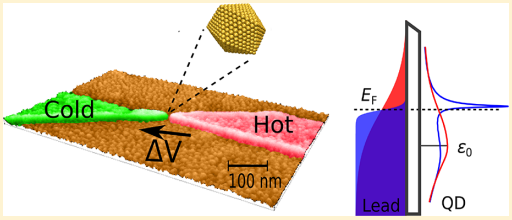

KEYWORDS: *Thermoelectricity, quantum transport, Kondo effect*

Exploring charge and heat transport at the level of single atoms or molecules in contact with voltage and temperature biased reservoirs constitutes the most fundamental probe of energy transfer at the nanoscale.[1,2] While purely electrical conductance measurements in various quantum dot junctions are by now well established, both experimentally and theoretically,[3−5] probing electrical and thermal current in fully controlled nanostructures under temperature gradients still constitutes a great experimental challenge. The two central thermoelectric quantities are the thermal conductance and the thermopower (also known as the Seebeck coefficient). These relate respectively to the heat current and the voltage resulting from a thermal imbalance in reservoirs tunnel-coupled through a nano-object under the condition of zero net electrical current. Both quantities have been investigated at the nanoscale in metallic tunnel contacts[6−9] and in single molecules probed by an STM tip.[10−13] Gate-tunable thermoelectric experiments, allowing to assess and control the electronic structure of individual quantum dots, have been conducted so far essentially using semiconducting structures.[14−17] Conversely, only very few studies in a molecular or nanoparticle transistor geometry have been performed[18,19] and only with limited gate coupling.

The rise in nanofabrication techniques has allowed connecting single quantum dots, small enough to display experimentally reachable level quantization, such as provided by electrostatically defined regions in two-dimensional (2D) electron gases, carbon nanotubes, single molecules and nanoparticles. This progress has led in recent years to quantitative understanding of electronic correlations at the nanoscale.[20−28] Because of the universal and robust nature of Coulomb blockade and Kondo effects in single quantum dot electronic junctions, the full characterization of thermoelectric properties of quantum dots still constitutes a milestone in the field of nanoscale charge and heat transfer, which delineates the central investigation in this Letter. In particular, the Kondo effect is a paradigmatic many-body effect of electrons in bulk metals with magnetic dopants,[29] also taking place in nanostructures in the regime of Coulomb blockade of the charge with an unpaired magnetic moment. Driven by the magnetic exchange interaction between the localized electronic orbital and the conduction electrons near the Fermi level E_F, a hybrid tunneling resonance of width k_BT_K develops at low temperature in the spectral function near E_F due to the entanglement of conduction electrons to the quantum dot electronic degrees of freedom below a characteristic Kondo temperature T_K.

Received: November 1, 2018
Revised: December 14, 2018
Published: December 19, 2018

DOI: 10.1021/acs.nanolett.8b04398
Nano Lett. 2019, 19, 506−511

Nano Letters Letter

Local electrical gating can shift in energy the localized orbital and thus break particle-hole symmetry. This drives strong thermoelectric effects in the tunneling current, associated with spectral asymmetries in the tunneling spectrum. However, in the standard picture of the Kondo resonance, it is schematically assumed that the Kondo peak is pinned exactly at the Fermi level, independently on the depth ε_0 of the localized state. While this picture is approximately true and amply sufficient to understand roughly the temperature dependence of the linear conductance in the Kondo regime, it is in fact totally inadequate for describing the thermopower of quantum dots.[30] For gate voltages close to the middle of odd charge Coulomb diamonds, the Kondo resonance peak energy differs very little from E_F (by much less than k_BT_K) due to nearly complete realization of particle-hole symmetry. In this regime, thermal transport also nearly vanishes due to compensating contributions from electron and hole states. However, this energy shift of the Kondo resonance increases to reach as much as about k_BT_K for gate voltages approaching the mixed valence regime in which the charge on the dot can freely fluctuate and where one can also anticipate enhanced thermoelectric effects (Figure 1d).[31]

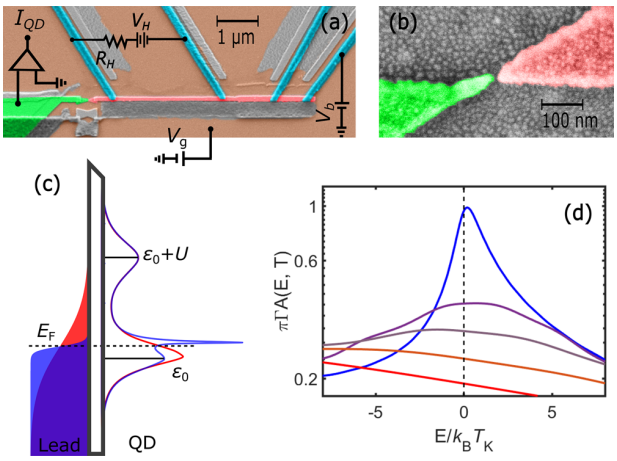

Figure 1. (a) False color scanning electron micrograph of the device, displaying the drain (green) and source (red) contacts to the quantum dot. Four superconducting aluminum leads (cyan) are connected to the source, for heating and biasing the junction. (b) Zoom-in of an electromigrated quantum dot junction between the source and the drain. (c) Sketch of the spectral function of the quantum dot (right) induced by the coupling to the lead (left), both at high (red) and low (blue) temperatures. The Kondo effect arises as a sharp resonance near yet not exactly at the Fermi level E_F at low temperatures. (d) Numerical renormalization group (NRG) calculation on the single level Anderson model with on-site Coulomb interaction U and level position ε_0. Here is shown the junction spectral function $A(E)$ at different temperatures T/T_K = 0.01, 2.8, 5, 10, 20 (from blue to red), for an asymmetric impurity level and a fixed Kondo temperature T_K, showing the spectral offset and asymmetry of the Kondo resonance.

This asymmetry of the Kondo resonance about the Fermi level, along with its strong temperature dependence, are crucial for understanding the low-temperature thermopower of Kondo-correlated quantum dots.[30,32] Although well established in theory,[33] these properties have not been directly observed by experiments to date. This is mainly because parasitic voltage offsets are unavoidable in low-temperature transport experiments, due to the signal amplification chain or thermoelectricity in the wiring, rendering the precise determination of the Fermi level E_F, and thus the relative position of the Kondo peak with respect to E_F, difficult. The situation is different when, in addition to a voltage bias, a temperature bias ΔT can be applied across a junction hosting the Kondo resonance, leading to thermoelectric effects. Experimentally, the Seebeck coefficient (or thermopower) is defined as $S = -V_{Th}/\Delta T$ in the linear regime with V_{Th} the thermovoltage established at zero direct current (dc) flowing. While the low-temperature linear conductance probes the amplitude of the junction spectral function $A(E)$ at E_F, the low-temperature thermopower is related to the spectral function derivative, $S \propto dA/dE|_{E_F}$. More generally, a nonzero Seebeck coefficient in the Kondo state implies that the Kondo resonance must be asymmetric about the Fermi level within a temperature window $\pm k_BT$. Yet, thermoelectric measurements in the presence of Kondo correlations have remained rare to date[34] and have either focused on the mixed valence regime[15] or on measurements of the thermocurrent rather than Seebeck coefficient.[35]

Here, we report on a direct measurement of the Seebeck coefficient from the Coulomb blockade to the Kondo regimes, using combined transport and thermopower measurements in a single quantum dot junction. From the variations of the thermopower with level depth at different temperatures, we experimentally verify two hallmarks of Kondo correlations in thermal transport. First, we report on a Seebeck signal that is breaking the 1e-periodicity with respect to the quantum dot charge state, which gives strong indication for single-spin induced effects on thermoelectric properties. Second, we find sign changes in the thermopower upon increasing temperature for fixed gate voltages in the Kondo-dominated odd-charge diamonds, while no such sign change is observed in the non-Kondo even-charge Coulomb diamonds (for fixed gate voltage). The former reflects the intricate spectral weight rearrangement of the asymmetric Kondo resonance from low to high energies as the Kondo peak is destroyed upon increasing temperature (see Figure 1, as well as Figure S6 in the Supporting Information). These observations are found in good agreement with predictions from NRG calculations on the Anderson model described in ref 30 and further developed in this work.

Our junctions are realized using the electromigration technique, which has been successfully applied for studying the Kondo effect in a variety of single quantum dot systems, such as single molecules and metallic nanoparticles.[26,36,37] Using electron-beam lithography and a three-angle shadow evaporation we fabricate devices such as pictured in Figure 1a on top of a local back gate. After lift-off, inspection, and thus exposure to air, we again evaporate a 1−1.5 nm gold layer over the entire sample surface. Because of its extreme thinness, this layer segregates into a discontinuous film of Au nanoparticles.[38] After cooling to 4.2 K, we form a nanometer-scale gap in the platinum constriction visible in Figure 1b by controlled electromigration. Devices displaying reproducible gate-dependent conductance features are then investigated at temperatures down to 60 mK in a thoroughly filtered dilution cryostat. The transport properties are determined by measuring the junction current I_{QD} as a function of the bias voltage V_b and a gate voltage V_g, applied from a local back gate. One lead of the quantum dot junction, defined as the drain in what follows, rapidly widens away from the electromigration

DOI: 10.1021/acs.nanolett.8b04398
Nano Lett. 2019, 19, 506−511

Nano Letters Letter

constriction, allowing for efficient heat draining on that side. In order to allow the application of a controlled temperature gradient, a normal metallic wire of length 5 μm provides the other contact to the quantum dot junction, called the source. The source side of the junction lead displays four high-transparency superconducting aluminum contacts. These allow for electrically connecting while thermally isolating the source at low enough temperatures. Further, we can heat the source electrons by applying a current between two such leads. In principle, the superconducting transport properties between two nearby leads across the source can also be used for local electron thermometry but due to one missing contact this was not available in this experiment.

Figure 2a,b shows the differential conductance $G = dI_{QD}/dV_b$ map of the device, as a function of bias and gate voltage.

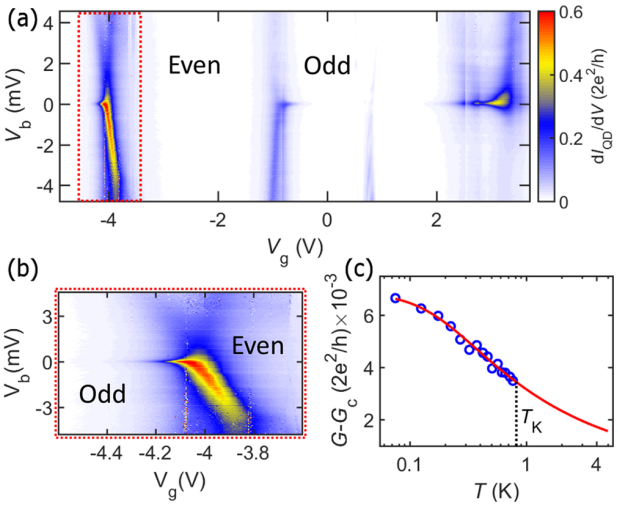

Figure 2. (a) Differential conductance map of the device, measured at base temperature and without applying a thermal gradient. Three high conductance degeneracy points separate Coulomb blockaded regions. Every other Coulomb diamond displays a zero-bias resonance with decreasing intensity when moving away from the degeneracy point. From this, the parity of the electron occupation number can be deduced. Note that the conductance map displays the signature of another quantum dot connected in parallel to the main device, visible near V_g = 0.7 V (see discussion in Section III of the Supporting Information). (b) Zoom-in of the Kondo ridge near V_g = −4.2 V. (c) Temperature dependence of the linear conductance G (minus a constant background value $G_c \simeq 0.004(2e^2/h)$) on the Kondo ridge at V_g = −0.295 V. The line is a fit using a frequently used phenomenological expression,[21] matching well NRG calculations. At this gate voltage, T_K = 820 mK is defined as the temperature at which the conductance peak height is equal to half its zero-temperature value.

Four Coulomb diamonds, separated by the degeneracy points of the quantum dot charge states, can be seen and point to a dot charging energy $U \approx 58$ meV (in notation of the Anderson impurity model introduced below). In the device studied here, a second quantum dot appears as a faint conductance feature near V_g = 0.8 V seen in the global transport map of Figure 2a. It has very different transport characteristics and is discussed in more detail in Section III of the Supporting Information. Notably, the thermopower signal associated with the latter appeared only in a very small gate voltage window, well separated from that of the more strongly coupled quantum dot. The gate voltage region above V_g = 3 V was subject to electrostatic switches, which did not allow accessing quantitatively the full amplitude of the device response in this region. In two nonadjacent Coulomb diamonds of the main device ($V_g < -4.0$ V and $3.5 \text{ V} > V_g > -0.9$ V), a transport resonance near zero bias is observed near the degeneracy points. This points to a Kondo resonance based on the degeneracy of the electronic spin −1/2 doublet in oddly occupied charge states. From the temperature dependence of the resonance amplitude (Figure 2c) we can estimate the value of T_K, which decreases with ε_0 moving toward $-U/2$, that is, for V_g approaching the center of the odd Coulomb diamond.[21] In the differential conductance data, we observe a finite background G_c, which is constant both with V_b and T. We attribute this to parallel direct tunneling between the contacts, owing to the narrowness of the crack separating electromigrated leads, as is frequently observed in single QD junctions. Because this background conductance is ohmic, it does not contribute to the thermopower.

The peak conductance of the Kondo resonance saturates at values $<0.012 \times (2e^2/h)$ in the low temperature limit, from which we can infer that the quantum dot is rather asymmetrically tunnel coupled.[39] This asymmetry simplifies the theoretical description, as Kondo correlations can be considered as occurring in equilibrium with the more strongly coupled lead, the other lead acting only as weak probe. In this study, this strongly coupled lead will thus also serve as the only reference for the Fermi level, near which the Kondo resonance develops. The tunnel coupling on the strongly coupled side, $\Gamma \approx 2.6$ meV, can be determined from the widths of the Coulomb diamond edges (see ref 40 for details pertaining to effects related to the charge parity on the quantum dot that we have taken into account). As opposed to most experiments based on semiconducting systems, neither the quantum dot nor the tunnel barriers are electrostatically defined here. Thus, Γ is essentially independent of the gate voltage here, which simplifies the theoretical comparison.

We now move to the thermoelectric response of the device. We have performed thermoelectric experiments by providing a constant heating power to the source island, leading to three device temperatures, labeled $T_{low} < T_{mid} < T_{high}$. The lowest temperature T_{low} is in the range of a 300 mK, whereas T_{high} is close to 4.4 K, and T_{mid} is around 1.5 K. Details of the estimation of these temperatures is given in Section III of the Supporting Information. Measuring the thermopower of a quantum dot junction requires in principle to address the open-circuit voltage of a high-impedance device. This is experimentally challenging, first because the voltmeter itself may shunt the divergent impedance of the device and, second, because the equilibration time to reach the true zero-current state (as required by the definition of the Seebeck coefficient S) at such high impedances can be extremely long. For this reason, several experiments have preferred focusing on the thermocurrent at zero applied bias rather than on the Seebeck coefficient, although only the latter has a direct physical interpretation as a fundamental transport coefficient. In our measurements, we sweep for each gate voltage value the bias voltage and measure the full $I_{QD}(V_b)$ characteristic (Figure 3). From thereon, we can define $-V_{Th}$ as the bias voltage at which the current goes through zero, realizing thus perfect open-circuit conditions.[41] An overall constant offset of the bias of order 100 μV can be caused by amplifier offsets, thermoelectricity in the cabling, and a potential drop inside the source island due to the heating current. This offset is subtracted from

DOI: 10.1021/acs.nanolett.8b04398
Nano Lett. 2019, 19, 506−511

Nano Letters Letter

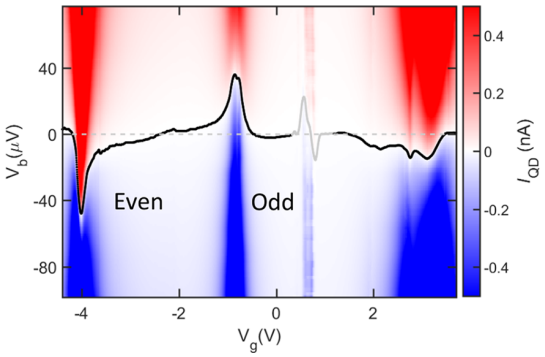

Figure 3. Current map for small applied biases in the presence of a temperature gradient at intermediate temperature $T_{mid} \simeq 1.5$ K. The black line follows the points of vanishing current; it is thus equal to $-V_{Th}$. The thermoresponse at about $V_g = 0.7$ V, associated with the second, weakly coupled quantum dot, is grayed out for better readability.

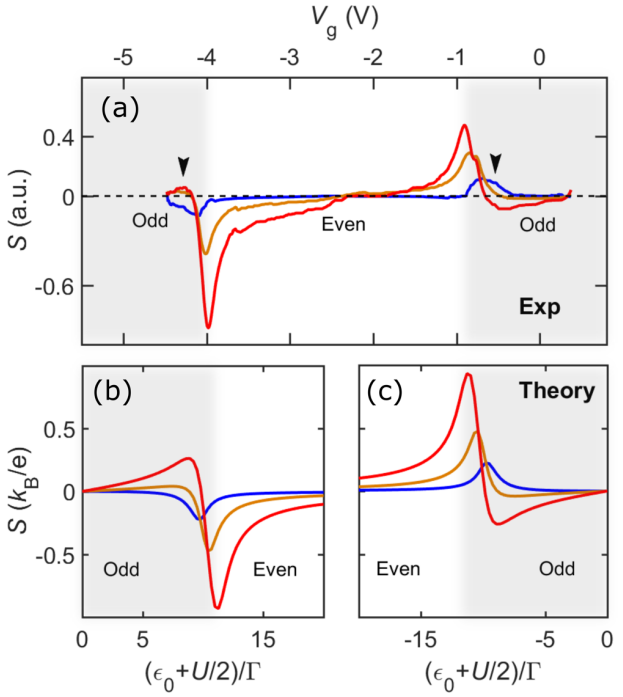

Figure 4. (a) Experimental thermopower $S = -V_{Th}/\Delta T$ at the three experimental device temperatures $T_{low} = 300$ mK $= 0.01\Gamma$ (blue), $T_{mid} = 1.5$ K $= 0.05\Gamma$ (orange), and $T_{high} = 4.4$ K $= 0.14\Gamma$ (red). The arrows highlight the level depths in the Kondo regime near which the thermopower changes sign at a temperature $T_1 \approx \Gamma/(10k_B)$. (b,c) Corresponding NRG calculation using experimental parameters $U = 58$ meV, $\Gamma = 2.6$ meV and for the same set of temperatures T/Γ (with the same color code). The calculation assumes a single orbital level, predicting therefore correctly $S = 0$ in the center of an oddly occupied Coulomb diamond ($\epsilon_0 + U/2 = 0$). For the sake of comparison with the experimental data, the calculations at negative $\epsilon_0 + U/2$ are placed to the right-hand panel. Neglecting higher orbital levels in the NRG calculation does not allow to map the complete transition region in the center of the even diamond so that the theoretical comparison is done using two disjointed panels.

V_b such that $V_{Th} = 0$ in the center of the evenly occupied diamond. The result is shown as the black line on the same figure. Strikingly, the thermovoltage changes sign at consecutive integer charge states, resulting in a $2e$-periodicity of the thermopower response, that directly follows from the presence of Kondo anomalies in odd charge diamonds. In more detail, the $2e$-periodicity reflects the fact that the junction spectral function has its maximal weight alternating above and below the Fermi level depending on if the level depth ϵ_0 of the doublet spin state is either approaching E_F from below (in which case the dot transits from single to zero occupancy in the active orbital), or $E_F - U$ from above (in which case the highest occupied electronic orbital starts to become singly occupied and develops the next Kondo ridge).

While this $2e$-periodic response of thermopower with the quantum dot charge state is in good agreement with what is expected for the Kondo effect, it is not by itself a proof thereof. Indeed, in a quantum description of the level hybridization, the inclusion of the electron spin degree of freedom leads to a doubling of the spectral function width when the charge states changes parity,[40] breaking thus the $1e$ periodicity naively expected from a sequential or cotunneling description neglecting the spin.[42,43]

A much more characteristic signature of the singlet nature of the Kondo state resides in multiple sign changes of the thermopower as a function of gate voltage, occurring both in the center of Coulomb-blockaded even and odd charge states, but also at the onset of the Kondo regime within the odd charge diamond. This Kondo-related sign change takes place as temperature is increased from below to above a characteristic temperature T_1, which is a weak function of gate voltage in the Kondo regime (see Figure S5 of the Supporting Information and ref 30). The other Coulomb-related sign changes are temperature independent and occur when the bare quantum dot energy level is such that $\epsilon_0 + U/2 = 0$ (for a single orbital model). In Figure 4a, we show the gate traces of the Seebeck coefficient of the same device at different temperatures. At the lowest temperature T_{low} (such that $k_B T_{low}/\Gamma < 0.015$), the thermopower inside the Kondo-correlated Coulomb diamonds (for $V_g < -4.1$ V and $V_g > -0.9$ V) has a markedly different behavior with respect to the higher temperature data, confirming this sign change.

Our data can be compared with NRG predictions[30] of the Seebeck coefficient of a quantum dot with the parameter value $U/\Gamma \simeq 22$ taken from the experiment. The simulations are performed within a two-leads single orbital Anderson impurity model with Hamiltonian

$$H = \sum_{\sigma} \epsilon_0 d_\sigma^\dagger d_\sigma + U d_\uparrow^\dagger d_\uparrow d_\downarrow^\dagger d_\downarrow + \sum_{k\alpha\sigma} \epsilon_{k\sigma} c_{k\alpha\sigma}^\dagger c_{k\alpha\sigma} + \sum_{k\alpha\sigma} t_\alpha (c_{k\alpha\sigma}^\dagger d_\sigma + H.c.) \quad (1)$$

The first term describes the quantum dot level energy ϵ_0 (measured relative to the Fermi level E_F, which is set to zero in our calculations). The dot level is controlled in the experiment with the gate voltage V_g. The second term with charging energy U is the local Coulomb repulsion on the dot. The third term describes the Fermi sea in the reservoirs, where $\alpha = L,R$ labels the two contacts, and $\epsilon_{k\sigma}$ is the kinetic energy of the lead electrons. The last term describes the tunneling of electrons from the leads onto and off the dot with tunneling amplitudes t_α. By using even and odd combinations of lead electron states, the odd channel decouples, resulting in a single-channel Anderson model with an effective tunnel matrix element t given by $t^2 = t_L^2 + t_R^2$. The hybridization is then characterized by

DOI: 10.1021/acs.nanolett.8b04398
Nano Lett. 2019, 19, 506−511

the lead-dot tunneling rate $\Gamma = 2\pi N_F t^2$ with N_F the lead electron density of states at the Fermi level.

The conductance $G(T)$ and thermopower $S(T)$ of the Anderson model (1) can be written in terms of the zeroth, $I_0(T)$, and first, $I_1(T)$, moments of the NRG impurity spectral function $A(E,T)$ within the Fermi temperature window

$$G(T) = G_0 I_0(T) \tag{2}$$

$$S(T) = -\frac{1}{|e|T}\frac{I_1(T)}{I_0(T)} \tag{3}$$

$$I_n(T) = \int_{-\infty}^{+\infty} -\frac{\partial f(E,T)}{\partial E} E^n A(E,T)\mathrm{d}E \tag{4}$$

where G_0 is the zero temperature conductance at midvalley and $f(E,T)$ is the Fermi distribution of the leads at temperature T. In this formalism, the spectral function defined above plays an analogue role to the energy-dependent transmission $\mathcal{T}(E)$ in the Landauer picture. The latter is an appropriate tool for describing quantum transport in the absence of interactions, whereas the spectral function picture is better adapted to accounting for interactions.

The above expression for $S(T)$ implies that a sign change in the thermopower occurs due to a crossover between the negative (electron-like) and positive (hole-like) energy contributions of the first moment of the spectral function in the Fermi temperature window $-k_BT < E < +k_BT$. At particle-hole symmetric points, such as for perfect integer fillings, for example, exactly in the middle of even or odd Coulomb diamonds, the spectral function $A(E,T)$ is symmetric about E_F, so that $S(T)$ vanishes identically. The calculated thermopower is plotted in Figure 4b,c as a function of the dimensionless gate voltage $(\epsilon_0 + U/2)/\Gamma$, so that the center of the odd charge Coulomb diamond at $\epsilon_0 = -U/2$ is clearly identified by a trivially vanishing Seebeck coefficient at that point for any temperature (due to exact particle-hole symmetry). Strikingly, the thermopower anomaly seen near the mixed valence regime presents two distinct regimes: at low temperature, a small thermoelectric signal occurs with a fixed sign, whereas at high temperature a larger signal displays a clear sign change as a function of gate voltage, defining a crossover temperature T_1. These predictions compare favorably with the experimental data in Figure 4a, where the gate-dependent signal shows the same sign inversion at temperatures $k_BT_1/\Gamma \approx 0.1$, depending slightly on the gate voltage (see Figure S5 of Supporting Information). If the experimental values of ΔT are assumed to be 0.14, 1.0, and 0.4 K, respectively (from blue to red) in the thermopower measurements, the arbitrary units (a.u.) scale of the experimental Y-axis are to be read in units of k_B/e, leading to quantitative agreement with theory. One can note here that the two data sets at T_{low} and T_{mid} are then not quite in the linear response regime $\Delta T \ll T$, which however does not qualitatively affect the thermopower as long as ΔT is not much larger than T_K. We note that, ultimately, the sign change of the Seebeck coefficient S upon increasing temperature from $T < T_1$ to $T > T_1 > T_K$ reflects the spectral weight rearrangement of the asymmetrically located Kondo resonance about E_F (see Figure 1d, and Section IV−C of the Supporting Information for details).

In conclusion, this work provides a direct measurement of the Seebeck coefficient for a Kondo-correlated single quantum dot tunnel coupled to purely thermal-biased reservoirs. In particular, our measurements bring compelling experimental evidence for a frequently overseen property of the Kondo effect occurring between a spin-degenerate local level and an electron reservoir. By measuring the temperature and gate dependence of the Seebeck coefficient in a single quantum dot junction, we find that it exhibits characteristic sign changes in the Kondo regime upon increasing temperature, which reflect the strong temperature dependence of the Kondo peak that is not exactly pinned at the reservoir Fermi level, as predicted by theory. This work finally demonstrates that electromigrated single quantum dot junctions can now be integrated into more complex circuits, including local electronic heaters and thermometers. This development paves the way for precisely accessing the thermoelectric figure of merit of individual molecules, which requires measuring simultaneously the charge and heat conductance as well as the thermopower, for a large spectrum of molecular devices.

■ ASSOCIATED CONTENT

Supporting Information

The Supporting Information is available free of charge on the ACS Publications website at DOI: 10.1021/acs.nanolett.8b04398.

Sample fabrication process, the electrical characterization of the Kondo-correlated quantum dot, the determination of average temperatures of the device under heating conditions, and an outline of the theory of the thermoelectric properties of Kondo correlated quantum dots, which is relevant to the present paper. NRG calculations provide also new insights and detailed analysis on the thermopower of these systems (PDF)

■ AUTHOR INFORMATION

Corresponding Author

*E-mail: clemens.winkelmann@neel.cnrs.fr.

ORCID

Bivas Dutta: 0000-0002-5354-3426

Clemens B. Winkelmann: 0000-0003-4320-994X

Notes

The authors declare no competing financial interest.

■ ACKNOWLEDGMENTS

This work has received funding from the European Union's Horizon 2020 research and innovation programme under the Marie Skłodowska-Curie Grant Agreement 766025. B.D. acknowledges support from the Nanosciences Foundation under the auspices of the Université Grenoble Alpes Foundation. The samples were realized at the Nanofab platform at Institut Néel with extensive help from T. Crozes. We are deeply indebted to F. Taddei for theoretical guidance about the cotunneling analysis of the thermovoltage. Supercomputer support by the John von Neumann Institute for Computing (Jülich) is gratefully acknowledged. We further acknowledge inspiring discussions with N. Roch and J. Pekola.

■ REFERENCES

(1) Bergfield, J. P.; Ratner, M. A. Forty years of molecular electronics: Non-equilibrium heat and charge transport at the nanoscale. *Phys. Status Solidi B* **2013**, *250*, 2249−2266.

(2) Thoss, M.; Evers, F. Perspective: Theory of quantum transport in molecular junctions. *J. Chem. Phys.* **2018**, *148*, 030901.

(3) Pustilnik, M.; Glazman, L. Kondo effect in quantum dots. *J. Phys.: Condens. Matter* **2004**, *16*, R513.

DOI: 10.1021/acs.nanolett.8b04398
Nano Lett. 2019, 19, 506−511

(4) Grobis, M.; Rau, I. M.; Potok, R. M.; Goldhaber-Gordon, D. Kondo effect in mesoscopic quantum dots. In *Handbook of Magnetism and Magnetic Materials*; Wiley, 2007; Vol. 2.
(5) Bulla, R.; Costi, T. A.; Pruschke, T. Numerical renormalization group method for quantum impurity systems. *Rev. Mod. Phys.* **2008**, *80*, 395−450.
(6) Schwab, K.; Henriksen, E. A.; Worlock, J. M.; Roukes, M. L. Measurement of the quantum of thermal conductance. *Nature* **2000**, *404*, 974−977.
(7) Meschke, M.; Guichard, W.; Pekola, J. P. Single-mode heat conduction by photons. *Nature* **2006**, *444*, 187−190.
(8) Jézouin, S.; Parmentier, F. D.; Anthore, A.; Gennser, U.; Cavanna, A.; Jin, Y.; Pierre, F. Quantum Limit of Heat Flow Across a Single Electronic Channel. *Science* **2013**, *342*, 601−604.
(9) Dutta, B.; Peltonen, J.; Antonenko, D.; Meschke, M.; Skvortsov, M.; Kubala, B.; König, J.; Winkelmann, C. B.; Courtois, H.; Pekola, J. Thermal conductance of a single-electron transistor. *Phys. Rev. Lett.* **2017**, *119*, 077701.
(10) Reddy, P.; Yang, S.; Segalman, R.; Majumdar, A. Thermoelectricity in molecular junctions. *Science* **2007**, *315*, 1568.
(11) Widawsky, J. R.; Darancet, P.; Neaton, J. B.; Venkataraman, L. Simultaneous determination of conductance and thermopower of single molecule junctions. *Nano Lett.* **2012**, *12*, 354−358.
(12) Evangeli, C.; Matt, M.; Rincon-Garcia, L.; Pauly, F.; Nielaba, P.; Rubio-Bollinger, G.; Cuevas, J. C.; Agrait, N. Quantum Thermopower of Metallic Atomic-Size Contacts at Room Temperature. *Nano Lett.* **2015**, *15*, 1006−1011.
(13) Cui, L.; Miao, R.; Wang, K.; Thompson, D.; Zotti, L. A.; Cuevas, J. C.; Meyhofer, E.; Reddy, P. Peltier cooling in molecular junctions. *Nat. Nanotechnol.* **2018**, *13*, 122.
(14) Staring, A.; Molenkamp, L.; Alphenaar, B.; Van Houten, H.; Buyk, O.; Mabesoone, M.; Beenakker, C.; Foxon, C. Coulomb-blockade oscillations in the thermopower of a quantum dot. *EPL (Europhys. Lett.)* **1993**, *22*, 57.
(15) Scheibner, R.; Buhmann, H.; Reuter, D.; Kiselev, M.; Molenkamp, L. Thermopower of a Kondo spin-correlated quantum dot. *Phys. Rev. Lett.* **2005**, *95*, 176602.
(16) Svensson, S. F.; Hoffmann, E. A.; Nakpathomkun, N.; Wu, P. M.; Xu, H.; Nilsson, H. A.; Sánchez, D.; Kashcheyevs, V.; Linke, H. Nonlinear thermovoltage and thermocurrent in quantum dots. *New J. Phys.* **2013**, *15*, 105011.
(17) Josefsson, M.; Svilans, A.; Burke, A. M.; Hoffmann, E. A.; Fahlvik, S.; Thelander, C.; Leijnse, M.; Linke, H. A quantum-dot heat engine operating close to the thermodynamic efficiency limits. *Nat. Nanotechnol.* **2018**, *13*, 920.
(18) Kim, Y.; Jeong, W.; Kim, K.; Lee, W.; Reddy, P. Electrostatic control of thermoelectricity in molecular junctions. *Nat. Nanotechnol.* **2014**, *9*, 881.
(19) Gehring, P.; Harzheim, A.; Spiece, J.; Sheng, Y.; Rogers, G.; Evangeli, C.; Mishra, A.; Robinson, B. J.; Porfyrakis, K.; Warner, J. H. Field-Effect Control of Graphene−Fullerene Thermoelectric Nanodevices. *Nano Lett.* **2017**, *17*, 7055−7061.
(20) Glazman, L.; Raikh, M. Resonant Kondo transparency of a barrier with quasilocal impurity states. *JETP Lett.* **1988**, *47*, 452−455.
(21) Goldhaber-Gordon, D.; Shtrikman, H.; Mahalu, D.; Abusch-Magder, D.; Meirav, U.; Kastner, M. Kondo effect in a single-electron transistor. *Nature* **1998**, *391*, 156.
(22) Cronenwett, S. M.; Oosterkamp, T. H.; Kouwenhoven, L. P. A tunable Kondo effect in quantum dots. *Science* **1998**, *281*, 540−544.
(23) Pustilnik, M.; Glazman, L. Kondo effect in real quantum dots. *Phys. Rev. Lett.* **2001**, *87*, 216601.
(24) Sasaki, S.; De Franceschi, S.; Elzerman, J.; Van der Wiel, W.; Eto, M.; Tarucha, S.; Kouwenhoven, L. Kondo effect in an integer-spin quantum dot. *Nature* **2000**, *405*, 764.
(25) Yu, L. H.; Natelson, D. The Kondo effect in C60 single-molecule transistors. *Nano Lett.* **2004**, *4*, 79−83.
(26) Roch, N.; Florens, S.; Bouchiat, V.; Wernsdorfer, W.; Balestro, F. Quantum phase transition in a single-molecule quantum dot. *Nature* **2008**, *453*, 633.
(27) Iftikhar, Z.; Anthore, A.; Mitchell, A.; Parmentier, F.; Gennser, U.; Ouerghi, A.; Cavanna, A.; Mora, C.; Simon, P.; Pierre, F. Tunable quantum criticality and super-ballistic transport in a charge Kondo circuit. *Science* **2018**, *360*, No. 1315.
(28) Frisenda, R.; Gaudenzi, R.; Franco, C.; Mas-Torrent, M.; Rovira, C.; Veciana, J.; Alcon, I.; Bromley, S. T.; Burzurí, E.; Van der Zant, H. S. Kondo effect in a neutral and stable all organic radical single molecule break junction. *Nano Lett.* **2015**, *15*, 3109−3114.
(29) Kondo, J. Resistance minimum in dilute magnetic alloys. *Prog. Theor. Phys.* **1964**, *32*, 37−49.
(30) Costi, T.; Zlatić, V. Thermoelectric transport through strongly correlated quantum dots. *Phys. Rev. B: Condens. Matter Mater. Phys.* **2010**, *81*, 235127.
(31) Dong, B.; Lei, X. Effect of the Kondo correlation on the thermopower in a quantum dot. *J. Phys.: Condens. Matter* **2002**, *14*, 11747.
(32) Costi, T.; Hewson, A.; Zlatic, V. Transport coefficients of the Anderson model via the numerical renormalization group. *J. Phys.: Condens. Matter* **1994**, *6*, 2519.
(33) Hewson, A. C. *The Kondo problem to heavy fermions*; Cambridge University Press, 1997; Vol. 2.
(34) Thierschmann, H. Ph.D. thesis, University of Würzburg, 2014.
(35) Svilans, A.; Josefsson, M.; Burke, A. M.; Fahlvik, S.; Thelander, C.; Linke, H.; Leijnse, M. Thermoelectric characterization of the Kondo resonance in nanowire quantum dots. *Phys. Rev. Lett.* **2018**, *121*, 206801.
(36) Park, J.; Pasupathy, A. N.; Goldsmith, J. I.; Chang, C.; Yaish, Y.; Petta, J. R.; Rinkoski, M.; Sethna, J. P.; Abruña, H. D.; McEuen, P. L. Coulomb blockade and the Kondo effect in single-atom transistors. *Nature* **2002**, *417*, 722.
(37) Liang, W.; Shores, M. P.; Bockrath, M.; Long, J. R.; Park, H. Kondo resonance in a single-molecule transistor. *Nature* **2002**, *417*, 725.
(38) Bolotin, K.; Kuemmeth, F.; Pasupathy, A.; Ralph, D. Metal-nanoparticle single-electron transistors fabricated using electromigration. *Appl. Phys. Lett.* **2004**, *84*, 3154−3156.
(39) Simmel, F.; Blick, R.; Kotthaus, J.; Wegscheider, W.; Bichler, M. Anomalous Kondo effect in a quantum dot at nonzero bias. *Phys. Rev. Lett.* **1999**, *83*, 804.
(40) Aligia, A.; Roura-Bas, P.; Florens, S. Impact of capacitance and tunneling asymmetries on Coulomb blockade edges and Kondo peaks in nonequilibrium transport through molecular quantum dots. *Phys. Rev. B: Condens. Matter Mater. Phys.* **2015**, *92*, 035404.
(41) Evangeli, C.; Gillemot, K.; Leary, E.; Gonzalez, M. T.; Rubio-Bollinger, G.; Lambert, C. J.; Agraït, N. Engineering the thermopower of C_{60} molecular junctions. *Nano Lett.* **2013**, *13*, 2141−2145.
(42) Beenakker, C.; Staring, A. Theory of the thermopower of a quantum dot. *Phys. Rev. B: Condens. Matter Mater. Phys.* **1992**, *46*, 9667.
(43) Turek, M.; Matveev, K. Cotunneling thermopower of single electron transistors. *Phys. Rev. B: Condens. Matter Mater. Phys.* **2002**, *65*, 115332.

DOI: 10.1021/acs.nanolett.8b04398
Nano Lett. 2019, 19, 506−511

B.2 Nb three-terminal device

Journal Name

ARTICLE TYPE

Cite this: DOI: 00.0000/xxxxxxxxxx

Targeted modifications of monolithic multiterminal superconducting weak-links†

Simon Collienne,[a] Danial Majidi,[b] Joris Van de Vondel,[c] Clemens B. Winkelmann,[b] and Alejandro V. Silhanek [a]

Received Date
Accepted Date

DOI: 00.0000/xxxxxxxxxx

In a multi-branch metallic interconnect we demonstrate the possibility to induce targeted modifications of the material properties by properly selecting the intensity and polarity of the applied current. We illustrate this effect in Y-shape multiterminal devices made of Nb on sapphire for which we show that superconducting critical current can be lowered in a controlled manner in a preselected junction. We further observe the gradual appearance of Fraunhofer-like critical current oscillations with magnetic field which indicates the gradual modification of a superconducting weak link. This method permits progressive modifications of a hand-picked junction without affecting the neighboring terminals. The proposed approach has the benefit of being inexpensive and requiring conventional electronics. This technique represents a major step toward all-electric control of multiterminal Josephson junctions.

1 Introduction

Nanoscale metallic multiterminal interconnects represent an ubiquitous layout in low dimensional electronic devices. On the technological side, for instance, on-chip power distribution networks and interconnects in clock grids normally involve multi-branched metal segments[1,2]. The conventional and widely implemented four-probe and Hall electrical transport measurement configuration is yet another example where several voltage and current probes branch out from a transport bridge. Arguably, the most fervent interest on multiterminal devices can be found in superconducting electronics. In this context, a three-terminal device, so-called yTron, has been proposed as a sensor and readout of current-flow in a superconductor[3] whereas tunable superconducting weak links have been realized by injecting a normal current into the junction[4–14].

More recently, substantial theoretical[15–18] and experimental[19–23] efforts have been devoted to the investigation of multiterminal Josephson junctions, in part fueled by the possibility of developing topological Andreev bands in systems composed by multiple superconducting leads coupled through a central normal scattering region. Typically these devices require involved fabrication procedures (overlay lithography, shadow evaporation, multilayers, etc.) and although tunability of the junction properties has been demonstrated via gating, it would require significant further effort to control each individual junction separately. Therefore, developing new approaches with high efficiency and accurate tunability of individual junctions have a promising potential in superconductor science and technology.

In this work, we report on a simple and yet powerful electroannealing (EA) technique to induce selective modification of conducting and superconducting multiterminal junctions by applying high electrical current density. A scanning electron microscopy (SEM) image of a representative device is shown in Fig. 1(a,b) (see ESI† for fabrication details). The voltage contacts are placed at about 1.2 μm away from the constrictions. In the electroannealing process, a bias voltage across the device is slowly swept up while simultaneously monitoring the increase of resistance until reaching a pre-established value. Sudden increases of resistance leading to thermal runaway and eventually sample destruction are avoided by a reactive feedback loop[24]. Unlike electromigration[25], EA is mainly driven (but not only) by the Joule heating produced by high current densities only achievable in refractory materials such as Nb. We have recently reported the successful implementation of this approach[26] for producing targeted modifications of the superconducting properties in bowtie Nb nanoconstrictions. In this work, this procedure is extended to three constrictions following the protocol described in Ref.[24]. Fig. 1(c) shows a typical evolution of the resistance measured between voltage pads 1-3 during the EA process. This curve exhibits an initial parabolic shape at low currents corresponding to Joule heating, followed by a sharp irreversible increase of resistance

[a] Experimental Physics of Nanostructured Materials, Q-MAT, CESAM, Université de Liège, B-4000 Sart Tilman, Belgium
[b] Univ. Grenoble Alpes, CNRS, Grenoble INP, Institut Néel, 38000 Grenoble, France
[a] Quantum Solid-State Physics, Department of Physics and Astronomy, KU Leuven, Celestijnenlaan 200D, B-3001 Leuven, Belgium

† Electronic Supplementary Information (ESI) available. See DOI: 00.0000/00000000.

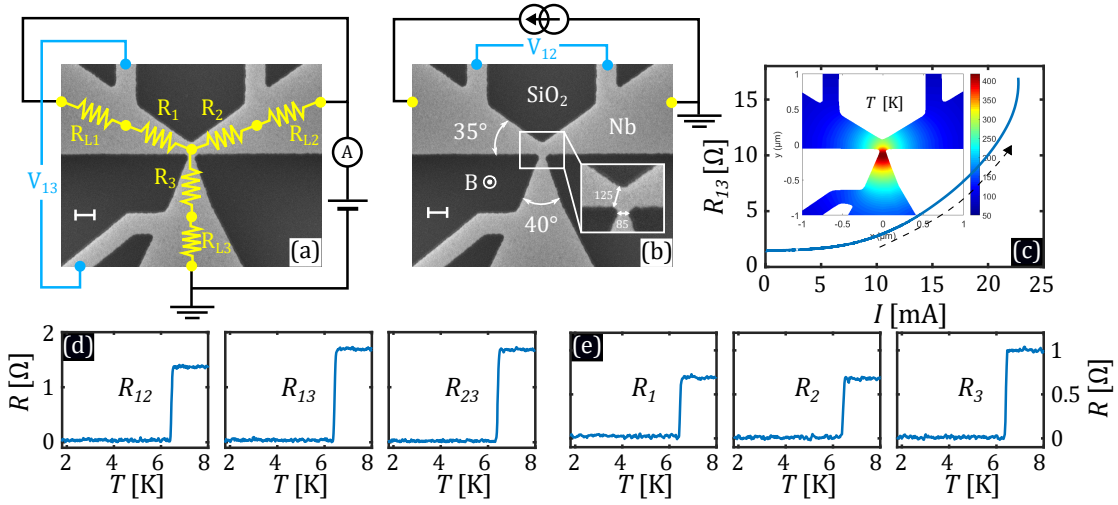

Fig. 1 SEM image of the pristine Nb three-terminal device (a,b). The white scale bar corresponds to 200 nm. As an example, the electrical connections to performed controlled EA of junction 3 is shown in panel (a) along with the star-shape equivalent lump circuit represented in yellow color. The resistances R_i are affected during the EA whereas the resistance R_{Li} of the leads remains unaffected. Panel (b) shows the configuration to measure the electrical response of junction formed by the terminals 1 and 2. The inset in panel (b) is a zoom in at the center of the device where the width of the junctions are given in nm. A representative resistance evolution during an EA process at 10 K is shown in panel (c). The inset in panel (c) shows the temperature distribution simulation for an intermediate current value 13 mA whose applied polarities lead to a localized temperature peak in the junction traversed by the highest current density. Panel (d) shows the actual measured temperature dependence of the resistance between two voltage contacts and panel (e) shows the calculated resistance of each junction.

at high currents. After the bias voltage is set off, the addressed contact exhibits a resistance higher than the initial state. In three-terminal device we demonstrate the possibility to increase locally the resistance while simultaneously decreasing the critical current of a predefined junction without affecting the neighboring terminals. In this way, we are able to induce Fraunhofer-like critical current oscillation as a function of magnetic field in the selected junction. In other words, this technique permits to transform superconducting contacts in an otherwise monolithic sample into Josephson junctions by creating weak-links[27,28] without the need to invoke complex multi-step fabrication processing. A somewhat similar method coined electroburning has been implemented to generate nano-gaps in a graphene three-terminal single-electron transistor[29].

2 Results

A unique advantage of multiterminal junctions with respect to a single junction[26] is the possibility to deduce the resistance of each individual junction to the central node. Indeed, the total resistance R_{ij} between two voltage contacts i and j, with $i,j=1,2,3$ and $i\neq j$, can be considered as resulting from the resistance R_i associated to the zone between voltage contact i and the central point where the three terminals converge, plus the resistance R_j corresponding to the segment between the central point and voltage contact j. The equivalent lump circuit is illustrated in Fig. 1(a). The relation $R_{ij}=R_i+R_j$ represents a linear system of three equations with three unknowns which can be inverted to isolate each individual R_i. Note that the EA process does not modify the entire branch between the corresponding voltage contact and the central point, but rather a small region next to the central point where the current crowding leads to a high local temperature as confirmed by finite elements modelling (inset of Fig. 1(c), see ESI†). As a first approximation, one can assume that the individual resistance R_i is inversely proportional to the width of the junction i. This approximation is more accurate if the opening angle of each branch is large. Fig. 1(d) shows the measured resistances R_{ij} as a function of temperature around the superconducting transition $T_c=6.4$ K. Note that $R_{13}=R_{23}>R_{12}$ which is consistent with a mirror symmetric structure with a narrower junction 3, as shown in the scanning microscopy image of Fig. 1(b). In Fig. 1(e) we show the calculated resistances R_i corresponding to each junction confirming that $R_1=R_2<R_3$. Moreover, $R_3/R_1\sim 1.42$ which is close to the ratio of constriction widths $w_1/w_3\sim 1.47$.

Let us now explore the possibility to modify via EA process a predefined constriction, without affecting the other two neighboring terminals. In order to target junction i we ground the corresponding junction and feed the current from the remaining two. It is worth mentioning here that the polarity of the bias current plays a crucial role since it determines on which side of the constriction the material modification will take place (see atomic force microscopy experiment in the ESI†). Subsequently we measure $R_{ij}(T)$ and calculate the individual junction resistances $R_i(T)$. A selected set of these measurements are sum-

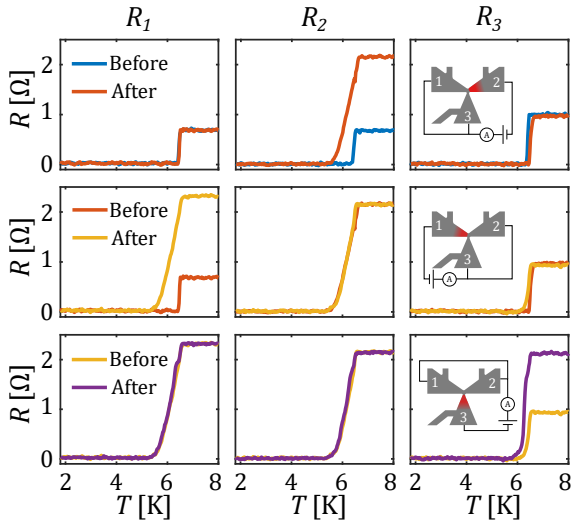

Fig. 2 Temperature dependence of the resistance associated to junction 1 (left column), junction 2 (middle column) and junction 3 (left column) before and after EA. In the upper, middle and lower rows, junctions 2, 1 and 3 have been respectively targeted using the circuits shown in the corresponding insets. In the upper row, the blue lines correspond to the pristine sample response. These curves have been measured with a bias current of 1 μA RMS at zero magnetic field.

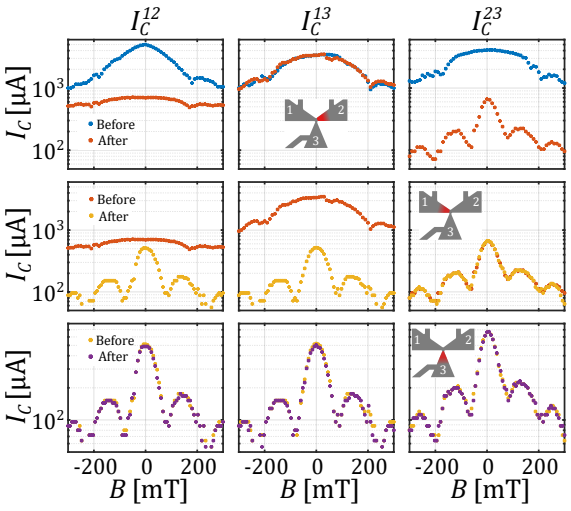

Fig. 3 Field-dependent critical currents obtained at 1.8 K through the junctions 1-2 (leftmost column), junctions 1-3 (central column) and junctions 2-3 (rightmost column) before and after EA. In the upper row, the blue dots correspond to the pristine sample and the red dots to the response after junction 2 has been modified by EA. In the middle row, junction 1 is addressed whereas in the lower row it is the junction 3 which is modified.

marized in Fig. 2. The electric circuit used to electroanneal each of the three junctions is shown as inset in the rightmost column whereas each column shows the computed junction resistance $R_i(T)$ before and after modification by EA. We proceed chronologically, first modifying constriction 2 (upper row) up to more than doubling its resistance while junctions 1 and 3 remain intact. Then, in a next step, we aim to junction 1 on the same device (middle row). Finally, junction 3 is targeted (lower row) to achieve a final state in which the three junctions exhibit similar resistance values.

As we mentioned above, it is the opening angle of each branch which determines the spatial extent to the electroannealed region. In this particular study, we have purposely designed each branch with angles larger than 30° in such a way to guarantee modifications of the structure in a narrow region thus permitting phase coherent transport through the so created weak link[27,28]. This effect is unambiguously demonstrated by measuring the critical current I_c^{ij} between two neighboring voltage probes as a function of the magnetic field B applied normal to the plane of the device. In Fig. 3 we show the resulting $I_c^{ij}(B)$ curves, obtained with a 10 μV criterion at 1.8 K, for the same states described in Fig. 2. The blue datapoints in the upper row correspond to the pristine sample. Note that the zero-field critical current is larger for the I_{12} connection suggesting that the narrowest junction 3 limits the maximum critical current compared to the other two junctions.

Interestingly, all three curves show oscillations with a period $\Delta B \sim 190$ mT which could be associated to one flux quantum in a junction area of 0.0109 μm^2 which is more than double the area of the central isosceles triangle formed by the converging terminals. This discrepancy is not surprising as already discussed in Ref.[26]. After modifying junction 2 (red data points), I_c^{13} remains invariant as expected, whereas both I_c^{12} and I_c^{23} decrease in amplitude. More importantly, the oscillation period in $I_c^{23}(B)$ is substantially reduced which could be associated to an increase of the effective junction area after EA. The fact that a modification of R_2 affects differently I_c^{12} and I_c^{23} is puzzling.

The middle row in Fig. 3 shows the evolution of the critical current when junction 1 is modified. In this case, I_c^{23} remains unchanged, whereas I_c^{12} and I_c^{13} decrease in amplitude and develop Fraunhofer-like oscillations[30]. In the lower row of Fig. 3, the EA of junction 3 does not lead to discernable changes in any of the critical currents thus indicating that the critical current remains dominated by the weaker links of junctions 1 and 2.

As we pointed out above, for the sake of clarity in Fig. 2 and 3 we have presented a selected set of three EA processes out of an ensemble of eight EA steps. The upper row of Fig. 4 shows the normal state resistance $R_N = R(10\text{ K} > T_c)$ and the superconducting critical temperature T_c of each of the junctions as a function of the EA step (EA#). The R_N (blue symbols) shown in the upper row demonstrate full control of the targeted junction following the order EA1-EA2 junction 2 → EA3-EA4 junction 1 → EA5 junction 3 → EA6 junction 1 → EA7 junction 2 → EA8 junction 3. Local increase of R_i during EA tends to decrease the T_c of the targeted junction (red symbols, upper row).

The middle row of Fig. 4 shows the maximum critical current obtained at $B = 0$ and the period of the Fraunhofer-like pattern ΔB measured through a pair of terminals as a function of the EA step. The critical current I_c^{ij} is determined by the largest value

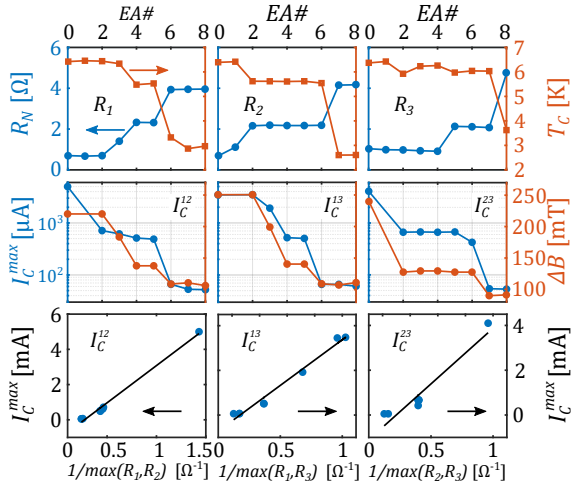

Fig. 4 Upper row: Computed normal state resistance R_N (blue symbols) and superconducting critical temperature T_c (red symbols) of each individual junction as a function of the EA step (EA#). Middle row: Maximum critical current (blue symbols) measured through a pair of terminals and magnetic field period of the Fraunhofer-like oscillation as a function of the EA step. Lower row: linear correlation between I_c^{ij} and $1/max(R_i,R_j)$. The arrows indicate the corresponding ordinate axis.

between R_i and R_j. This is demonstrated by the linear correlation between I_c^{ij} and $1/max(R_i,R_j)$ in the bottom row of Fig. 4 which could be used to extract the individual critical currents I_c^i as long as $R_i \neq R_j$. Although all the data presented in this work has been acquired in one single device, the all-electrical control of the junction properties has been confirmed in one another similar sample and also at ambient temperature with atomic force microscopy imaging (see ESI†).

3 Conclusion

In brief, we have presented a technique particularly adapted to control individually the junction properties of each branch in a multiterminal device. The primary advantage of the proposed approach lies on its simplicity, offering full control of the material modifications and unprecedented high degree of selectivity. Although in the present study we focus on three terminal devices, the method can be extended to N-terminal devices or even several N-terminal devices interconnected. Two important parameters to consider are the terminal geometry and the polarity of the EA current. The exact nature of the Josephson junction created by EA is still uncertain, and may be either of the SNS type where N is a non-intrinsic superconductor or of the SS'S type where S' denotes a superconductor of lower critical temperature, is another motivation for future work.

Author Contributions

A.V.S. initiated and supervised the experiment. D.M. performed sample fabrication. S.C. and J.V.d.V. conducted the low-temperature experiments. S.C. and A.V.S. analysed the results and prepared the manuscript. All authors reviewed the manuscript.

Conflicts of interest

There are no conflicts to declare.

Acknowledgements

We thank Alexei Aladyshkin and Hervé Courtois for insipring discussions.

This work was supported by the Fonds de la Recherche Scientifique - FNRS under the grant U.N027.18, the Research Foundation-Flanders (FWO, Belgium), Grant No. G0B5315N and by COST (European Cooperation in Science and Technology) through COST Action CA16218 "NanoCoHybri". The work of A.V.S. is partially supported by CDR J.0151.19 and EQP U.N027.18 of the F.R.S.-FNRS. This work received support from the European Union under the Marie Sklodowaska-Curie Grand No. 766025.

Notes and references

1 H. Chen, S. X. D. Tan, V. Sukharev, X. Huang and T. Kim, *52nd ACM/EDAC/IEEE Design Automation Conference (DAC)*, 2015, 1–6.

2 L. Chen, S. X. D. Tan, Z. Sun, S. Peng, M. Tang and J. Mao, *IEEE Transactions on Very Large Scale Integration (VLSI) Systems*, 2020, **28**, 421–432.

3 A. N. McCaughan, N. S. Abebe, Q. Y. Zhao and K. K. Berggren, *Nano Lett.*, 2016, **16**, 7626–7631.

4 A. F. Volkov, *Phys. Rev. Lett.*, 1995, **74**, 4730–4733.

5 R. de Bruyn Ouboter, A. N. Omelyanchouk and E. D. Vol, *Phys. B: Condens. Matter*, 1995, **205**, 153–162.

6 A. F. Volkov and H. Takayanagi, *Phys. Rev. B*, 1997, **56**, 11184–11194.

7 A. F. Morpurgo, T. M. Klapwijk and B. J. van Wees, *Appl. Phys. Lett.*, 1998, **72**, 966–968.

8 K. Neurohr, T. Schäpers, J. Malindretos, S. Lachenmann, A. I. Braginski, H. Lüth, M. Behet, G. Borghs and A. A. Golubov, *Phys. Rev. B*, 1999, **59**, 11197–11200.

9 J. A. Baselmans, A. F. Morpurgo, B. J. van Wees and T. M. Klapwijk, *Nature*, 1999, **397**, 43–45.

10 R. Shaikhaidarov, A. F. Volkov, H. Takayanagi, V. T. Petrashov and P. Delsing, *Phys. Rev. B*, 2000, **62**, R14649–R14652.

11 M. H. S. Amin, A. N. Omelyanchouk and A. M. Zagoskin, *Phys. C: Supercond. Appl.*, 2002, **372-376**, 178–180.

12 M. H. S. Amin, A. N. Omelyanchouk, A. Blais, A. M. v. d. Brink, G. Rose, T. Duty and A. M. Zagoskin, *Phys. C: Supercond. Appl.*, 2002, **368**, 310–314.

13 J. J. A. Baselmans, B. J. van Wees and T. M. Klapwijk, *Phys. Rev. B*, 2002, **65**, 224513.

14 R. Winik, I. Holzman, E. G. Dalla Torre, E. Buks and Y. Ivry, *Appl. Phys. Lett.*, 2018, **112**, 122601.

15 B. van Heck, S. Mi and A. R. Akhmerov, *Phys. Rev. B*, 2014, **90**, 155450.

16 R. P. Riwar, M. Houzet, J. S. Meyer and Y. V. Nazarov, *Nat. Commun.*, 2016, **7**, 11167.

17 J. S. Meyer and M. Houzet, *Phys. Rev. B*, 2021, **103**, 174504.

18 L. Peralta Gavensky, G. Usaj and C. A. Balseiro, *Phys. Rev. B*, 2019, **100**, 014514.

19 A. Pfeffer, J. E. Duvauchelle, H. Courtois, R. Mélin, D. Feinberg and F. Lefloch, *Phys. Rev. B*, 2014, **90**, 075401.

20 Y. Cohen, Y. Ronen, J. H. Kang, M. Heiblum, D. Feinberg, R. Mélin and H. Shtrikman, *Proc. Natl. Acad. Sci. U. S. A.*, 2018, **115**, 6991–6994.

21 A. W. Draelos, M. T. Wei, A. Seredinski, H. Li, Y. Mehta, K. Watanabe, T. Taniguchi, I. V. Borzenets, F. Amet and G. Finkelstein, *Nano Lett.*, 2019, **19**, 1039–1043.

22 N. Pankratova, H. Lee, R. Kuzmin, K. Wickramasinghe, W. Mayer, J. Yuan, M. G. Vavilov, J. Shabani and V. E. Manucharyan, *Phys. Rev. X*, 2020, **10**, 031051.

23 E. G. Arnault, T. F. Q. Larson, A. Seredinski, L. Zhao, S. Idris, A. McConnell, K. Watanabe, T. Taniguchi, I. Borzenets, F. Amet and G. Finkelstein, *Nano Lett.*, 2021, **21**, 9668–9674.

24 V. S. Zharinov, X. D. A. Baumans, A. V. Silhanek, E. Janssens and J. Van de Vondel, *Rev. Sci. Instrum.*, 2018, **89**, 043904.

25 W. Keijers, X. D. A. Baumans, R. Panghotra, J. Lombardo, V. S. Zharinov, R. B. G. Kramer, A. V. Silhanek and J. Van de Vondel, *Nanoscale*, 2018, **10**, 21475–21482.

26 J. Lombardo, Z. L. Jelić, X. D. A. Baumans, J. E. Scheerder, J. P. Nacenta, V. V. Moshchalkov, J. Van de Vondel, R. B. G. Kramer, M. V. Milošević and A. V. Silhanek, *Nanoscale*, 2018, **10**, 1987–1996.

27 K. K. Likharev, *Rev. Mod. Phys.*, 1979, **51**, 101–159.

28 A. A. Golubov, M. Y. Kupriyanov and E. Il'ichev, *Rev. Mod. Phys.*, 2004, **76**, 411–469.

29 P. Puczkarski, P. Gehring, C. S. Lau, J. Liu, A. Ardavan, J. H. Warner, G. A. D. Briggs and J. A. Mol, *Appl. Phys. Lett.*, 2015, **107**, 133105.

30 M. Tinkham, *Introduction to Superconductivity*, Dover publications, Inc., 2nd edn, 1996.

B.3 Real time measurements of an instantaneous heat

Calorimetry of a Quantum Phase Slip

E. Gümüş,[1] D. Majidi,[1] D. Nikolić,[2] P. Raif,[1,2] B. Karimi,[3] J. T. Peltonen,[3]
E. Scheer,[2] J. P. Pekola,[3] H. Courtois,[1] W. Belzig,[2] and C. B. Winkelmann[1]

[1] *Univ. Grenoble Alpes, CNRS, Grenoble INP, Institut Néel, 25 rue des Martyrs, Grenoble, France*
[2] *Fachbereich Physik, Universität Konstanz, D-78457 Konstanz, Germany*
[3] *QTF Centre of Excellence, Department of Applied Physics, Aalto University School of Science, P.O. Box 13500, 00076 Aalto, Finland*

In a Josephson junction, which is the central element in superconducting quantum technology, irreversibility arises from abrupt slips of the gauge-invariant quantum phase difference across the contact. A quantum phase slip (QPS) is often visualized as the tunneling of a flux quantum in the transverse direction to the superconducting weak link, which produces dissipation. Here, we detect the instantaneous heat release caused by a QPS in a Josephson junction using time-resolved electron thermometry on a nanocalorimeter, signaled by an abrupt increase of the local electronic temperature in the weak link and subsequent relaxation back to equilibrium. Beyond providing a cornerstone in experimental quantum thermodynamics in form of observation of heat in an elementary quantum process, this result sets the ground for experimentally addressing the ubiquity of dissipation, including that in superconducting quantum sensors and qubits.

The magnetic flux threading a superconducting loop is quantized in units of the flux quantum $\Phi_0 = h/2e$. The tunneling of a flux quantum in or out of such a loop is associated to a change of 2π in the winding of the phase of the quantum wave function along the loop. The manipulation of individual flux quanta is at the core of superconducting circuit logics, both in the classical and in the quantum information regime [1–3]. Rapid single-flux-quantum (RSFQ) logic can operate up to 100 GHz frequencies and is considered as promising classical control electronics of qubits [4–6]. In the quantum regime, the coherent superposition and manipulation of flux states is at the basis of flux qubits [7, 8] and the fluxonium [9, 10].

Slips of the quantum phase occur when the gauge-invariant phase difference across a weak link, that is, a Josephson junction, in the superconducting loop suddenly relaxes (Fig. 1). Quantum phase slips (QPSs) are ubiquitous in superconducting electronics and can be seen as the dual process to Cooper pair tunneling. Furthermore, coherent QPSs have been proposed as a building block for phase-slip qubit devices [1, 2, 11]. On the other hand, their proliferation is responsible for the destruction of superconductivity in one dimension [12] and can lead to thermal avalanches in current-biased Josephson junctions [13]. In essence, a QPS can be considered the *quantum of dissipation* in superconducting electronics.

In this work, we investigate the thermal signature of incoherent individual quantum phase slips in a superconducting Josephson junction. Applying a MHz-bandwidth electron thermometry technique to a Josephson junction, we measure the heat generated by a single QPS as well as the subsequent thermal relaxation. The data are in good agreement with a theoretical model that we developed for describing the superconducting properties of the device. Our work therefore demonstrates the possibility to quantitatively account for dissipative effects in quantum nanoelectronics, with evident applications to quantum computing.

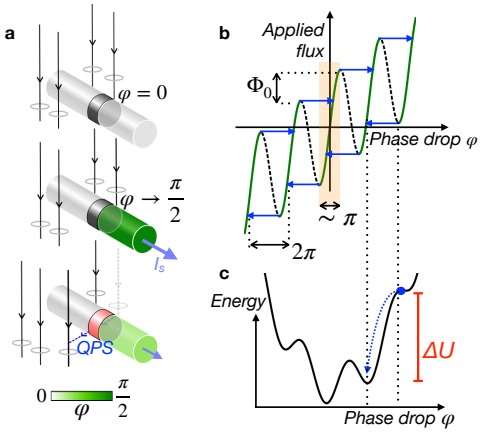

Figure 1. **Quantum phase slip in a Josephson junction.** (a) Real-space sketch of the QPS mechanism: at the instability point of the $\Phi_x(\varphi)$ relation, the phase drop φ and the screening current I_s relax abruptly to smaller values, as a quantum of flux tunnels perpendicular to the Josephson junction (dark grey), releasing heat. (b) Phase drop φ across the SNS junction versus applied flux to the SQUIPT, following Eq. (1) with $\beta = 10$. The dashed part of the curve cannot be accessed. In a quantum phase slip (blue arrows), φ changes by slightly less than 2π. (c) Potential energy of the SQUIPT as a function of φ. A local energy minimum can become unstable as the externally applied flux is changed. By macroscopic quantum tunneling of the phase, a lower energy valley is reached, releasing an energy ΔU.

The experimental core element is a superconducting quantum interference device (SQUID), that is, a superconducting loop containing one (as is the case here) or more Josephson junctions, and to which a magnetic flux

Φ_x is applied. The difference between the applied and the physical flux is absorbed by screening supercurrents, leading to a gradient in the phase of the quantum wave function along the loop, and, to a large extent, across the Josephson weak link. The relation between Φ_x and the phase drop φ across the Josephson junction can be written as

$$2\pi(\Phi_x/\Phi_0) = \varphi + \beta\sin(\varphi), \tag{1}$$

with the screening parameter $\beta = 2\pi LI_c/\Phi_0$, where L is the loop inductance and I_c the Josephson junction's critical current [14]. Irreversibility arises when the SQUID's magnetic screening parameter β exceeds 1 and Eq. (1) is no longer single-valued, as illustrated in Fig. 1b,c. In this situation, the penetration of an additional flux quantum into the SQUID loop does not occur smoothly and reversibly, but via a sudden tunneling of the phase, that is, a quantum phase slip.

The above concepts are the basis of extensive applications in superconducting electronics, such as SQUID magnetometry and superconducting flux qubits [7, 15, 16]. Notably, the Josephson weak links used in such SQUIDs can be provided by a variety of junction types, including tunnel junctions, micro-bridges, and proximity weak links [17]. In the latter, a short, non-intrinsically-superconducting element, such as a normal metallic wire allows for superconducting correlations to propagate between both superconducting reservoirs. Due to the wire's usually low normal state resistance, following the resistively and capacitively shunted Josephson junction model, the quantum phase dynamics in such superconductor-normal metal-superconductor (SNS) Josephson junctions are inherently overdamped [14]. This ensures that upon a QPS, the quantum phase only evolves towards the nearest neighboring potential valley (Fig. 1c). This releases an energy

$$\Delta U = \frac{\Phi_0}{2\pi L}\int \Phi_x\, d\varphi, \tag{2}$$

which depends on the magnitude of the quantum phase slip. In the large β limit, the phase jumps by about 2π, and $\Delta U \approx I_c\Phi_0$.

Our device consists of a SQUID with a single Josephson junction, provided by an SNS weak link of length 520 nm (Fig. 2a). Here, the superconducting circuit parts are made of aluminum, while the metal N is made of copper. While the loop is grounded, the center of N is further contacted by another superconducting finger through a tunnel junction (Fig. 2a), with normal state resistance $R_T \approx 7$ kΩ. This SQUID variant was named SQUIPT [18], where PT stands for proximity transistor. Our SQUIPT was designed to be in the hysteretic regime. For this, we took into account the geometric and kinetic inductance contributions, leading here to $L \approx 630 \pm 50$ pH. The SNS junction critical current I_c cannot be determined independently in this device, but is expected from similar SNS devices in a current-biased geometry to be of a few μA [19–21]. From this, values of the screening parameter $\beta \sim 10$ can be anticipated, in good agreement with experiments, as discussed below.

Applying a dc voltage V_b to the tunnel junction, we can perform tunnel spectroscopy by measuring its differential conductance $G(V_b)$. Here, G is not read out, as usual, by a low-frequency transport measurement, but by a radio-frequency (RF) technique, using a superconducting LC resonator with resonant frequency 575 MHz [22–24]. By embedding the tunnel junction in parallel to the resonator, and for a fixed incident RF power $P_{\rm in}$, changes in G can be read out by their effect on the transmitted power at resonance $P_{\rm out}$, which we record after cryogenic amplification (details in Supp. Info. file). This has the paramount advantage of allowing for extremely rapid measurements, limited by the resonator bandwidth, of about 10 MHz here.

Figure 2b shows measurements of $P_{\rm out}(V_b)$ at two temperatures. Several characteristic spectroscopic features stand out, in particular (i) a spectroscopic gap of total width 480 μV, (ii) subgap resonances near $\pm 190\,\mu$V visible only at 400 mK, and (iii) three low-energy resonances at 0 and $\pm 15\,\mu$V, respectively. Keeping in mind that the tunnel junction connects an intrinsic superconductor with gap Δ and a proximized metal with a (smaller) induced gap E_g, we can evaluate the total spectroscopic gap as $2(\Delta + E_g)/e$. At intermediate temperatures, thermally activated conductance resonances occur at $\pm|\Delta - E_g|/e$, which we identify as feature (ii). From the two above relations we find a gap $\Delta = 210 \pm 5\,\mu$eV in the superconducting probe electrode at 400 mK (225 μeV at 50 mK), a typical value in nanostructured aluminum. We further extract $E_g = 29\,\mu$eV, in good agreement with theoretical estimates (details in the Supp. Info. file). Eventually, the conductance resonance at $V_b = 0$ (feature (iii)) is a signature of the Josephson coupling across the tunnel junction, which was purposely designed to have an intermediate transparency [24]. The satellite peaks at $\pm 15\,\mu$V are probably the signature of inelastic Cooper pair tunneling [24] and are not of central relevance to this work.

As visible in Fig. 2b,c and already discussed in detail in [24–26], the zero-bias conductance of the tunnel junction, and therefore $P_{\rm out}(V_b = 0)$, is a sensitive probe of the electron temperature T in N. Accordingly, we set $V_b = 0$ in the remainder of this work and use $P_{\rm out}$ for both static and dynamic electron thermometry, after initial calibration under equilibrium conditions (Fig. 2c). However, and in contrast to previous work [24–26] in which N was not subject to a phase drop, in the present device the tunnel junction conductance and thus $P_{\rm out}$ are clearly also a function of the phase φ across the SNS junction. This is seen in Fig. 2d, where sweeping the applied flux translates into a phase variation via Eq. (1). As $\varphi \to \pi/2$, the decrease of E_g [27, 28] entails a rapidly shrinking Joseph-

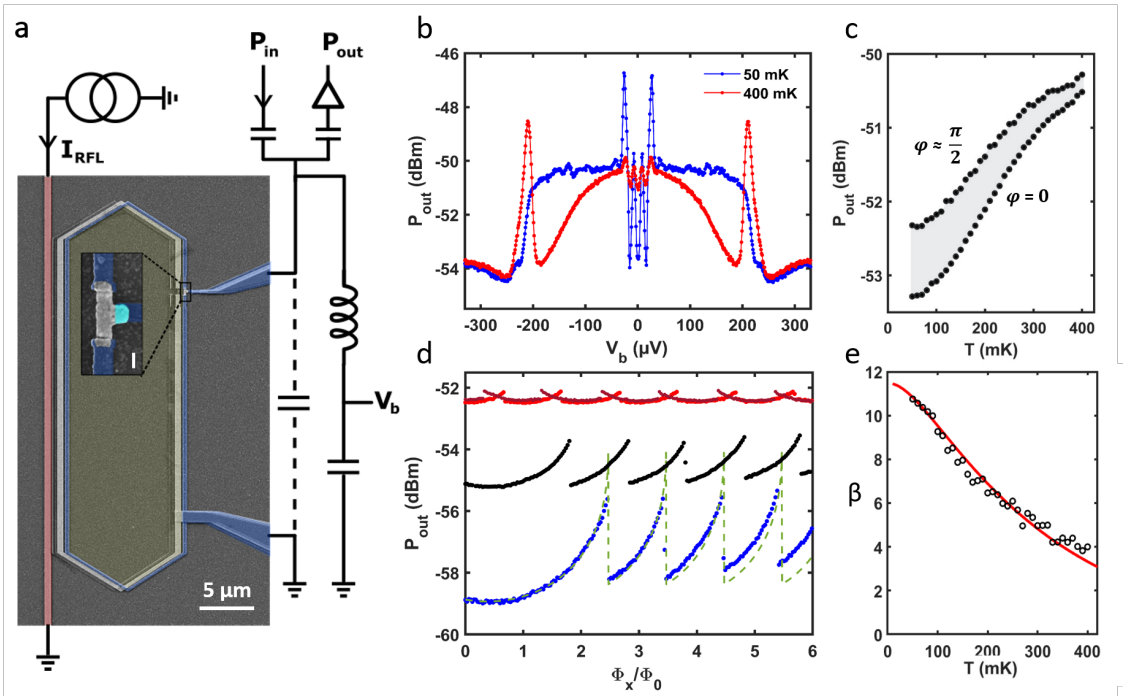

Figure 2. **Hysteretic RF-SQUIPT.** (a) Device schematics, including a false-color scanning electron micrograph (scale bar 5 μm) of the SQUIPT loop (yellow area) and the rapid flux line (pink). The zoom highlights the SNS junction (Al = blue, Cu = grey), connected laterally by the tunnel contact (cyan) (scale bar 200 nm), connected to the resonator. (b) Bias spectroscopy $P_{\rm out}(V_b)$ at cryostat temperatures 50 mK (blue) and 400 mK (red). (c) Calibration of $P_{\rm out}(V_b = 0)$ versus cryostat temperature at equilibrium, under two different phase drops. The grey shaded region thus covers all possible values of $P_{\rm out}(T, \varphi)$. (d) Resonator response at $V_b = 0$ as a function of increasing applied magnetic flux, at three cryostat temperatures (50 mK, blue; 200 mK, black; 400 mK, red). The dark red line exemplifies the response to a downward sweep of the flux. The dashed line is a calculation (see text). (e) Temperature dependence of the screening parameter β, extracted from (d), and theoretical fit (red line, see text).

son energy E_J of the tunnel junction, and thus a decrease of $G(0)$, that is, an increase of $P_{\rm out}$. When the switching point in the $\Phi_x(\varphi)$ relation is reached, φ suddenly relaxes to a smaller value (modulo 2π), restoring E_J and thus leading to an abrupt drop in $P_{\rm out}$. As expected, the same pattern is repeated with period Φ_0 in the applied flux and mirror symmetric under inversion of the sweep direction [29]. At higher temperatures, $\beta \propto I_c$ decreases and the modulation amplitude of $P_{\rm out}(\Phi_x)$ shrinks, while the Φ_0-periodicity of the signal is preserved.

For a quantitative understanding of the RF-SQUIPT, we use the quasi-classical Usadel equations [27, 30–32], with a single consistent set of microscopic parameters, described in detail in the Supp. Info. file. The density of states in N is known to display a minigap, which depends approximately on φ like $E_g(\varphi) = E_g(0)\,|\cos(\varphi/2)|$ [27]. The tunnel junction connecting the condensate in N to the superconducting probe electrode has a Josephson energy $E_J(\varphi, T)$ and thus a zero-bias conductance $G(\varphi, T)$, which can be drawn back analytically to $E_g(\varphi)$ and the critical current I_c of the SNS junction. In combination with Eq. (1) and the relation between G and $P_{\rm out}$, the calculation provides an accurate description of the applied-flux dependence of the RF signal (Fig. 2d), the only adjustable parameter being the magnitude of β.

The temperature dependence of β extracted from the data in Fig. 2d is plotted in Fig. 2e, following the trend expected for $I_c(T)$ in an SNS junction. The solid line shows the calculation from the same model as above, yielding a 5.9 μA zero-temperature critical current in the SNS junction. The parameters entering the calculation, and in particular the minigap, are determined independently using the tunnel spectra (Fig. 2b). We attribute the slight underestimation of β by theory above 300 mK to the temperature dependence of the kinetic inductance, which was not accounted for.

The data discussed so far, and summarized in Fig. 2, provide a consistent physical understanding of the RF-

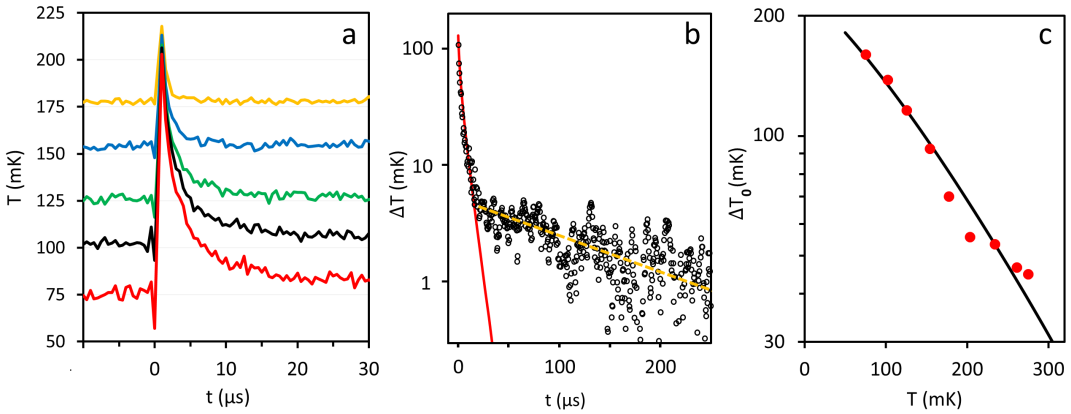

Figure 3. **Heat relaxation dynamics after a QPS.** (a) Time-resolved electron temperature in the absorber, at different starting temperatures set by the cryostat bath, following a 70-ns flux pulse at $t = 0$. The data sampling rate is 2 MHz, the data shown are the result of averaging over 10^5 pulses, at a repetition rate of 2 kHz. (b) Return to equilibrium $\Delta T(t)$ at 100 mK, following a flux pulse. Same data as the black curve in (a), but in a semi-log-scale representation and over a wider time window. The red line is a calculation based on the model discussed in the text. The dashed line is an exponential fit (with time constant $\tau \approx 140\,\mu$s) to the long-term relaxation, evidencing the presence of a second slowly relaxing bath. (c) Magnitude of the initial temperature rise ΔT_0 at $t = 0$, determined by the fit as shown in (b) (bullets). The solid line is a calculation (see text).

SQUIPT under time-averaged, and thus isothermal conditions. We now move to the time-resolved response $P_{\rm out}(t)$, which displays the calorimetric signature of the heat deposited by individual QPS events. In addition to the static flux bias, we apply a time-dependent (square-wave or pulsed) flux, by passing a current $I_{\rm RFL}(t)$ through the superconducting rapid flux line (RFL), visible on the left side of the SQUIPT in Fig. 2a. The instantaneous flux bias is $\Phi_x(t) = M\, I_{\rm RFL}(t)$, with a mutual inductance $M = 12.1$ pH further discussed in the Supp. Info. file. In order to increase the signal-to-noise ratio, we average the resonator response over a large number of periodically generated identical 70 ns flux pulses.

As long as the amplitude of the flux pulses does not exceed the threshold leading to a QPS, $P_{\rm out}$ follows changes in $\Phi_x(t)$ instantaneously (not shown, see Supp. Info. file for details). However, as soon as the threshold to instability of the flux state is overcome, $P_{\rm out}(t)$ displays in addition a slower relaxation to its novel equilibrium, which is indicative of thermalization. As evidenced from Fig. 3a, the relaxation dynamics after a flux pulse are strongly temperature dependent, as expected for instance from a dominantly electron-phonon (e-ph) coupling-driven thermalization after an initial heating event [23]. Above 300 mK, the relaxation times become too short ($< 1\,\mu$s) to be measured.

The thermal dynamics can be described by a heat balance equation, basing on the standard assumption that variations of the absorber's internal energy U are evacuated to a heat bath via electron-phonon coupling. In metallic nanostructures at low temperatures, this power is usually written $\dot{Q}_{e-ph} = \Sigma\mathcal{V}(T^5 - T_0^5)$, where $\Sigma = 2\times10^9$ W K^{-5} m^{-3} is the electron-phonon coupling constant in copper [33, 34], and $\mathcal{V} \approx 8\times10^{-21}$ m^{-3} the geometrically estimated absorber volume. Given the rather small E_g in the SNS junction, our calculations indicate that the proximity effect should only lead to negligibly small departures from the normal-state electron-phonon coupling and heat capacity C, at the experimental temperatures. Therefore we write $U = \gamma T^2/2$, using a reported $\gamma = 71$ J m^{-3} K^{-2} in nanostructured Cu [34]. As seen in Fig. 3a, the temperature increase after the initial heat pulse can be large compared to the starting temperature. The dynamical heat balance differential equation thus cannot be linearized in $\Delta T = T - T_b$, and must be solved numerically. The result at $T_b = 100$ mK is shown in Fig. 3b (red line), where the only free parameter is the initial temperature increase ΔT_0. The calculation follows closely the data during the first period of the thermal relaxation. Interestingly, the initial fast decay is rapidly taken over by a much slower process, which was already reported for nanoscale Cu absorbers [34, 35]. This might be due to another heat reservoir, for instance in surface states of the Cu absorber.

The initial temperature increase ΔT_0 after a flux pulse is plotted as a function of the starting temperature in Fig. 3c. Naturally, the temperature rise is highest when starting from the lowest base temperature, because at higher temperature both C increases and $\Delta U \sim I_c\Phi_0$ decreases. For a quantitative modeling, one must bear in

mind that a flux pulse induces necessarily two QPSs: one while ramping up the flux bias, and the second when returning to the initial state. We account for the fact that the return QPS occurs at a higher electronic temperature and thus produces less dissipation. The sudden temperature rise after the first QPS could also lead the sinusoidal potential energy landscape modulation (see Fig. 1c) to collapse to the point that the reached valley also becomes unstable and the phase eventually jumps by 4π, or more. This was actually observed in another device, which we describe in the Supp. Info. file, but does not apply in the sample described here. Finally, the quasi-classical Usadel formalism with the same set of microscopic parameters as previously, in combination with Eqs. (1,2) and the known values of γ and $\mathcal{V}$, describes very accurately (red line in Fig. 3c) the initial temperature rise ΔT_0.

Our findings of microsecond-scale thermal relaxation following a QPS tracked in real time highlight both the paramount effect dissipation can produce in quantum circuits, and the potential of large-bandwidth electron thermometry for quantum thermodynamics in nanoelectronic circuits. The detection of a *quantum of dissipation* in a Josephson junction opens promising perspectives for future experiments. These would aim, for instance, at detecting the minute dissipation arising from a projective qubit measurement with emission of a single microwave photon [36], or the detection of the elusive axion with even smaller energy [37]. On the other hand, the proper measurement and control of dissipation in QPS-based circuits will allow for overcoming self-heating-limited device performances.

We acknowledge help from A. Théry and T. Crozes. The samples were fabricated at the Nanofab platform at Institut Néel. This work received support from the European Union under the Marie Sklodowska-Curie Grant Agreement No. 766025 (QuESTech), from the Agence Nationale de la Recherche under the program "Investissements d'avenir" (ANR-15-IDEX-02), from the Laboratoire d'excellence LANEF (ANR-10-LABX-51-01), and from Deutsche Forschungsgemeinschaft (DFG; German Research Foundation) via SFB 1432 (Project No. 425217212).

[1] J. E. Mooij and C. J. P. M. Harmans, "Phase-slip flux qubits," New J. Phys. **7**, 219 (2005).

[2] J. E. Mooij and Yu. V. Nazarov, "Superconducting nanowires as quantum phase-slip junctions," Nat. Phys. **2**, 169–172 (2006).

[3] P. J. Liebermann and F. K. Wilhelm, "Optimal qubit control using single-flux quantum pulses," Phys. Rev. Appl. **6**, 024022 (2016).

[4] E. Leonard, M. A. Beck, J. Nelson, B. G. Christensen, T. Thorbeck, C. Howington, A. Opremcak, I. V. Pechenezhskiy, K. Dodge, N. P. Dupuis, M. D. Hutchings, J. Ku, F. Schlenker, J. Suttle, C. Wilen, S. Zhu, M. G. Vavilov, B. L. T. Plourde, and R. McDermott, "Digital Coherent Control of a Superconducting Qubit," Phys. Rev. Appl. **11**, 014009 (2019).

[5] C. Howington, A. Opremcak, R. McDermott, A. Kirichenko, O. A. Mukhanov, and B. L. T. Plourde, "Interfacing Superconducting Qubits With Cryogenic Logic: Readout," IEEE Transactions on Applied Superconductivity **29**, 1–5 (2019).

[6] R. McDermott, M. G. Vavilov, B. L. T. Plourde, F. K. Wilhelm, P. J. Liebermann, O. A. Mukhanov, and T. A. Ohki, "Quantum–classical interface based on single flux quantum digital logic," Quantum Science and Technology **3**, 024004 (2018).

[7] I. Chiorescu, Y. Nakamura, C. J. P. Harmans, and J. E. Mooij, "Coherent quantum dynamics of a superconducting flux qubit," Science **299**, 1869–1871 (2003).

[8] F. Yan, S. Gustavsson, A. Kamal, J. Birenbaum, A. P. Sears, D. Hover, T. J. Gudmundsen, D. Rosenberg, G. Samach, S. Weber, *et al.*, "The flux qubit revisited to enhance coherence and reproducibility," Nat. Commun. **7**, 1–9 (2016).

[9] V. E. Manucharyan, J. Koch, L. I. Glazman, and M. H. Devoret, "Fluxonium: Single Cooper-pair circuit free of charge offsets," Science **326**, 113 (2009).

[10] L. B. Nguyen, Y.-H. Lin, A. Somoroff, R. Mencia, N. Grabon, and V. E Manucharyan, "High-coherence fluxonium qubit," Phys. Rev. X **9**, 041041 (2019).

[11] O. V. Astafiev, L. B. Ioffe, S. Kafanov, Y. A. Pashkin, K. Y. Arutyunov, D. Shahar, O. Cohen, and J. S. Tsai, "Coherent quantum phase slip," Nature **484**, 355–358 (2012).

[12] D. S. Golubev and A. D. Zaikin, "Quantum tunneling of the order parameter in superconducting nanowires," Phys. Rev. B **64**, 014504 (2001).

[13] M. Sahu, M. Bae, A. Rogachev, D. Pekker, T.-C. Wei, N. Shah, P. M. Goldbart, and A. Bezryadin, "Individual topological tunnelling events of a quantum field probed through their macroscopic consequences," Nat. Phys. **5**, 503–508 (2009).

[14] M. Tinkham, *Introduction to Superconductivity* (Dover, New York, 2nd edition, 1996).

[15] C. H. van Der Wal, A. C. J. Ter Haar, F. K. Wilhelm, R. N. Schouten, C. J. P. M. Harmans, T. P. Orlando, S. Lloyd, and J. E. Mooij, "Quantum superposition of macroscopic persistent-current states," Science **290**, 773–777 (2000).

[16] J. R. Friedman, V. Patel, W. Chen, S. K. Tolpygo, and J. E. Lukens, "Quantum superposition of distinct macroscopic states," Nature **406**, 43–46 (2000).

[17] K. K. Likharev, "Superconducting weak links," Rev. Mod. Phys. **51**, 101 (1979).

[18] F. Giazotto, J. T. Peltonen, M. Meschke, and J. P Pekola, "Superconducting quantum interference proximity transistor," Nat. Phys. **6**, 254–259 (2010).

[19] H. Courtois, M. Meschke, J. T. Peltonen, and J. P Pekola, "Origin of hysteresis in a proximity Josephson junction," Phys. Rev. Lett. **101**, 067002 (2008).

[20] L. Angers, F. Chiodi, G. Montambaux, M. Ferrier, S. Guéron, H. Bouchiat, and J. C. Cuevas, "Proximity dc squids in the long-junction limit," Phys. Rev. B **77**, 165408 (2008).

[21] B. Dutta, D. Majidi, N. W. Talarico, N. Lo Gullo, H. Courtois, and C. B. Winkelmann, "Single-quantum-

dot heat valve," Phys. Rev. Lett. **125**, 237701 (2020).

[22] D. R. Schmidt, C. S. Yung, and A. N. Cleland, "Nanoscale radio-frequency thermometry," Appl. Phys. Lett. **83**, 1002–1004 (2003).

[23] S. Gasparinetti, K. L. Viisanen, O.-P. Saira, T. Faivre, M. Arzeo, M. Meschke, and J. P. Pekola, "Fast electron thermometry for ultrasensitive calorimetric detection," Phys. Rev. Appl. **3**, 014007 (2015).

[24] B. Karimi and J. P Pekola, "Noninvasive thermometer based on the zero-bias anomaly of a superconducting junction for ultrasensitive calorimetry," Phys. Rev. Appl. **10**, 054048 (2018).

[25] B. Karimi, D. Nikolić, T. Tuukkanen, J. T. Peltonen, W. Belzig, and J. P Pekola, "Optimized proximity thermometer for ultrasensitive detection," Phys. Rev. Appl. **13**, 054001 (2020).

[26] B. Karimi, F. Brange, P. Samuelsson, and J. P Pekola, "Reaching the ultimate energy resolution of a quantum detector," Nat. Commun. **11**, 1–6 (2020).

[27] F. Zhou, P. Charlat, B. Spivak, and B. Pannetier, "Density of states in superconductor-normal metal-superconductor junctions," J. Low Temp. Phys. **110**, 841–850 (1998).

[28] H. Le Sueur, P. Joyez, H. Pothier, C. Urbina, and D. Estève, "Phase controlled superconducting proximity effect probed by tunneling spectroscopy," Phys. Rev. Lett. **100**, 197002 (2008).

[29] N. Ligato, E. Strambini, F. Paolucci, and F. Giazotto, "Preliminary demonstration of a persistent Josephson phase-slip memory cell with topological protection," Nat. Commun. **12**, 1–8 (2021).

[30] A. L. Larkin and Yu. N. Ovchinnikov, "Quasiclassical method in the theory of superconductivity," Zh. Eksp. Teor. Fiz. **55**, 2262 (1968).

[31] K. D. Usadel, "Generalized diffusion equation for superconducting alloys," Phys. Rev. Lett. **25**, 507 (1970).

[32] W. Belzig, F. K. Wilhelm, C. Bruder, G. Schön, and A. D. Zaikin, "Quasiclassical Green's function approach to mesoscopic superconductivity," Superlattices Microstruct. **25**, 1251 (1999).

[33] F. Giazotto, T. T. Heikkilä, A. Luukanen, A. M. Savin, and J. P. Pekola, "Opportunities for mesoscopics in thermometry and refrigeration: Physics and applications," Rev. Mod. Phys. **78**, 217 (2006).

[34] K. L. Viisanen and J. P. Pekola, "Anomalous electronic heat capacity of copper nanowires at sub-kelvin temperatures," Phys. Rev. B **97**, 115422 (2018).

[35] L. B. Wang, D. S. Golubev, Y. M. Galperin, and J. P. Pekola, "Dynamic thermal relaxation in metallic films at sub-kelvin temperatures," arXiv preprint arXiv:1910.09448 (2019).

[36] J. P. Pekola and B. Karimi, "Ultrasensitive calorimetric detection of single photons from qubit decay," Phys. Rev. X **12**, 011026 (2022).

[37] T. Braine, R. Cervantes, N. Crisosto, N. Du, S. Kimes, L. J. Rosenberg, G. Rybka, J. Yang, D. Bowring, A. S. Chou, *et al.*, "Extended search for the invisible axion with the axion dark matter experiment," Phys. Rev. Lett. **124**, 101303 (2020).

References

[1] L. D. Hicks, M. S. Dresselhaus, Thermoelectric figure of merit of a one-dimensional conductor, Physical review B 47 (24) (1993) 16631.

[2] P. M. Wu, J. Gooth, X. Zianni, S. F. Svensson, J. G. Gluschke, K. A. Dick, C. Thelander, K. Nielsch, H. Linke, Large thermoelectric power factor enhancement observed in inas nanowires, Nano letters 13 (9) (2013) 4080–4086.

[3] M. Josefsson, A. Svilans, A. M. Burke, E. A. Hoffmann, S. Fahlvik, C. Thelander, M. Leijnse, H. Linke, A quantum-dot heat engine operating close to the thermodynamic efficiency limits, Nature nanotechnology 13 (10) (2018) 920–924.

[4] I.-J. Chen, A. Burke, A. Svilans, H. Linke, C. Thelander, Thermoelectric power factor limit of a 1d nanowire, Physical review letters 120 (17) (2018) 177703.

[5] D. Prete, P. A. Erdman, V. Demontis, V. Zannier, D. Ercolani, L. Sorba, F. Beltram, F. Rossella, F. Taddei, S. Roddaro, Thermoelectric conversion at 30 k in inas/inp nanowire quantum dots, Nano letters 19 (5) (2019) 3033–3039.

[6] S. Jezouin, F. Parmentier, A. Anthore, U. Gennser, A. Cavanna, Y. Jin, F. Pierre, Quantum limit of heat flow across a single electronic channel, Science 342 (6158) (2013) 601–604.

[7] M. Dresselhaus, G. Dresselhaus, X. Sun, Z. Zhang, S. Cronin, T. Koga, Low-dimensional thermoelectric materials, Physics of the Solid State 41 (5) (1999) 679–682.

[8] R. Scheibner, H. Buhmann, D. Reuter, M. Kiselev, L. Molenkamp, Thermopower of a kondo spin-correlated quantum dot, Physical review letters 95 (17) (2005) 176602.

[9] A. Dzurak, C. Smith, C. Barnes, M. Pepper, L. Martín-Moreno, C. Liang, D. Ritchie, G. Jones, Thermoelectric signature of the excitation spectrum of a quantum dot, Physical Review B 55 (16) (1997) R10197.

[10] S. Godijn, S. Möller, H. Buhmann, L. Molenkamp, S. Van Langen, Thermopower of a chaotic quantum dot, Physical review letters 82 (14) (1999) 2927.

[11] G. Jaliel, R. Puddy, R. Sánchez, A. Jordan, B. Sothmann, I. Farrer, J. Griffiths, D. Ritchie, C. Smith, Experimental realization of a quantum dot energy harvester, Physical review letters 123 (11) (2019) 117701.

[12] P. Kim, L. Shi, A. Majumdar, P. L. McEuen, Thermal transport measurements of individual multiwalled nanotubes, Physical review letters 87 (21) (2001) 215502.

[13] Z. Huang, F. Chen, R. D'agosta, P. A. Bennett, M. Di Ventra, N. Tao, Local ionic and electron heating in single-molecule junctions, Nature nanotechnology 2 (11) (2007) 698–703.

[14] M. Tsutsui, M. Taniguchi, T. Kawai, Local heating in metal- molecule- metal junctions, Nano letters 8 (10) (2008) 3293–3297.

[15] B. Sothmann, R. Sánchez, A. N. Jordan, Thermoelectric energy harvesting with quantum dots, Nanotechnology 26 (3) (2014) 032001.

[16] T. Humphrey, H. Linke, Reversible thermoelectric nanomaterials, Physical review letters 94 (9) (2005) 096601.

[17] P. Reddy, S.-Y. Jang, R. A. Segalman, A. Majumdar, Thermoelectricity in molecular junctions, Science 315 (5818) (2007) 1568–1571.

[18] P. Murphy, S. Mukerjee, J. Moore, Optimal thermoelectric figure of merit of a molecular junction, Phys. Rev. B 78 (16) (2008) 161406.

[19] Y. Dubi, M. Di Ventra, Colloquium: Heat flow and thermoelectricity in atomic and molecular junctions, Rev. Mod. Phys. 83 (1) (2011) 131.

[20] G. Mahan, J. Sofo, The best thermoelectric, Proceedings of the National Academy of Sciences 93 (15) (1996) 7436–7439.

[21] T. Humphrey, R. Newbury, R. Taylor, H. Linke, Reversible quantum brownian heat engines for electrons, Physical review letters 89 (11) (2002) 116801.

[22] B. Dutta, J. T. Peltonen, D. S. Antonenko, M. Meschke, M. A. Skvortsov, B. Kubala, J. König, C. B. Winkelmann, H. Courtois, J. P. Pekola, Thermal conductance of a single-electron transistor, Physical review letters 119 (7) (2017) 077701.

[23] D. Halbertal, J. Cuppens, M. B. Shalom, L. Embon, N. Shadmi, Y. Anahory, H. Naren, J. Sarkar, A. Uri, Y. Ronen, et al., Nanoscale thermal imaging of dissipation in quantum systems, Nature 539 (7629) (2016) 407–410.

[24] A. Marguerite, J. Birkbeck, A. Aharon-Steinberg, D. Halbertal, K. Bagani, I. Marcus, Y. Myasoedov, A. K. Geim, D. J. Perello, E. Zeldov, Imaging work and dissipation in the quantum hall state in graphene, Nature 575 (7784) (2019) 628–633.

[25] L. Molenkamp, T. Gravier, H. Van Houten, O. Buijk, M. Mabesoone, C. Foxon, Peltier coefficient and thermal conductance of a quantum point contact, Physical review letters 68 (25) (1992) 3765.

[26] J. Prance, C. Smith, J. Griffiths, S. Chorley, D. Anderson, G. Jones, I. Farrer, D. Ritchie, Electronic refrigeration of a two-dimensional electron gas, Physical review letters 102 (14) (2009) 146602.

[27] E. Sivre, A. Anthore, F. Parmentier, A. Cavanna, U. Gennser, A. Ouerghi, Y. Jin, F. Pierre, Heat coulomb blockade of one ballistic channel, Nature Physics 14 (2) (2018) 145–148.

[28] M. Banerjee, M. Heiblum, V. Umansky, D. E. Feldman, Y. Oreg, A. Stern, Observation of half-integer thermal hall conductance, Nature 559 (7713) (2018) 205–210.

[29] E. Tikhonov, D. Shovkun, D. Ercolani, F. Rossella, M. Rocci, L. Sorba, S. Roddaro, V. Khrapai, Noise thermometry applied to thermoelectric measurements in inas nanowires, Semiconductor Science and Technology 31 (10) (2016) 104001.

[30] F. Giazotto, T. T. Heikkilä, A. Luukanen, A. M. Savin, J. P. Pekola, Opportunities for mesoscopics in thermometry and refrigeration: Physics and applications, Reviews of Modern Physics 78 (1) (2006) 217.

[31] M. Nahum, T. M. Eiles, J. M. Martinis, Electronic microrefrigerator based on a normal-insulator-superconductor tunnel junction, Applied Physics Letters 65 (24) (1994) 3123–3125.

[32] M. Meschke, J. Peltonen, H. Courtois, J. Pekola, Calorimetric readout of a superconducting proximity-effect thermometer, Journal of Low Temperature Physics 154 (5) (2009) 190–198.

[33] L. Wang, O.-P. Saira, J. Pekola, Fast thermometry with a proximity josephson junction, Applied Physics Letters 112 (1) (2018) 013105.

[34] A. Ronzani, B. Karimi, J. Senior, Y.-C. Chang, J. T. Peltonen, C. Chen, J. P. Pekola, Tunable photonic heat transport in a quantum heat valve, Nature Physics 14 (10) (2018) 991–995.

[35] B. Kubala, J. König, J. Pekola, Violation of the Wiedemann-Franz law in a single-electron transistor, Physical review letters 100 (6) (2008) 066801.

[36] H. Edwards, Q. d. Niu, A. De Lozanne, A quantum-dot refrigerator, Applied physics letters 63 (13) (1993) 1815–1817.

[37] G. Benenti, G. Casati, K. Saito, R. S. Whitney, Fundamental aspects of steady-state conversion of heat to work at the nanoscale, Physics Reports 694 (2017) 1–124.

[38] V. Ambegaokar, L. Tewordt, Theory of the electronic thermal conductivity of superconductors with strong electron-phonon coupling, Physical Review 134 (4A) (1964) A805.

[39] S. Lee, K. Hippalgaonkar, F. Yang, J. Hong, C. Ko, J. Suh, K. Liu, K. Wang, J. J. Urban, X. Zhang, et al., Anomalously low electronic thermal conductivity in metallic vanadium dioxide, Science 355 (6323) (2017) 371–374.

[40] H. Pan, J. D. Sau, S. Das Sarma, Three-terminal nonlocal conductance in Majorana nanowires: Distinguishing topological and trivial in realistic systems with disorder and inhomogeneous potential, Phys. Rev. B 103 (1) (2021) 014513.

[41] J. Crossno, J. K. Shi, K. Wang, X. Liu, A. Harzheim, A. Lucas, S. Sachdev, P. Kim, T. Taniguchi, K. Watanabe, et al., Observation of the dirac fluid and the breakdown of the wiedemann-franz law in graphene, Science 351 (6277) (2016) 1058–1061.

[42] X. Zianni, Coulomb oscillations in the electron thermal conductance of a dot in the linear regime, Phys. Rev. B 75 (4) (2007) 045344.

[43] M. Krawiec, K. I. Wysokiński, Thermoelectric effects in strongly interacting quantum dot coupled to ferromagnetic leads, Phys. Rev. B 73 (7) (2006) 075307.

[44] M. Krawiec, K. I. Wysokinski, Thermoelectric phenomena in a quantum dot asymmetrically coupled to external leads, Phys. Rev. B 75 (15) (2007) 155330.

[45] M. Tsaousidou, G. P. Triberis, Thermoelectric properties of a weakly coupled quantum dot: enhanced thermoelectric efficiency, J. Phys.: Cond. Matt. 22 (35) (2010) 355304.

[46] P. A. Erdman, F. Mazza, R. Bosisio, G. Benenti, R. Fazio, F. Taddei, Thermoelectric properties of an interacting quantum dot based heat engine, Phys. Rev. B 95 (24) (2017) 245432.

[47] B. Dutta, D. Majidi, N. Talarico, N. L. Gullo, H. Courtois, C. Winkelmann, Single-quantum-dot heat valve, Physical Review Letters 125 (23) (2020) 237701.

[48] B. Dutta, D. Majidi, A. Garcia Corral, P. A. Erdman, S. Florens, T. A. Costi, H. Courtois, C. B. Winkelmann, Direct probe of the seebeck coefficient in a kondo-correlated single-quantum-dot transistor, Nano letters 19 (1) (2018) 506–511.

[49] G. Chen, Nanoscale energy transport and conversion: a parallel treatment of electrons, molecules, phonons, and photons, Oxford university press, 2005.

[50] L. Mark, Fundamentals of carrier transport (2000).

[51] S. Datta, Electronic transport in mesoscopic systems, Cambridge university press, 1997.

[52] A. C. Smith, J. F. Janak, R. B. Adler, Electronic conduction in solids, Tech. rep., McGraw-Hill, (1967).

[53] T. J. Seebeck, Ueber die magnetische polarisation der metalle und erze durch temperaturdifferenz, Annalen der Physik 82 (3) (1826) 253–286.

[54] J. C. A. Peltier, Nouvelles expériences sur la caloricité des courans électriques, 1834.

[55] U. Sivan, Y. Imry, Multichannel Landauer formula for thermoelectric transport with application to thermopower near the mobility edge, Phys. Rev. B 33 (1) (1986) 551.

[56] J. H. Davies, The physics of low-dimensional semiconductors: an introduction, Cambridge University Press, Cambridge, 1998.

[57] R. Kim, S. Datta, M. S. Lundstrom, Influence of dimensionality on thermoelectric device performance, Journal of Applied Physics 105 (3) (2009) 034506.

[58] T. Ihn, Semiconductor Nanostructures: Quantum states and electronic transport, Oxford university press, 2010.

[59] A. A. M. Staring, L. W. Molenkamp, B. W. Alphenaar, H. van Houten, O. J. A. Buyk, M. A. A. Mabesoone, C. W. J. Beenakker, C. T. Foxon, Coulomb-blockade oscillations in the thermopower of a quantum dot, EPL (Europhysics Letters) 22 (1) (1993) 57.

[60] A. Ofarim, B. Kopp, T. Möller, L. Martin, J. Boneberg, P. Leiderer, E. Scheer, Thermo-voltage measurements of atomic contacts at low temperature, Beilstein journal of nanotechnology 7 (1) (2016) 767–775.

[61] C. Evangeli, M. Matt, L. Rincón-García, F. Pauly, P. Nielaba, G. Rubio-Bollinger, J. C. Cuevas, N. Agraït, Quantum thermopower of metallic atomic-size contacts at room temperature, Nano letters 15 (2) (2015) 1006–1011.

[62] M. Turek, K. A. Matveev, Cotunneling thermopower of single electron transistors, Phys. Rev. B 65 (2002) 115332.

[63] C. W. J. Beenakker, A. A. M. Staring, Theory of the thermopower of a quantum dot, Phys. Rev. B 46 (1992) 9667–9676.

[64] L. A. Zotti, M. Bürkle, F. Pauly, W. Lee, K. Kim, W. Jeong, Y. Asai, P. Reddy, J. C. Cuevas, Heat dissipation and its relation to thermopower in single-molecule junctions, New Journal of Physics 16 (1) (2014) 015004.

[65] A. Svilans, M. Josefsson, A. M. Burke, S. Fahlvik, C. Thelander, H. Linke, M. Leijnse, Thermoelectric characterization of the kondo resonance in nanowire quantum dots, Physical review letters 121 (20) (2018) 206801.

[66] A. Staring, L. Molenkamp, B. Alphenaar, H. Van Houten, O. Buyk, M. Mabesoone, C. Beenakker, C. Foxon, Coulomb-blockade oscillations in the thermopower of a quantum dot, EPL (Europhysics Letters) 22 (1) (1993) 57.

[67] C. Evangeli, K. Gillemot, E. Leary, M. T. Gonzalez, G. Rubio-Bollinger, C. J. Lambert, N. Agrait, Engineering the thermopower of c60 molecular junctions, Nano letters 13 (5) (2013) 2141–2145.

[68] J. Peltier, Investigation of the heat developed by electric currents in homogeneous materials and at the junction of two different conductors, Ann. Chim. Phys 56 (1834) (1834) 371.

[69] A. Feshchenko, J. Koski, J. P. Pekola, Experimental realization of a coulomb blockade refrigerator, Physical Review B 90 (20) (2014) 201407.

[70] B. Karimi, J. Pekola, Otto refrigerator based on a superconducting qubit: Classical and quantum performance, Physical Review B 94 (18) (2016) 184503.

[71] A. Niskanen, K. Harrabi, F. Yoshihara, Y. Nakamura, S. Lloyd, J. S. Tsai, Quantum coherent tunable coupling of superconducting qubits, Science 316 (5825) (2007) 723–726.

[72] M. Leivo, J. Pekola, D. Averin, Efficient peltier refrigeration by a pair of normal metal/insulator/superconductor junctions, Applied physics letters 68 (14) (1996) 1996–1998.

[73] M. Thesberg, H. Kosina, N. Neophytou, On the lorenz number of multiband materials, Physical Review B 95 (12) (2017) 125206.

[74] G. Mahan, M. Bartkowiak, Wiedemann–franz law at boundaries, Applied physics letters 74 (7) (1999) 953–954.

[75] L. Cui, W. Jeong, S. Hur, M. Matt, J. C. Klöckner, F. Pauly, P. Nielaba, J. C. Cuevas, E. Meyhofer, P. Reddy, Quantized thermal transport in single-atom junctions, Science 355 (6330) (2017) 1192–1195.

[76] N. Mosso, U. Drechsler, F. Menges, P. Nirmalraj, S. Karg, H. Riel, B. Gotsmann, Heat transport through atomic contacts, Nature nanotechnology 12 (5) (2017) 430–433.

[77] B. Kubala, J. König, J. Pekola, Violation of the wiedemann-franz law in a single-electron transistor, Physical review letters 100 (6) (2008) 066801.

[78] U. Meirav, M. Kastner, M. Heiblum, S. Wind, One-dimensional electron gas in gaas: periodic conductance oscillations as a function of density, Physical Review B 40 (8) (1989) 5871.

[79] S. B. Field, M. Kastner, U. Meirav, J. Scott-Thomas, D. Antoniadis, H. I. Smith, S. Wind, Conductance oscillations periodic in the density of one-dimensional electron gases, Physical Review B 42 (6) (1990) 3523.

[80] E. Bonet, M. M. Deshmukh, D. Ralph, Solving rate equations for electron tunneling via discrete quantum states, Physical Review B 65 (4) (2002) 045317.

[81] C. W. Beenakker, Theory of coulomb-blockade oscillations in the conductance of a quantum dot, Physical Review B 44 (4) (1991) 1646.

[82] J. M. Thijssen, H. S. Van der Zant, Charge transport and single-electron effects in nanoscale systems, physica status solidi (b) 245 (8) (2008) 1455–1470.

[83] H. Park, J. Park, A. K. Lim, E. H. Anderson, A. P. Alivisatos, P. L. McEuen, Nanomechanical oscillations in a single-c 60 transistor, Nature 407 (6800) (2000) 57–60.

[84] A. G. Corral, Yu-shiba-rusinov states in superconductor-quantum dot transistors made by electromigration, Ph.D. thesis, Université Grenoble Alpes [2020] (2020).

[85] C. B. Winkelmann, N. Roch, W. Wernsdorfer, V. Bouchiat, F. Balestro, Superconductivity in a single-c 60 transistor, Nature Physics 5 (12) (2009) 876–879.

[86] D. S. Duncan, C. Livermore, R. M. Westervelt, K. D. Maranowski, A. C. Gossard, Direct measurement of the destruction of charge quantization in a single-electron box, Applied physics letters 74 (7) (1999) 1045–1047.

[87] S. De Franceschi, S. Sasaki, J. Elzerman, W. Van Der Wiel, S. Tarucha, L. P. Kouwenhoven, Electron cotunneling in a semiconductor quantum dot, Physical review letters 86 (5) (2001) 878.

[88] M. Nilsson, L. Namazi, S. Lehmann, M. Leijnse, K. A. Dick, C. Thelander, Single-electron transport in inas nanowire quantum dots formed by crystal phase engineering, Physical Review B 93 (19) (2016) 195422.

[89] B. Dutta, J. T. Peltonen, D. S. Antonenko, M. Meschke, M. A. Skvortsov, B. Kubala, J. König, C. B. Winkelmann, H. Courtois, J. P. Pekola, Thermal conductance of a single-electron transistor, Phys. Rev. Lett. 119 (2017) 077701.

[90] M. Josefsson, A. Svilans, H. Linke, M. Leijnse, Optimal power and efficiency of single quantum dot heat engines: Theory and experiment, Physical Review B 99 (23) (2019) 235432.

[91] N. Roch, S. Florens, V. Bouchiat, W. Wernsdorfer, F. Balestro, Quantum phase transition in a single-molecule quantum dot, Nature 453 (7195) (2008) 633.

[92] J. Park, A. N. Pasupathy, J. I. Goldsmith, C. Chang, Y. Yaish, J. R. Petta, M. Rinkoski, J. P. Sethna, H. D. Abruña, P. L. McEuen, Coulomb blockade and the kondo effect in single-atom transistors, Nature 417 (6890) (2002) 722.

[93] W. Liang, M. P. Shores, M. Bockrath, J. R. Long, H. Park, Kondo resonance in a single-molecule transistor, Nature 417 (6890) (2002) 725.

[94] B. Dutta, Energétique dans les dispositifs a un seul électron basés sur des îlots métalliques et des points quantiques, Ph.D. thesis, Grenoble Alpes (2018).

[95] D. Van Zanten, Dynamique quantique dans un tourniquet à électrons basé sur une boîte quantique, Ph.D. thesis, Université Grenoble Alpes (ComUE) (2015).

[96] F. Lecocq, I. M. Pop, Z. Peng, I. Matei, T. Crozes, T. Fournier, C. Naud, W. Guichard, O. Buisson, Junction fabrication by shadow evaporation without a suspended bridge, Nanotechnology 22 (31) (2011) 315302.

[97] E. Philofsky, Intermetallic formation in gold-aluminum systems, Solid-State Electronics 13 (10) (1970) 1391–1394.

[98] G. Clatterbaugh, J. Weiner, H. Charles, Gold-aluminum intermetallics: Ball bond shear testing and thin film reaction couples, IEEE transactions on components, hybrids, and manufacturing technology 7 (4) (1984) 349–356.

[99] S. I. Khondaker, K. Luo, Z. Yao, The fabrication of single-electron transistors using dielectrophoretic trapping of individual gold nanoparticles, Nanotechnology 21 (9) (2010) 095204.

[100] W. Liu, C. Wang, H. Ding, J. Shao, Y. Ding, Ac electric field induced dielectrophoretic assembly behavior of gold nanoparticles in a wide frequency range, Applied Surface Science 370 (2016) 184–192.

[101] S. Kumar, S.-H. Yoon, G.-H. Kim, Bridging the nanogap electrodes with gold nanoparticles using dielectrophoresis technique, Current Applied Physics 9 (1) (2009) 101–103.

[102] M. L. Li, S. L. Leung, Y. L. Qu, Z. L. Dong, W. J. Li, Dielectrophoretic assembly of 2 nm gold particles for nano-sensing applications, in: 2010 IEEE 5th International Conference on Nano/Micro Engineered and Molecular Systems, IEEE, 2010, pp. 932–936.

[103] K. Bolotin, F. Kuemmeth, A. Pasupathy, D. Ralph, Metal-nanoparticle single-electron transistors fabricated using electromigration, Applied Phys. Lett. 84 (16) (2004) 3154–3156.

[104] H. Park, A. K. L. Lim, A. P. Alivisatos, J. Park, P. L. McEuen, Fabrication of metallic electrodes with nanometer separation by electromigration, Applied Physics Letters 75 (2) (1999) 301–303.

[105] D. R. Strachan, D. E. Smith, D. E. Johnston, T.-H. Park, M. J. Therien, D. A. Bonnell, A. T. Johnson, Controlled fabrication of nanogaps in ambient environment for molecular electronics, Applied Physics Letters 86 (4) (2005) 043109.

[106] Z. M. Wu, M. Steinacher, R. Huber, M. Calame, S. J. van der Molen, C. Schönenberger, Feedback controlled electromigration in four-terminal nanojunctions, Applied Physics Letters 91 (5) (2007) 053118.

[107] H. Park, A. K. Lim, A. P. Alivisatos, J. Park, P. L. McEuen, Fabrication of metallic electrodes with nanometer separation by electromigration, Applied Physics Letters 75 (2) (1999) 301–303.

[108] T. Kontos, M. Aprili, J. Lesueur, X. Grison, L. Dumoulin, Superconducting proximity effect at the paramagnetic-ferromagnetic transition, Physical review letters 93 (13) (2004) 137001.

[109] S. F. Svensson, S. Jeppesen, C. Thelander, L. Samuelson, H. Linke, K. Dick, Control and understanding of kink formation in inas–inp heterostructure nanowires, Nanotechnology 24 (34) (2013) 345601.

[110] S. F. Svensson, Thermoelectric Phenomena in Quantum Dots, Citeseer, 2014.

[111] B. Ohlsson, M. T. Björk, M. Magnusson, K. Deppert, L. Samuelson, L. Wallenberg, Size-, shape-, and position-controlled gaas nano-whiskers, Applied Physics Letters 79 (20) (2001) 3335–3337.

[112] D. Wharam, T. J. Thornton, R. Newbury, M. Pepper, H. Ahmed, J. Frost, D. Hasko, D. Peacock, D. Ritchie, G. Jones, One-dimensional transport and the quantisation of the ballistic resistance, Journal of Physics C: solid state physics 21 (8) (1988) L209.

[113] C. Thelander, M. Björk, M. Larsson, A. Hansen, L. Wallenberg, L. Samuelson, Electron transport in inas nanowires and heterostructure nanowire devices, Solid State Communications 131 (9-10) (2004) 573–579.

[114] S. Bhargava, H.-R. Blank, V. Narayanamurti, H. Kroemer, Fermi-level pinning position at the au–inas interface determined using ballistic electron emission microscopy, Applied physics letters 70 (6) (1997) 759–761.

[115] M. W. Larsson, J. B. Wagner, M. Wallin, P. Håkansson, L. E. Fröberg, L. Samuelson, L. R. Wallenberg, Strain mapping in free-standing heterostructured wurtzite inas/inp nanowires, Nanotechnology 18 (1) (2006) 015504.

[116] M. Björk, B. Ohlsson, C. Thelander, A. Persson, K. Deppert, L. Wallenberg, L. Samuelson, Nanowire resonant tunneling diodes, Applied Physics Letters 81 (23) (2002) 4458–4460.

[117] L. E. Jensen, M. T. Björk, S. Jeppesen, A. I. Persson, B. J. Ohlsson, L. Samuelson, Role of surface diffusion in chemical beam epitaxy of inas nanowires, Nano Letters 4 (10) (2004) 1961–1964.

[118] A. Persson, L. Fröberg, S. Jeppesen, M. Björk, L. Samuelson, Surface diffusion effects on growth of nanowires by chemical beam epitaxy, Journal of Applied Physics 101 (3) (2007) 034313.

[119] Y. Kawamura, K. Toyoda, S. Namba, Deep uv submicron lithography by using a pulsed high-power excimer laser, Journal of Applied Physics 53 (9) (1982) 6489–6490.

[120] A. A. Tseng, K. Chen, C. D. Chen, K. J. Ma, Electron beam lithography in nanoscale fabrication: recent development, IEEE Transactions on electronics packaging manufacturing 26 (2) (2003) 141–149.

[121] B. Karimi, J. P. Pekola, Noninvasive thermometer based on the zero-bias anomaly of a superconducting junction for ultrasensitive calorimetry, Physical Review Applied 10 (5) (2018) 054048.

[122] J. P. Pekola, Towards quantum thermodynamics in electronic circuits, Nature Physics 11 (2) (2015) 118–123.

[123] O.-P. Saira, M. Meschke, F. Giazotto, A. M. Savin, M. Möttönen, J. P. Pekola, Heat transistor: Demonstration of gate-controlled electronic refrigeration, Physical review letters 99 (2) (2007) 027203.

[124] S. P. Langley, The" bolometer", The Society, 1881.

[125] P. Richards, Bolometers for infrared and millimeter waves, Journal of Applied Physics 76 (1) (1994) 1–24.

[126] F. Wellstood, C. Urbina, J. Clarke, Hot-electron effects in metals, Physical Review B 49 (9) (1994) 5942.

[127] L. Wang, D. Golubev, Y. Galperin, J. Pekola, Dynamic thermal relaxation in metallic films at sub-kelvin temperatures, arXiv preprint arXiv:1910.09448 (2019).

[128] S. Gasparinetti, K. Viisanen, O.-P. Saira, T. Faivre, M. Arzeo, M. Meschke, J. P. Pekola, Fast electron thermometry for ultrasensitive calorimetric detection, Physical Review Applied 3 (1) (2015) 014007.

[129] K. L. Viisanen, S. Suomela, S. Gasparinetti, O.-P. Saira, J. Ankerhold, J. P. Pekola, Incomplete measurement of work in a dissipative two level system, New Journal of Physics 17 (5) (2015) 055014.

[130] K. Viisanen, J. Pekola, Anomalous electronic heat capacity of copper nanowires at sub-kelvin temperatures, Physical Review B 97 (11) (2018) 115422.

[131] E. Tikhonov, D. Shovkun, D. Ercolani, F. Rossella, M. Rocci, L. Sorba, S. Roddaro, V. Khrapai, Local noise in a diffusive conductor, Scientific reports 6 (1) (2016) 1–7.

[132] F. Giazotto, M. J. Martínez-Pérez, The josephson heat interferometer, Nature 492 (7429) (2012) 401–405.

[133] B. D. Josephson, Possible new effects in superconductive tunnelling, Physics letters 1 (7) (1962) 251–253.

[134] K. Likharev, Superconducting weak links, Reviews of Modern Physics 51 (1) (1979) 101.

[135] L. Angers, F. Chiodi, G. Montambaux, M. Ferrier, S. Guéron, H. Bouchiat, J. Cuevas, Proximity dc squids in the long-junction limit, Physical Review B 77 (16) (2008) 165408.

[136] M. Crosser, J. Huang, F. Pierre, P. Virtanen, T. T. Heikkilä, F. Wilhelm, N. O. Birge, Nonequilibrium transport in mesoscopic multi-terminal sns josephson junctions, Physical Review B 77 (1) (2008) 014528.

[137] P. Dubos, H. Courtois, B. Pannetier, F. Wilhelm, A. Zaikin, G. Schön, Josephson critical current in a long mesoscopic sns junction, Physical Review B 63 (6) (2001) 064502.

[138] H. Courtois, M. Meschke, J. Peltonen, J. P. Pekola, Origin of hysteresis in a proximity josephson junction, Physical review letters 101 (6) (2008) 067002.

[139] H. B. Heersche, P. Jarillo-Herrero, J. B. Oostinga, L. M. Vandersypen, A. F. Morpurgo, Bipolar supercurrent in graphene, Nature 446 (7131) (2007) 56–59.

[140] Y.-J. Doh, J. A. van Dam, A. L. Roest, E. P. Bakkers, L. P. Kouwenhoven, S. De Franceschi, Tunable supercurrent through semiconductor nanowires, science 309 (5732) (2005) 272–275.

[141] J.-P. Cleuziou, W. Wernsdorfer, V. Bouchiat, T. Ondarçuhu, M. Monthioux, Carbon nanotube superconducting quantum interference device, Nature nanotechnology 1 (1) (2006) 53–59.

[142] A. de Cecco, Quantum electronics in nanostructures explored by scanning probe microscopy, Ph.D. thesis, Université Grenoble Alpes (2018).

[143] M. Tinkham, Dover.“, Introduction to Superconductivity”, 2nd edition: New York (1996).

[144] K. K. Likharev, J. Lukens, Dynamics of josephson junctions and circuits, Physics Today 41 (11) (1988) 122.

[145] B. Pannetier, H. Courtois, Andreev reflection and proximity effect, Journal of low temperature physics 118 (5) (2000) 599–615.

[146] P. D. Saint-James, Excitations élémentaires au voisinage de la surface de séparation d'un métal normal et d'un métal supraconducteur, in: PG De Gennes' Impact on Science—Volume I: Solid State and Liquid Crystals, World Scientific, 2009, pp. 34–40.

[147] A. Andreev, Thermal conductivity of superconductors intermediate state, Soviet Phys. ZhETP 46 (5) (1964) 1823–1828.

[148] P. Dubos, H. Courtois, O. Buisson, B. Pannetier, Coherent low-energy charge transport in a diffusive sns junction, Physical review letters 87 (20) (2001) 206801.

[149] F. K. Wilhelm, A. D. Zaikin, G. Schön, Supercurrent in a mesoscopic proximity wire, Journal of Low Temperature Physics 106 (3-4) (1997) 305–310.

[150] A. Bishop, S. Trullinger, Josephson-junction threshold viewed as a critical point, Physical Review B 17 (5) (1978) 2175.

[151] M. Meschke, Nanosized electronic cooler combined with superconducting proximity effect thermometry, Journal of Low Temperature Physics 175 (5) (2014) 838–849.

[152] M. Zgirski, M. Foltyn, A. Savin, K. Norowski, M. Meschke, J. Pekola, Nanosecond thermometry with josephson junctions, Physical Review Applied 10 (4) (2018) 044068.

[153] D. Averin, K. Likharev, Mesoscopic phenomena in solids, edited by bl altshuler, PA Lee and RA Webb 173 (1991).

[154] G.-L. Ingold, Y. V. Nazarov, Charge tunneling rates in ultrasmall junctions, in: Single charge tunneling, Springer, 1992, pp. 21–107.

[155] S. Rajauria, Electronic refrigeration using superconducting tunnel junctions, Ph.D. thesis, Université Joseph-Fourier-Grenoble I (2008).

[156] L. Solymar, Superconducting Tunneling and Applications, Chapman and Hall, London, 1972.

[157] J.-G. Gluschke, S. F. Svensson, C. Thelander, H. Linke, Fully tunable, non-invasive thermal biasing of gated nanostructures suitable for low-temperature studies, Nanotechnology 25 (38) (2014) 385704.

[158] A. Svilans, M. Leijnse, H. Linke, Experiments on the thermoelectric properties of quantum dots, Comptes Rendus Physique 17 (10) (2016) 1096–1108.

[159] D. Majidi, M. Josefsson, M. Kumar, M. Leijnse, L. Samuelson, H. Courtois, C. Winkelmann, V. Maisi, Quantum confinement suppressing electronic heat flow below the wiedemann-franz law, arXiv preprint arXiv:2106.06229 (2021).

[160] S. Roddaro, D. Ercolani, M. A. Safeen, F. Rossella, V. Piazza, F. Giazotto, L. Sorba, F. Beltram, Large thermal biasing of individual gated nanostructures, Nano Research 7 (4) (2014) 579–587.

[161] A. O. Denisov, E. S. Tikhonov, S. U. Piatrusha, I. N. Khrapach, F. Rossella, M. Rocci, L. Sorba, S. Roddaro, V. S. Khrapai, Strategy for accurate thermal biasing at the nanoscale, Nanotechnology 31 (32) (2020) 324004.

[162] S. F. Svensson, E. A. Hoffmann, N. Nakpathomkun, P. M. Wu, H. Xu, H. A. Nilsson, D. Sánchez, V. Kashcheyevs, H. Linke, Nonlinear thermovoltage and thermocurrent in quantum dots, New Journal of Physics 15 (10) (2013) 105011.

[163] J. P. Small, K. M. Perez, P. Kim, Modulation of thermoelectric power of individual carbon nanotubes, Physical Review Letters 91 (25) (2003) 256801.

[164] H. Van Houten, L. Molenkamp, C. Beenakker, C. Foxon, Thermo-electric properties of quantum point contacts, Semiconductor Science and Technology 7 (3B) (1992) B215.

[165] E. A. Hoffmann, H. A. Nilsson, J. E. Matthews, N. Nakpathomkun, A. I. Persson, L. Samuelson, H. Linke, Measuring temperature gradients over nanometer length scales, Nano letters 9 (2) (2009) 779–783.

[166] Y. Tian, M. R. Sakr, J. M. Kinder, D. Liang, M. J. MacDonald, R. L. Qiu, H.-J. Gao, X. P. Gao, One-dimensional quantum confinement effect modulated thermoelectric properties in inas nanowires, Nano letters 12 (12) (2012) 6492–6497.

[167] J. Moon, J.-H. Kim, Z. C. Chen, J. Xiang, R. Chen, Gate-modulated thermoelectric power factor of hole gas in ge–si core–shell nanowires, Nano letters 13 (3) (2013) 1196–1202.

[168] R. Mitdank, M. Handwerg, C. Steinweg, W. Töllner, M. Daub, K. Nielsch, S. Fischer, Enhanced magneto-thermoelectric power factor of a 70 nm ni-nanowire, Journal of Applied Physics 111 (10) (2012) 104320.

[169] M. L. Roukes, M. Freeman, R. Germain, R. Richardson, M. Ketchen, Hot electrons and energy transport in metals at millikelvin temperatures, Physical review letters 55 (4) (1985) 422.

[170] P. Echternach, M. Thoman, C. Gould, H. Bozler, Electron-phonon scattering rates in disordered metallic films below 1 k, Physical Review B 46 (16) (1992) 10339.

[171] M. Kanskar, M. Wybourne, Crossover between dissipative and nondissipative electron transport in metal wires, Physical review letters 73 (15) (1994) 2123.

[172] A. Vinante, P. Falferi, R. Mezzena, M. Mück, Hot-electron effect in palladium thin films, Physical Review B 75 (10) (2007) 104303.

[173] F. Hekking, A. Niskanen, J. P. Pekola, Electron-phonon coupling and longitudinal mechanical-mode cooling in a metallic nanowire, Physical Review B 77 (3) (2008) 033401.

[174] D. Belitz, S. D. Sarma, Inelastic phase-coherence time in thin metal films, Physical Review B 36 (14) (1987) 7701.

[175] J. Peltonen, P. Virtanen, M. Meschke, J. Koski, T. Heikkilä, J. P. Pekola, Thermal conductance by the inverse proximity effect in a superconductor, Physical review letters 105 (9) (2010) 097004.

[176] D. Ralph, C. Black, M. Tinkham, Spectroscopic measurements of discrete electronic states in single metal particles, Physical review letters 74 (16) (1995) 3241.

[177] H. Pothier, S. Guéron, N. O. Birge, D. Esteve, M. Devoret, Energy distribution function of quasiparticles in mesoscopic wires, Physical review letters 79 (18) (1997) 3490.

[178] F. Pierre, A. Anthore, H. Pothier, C. Urbina, D. Esteve, Multiple andreev reflections revealed by the energy distribution of quasiparticles, Physical review letters 86 (6) (2001) 1078.

[179] D. Schmidt, R. Schoelkopf, A. Cleland, Photon-mediated thermal relaxation of electrons in nanostructures, Physical review letters 93 (4) (2004) 045901.

[180] B. Karimi, F. Brange, P. Samuelsson, J. P. Pekola, Reaching the ultimate energy resolution of a quantum detector, Nature communications 11 (1) (2020) 1–6.

[181] G. Stefanucci, R. Van Leeuwen, Nonequilibrium many-body theory of quantum systems: a modern introduction, Cambridge University Press, 2013.

[182] N. Talarico, S. Maniscalco, N. L. Gullo, Study of the energy variation in many-body open quantum systems: Role of interactions in the weak and strong coupling regimes, Physical Review B 101 (4) (2020) 045103.

[183] Y. Kim, W. Jeong, K. Kim, W. Lee, P. Reddy, Electrostatic control of thermoelectricity in molecular junctions, Nature nanotechnology 9 (11) (2014) 881–885.

[184] C. Fasth, A. Fuhrer, L. Samuelson, V. N. Golovach, D. Loss, Direct measurement of the spin-orbit interaction in a two-electron inas nanowire quantum dot, Physical review letters 98 (26) (2007) 266801.

[185] J. Matthews, E. A. Hoffmann, C. Weber, A. Wacker, H. Linke, Heat flow in InAs/InP heterostructure nanowires, Phys. Rev. B 86 (17) (2012) 174302.

[186] S. Chuang, Q. Gao, R. Kapadia, A. C. Ford, J. Guo, A. Javey, Ballistic inas nanowire transistors, Nano letters 13 (2) (2013) 555–558.

[187] L. P. Kouwenhoven, D. Austing, S. Tarucha, Few-electron quantum dots, Reports on Progress in Physics 64 (6) (2001) 701.

[188] C. Fasth, A. Fuhrer, M. T. Björk, L. Samuelson, Tunable double quantum dots in inas nanowires defined by local gate electrodes, Nano letters 5 (7) (2005) 1487–1490.

[189] M. T. Björk, C. Thelander, A. E. Hansen, L. E. Jensen, M. W. Larsson, L. R. Wallenberg, L. Samuelson, Few-electron quantum dots in nanowires, Nano Letters 4 (9) (2004) 1621–1625.

[190] C. Prasad, D. K. Ferry, H. H. Wieder, Energy relaxation studies in $In_{0.52}Al_{0.48}As$/ $In_{0.53}Ga_{0.47}As$/$In_{0.52}Al_{0.48}As$ two-dimensional electron gases and quantum wires, Semicond. Sci. Technol. 19 (4) (2004) S60.

[191] T. Sugaya, J. P. Bird, D. K. Ferry, A. Sergeev, V. Mitin, K.-Y. Jang, M. Ogura, Y. Sugiyama, Experimental studies of the electron–phonon interaction in InGaAs quantum wires, Appl. Phys. Lett. 81 (4) (2002) 727–729.

[192] S. Roddaro, D. Ercolani, M. A. Safeen, S. Suomalainen, F. Rossella, F. Giazotto, L. Sorba, F. Beltram, Giant thermovoltage in single InAs nanowire field-effect transistors, Nano Lett. 13 (8) (2013) 3638–3642.

[193] R. López, D. Sánchez, Nonlinear heat transport in mesoscopic conductors: Rectification, Peltier effect, and Wiedemann-Franz law, Phys. Rev. B 88 (4) (2013) 045129.

[194] Y. Dubi, M. Di Ventra, Colloquium: Heat flow and thermoelectricity in atomic and molecular junctions, Reviews of Modern Physics 83 (1) (2011) 131.

[195] A. Harzheim, J. K. Sowa, J. L. Swett, G. A. D. Briggs, J. A. Mol, P. Gehring, Role of metallic leads and electronic degeneracies in thermoelectric power generation in quantum dots, Physical Review Research 2 (1) (2020) 013140.

[196] J. König, H. Schoeller, G. Schön, Cotunneling at resonance for the single-electron transistor, Physical review letters 78 (23) (1997) 4482.

[197] M. Leijnse, M. Wegewijs, Kinetic equations for transport through single-molecule transistors, Physical Review B 78 (23) (2008) 235424.

[198] N. Gergs, S. Bender, R. Duine, D. Schuricht, Spin switching via quantum dot spin valves, Physical review letters 120 (1) (2018) 017701.

[199] D. Goldhaber-Gordon, H. Shtrikman, D. Mahalu, D. Abusch-Magder, U. Meirav, M. Kastner, Kondo effect in a single-electron transistor, Nature 391 (6663) (1998) 156–159.